Experimental study of dense suspension flow under cone-plate device

Wei Zhu

▶ **To cite this version:**

Wei Zhu. Experimental study of dense suspension flow under cone-plate device. Fluids mechanics [physics.class-ph]. Ecole Centrale Marseille, 2016. English. NNT : 2016ECDM0007 . tel-01562493

HAL Id: tel-01562493

https://theses.hal.science/tel-01562493

Submitted on 15 Jul 2017

HAL is a multi-disciplinary open access archive for the deposit and dissemination of scientific research documents, whether they are published or not. The documents may come from teaching and research institutions in France or abroad, or from public or private research centers.

L'archive ouverte pluridisciplinaire **HAL**, est destinée au dépôt et à la diffusion de documents scientifiques de niveau recherche, publiés ou non, émanant des établissements d'enseignement et de recherche français ou étrangers, des laboratoires publics ou privés.

ECOLE CENTRALE DE MARSEILLE

ED 353 – SCIENCES POUR L'INGENIEUR : MECANIQUE, PHYSIQUE, MICRO ET NANOELECTRONIQUE

IRPHE UMR 7342, Equipe Biomécanique

Thèse présentée pour obtenir le grade universitaire de docteur

Discipline: Mécanique et Physique des fluides

Wei ZHU

Experimental study of dense suspension flow under cone-plate device

Soutenue le 14/10/2016 devant le jury :

Cécile LEGALLAIS, Directrice de recherche CNRS, BMBI, Compiègne, Rapporteur
Stéphane NOTTIN, Maître de Conférences, Univ d'Avignon, LaPEC, Rapporteur
Nadine CANDONI, Professeur Aix-Marseille Université, CINaM, Examinatrice
Valérie DEPLANO, Directrice de recherche CNRS, IRPHE, Directrice de thèse
Yannick KNAPP, Maître de Conférences, Univ d'Avignon, Co-directeur de thèse

Résumé

Par rapport à un fluide Newtonien, les suspensions denses de particules présentent des propriétés rhéologiques différentes. Des comportements rhéofluidifiants ou rhéoépaississants lié à des phénomènes de migration de particules peuvent apparaitre.

Pour des suspensions, le taux de cisaillement, la concentration et la taille des particules ont une grande influence sur ce comportement rhéologique (Denn et Morris 2014). Pour observer l'influence de ces facteurs, l'un des meilleurs moyens est de disposer d'un système simple dans lequel tous les facteurs mentionnés ci-dessus sont bien contrôlés. Ceci peut être réalisé par le développement d'une plate-forme expérimentale, sur laquelle les comportements d'écoulement de suspension (profil de vitesse et concentration locale de particules) à des vitesses de cisaillement et des concentrations de particules bien contrôlées peuvent être étudiés.

Dans l'étude actuelle, 4 tâches ont été réalisées:

1) Le développement d'une nouvelle formulation pour la préparation d'une suspension adaptée en indice de réfraction et en densité basée sur des particules de PMMA.
2) Le développement d'un dispositif expérimental consacré à l'étude des flux de suspension dense sous une large gamme de taux de cisaillement constant.
3) La caractérisation des profils de vitesse des flux de suspension dense sous un dispositif cône-plan utilisant des techniques de micro-PIV.
4) Une mesure préliminaire de la concentration locale de particules de la suspension sous écoulement cône-plan en utilisant des méthodes de traitement d'image.

Mots clés : suspension, rhéologie, adaptation de l'indice de réfraction et de la densité, micro-vélocimétrie par images de particules

Abstract

Compared to general Newtonian fluids, highly concentrated mixtures of particles and fluid, so called dense suspensions, have different rheological properties and fluid dynamic behaviors. Such as, shear-thinning or shear-thickening effect, and apparent slip and particle migration behaviors under certain shear flow conditions. These properties are related to the application of suspension flow in real systems, for example, the blood.

For suspensions, shear rate, particle concentration and particle size have a big influence of on their rheological behaviors (Denn and Morris 2014). To observe the influence of these factors, one of the best ways is to start the research from a simple case in which all the above mentioned factors are well controlled. This can be realized by developing such an experimental platform, on which the suspension flow behaviors (velocity profile and local particle concentration) at different shear rates and particle concentrations can be investigated.

In the current study, 4 tasks were achieved:

1) The development of a new recipe for the preparation of density and refractive index matched suspension with PMMA particles.
2) The development of an experimental set-up devoted to the investigation of dense suspension flow under a large range of constant shear rate.
3) The characterization of the velocity profiles of dense suspension flows under a cone-plate device by using micro-PIV techniques.
4) A preliminary measurement of the local particle concentration of the suspension flow by using image processing techniques.

Keywords: suspension, rheology, refractive index and density matching, micro particle image Velocimetry, cone-plate, defocused particle locating

Acknowledgements

In the study of my thesis, I thank all the people who have helped me and encouraged me.

My deepest gratitude goes first and foremost to my co-director Yannick Knapp, for his constant encouragement and guidance. He has walked me through all the stages of the work of this thesis. Without his consistent and illuminating instruction, this thesis could not have reached its present form.

Secondly, I would thank my director Valérie Deplano, who has shown much patience to help me to improve my presentation skill, and to help me to develop a rigorous academic habit.

Besides my advisors, I would like to thank the rest of my thesis committee: Dr. Cécile Legallais, Prof. Nadine Candoni, and Dr. Nottin Stéphane, for their insightful comments and encouragement, but also for the hard question which incented me to widen my research from various perspectives.

I thank Eric Bertrand, who helped me to make some experimental components and to fix some problems of the experimental set-up. I thank also Massimiliano Rossi, who gave me his code and some useful consultant on image processing.

Last, my thanks would go to my family for their loving considerations and great confidence in me all through these years. Especially, my mother keeps supporting and encouraging me in all the tough moments. I also owe my sincere gratitude to my friends, Rizqie Arbie, Medamine Chetoui, Adam Scheinherr, Kaili Xie, Zhuang Pei, Jun Chen, Zhanle Yu, Wen Ou, Rui Liu, Kailang Liu and Wei He, who gave me their help and time in listening to me and helping me work out my problems during the difficult course of the thesis.

Contents

Résumé i
Abstract ii
Acknowledgements iii
Contents iv
List of figures vii
List of tables xi
List of abbreviations xii
Notation xiii
Introduction 1
2 Literature review 5
2.1 Suspensions 5
2.1.1 Introduction 5
2.1.2 Classification of suspensions 6
2.1.3 Suspension viscosity 8
2.2 Flow geometries 19
2.2.1 Introduction 20
2.2.2 Drag flow geometries 20
2.2.3 Pressure driven flow geometries 22
2.3 Dense suspension flow dynamics 23
2.3.1 Introduction 23
2.3.2 Secondary flow 23
2.3.3 Apparent slip 25
2.3.4 Shear induced particle migration 28
2.4 Measurement techniques for suspension flow 30
2.4.1 Introduction 30

2.4.2 Micro-PIV 31
2.4.3 Particle locating method 39
2.5 Positioning of the study 45
3 Density and refractive index matched suspension model 47
3.1 Suspension preparation process 47
3.2 Suspension rheology 56
3.2.1 Measurement conditions 57
3.2.2 Results 57
3.2.3 Suspension rheology discussion 62
4 Experimental set-up and measurement techniques 67
4.1 Experimental set-up 67
4.1.1 Flow generation system 68
4.1.2 Flow measurement system 71
4.1.3 Environment control system 71
4.2 Velocity profile measurement 72
4.2.1 Determination of the velocity profile 72
4.2.2 $dH_{plane}/dH_{objective}$ ratio 73
4.2.3 Micro-PIV system parameters 75
4.3 Validation of experimental set-up 79
4.3.1 Threshold velocity of secondary flow 79
4.3.2 Velocity profiles of 0% particle suspension 80
4.4 Particle concentration measurement 83
4.4.1 Measurement principle 83
4.4.2 Particle locating program 85
4.4.3 Local particle concentration calculation 88
5 Experimental results 89
5.1 Suspension velocity profiles 89
5.1.1 Evolution of velocity profiles 89
5.1.2 Relative difference of shear rates 96
5.2 Apparent slip 97

5.2.1 Apparent slip characterization 97
5.2.2 Apparent slip discussion 103
5.3 Local particle concentration 106
5.3.1 N_{rp} value 106
5.3.2 Particle position determination 107
5.3.3 Local particle concentration calculation 113
5.4 Discussion 118
5.4.1 Particle migration 118
5.4.2 The influence on velocity profile measurement 121
6 Conclusion and perspective 125
Appendix A Equations of motion for cone-plate flow 129
Appendix B Viscosity data 134
Appendix C Velocity profiles 135
Appendix D Relative differences of shear rates 139
Appendix E Calculation of uncertainties 140
Glossary 142
References 143

List of figures

Fig 2.1 Conceptual classification of the rheophysical regimes of a suspension as a function of shear rate and solid fraction on a logarithmic scale (Coussot and Ancey 1999). 7
Fig 2.2 Relative viscosity vs. particle volume fraction predicted by Einstein's equation for dilute hard-sphere suspensions (Equation (2.6) with B = 2.5), and Krieger–Dougherty's equation for concentrated hard-sphere suspensions (Equation (2.9) with ϕ_m = 0.6) 10
Fig 2.3 Representation of relative viscosity versus shear rate for a fluid suspension (Stickel and Powell 2005). 11
Fig 2.4 Illustration of the alignment of the suspended particles following the flow direction (a) compared to the initial disordered state (b) 12
Fig 2.5 1.25μm PVC particles in dioctyl phthalate (R. L. Hoffman 1972) 13
Fig 2.6 Variation of critical shear rate with respect to ϕ 13
Fig 2.7 "Phase diagram" for suspension rheology, based solely on a dimensional analysis (Stickel and Powell 2005). 14
Fig 2.8 Contour plot of particle pair relative flux, for ϕ = 31.5%: a) Re = 0.1, b) Re = 10. (Picano et al. 2013) 15
Fig 2.9 Instantaneous configurations of transient clusters in the shear thickening regime, observed using fast confocal microscope. Different colors indicate different clusters. Particles outside the large clusters are drawn with smaller size for clarity (Cheng et al. 2011). 15
Fig 2.10 Variations of blood viscosity under different conditions as a function of shear rate (Chien 1970) 18
Fig 2.11 Rouleaux of human red cells photographed on a microscope slide showing single linear and branched aggregates (left part) and a network (right part). The number of cells in linear array are 2, 4, 9, 15, and 36 in a, b, c, d, f, respectively (Fung 1993). 18
Fig 2.12 Schematic illustration of parallel shear plates 20
Fig 2.13 Schematic illustration of Couette cell device 21
Fig 2.14 Schematic illustration of rotational parallel disks 21
Fig 2.15 Schematic illustration of cone-plate 22
Fig 2.16 Schematic illustration of capillary and micro channel 22
Fig 2.17 Normalized radial velocity profile of the theoretical deduction of Sdougos et al.(1983). Here u positive represents outward radial movement. 24
Fig 2.18 Schematic presentation of different boundary conditions: a) no-slip, b) true slip and c) apparent wall slip (Korhonen et al. 2015). 26
Fig 2.19 Layering of particle near the wall in concentric cylindrical Couette cell (Blanc et al. 2013) 27
Fig 2.20 Concentration profiles measured across the gap between rotating concentric cylinders using magnetic resonance imaging for suspensions with mean values of ϕ=0.58 (squares), 0.59 (circles), and 0.60 (triangles). (Ovarlez, Bertrand, and Rodts 2006) 29
Fig 2.21 Variation of the shear rate across the gap between rotating concentric cylinders, data source from (Ovarlez, Bertrand, and Rodts 2006) 29
Fig 2.22 Schematic illustration of a micro-PIV set-up (Lindken et al. 2009) 31
Fig 2.23 An example of the formation of the correlation plane by direct cross-correlation: here a 4×4 pixel

template is correlated with a larger 8×8 pixel sample to produce a 5×5 pixel correlation plane (Raffel et al. 2007a) 32
Fig 2.24 Peaks in a cross-correlation map with different shift distances, S_x and S_y represent the shift in the x and y directions respectively (Raffel et al. 2007a) 33
Fig 2.25 Schematic illustration of depth of focus and measurement plane width (Koutsiaris 2012) 34
Fig 2.26 Optical geometry used in deriving the particle image diameter (Rossi et al. 2011) 39
Fig 2.27 Schematic representation of the cross section of particle image intensity for different z-position based on equation (2.42) and (2.44), the particle image diameter d_τ increases for increasing z, while the peak intensity $I(r, z)$ decreases. The dashed line represents the geometrical spreading of an image of out of focus particle (Kloosterman, Poelma, and Westerweel 2010) 41
Fig 2.28 Illustration the position of a particle in the Cartesian coordinate based on the image plane 42
Fig 2.29 GDPT working principle: a target particle image I_t is compared to a set of calibration images I_c by using the normalized cross correlation. The out-of-plane coordinate z_t for the target particle is found where the maximum correlation C_m is the highest as a function of the out-of-plane coordinate Z (Barnkob, Kähler, and Rossi 2015). 44
Fig 3.1 Viscosity variations of 41μm particle suspensions at different concentrations with respect to shear rate. (The viscosity of the 2% 41μm particle suspension is not shown since it is too close to that of 0%. All the error bars are removed as they are too small compared to the minimum scale.) 58
Fig 3.2 Viscosity variations of 4.62μm particle suspensions at different concentrations with respect to shear rate. (The viscosity of the 2% 4.62μm particle suspension is not shown since it is too close to that of 0%. All the error bars are removed as they are too small compared to the minimum scale.) 59
Fig 3.3 Viscosity variation of 4.62μm particle suspension at ϕ=35% with respect to shear rate 60
Fig 3.4 Viscosity variation of 4.62μm particle suspension at ϕ=45% with respect to shear rate 60
Fig 3.5 Relative viscosities of 41μm particle suspensions at different shear rates as a function of particle concentration, where ϕ_m=0.582 is taken for the Krieger-Daugherty model. 61
Fig 3.6 Relative viscosities of 4.62μm particle suspensions at different shear rate as a function of particle concentration, where ϕ_m=0.596 is taken for the Krieger-Daugherty model. 62
Fig 3.7 “Phase diagram” for suspension rheology, based solely on a dimensional analysis. Image source from (Stickel and Powell 2005). 64
Fig 3.8 Relative viscosities of 4.62μm and 41μm particle suspensions at concentration of 45% compared to the relative viscosities of blood measured by Chien (1970) and Whitmore (1968) as a function of shear rate. 65
Fig 4.1 Illustration of the components under the cover 68
Fig 4.2 Illustration of the experimental set-up 68
Fig 4.3 Schematic illustration of the cone-plate device 69
Fig 4.4 Schematic illustration of the measured region in the x-y plane 69
Fig 4.5 Velocity profile (a) and the normalized velocity profile (b) of the flow under the cone-plate device with no slip and no secondary flow 70
Fig 4.6 Cover, temperature control module and foam cushion 72
Fig 4.7 An example of multi-plane of velocity fields and the generation of the corresponding velocity profile 73
Fig 4.8 Schematic illustration of the light path in the experimental set-up 74
Fig 4.9 Illustrations of the measured $-\mathrm{dH}_{\mathrm{plane}}$ and $\mathrm{dH}_{\mathrm{objective}}$ 74
Fig 4.10 Variations of the vector length (v) as a function of image pair of 0% and 20% 41μm particle suspension at 50 s^{-1} and at H=524μm. 79

Fig 4.11 Illustrations of secondary flow in a cone-plate device, a) the flow direction of secondary flow, b) illustration of the velocity vector near the cone surface and near the plate surface 80
Fig 4.12 Normalized velocity profiles of 0% particle suspension at: a)100s^{-1}, 50s^{-1} and 10s^{-1}, b) 5s^{-1}, 1$s^{-1}$and 0.5s^{-1}. 81
Fig 4.13 Normalized radial velocity profile of the theoretical deduction of Sdougos et al.(1983), and normalized radial velocity profile of the 0% particle suspension at 100s^{-1}, here u positive means outward radial movement. 82
Fig 4.14 u/v ratio based on the theoretical deduction of Sdougos et al.(1983), and of the 0% particle suspension at 100s^{-1}, here u positive means outward radial movement. 82
Fig 4.15 Schematic illustration of the local particle concentration measurement principle, where H is the measured height, the measurement plane width is 2d which will be described in section (4.4.3). 84
Fig 4.16 Illustrations of the particle position locating procedures 86
Fig 4.17 Illustration of the image calibration and z-position determination in measurement 87
Fig 4.18 Illustrations of the particle positions for local particle concentration calculation 88
Fig 5.1 Normalized velocity profiles of 41μm particle suspensions at ϕ=45%, 35%, 20% and at 10s^{-1}. 90
Fig 5.2 Normalized velocity profiles of 4.62μm particle suspensions at ϕ=45%, 35%, 20% and at 10s^{-1}. 90
Fig 5.3 Normalized velocity profiles of 41μm particle suspensions at ϕ=45%, 35%, 20% and at 1s^{-1}. 91
Fig 5.4 Normalized velocity profiles of 4.62μm particle suspensions at ϕ=45%, 35%, 20% and at 1s^{-1}. 92
Fig 5.5 Normalized velocity profiles of 45% 41μm particle suspension at 1s^{-1}, 10s^{-1}, and 100s^{-1}. 93
Fig 5.6 Normalized velocity profiles of 35% 41μm particle suspension at 1s^{-1}, 10s^{-1}, and 100s^{-1}. 93
Fig 5.7 Normalized velocity profiles of 20% 41μm particle suspension at 1s^{-1}, 10s^{-1}, and 100s^{-1}. 94
Fig 5.8 Normalized velocity profiles of 45% 4.62μm particle suspension at 1s^{-1}, 10s^{-1}, and 100s^{-1}. 95
Fig 5.9 Normalized velocity profiles of 45% 4.62μm particle suspension at 0.5s^{-1}, 5s^{-1}, and 50s^{-1}. 95
Fig 5.10 Relative differences of shear rates as a function of $\dot{\gamma}$ of 41μm particle suspension, the error bars of suspension at ϕ=10%, 5% and 0% are not shown. 96
Fig 5.11 Relative differences of shear rates as a function of $\dot{\gamma}$ of 4.62μm particle suspension, the error bars of suspension at ϕ=35%, 20%, 10%, 5% and 0% are not shown. 97
Fig 5.12 Schematic illustration of the slip layer in the parallel shear plates device 98
Fig 5.13 Schematic illustration of the velocity profile in the parallel shear plates device with the presence of apparent slip 98
Fig 5.14 v_s/V_{max} with respect to $\Delta\dot{\gamma}/\dot{\gamma}$ 101
Fig 5.15 Variations of the slip ratios: a) for 41μm particle suspensions at ϕ=45%, 35%, 20%, b) for 4.62μm particle suspensions at ϕ=45%. 102
Fig 5.16 Variations of slip layer thickness: a) for 41μm particle suspensions at ϕ=45%, 35% and 4.62μm particle suspensions at ϕ=45%, b) for 41μm particle suspensions at ϕ=20%. 102
Fig 5.17 An example of identified particle images, where the gray level threshold is 500, and the mini area threshold is 3000. The unit is pixels. 108
Fig 5.18 The measured Z position (blue, left Y-axis) with the corresponding correlation coefficient (orange, right Y-axis) as a function of the actual *Z* position, here the real unit is μm. 109
Fig 5.19 Variations of particle image at different Z positions, where the objective is approaching, then leaving the particle, Z=0 corresponds to the image taken at the furthest distance to the objective. 110
Fig 5.20 Variations of the intensity of the line pass image center following the increase of image number 110
Fig 5.21 Variation of the effective particle diameter (d_τ) with respect to Z position 111
Fig 5.22 C_m values with respect to Z positions in 45% 41μm particle suspension at 50s^{-1}: a) H=181μm, b)

H=812μm 112
Fig 5.23 C_m values with respect to Z position in 20% 41μm particle suspension at 50s^{-1}: a) H=181μm, b) H=812μm 112
Fig 5.24 Variations of ϕ_{local} following the increase of N_{im} for 45% 41μm particle suspension at different heights and at: a) $\dot{\gamma}$=50s^{-1}, b) $\dot{\gamma}$=1s^{-1}, the black line indicates the global particle concentration. 115
Fig 5.25 Variations of ϕ_{local} following the increase of N_{im} for 20% 41μm particle suspension at different heights and at: a) $\dot{\gamma}$=50s^{-1}, b) $\dot{\gamma}$=1s^{-1}, the black line indicates the global particle concentration. 115
Fig 5.26 Variations of ϕ_{local} following the increase of measurement plane width for 45% 41μm particle suspension at different heights and at: a)$\dot{\gamma}$=50s^{-1}, b) $\dot{\gamma}$=1s^{-1}, the black line indicates the global particle concentration. 116
Fig 5.27 Variations of ϕ_{local} following the increase of measurement plane width for 20% 41μm particle suspension at different heights and at: a) $\dot{\gamma}$=50s^{-1}, b) $\dot{\gamma}$=1s^{-1}, the black line indicates the global particle concentration. 116
Fig 5.28 Comparison of the particle Z position distributions of 45% 41μm particle suspension at 50s^{-1} and at: a) H=181μm, b) H=812μm, the red line indicates the focal plane position. 117
Fig 5.29 Comparison of the particle Z position distributions of 20% 41um particle suspension at 1s^{-1} and at: a) H=181μm, b) H=812μm, the red line indicates the focal plane position. 118
Fig 5.30 Normalized velocity profiles of 20% 41μm particle suspension at 5s-1, measured at different time 122
Fig C.1 Normalized velocity profiles of 5% 41μm particle suspension at: a)100s^{-1}, 10s^{-1} and 1s^{-1}, b) 50s^{-1}, 5s^{-1}and 0.5s^{-1}. 135
Fig C.2 Normalized velocity profiles of 10% 41μm particle suspension at: a)100s^{-1}, 10s^{-1} and 1s^{-1}, b) 50s^{-1}, 5s^{-1}and 0.5s^{-1}. 135
Fig C.3 Normalized velocity profiles of 20% 41μm particle suspension at: a)100s^{-1}, 10s^{-1} and 1s^{-1}, b) 50s^{-1}, 5s^{-1}and 0.5s^{-1}. 136
Fig C.4 Normalized velocity profiles of 35% 41μm particle suspension at: a)100s^{-1}, 10s^{-1} and 1s^{-1}, b) 50s^{-1}, 5s^{-1}and 0.5s^{-1}. 136
Fig C.5 Normalized velocity profiles of 45% 41μm particle suspension at: a)100s^{-1}, 10s^{-1} and 1s^{-1}, b) 50s^{-1}, 5s^{-1}and 0.5s^{-1}. 136
Fig C.6 Normalized velocity profiles of 5% 4.62μm particle suspension at: a)100s^{-1}, 10s^{-1} and 1s^{-1}, b) 50s^{-1}, 5s^{-1}and 0.5s^{-1}. 137
Fig C.7 Normalized velocity profiles of 10% 4.62μm particle suspension at: a)100s^{-1}, 10s^{-1} and 1s^{-1}, b) 50s^{-1}, 5s^{-1}and 0.5s^{-1}. 137
Fig C.8 Normalized velocity profiles of 20% 4.62μm particle suspension at: a)100s^{-1}, 10s^{-1} and 1s^{-1}, b) 50s^{-1}, 5s^{-1}and 0.5s^{-1}. 137
Fig C.9 Normalized velocity profiles of 35% 4.62μm particle suspension at: a)100s^{-1}, 10s^{-1} and 1s^{-1}, b) 50s^{-1}, 5s^{-1}and 0.5s^{-1}. 138
Fig C.10 Normalized velocity profiles of 45% 4.62μm particle suspension at: a)100s^{-1}, 10s^{-1} and 1s^{-1}, b) 50s^{-1}, 5s^{-1}and 0.5s^{-1}. 138

List of tables

Tab 2.1 Models for the estimation of secondary flow in a cone plate device 25
Tab 3.1 Densities and refractive indexes of the four components at T=25°C 47
Tab 3.2 Corresponding Pe, Re and Sc values for the two sizes of particles at different shear rates 63
Tab 4.1 Shear rates and corresponding rotational speeds 70
Tab 4.2 Measured $-dH_{plane}/dH_{objective}$ ratios at different temperatures 75
Tab 4.3 General parameters of the micro-PIV experiments 76
Tab 4.4 Micro-PIV experiment characterization parameters 77
Tab 4.5 An example of the estimated Δt at different heights and at different shear rates for a displacement of 14 pixels, the time unit is μs. 77
Tab 4.6 Measurement error estimation 78
Tab 4.7 Threshold rotary speeds of secondary flow 80
Tab 4.8 u/v ratios of the 0% particle suspension at different heights and at different shear rates 83
Tab 5.1 Slip layer thicknesses and slip velocities of 45% 41μm particle suspension with H_{max}=963μm 100
Tab 5.2 Slip layer thicknesses and slip velocities of 35% 41μm particle suspension with H_{max}=1046μm 100
Tab 5.3 Slip layer thicknesses and slip velocities of 20% 41 μm particle suspension with H_{max}=1032μm100
Tab 5.4 Slip layer thicknesses and slip velocities of 45% 4.62 μm particle suspension with H_{max}=918μm 100
Tab 5.5 Comparisons of the slip layer thicknesses at different experiments 104
Tab 5.6 Corresponding Pe values of the two sizes of particle at different shear rates 105
Tab 5.7 Comparison of detected particles with different gray level thresholds and minimum area thresholds 108
Tab 5.8 Coordinates and correlation coefficients of detected particles in Fig 5.17, with gray level threshold equal to 500, and the mini area threshold equal to 3000. 108
Tab 5.9 Percentage of detected particles with C_m value > 0.9 111
Tab 5.10 Estimated local particle concentrations of 45% 41 μm particle suspension 113
Tab 5.11 Estimated local particle concentrations of 20% 41 μm particle suspension 114
Tab 5.12 Float (or sedimentation) velocity of particle 41 μm within different suspensions 119
Tab B.1 Measured viscosities of 41μm particle suspensions at different concentration and at different shear rate 134
Tab B.2 Measured viscosities of 4.62μm particle suspensions at different concentration and at different shear rate 134
Tab D.1 Relative difference of shear rates of 41μm particle suspension at different shear rates and at different particle concentrations 139
Tab D.2 Relative difference of shear rates of 4.62μm particle suspension at different shear rates and at different particle concentrations 139

List of abbreviations

DOC	Depth of correlation
DoF	Depth of focus
FFT	Fast Fourier Transform
GDPT	General Defocusing Particle Tracking
IW	Interrogation Window
MPW	Measurement Plane Width
NMR	Nuclear Magnetic Resonance
LDV	Laser Doppler Velocimetry
PBS	Phosphate Buffered Saline
PMMA	Poly Methyl MethAcrylate
PIV	Particle Image Velocimetry
PTV	Particle Tracking Velocimetry
RBC	Red Blood Cell
RPM	Rotation Per Minute
STD	Standard error
TDE	2.2'-Thiodiethanol

Notation

a	Depth of measurement
A	Measurement plane area
B	Intrinsic viscosity
B_1	Coefficient (Equation 2.6)
c	Coefficient (Equation 2.38)
C	Correlation coefficient
C_m	Maximum correlation coefficient
C_{tr}	Tracer particle concentration
d	½ measurement plane width
d_f	Defocused term of particle image
d_p	Particle diameter
d_{pL}	Diameter of large particle
d_{pS}	Diameter of small particle
d_s	Diffraction term of particle image
d_{step}	Incremental distance of calibration
d_τ	Particle image diameter
D	Diffusion coefficient
D_a	Objective lens diameter
D_{pixel}	Pixel size
f	Focal distance
$f_\#$	f number
g	Gravity
h	Height of the bulk fluid
H	Height
H_{gap}	Height of the gap
H_{max}	Maximum height
I	Particle image intensity
J_p	Flux of light
$k1, k2$	Constant (Equation 2.18)
k_B	Boltzmann's constant
k_p	Length to diameter ratio
l_p	Length of particle
L	Length
L_f	Thickness of the measured flow
m	Particle number density
M	Magnification of objective
n	Refractive index (RI)
n_0	RI of lens immersion fluid
n_L	RI of the observed fluid
N_{im}	Number of images
N_{rp}	Average number of particles represented by a dyed particle
NA	Numerical aperture
ΔP	Pressure drop
r	Coordinate sign
r_p	Particle radius
R	Radius
R_c	Cone radius
s_i	Image plane distance
s_o	Focal plane distance
t	Time
Δt	Time interval
T	Temperature
T_a	Absolute temperature
u, u	Radial Velocity
v, v	Tangential Velocity
v_s	Slip velocity
V	Velocity
V_{dye}	Volume of dyed particles
V_{fs}, V_∞	float/sedimentation velocity
V_z	Tracer particle visibility
V_{max}	Maximum velocity
x, X	Coordinate signs
y, Y	Coordinate signs
z, Z	Coordinate signs
$\tilde{z}$	Normalized height (Equation 2.15)

Greek letter

$\dot{\gamma}$	Shear rate
$\dot{\gamma}_m$	Measured shear rate
$\dot{\gamma}_c$	Critical shear rate
ϕ	Particle volume fraction
ϕ_m	Particle maximum packing fraction
ϕ_{m-eff}	Effective maximum packing fraction
ϕ_{local}	Local particle concentration
η	Dynamic viscosity
η_L	Dynamic viscosity of liquid
η_s	Dynamic viscosity of suspension
η_r	Relative viscosity
θ	Coordinate sign
β	Coefficient (Equation 2.24)
ω	Rotary speed
α	Cone angle
δ	Slip layer thickness
ρ_p	Particle density
ρ_L	Fluid density
$\Delta\rho$	Density difference
ε	Coefficient (Equation 2.22)
ε_{rd}	Random error
ε_x	Brownian motion error
λ	Laser wavelength
τ_p	Response time
τ_w	Wall shear stress

Dimensionless number

Pe	Peclet number
Re	Reynolds number
$\widetilde{Re}$	Pseudo Reynolds number
Sc	Schmidt number

Introduction

Compared to general Newtonian fluids, highly concentrated mixtures of particles and fluid, so called dense suspensions, have different rheological properties and fluid dynamic behaviors. Blood is an example of dense suspension as it is a concentrated mixture of red blood cells (45% v/v) suspended in plasma, a Newtonian fluid. One can therefore expect to study the rheological behavior of blood taking in account the abundant literature on suspension flows. Red blood cells (RBC) are small deformable particles of disk like particles, 6-8 microns in diameter and 3 to 5microns thick. Their deformability plays also an important role in the rheological behavior of the suspension : (i) RBCs undergo high deformations under high shear rates (and even lysis/breakup in some conditions) in order to allow RBC transport in capillaries of diameter smaller than the RBC themselves, (ii) RBC deformability promotes aggregation under small shear rates; RBCs assembles to form so called rouleaux structures.

RBC aggregation is a common homeostatic process, but in some pathological conditions, abnormal hyper-aggregation can be observed; deep venous thrombosis, atherosclerosis, and diabetes mellitus are from the much pathology that exhibits such symptoms. Here assemblies of several dozens of RBCs can form large size assemblies with no specific shape. This abnormal aggregation is still a research topic and its study will be one of the motivations of the present research developments. **The objective of the present research work is to develop an optical platform in which particle suspensions will be set in motion under controlled conditions. Such suspensions will be observed on the microscopic scale in order to quantify flow and particle dynamics of both individual particles mimicking RBC behavior and their aggregates.**

Moreover, in order to diagnose abnormal aggregation and their potential consequences it is common to analyze a blood sample obtained from a venipuncture; the blood is left at rest and settling time is measured. Even if more sophisticated procedures exist, it is quite reasonable to hypothesize that since the suspension of RBC and the individual RBCs are sensitive to shear rate such a method can only be used as a primary indicator for such a behavior; more sophisticated in vivo procedures should be made available in clinical routine. The development of such a technology is the second important background motivating the present study. In particular, part of the present work and its extension comes in support of the development of the determination of aggregate size and concentration by post processing of ultrasonic backscattered signals. The

implementation of such measurements in the aforementioned optical setup will add specific constraints both in the setup and in the blood mimicking suspensions that will be studied.

Thus, one long-term objective of this work is to validate a theoretical model and an ultrasonic method (Franceschini et al. 2010) developed by a team in Laboratory Acoustic and Mechanic which is used to measure the local concentration of blood in situ. One way to validate their model and method is to compare their measurement result with that of another method which can give a direct view on the particle concentration under known flow conditions. Therefore, the experimental set-up developed for the present work is supposed to host two ultrasonic captors in order to perform simultaneous acoustic and optical measurements of both flow and concentration.

The blood, as most biological samples, has safety and lifetime issues, but is mainly an opaque fluid with complex optical properties. These properties result from absorption of light at specific wavelengths by various molecules present in the suspension and diffusion of light from small scatterers like RBCs. For both reasons it is preferable to find a proper surrogate of such a fluid in order, in a first step, to overcome the limitations resulting from the aforementioned complexities.

A literature review on blood flow and on flow of highly concentrated suspensions of various solid materials shows that shear rate, particle size, and concentration, but also wall-fluid-particles interactions, play major roles in the suspension's rheological behavior. This behavior is governed by particle diffusion, migration and aggregation phenomena when the suspension is under flow. In order to be able to identify and quantify such phenomena it is important to maintain a clear and simple control on suspension and flow definitions. Although various flow conditions can be generated at the microscopic scale, a simple shear flow resulting from the relative displacement of two solid surfaces is chosen.

In this context the present work is declined in 3 coupled tasks:

- the definition and implementation of a transparent fluid-particle mixture as a surrogate for blood,
- the definition and implementation of an experimental setup in which the defined suspension is caused to flow,
- the definition and implementation of instrumental procedures able to give a quantitative characterization of fluid and particle dynamics.

Concerning the first task, as the present work is mainly exploratory the implementation of rigid particles was preferred. In addition, this choice offers the possibility to repeat

results presented in the literature. A preliminary sorting of solutions also described in the literature tended to promote the use of low density polymers as material for the particles. Such particles are commercially available in various sizes and can therefore be chosen in order for example to mimic RBCs (particles in the micron size range) and/or aggregates (particles in the 10 micron size range). The use of a material such as PMMA allows to focus the work on the definition of a suspending fluid able to adapt the refractive index and density of the particles.

Secondly, in order to facilitate the investigations, velocity controlled cone-plate geometry was chosen to generate the flow. Among different constraints the possibility to have an oscillating flow generated by a low inertial geometry but mainly the opportunity to have a simple optical access for both optical and future ultrasonic measurements has guided such a choice. This device was installed on a commercial inverted microscope so that experiments to characterize the flow and interactions of micron sized objects can be carried on.

Finally, concerning the third task, two main measurement techniques are considered. The first aims to characterize the flow dynamics of the sheared flow generated by the cone-plate gap. Microscopic particle image velocimetry measurements are therefore implemented. The second aims to give access to local particle concentrations. Specific image processing is to be developed for this purpose. Note that since both techniques rely on the optical detection of tracer particles, procedures to fabricate such tracers were developed and implemented.

The present manuscript is organized as follows:

Chapter 2 presents a literature review on the state of the art of the study of concentrated suspension flows. This part includes suspension classification, rheology, and flow behavior. Experimental techniques available in the literature to set the suspensions in motion and to characterize them optically are also presented.

Chapter 3 reports the definition of a refractive index and density matched fluid-particle mixture. This chapter introduces a new technique and recipe for the preparation of transparent dense suspensions based on PMMA particles. The rheological behavior of the developed suspensions is also presented.

In chapter 4, the experimental set-up and the measurement techniques used in this work are described and validated. Concerning the flow conditions the validation procedure is focused on the absence of secondary flow in the case of a suspension at 0% particles. Concerning the determination of local concentrations the methodology, image processing and validations are presented.

The 5th chapter addresses the main experimental results. The flow field characterizations in the cone-plane gap are first presented for various shear rates, particle concentrations and particle sizes. These characterizations are compared to those reported in the literature and main features and limitations of the experiments are identified. Secondly, the results for the particle concentrations measured under the same range of flow conditions are presented. Finally, correlations between the suspension's flow behavior and the concentration repartition in the cone-plane gap are discussed.

The last chapter presents the conclusion of the present work followed by some perspectives in terms of further technological developments of the setup and in terms of research studies that could be carried out with the developed setup and suspensions.

2 Literature review

2.1 Suspensions

2.1.1 Introduction

The word “suspension” has often been used to describe a biphasic system, where solid particles are suspended in a continuous fluid (Genovese 2012). It exists in biological systems (blood), in nature (mud, slurry, debris flow). The application of suspension is ubiquitous, such as food, paint, pharmaceutical products etc.

Since the year 60s and 70s studies about suspension have attracted the attention of many researchers. Lots of theoretical, experimental and numerical works were done. For example, Krieger (1959) proposed a model to describe the relationship between the suspension viscosity and the particle volume fraction. Lyon and Leal (1998a; 1998b) performed experiments to study suspension flow in micro-channel using Laser Doppler Velocimetry (LDV). Korhonen et al. (2015) studied the apparent wall slip effect of suspension flow under parallel shear disks by simulations.

Over the past two decades, several reviews about suspension were published. Coussot and Ancey (1999) concentrated on the characterization of dense suspensions by some physical parameters, such as the Reynolds number and the Peclet number. Stick and Powell (2005) reviewed non-Newtonian behaviors observed in concentrated suspensions of force-free spheres, and discussed their origins in terms of suspension microstructure. In the article of Genovese (2012), the rheology of suspension was elucidated and analyzed based on some simplified equations. Later, Denn and Morris (2014) updated the review with new results in recent years, mainly focused on non-Brownian dense suspension rheology and fluid mechanism.

According to the current literature, most researches about suspension can be divided into two categories. One category focuses on the viscosity properties of suspensions, for the purpose of determining the relationship between relative viscosity with particle concentration, shear rate or other factors. The other category is about measuring the velocity profiles and the particle concentration distributions of suspensions under flow geometries, such as Couette cells, capillaries and micro channels, in order to study the flow dynamics of suspensions.

In the following we will present a review of the various classifications proposed to define a suspension followed by a review on the behavior of the viscosity of a suspension resulting from the parameters used for these classifications.

2.1.2 Classification of suspensions

2.1.2.1 Classification based on particle concentration

Suspensions are usually classified by the particle volume fraction (ϕ), as the rheological property of suspension changes following the increase of particle concentration. For spherical particle suspension, the particle volume fraction can be expressed in the follow equation:

$$\phi = \frac{4}{3}\pi r_p^3 m \tag{2.1}$$

Where m is the particle number density, r_p is the particle radius. With respect to the viscosity, suspensions are often classified into 3 sections:

a) When $\phi < 5\%$, the suspension is considered to be a dilute suspension. Such suspension can be treated as the suspending fluid without significant difference in viscosity.
b) When $5\% \leqslant \phi \leqslant 25\%$, the suspension is considered as semi-dilute. Here the viscosity shows a higher order dependence on ϕ, but the behavior is still approximately Newtonian.
c) When $\phi \geq 25\%$, the suspension becomes dense or concentrated. Here, some specific phenomena are clearly shown. One example is the rapid growth of viscosity compared to that of other concentrations. Usually non-Newtonian effects can be found in such dense suspensions.

2.1.2.2 Classification based on dominant forces

Excluding the inertial force (which depends on shear rate $\dot{\gamma}$) when the suspension is moving, 3 main forces occur in a suspension:

a) Hydrodynamic force, which is the viscous force due to the relative motion of particles to the surrounding fluid,
b) Brownian force, which is the omnipresent thermal randomizing force,
c) Colloidal forces, such including excluded volume repulsion, electrostatic interaction and van der Waals force (Brader 2010). Colloidal forces are potential forces which depend on the particle size and the distance between particles (Qin et Zaman 2003).

For particle diameter (d_p) smaller than 1nm, Brownian force and colloidal forces predominate. While for particles larger than ~10μm, hydrodynamic force plays the most significant part. For particles in the intermediate range (10^{-3}μm < d_p < 10μm), they are affected by a combination of hydrodynamic, Brownian motion, and inter-particle forces (Qin and Zaman 2003).

In addition, as shown in Fig 2.1, following the variation of the particle volume fraction and the flow shear rate, the dominant force is different. Under low shear rates and low concentrations, the Brownian effect has the biggest influence (zone A). When the shear rate increases, hydrodynamic force takes place (zone B). While the particle volume fraction increases, the colloidal forces are the most important (zone C). At very high shear rates, the inertial forces dominate (zone D). In highly concentrated suspension, inter-particles forces dominate (zone E, F, G, not involved in the current study).

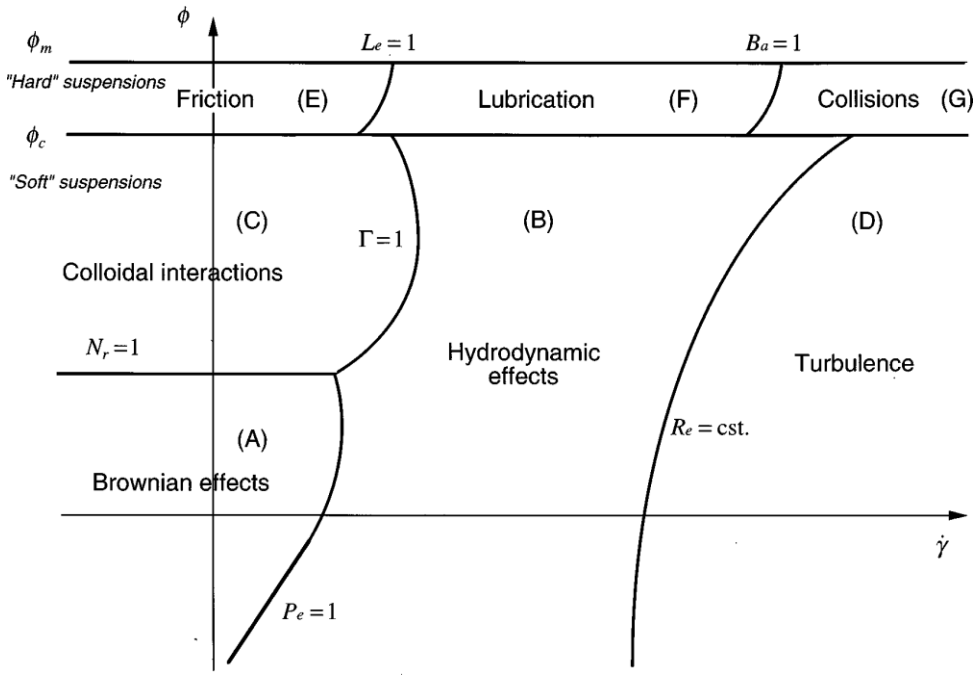

Fig 2.1 Conceptual classification of the rheophysical regimes of a suspension as a function of shear rate and solid fraction on a logarithmic scale (Coussot and Ancey 1999).

To describe the dominant force inside a suspension, some non-dimensional numbers are used, such as the Reynold number and the Peclet number.

The Reynolds numbers is the ratio of the inertial force to the hydrodynamic force (Stickel and Powell 2005), defined as:

$$Re = \frac{\rho_L r_p^2 \dot{\gamma}}{\eta_L} = \frac{\text{Inertial}}{\text{Hydrodynamic}} \tag{2.2}$$

Where ρ_L is the density of the suspending liquid, r_p is the particle radius, $\dot{\gamma}$ is the flow shear rate, η_L is the dynamic viscosity of the suspending liquid.

The Peclet number is the ratio between the hydrodynamic force and the Brownian force, defined as:

$$Pe = \frac{6\pi\eta_L r_p^3\dot{\gamma}}{k_B T_a} = \frac{\text{Hydrodynamic}}{\text{Brownian}} \tag{2.3}$$

Where k_B=1.38×10^{-23} J K^{-1} is the Boltzmann constant, T_a is the absolute temperature. Moreover, the ratio of the Peclet number to the Reynolds number is useful for the analysis later, named the Schmidt number, it is defined as:

$$Sc = \frac{6\pi r_p \eta_L^2}{\rho_L k_B T} = \frac{Pe}{Re} \tag{2.4}$$

2.1.2.3 Other classifications

Classifications can also be based on particle shape (spherical particle suspension and non-spherical particle suspension), number of particle types (mono-dispersed suspension, bi-dispersed suspension, poly-dispersed suspension), or particle deformability (deformable particle suspension or solid particle suspension), attractive force between particles (aggregating and non-aggregating particle suspension). Suspension can be classified by suspended particle size as well. For suspension with particle sizes in the range from a few nanometers to a few microns, it is referred as colloidal suspension. Besides, for particles with r_p <1μm, the Brownian force is noticeable (Zhou, Scales, and Boger 2001). So suspension can been classified as Brownian or non- Brownian, depending on their particle sizes (Qin and Zaman 2003).

In this work, we will focus on non-Brownian suspension, with particle diameter in the range of 10^0 to 10^2 μm suspended in a Newtonian fluid.

2.1.3 Suspension viscosity

The viscosity of particle suspension is influenced by many factors, such as particle volume fraction, shear rate, particle shape, particle size distribution, particle deformability etc. In general, the dynamic viscosity of the suspension (η_s) is proportional to the dynamic viscosity of the suspending liquid (η_L). Then, most rheological models are expressed in terms of the relative viscosity (η_r), defined as:

$$\eta_r = \frac{\eta_s}{\eta_L} \tag{2.5}$$

2.1.3.1 Effect of particle volume fraction

The particle volume fraction is one of the most important factors for suspension viscosity. Here the study is begun with a simple case: suspensions of mono-dispersed hard spheres. Hard spheres are defined as rigid spherical particles, with no inter-particle forces other than infinite repulsion in contact (Genovese 2012). The viscosity of hard-sphere suspensions is affected by hydrodynamic forces, Brownian motion, and the excluded volume of the particles.

In the dilute regime, the relative viscosity of hard-sphere suspensions was first addressed theoretically by Einstein (1956). He defined the following linear dependency:

$$\eta_r = 1 + B\phi + O(\phi^2) \tag{2.6}$$

Where B is the 'Einstein coefficient' or 'intrinsic viscosity', which takes the value B=2.5 for hard spheres.

For semi-dilute suspension, Batchelor and Green(1972) extended Einstein's equation to second order:

$$\eta_r = 1 + B\phi + B_1\phi^2 + O(\phi^3) \tag{2.7}$$

Where B_1 = 6.2 for Brownian suspensions in any flow, and B_1 = 7.6 for non-Brownian suspensions in pure straining flow (Batchelor 1977; Batchelor and Green 1972).

At higher concentrations, the distance between particles is much closer, the probability of collision increases. The resulting relative viscosity shows a significant positive deviation from the prediction of the equation (2.6). In this case, ϕ_m, the maximum volume fraction or maximum packing fraction of particles should be considered (Genovese 2012). When particle concentration approaches ϕ_m, there is no longer sufficient fluid to lubricate the relative motion of particles, jamming occurs and consequently the viscosity rises to infinity (Metzner 1985). For mono-dispersed spherical particle suspension, the theoretical value of ϕ_m is 0.74 (in a face centered cubic arrangement). However, there is no consensus on how to define the value of ϕ_m in real suspensions, even with mono-dispersed hard spheres. In general, observed ϕ_m values can range from 0.55 to 0.68 (Qi and Tanner 2011). Some experimental observations have shown that loose random packing is about 0.60, and the random close packing is close to 0.64 (McGEARY 1961; Qin and Zaman 2003; Quemada 2002).

Taking into account ϕ_m, equation (2.7) evolves to another form. One of the most accepted expressions is the semi-empirical equation of Krieger and Dougherty(1959) for mono-disperse suspensions:

$$\eta_r = (1 - \frac{\phi}{\phi_m})^{-B\phi_m} \tag{2.8}$$

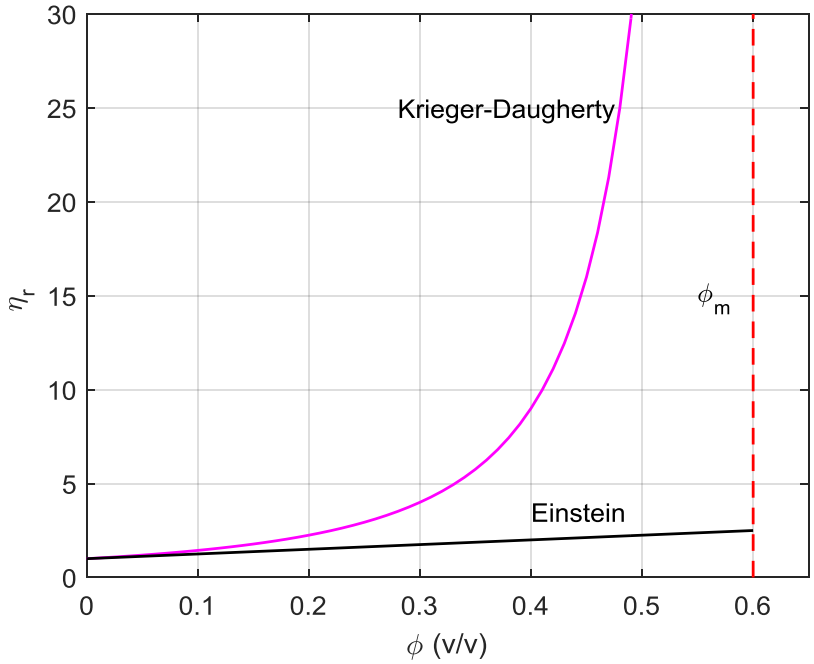

Fig 2.2 Relative viscosity vs. particle volume fraction predicted by Einstein's equation for dilute hard-sphere suspensions (Equation (2.6) with B = 2.5), and Krieger–Dougherty's equation for concentrated hard-sphere suspensions (Equation (2.9) with ϕ_m = 0.6).

The product B×ϕ_m in equation (2.7) is often around 2 for a variety of experiments (Maron and Pierce 1956; Quemada 2002; Russel and Sperry 1994). Therefore Krieger–Dougherty's equation is usually simplified to:

$$\eta_r = (1 - \frac{\phi}{\phi_m})^{-2} \tag{2.9}$$

As described in Fig 2.2, at low concentrations, the relative viscosity is close to the prediction of Einstein's equation (2.6). After a certain value of concentration the viscosity increases rapidly, following the prediction of Krieger and Dougherty's equation (2.9). Finally, when the concentration approach ϕ_m, it rises to infinity.

Other factors, such as shear rate, particle shape, particle size distribution, and particle deformability can also affect the relative viscosity (and ϕ_m) of suspensions (Genovese, Lozano, and Rao 2007; Zhou, Scales, and Boger 2001). For example, when the particles are bi-dispersed hard-spheres, the maximum packing fraction will deviate from the theoretical value, as the smaller particles can occupy the space between larger particles. In this situation, an effective maximum packing fraction $\phi_{m\text{-}eff}$, should replace ϕ_m in equation (2.9), which gives:

$$\eta_r = (1 - \frac{\phi}{\phi_{m-eff}})^{-2} \quad (2.10)$$

Equation (2.10) is a generally used to describe non hard-sphere suspensions. $\phi_{m\text{-}eff}$ is defined as the maximum packing fraction of non-hard sphere particle suspension. As $\phi_{m\text{-}eff}$ changes in each particular system, the influence of other factors can then be analyzed based on this equation.

2.1.3.2 Effect of shear rate

At low particle concentrations, the viscosity of hard-sphere suspensions is independent of shear rate (Equation (2.6)). At higher concentrations, the effect of shear rate is noticeable. Usually, the behaviors of the suspension relative viscosities can be separated into 4 domains depending on the shear rate: 1) at very low shear rates, they behave like a Newtonian fluid, with a constant zero-shear viscosity; 2) at intermediate shear rates they show shear-thinning effect; 3) at high shear rates the viscosity attains a limiting and constant value, and 4) after a certain limit of shear rate ($\dot{\gamma}_c$), the suspension is estimated to be shear-thickening (Barnes 1989; Stickel and Powell 2005). The behavior beyond the shear-thickening region is not clear, but some studies indicate shear-thinning will appear again (Barnes, Hutton, and Walters 1989; Hoffman 1972). Based on the above description, Fig 2.3 shows the estimated variations of relative viscosity with respect to shear rate. At low particle concentrations, they are Newtonian. Following the increase of particle concentration, the effect of shear-thinning and shear-thickening appear and become more apparent. The behaviors after shear-thickening are represented by dashed line, as they are not clear yet.

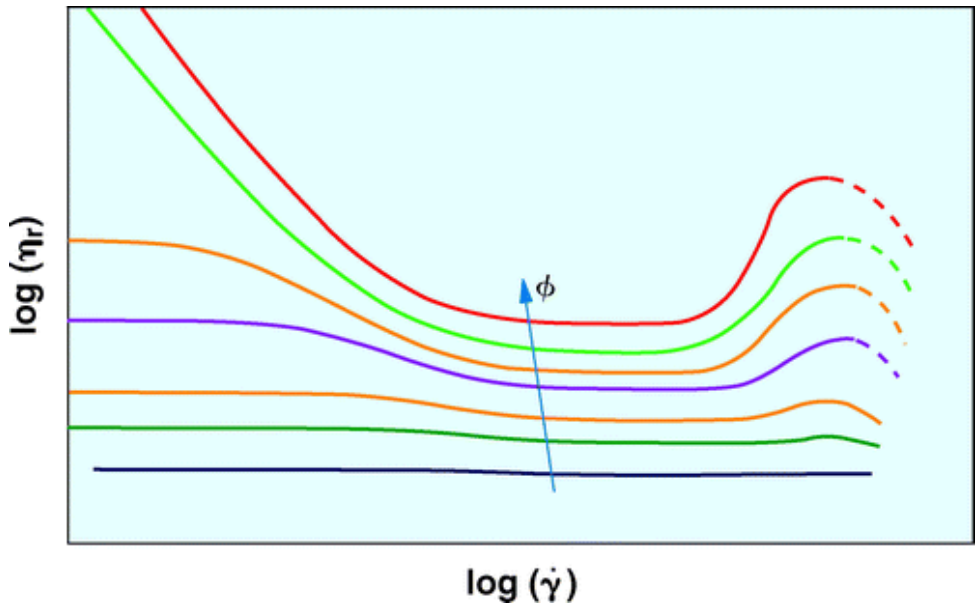

Fig 2.3 Representation of relative viscosity versus shear rate for a fluid suspension (Stickel and Powell 2005).

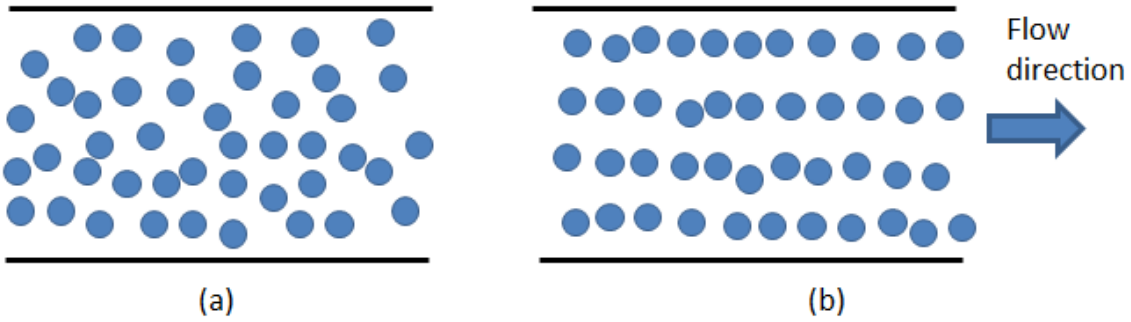

Fig 2.4 Illustration of the alignment of the suspended particles following the flow direction (a) compared to the initial disordered state (b)

Shear-thinning is a common case for suspension, which is linked to the alignment of suspended particle following the direction of the flow (Fig 2.4). While shear-thinning followed by shear-thickening behavior is not completely confirmed for all the suspensions, though it has been observed in highly concentrated suspensions (ϕ > 0.4–0.5) (Barnes 1989; D'Haene and Mewis 1994; Picano et al. 2013; Brown and Jaeger 2014; Wyart and Cates 2014; Cheng et al. 2011). One example is shown in figure (Fig 2.5), for suspension with 1.25μm particles at a concentration varying from 47% to 57%, after the shear rate reaches a certain critical value ($\dot{\gamma}_c$), the viscosity begins to increase again (Hoffman 1992). Shear-thickening can be divided into two categories: discontinuous shear-thickening and continuous shear thickening (Brown and Jaeger 2014). Continuous shear-thickening is that the re-augmentation of viscosity is mild (perhaps up to several tens of percent over the few decades of shear rates). Discontinuous shear-thickening means that the viscosity increases abruptly after a certain shear rate, for example, in Fig 2.5, the viscosities of the suspensions at ϕ =57% and 51% show a discontinuity after a certain shear rate respectively.

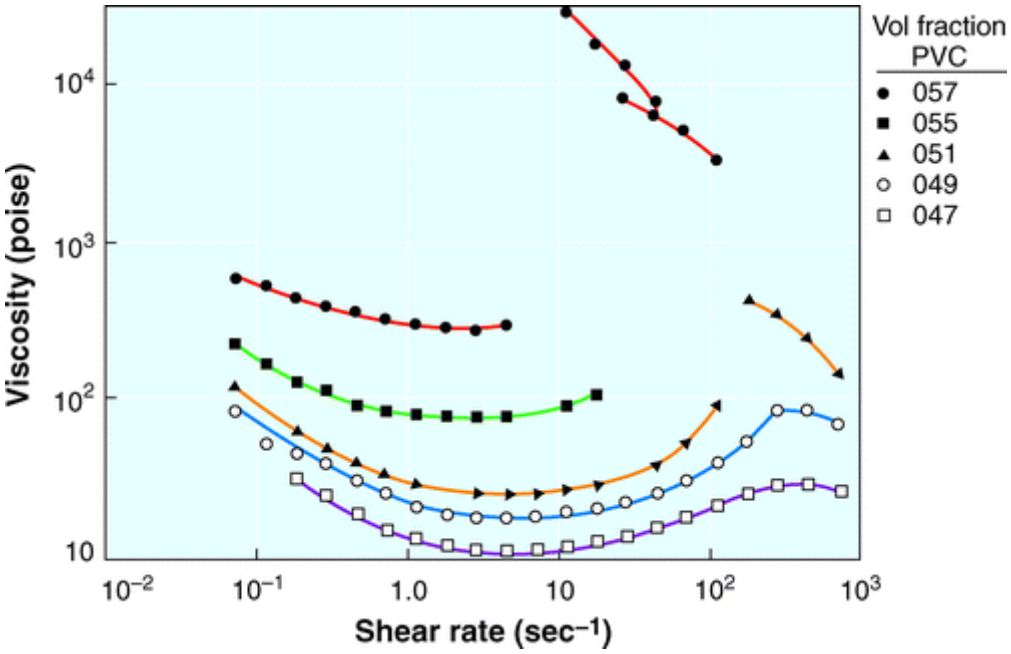

Fig 2.5 1.25μm PVC particles in dioctyl phthalate (R. L. Hoffman 1972)

Barnes (1989) reviewed shear-thickening behavior on non-aggregating solid particle suspensions. He summarized that shear-thickening is affected by particle volume fraction, particle size, particle size distribution, particle shape, and inter-particle interactions. He inferred that $\dot{\gamma}_c$ decreased with increasing values of ϕ, and that $\dot{\gamma}_c$ increased rapidly at $\phi \ll 0.5$ (Fig 2.6). It is therefore experimentally more and more difficult to attain $\dot{\gamma}_c$ when ϕ decreases below 50%. But not finding $\dot{\gamma}_c$ does not mean it does not exist, as he wrote "so many kinds of suspensions show shear-thickening that one is soon forced to the conclusion that given the right circumstances, all suspensions of solid particles will show the phenomenon."

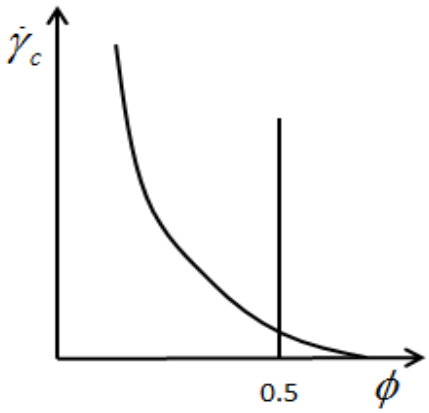

Fig 2.6 Variation of critical shear rate with respect to ϕ

As shear-thickening has been observed experimentally to become important at $Re \geq 10^{-3}$, (Barnes 1989; Hoffman 1972), based on the Reynold number (Equation (2.2)) and the Peclet number (Equation (2.3)), Stickel and Powell (2005) proposed a dimensional

criterion to characterize the behavior of suspension rheological behavior. Depending on the values of Re and Pe, they classified the rheological behavior of suspension into 4 regions: Shear-thinning, Newtonian, shear-thickening and an unknown region (Fig 2.7). They estimated that following the increase of shear rate, the behavior of suspension changes from shear-thinning to Newtonian, and finally to shear-thickening. In addition, they thought that a suspension might be expected to behave as a Newtonian fluid for greater ranges of shear rate, as particle size and fluid viscosity increased, such that Sc (Equation (2.4)) is far bigger than unity.

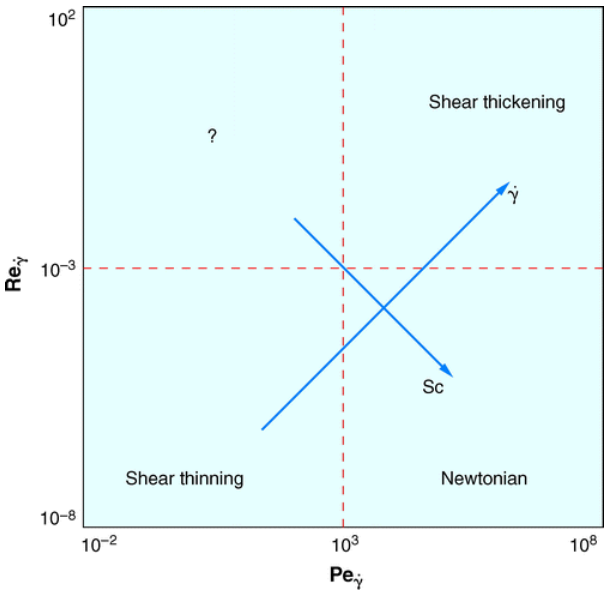

Fig 2.7 "Phase diagram" for suspension rheology, based solely on a dimensional analysis (Stickel and Powell 2005).

Recently, shear-thickening phenomena have caught more attention (Brown and Jaeger 2014; Mari et al. 2014; Wyart and Cates 2014). Picano et al. (2013) thought shear-thickening can be due to the augmentation of exclude volume of particles. Fluid inertia causes strong microstructure anisotropy that result in the formation of a shadow region with no relative flux of particles. As shown in Fig 2.8, 2a is the least distance between two particles of radius a, the region with vanishing probability to find another particle in relative motion increases at higher Reynolds numbers. This regions act as an increase of the effective volume of particles: the geometrical volume occupied by the particles plus the volume of the region, thus leading to the augmentation of the viscosity (Picano et al. 2013; Fornari et al. 2016).

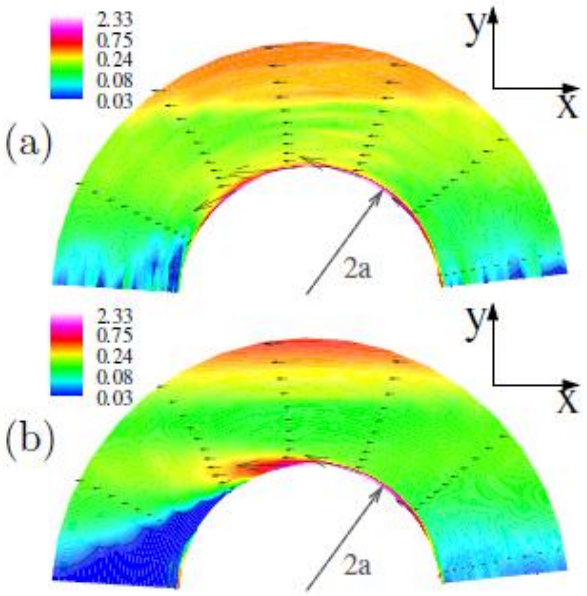

Fig 2.8 Contour plot of particle pair relative flux, for ϕ = 31.5%: a) Re = 0.1, b) Re = 10. (Picano et al. 2013)

Brown and Jaeger (2014) summarized that there are 3 mechanisms for shear-thickening:

1) Hydro-clustering formation of particles (N. J. Wagner and Brady 2009). Above a critical shear rate, particles stick together transiently by the lubrication forces and can grow into larger clusters (Fig 2.9). The large clusters result in a larger relative viscosity.
2) Order-disorder transition (Hoffman 1974). Following the increase of shear rate, the arrangement of particles changes from ordered layers to a disordered state, thus the viscosity increases.
3) Particle dilatancy (Brown and Jaeger 2012). When particles are sheared, they try to go around each other, but often cannot approach directly, so the packing volume of particles increases (dilates).

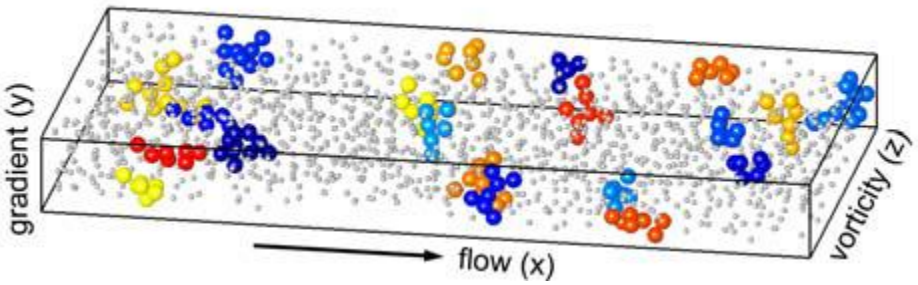

Fig 2.9 Instantaneous configurations of transient clusters in the shear thickening regime, observed using fast confocal microscope. Different colors indicate different clusters. Particles outside the large clusters are drawn with smaller size for clarity (Cheng et al. 2011).

In addition, they found that discontinuous shear-thickening may be related to the jamming effect of suspensions.

2.1.3.3 Other effects

Yield stress

Yield stress has mostly been observed at high concentrations ($\phi > 0.5$) and at low shear rates (Dabak and Yucel 1987; Dzuy and Boger 1983; Heymann, Peukert, and Aksel 2002; Hoffman 1992; Jomha et al. 1991; Zhu and Kee 2002). Although the concept of yield stress and its experimental measurement has been a matter of debates (Barnes 1999; Heymann, Peukert, and Aksel 2002; Moller et al. 2009; Nguyen and Boger 1992), most works acknowledged the existence of yield stress in fluids. One focal point of the argument is how to clarify and measure the yield stress experimentally. An apparent yield stress can be observed in a suspension that means the viscosity tends toward infinity at very small shear rates, or there is a finite shear stress without deformation over long experimental time scales (Moller et al. 2009).

Effect of size distribution

As demonstrated in many experimental or simulation studies of bi-dispersed or poly-dispersed suspensions, at the same particle packing fraction, the bi-dispersed or poly-dispersed suspension has a lower viscosity (Chingyi Chang 1994; D'Haene and Mewis 1994; Qi and Tanner 2011; Spangenberg et al. 2014). One widely accepted explanation is the increase of effective maximum volume fraction $\phi_{m\text{-}eff}$. Since small particles may occupy the space between larger particles, a higher effective packing fraction can be achieved (Metzner 1985). Then, according to equation (2.10), when $\phi_{m\text{-}eff}$ increases, the viscosity decreases. To understand this physically, the small particles can act as lubricants for the flow of the larger particles, thereby reducing the overall viscosity (Servais, Jones, and Roberts 2002).

In addition, $\phi_{m\text{-}eff}$ not only depends on the number of discrete size bands (mono-, bi-, tri-, tetra-dispersed, etc.), but also depends on the size ratio of the diameter of large particles (d_{pL}) to that of the smaller ones (d_{pS}) in the next particle class (d_{pL}/d_{pS}) . For a given particle size distribution, $\phi_{m\text{-}eff}$ increases with increasing d_{pL}/d_{pS} , and reaches a maximum value at infinite diameter ratio, which can be considered as a mono-dispersed suspension.

Models of maximum volume fraction versus particle size distribution can been found in many articles (Chang and Powell 1994; Chong, Christiansen, and Baer 1971; Shapiro and Probstein 1992; Dörr, Sadiki, and Mehdizadeh 2013; Ouchiyama and Tanaka 1981; Zou

et al. 2003; Farris 1968; Qi and Tanner 2011). Their results confirm the trend described above.

Effect of particle shape

When the particles are non-spherical, there is an extra energy dissipation when the suspension is under flow, which result in an increase of viscosity (Genovese 2012), and its contribution to suspension viscosity depends on the orientation of non-spherical particles. The use of arbitrary shape particles will change the maximum packing fraction and the intrinsic viscosity value (Equation (2.8)). Therefore, to determine the viscosities of non-spherical particle suspensions is to determine their effective maximum packing fraction and the changed intrinsic viscosity value. Generally, particle non-sphericity induces an increase of the intrinsic viscosity value B and a decrease of the effective maximum packing fraction $\phi_{m\text{-}eff}$. But their products remain ≈ 2 (Barnes, Hutton, and Walters 1989).

For example, Kitano et al. (1981) measured the viscosity of non-spherical particle suspensions. They used equation (2.10) to describe the viscosity of non-spherical particle suspensions. They found that the maximum packing fraction decreased with the increasing of the length (l_p) to diameter (d_p) ratio ($k_p = l_p/d_p$). When $k_p = 1$ (spheres), $\phi_{m\text{-}eff}$ = 0.68, when $6 < k_p < 8$ (crystals), $\phi_{m\text{-}eff}$ =0.44. The same tendency was found by Mueller et al. (2010), by measuring the viscosity of mono-dispersed prolate and oblate particle suspension.

Effect of particle deformability and particle aggregation : the case of blood

When particles are deformable, they can alter their shape when stresses are applied (shear stress, collision etc.). Then, they can squeeze each other in the flow of high particle concentration. By these effects, the maximum packing fraction of deformable particle suspension is bigger than that of hard-sphere suspension. According to equation (2.10), the viscosity is thus smaller. Studies about the influence of particle deformability can be found in the articles of Frith and lips (1995), Snabre and Mills (1999). Both their analysis are implemented by considering the change of maximum packing fraction and intrinsic viscosity based on equation (2.8).

One example of deformable particle suspension is blood (Baskurt and Meiselman 2003). Red blood cells are suspended in blood plasma (a Newtonian fluid), with a concentration about 45% in volume. RBCs contain a viscous liquid and are enclosed by a visco-elastic membrane, thus they are highly deformable(Zhang, Johnson, and Popel 2007). With such a structure, RBCs are able to get through the micro-capillary with a diameter of around 4

μm (Popel and Johnson 2005; Xu, Tian, and Deng 2012). The influence of RBCs deformability on the blood viscosity can be seen in Fig 2.10.

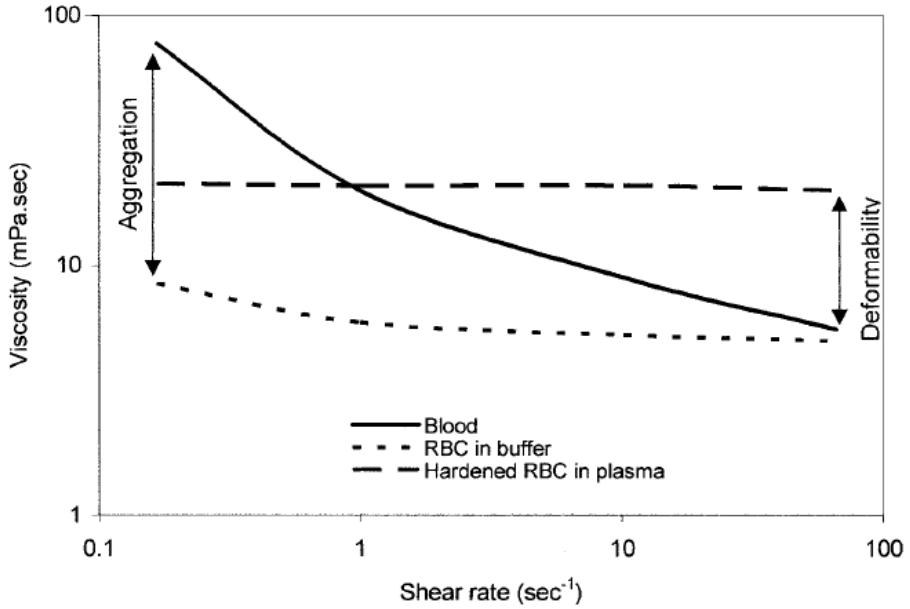

Fig 2.10 Variations of blood viscosity under different conditions as a function of shear rate (Chien 1970)

Due to the deformability of RBCs, the viscosity of blood is much smaller than hardened red blood cells in plasma at shear rates varying from $1s^{-1}$ to $100s^{-1}$.

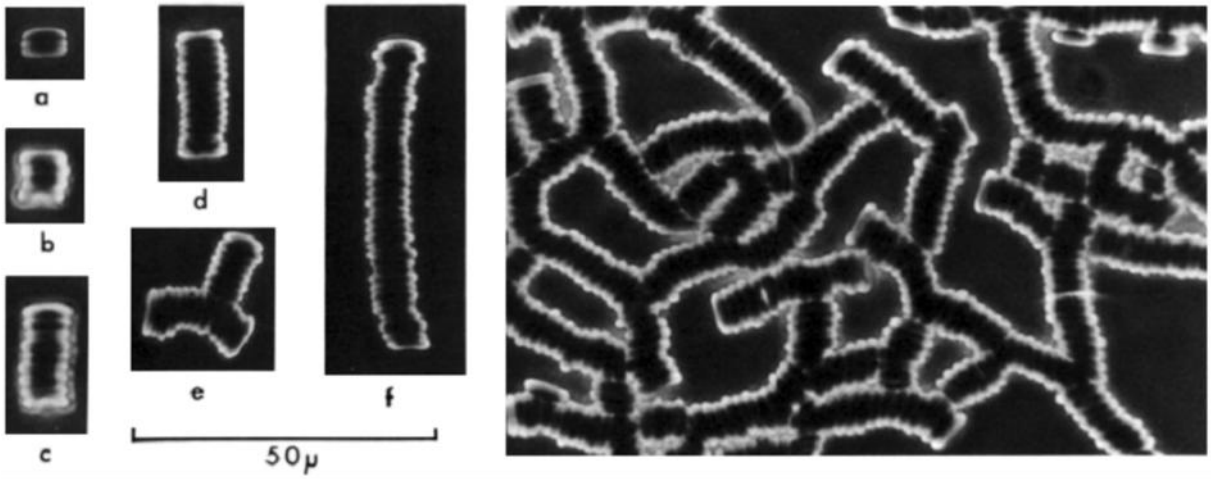

Fig 2.11 Rouleaux of human red cells photographed on a microscope slide showing single linear and branched aggregates (left part) and a network (right part). The number of cells in linear array are 2, 4, 9, 15, and 36 in a, b, c, d, f, respectively (Fung 1993).

Other than the deformability of RBCs, the aggregation of red blood cell can also influence the viscosity of blood. As shown in the Fig 2.10, the viscosity of the real blood is much higher than RBCs in buffer at low shear rate ($<1s^{-1}$). RBC aggregation causes a large

increase in viscosity at low shear rates. When shear rate is near zero, RBCs aggregate to form a big cluster, which then behave like a solid (Fig 2.11).

As the shear rate increases, RBCs aggregates tend to break up into small unit called rouleaux. As the shear rate continues to increase, the average number of RBCs in each rouleaux decreases. If the shear rate is larger than a certain critical value, the rouleaux breaks up into individual cells (Yilmaz and Gundogdu 2008). RBCs tend to aggregate at low shear rates, but when they are in buffer, they do not aggregate. Researchers have proven that the presence of fibrinogen, dextran and globulin proteins in plasma cause the aggregation of RBCs (Fung 1993; C. Wagner, Steffen, and Svetina 2013). According to Yilmaz and Gundogdu (2008), the mechanisms of RBC aggregation can be explained as a balance of aggregation and disaggregation force. Disaggregation forces mainly consist of shear force, repulsive force, and elastic energy of RBC membrane. However, the mechanism of aggregation force is still unclear. There are mainly two models to explain the mechanism of aggregation force based either on bridging or depletion (Wagner et al. 2013).

In a clinical view, studying RBC aggregation is of particular relevance. Quoting Baskurt and Meiselman (2010), "RBCs aggregation should not only be considered as a factor influencing vascular control mechanisms that regulate the distribution of blood flow to various organs and tissues, but should also be considered, more generally, as a phenomenon that interferes with endothelial function and vascular health". RBC aggregation and its interaction with the surrounding vascular endothelium is now also considered as the central factor to some important vascular functions, such as the regulation of hemostasis, inflammatory response, angiogenesis and vasomotor control. In addition, RBCs aggregates can form large clot, which might completely stop the blood flow. Clot formation is an advantage for wound healing, but in a healthy vessel it might lead to a stroke (thrombus), which is the main cause of death in the developed countries (C. Wagner, Steffen, and Svetina 2013).

The complexity of the in vivo process and studies justifies to split these research works in several simplified problems one of these then concerning the interactions of RBCs and RBC aggregates like in the present work.

Several studies about RBC behaviors in vivo or in vitro have been reviewed such as for microcirculation (Cristini and Kassab 2005; Roman et al. 2013), for venous (Bishop et al. 2001) and for general studies (Baskurt and Meiselman 2003; Baskurt and Meiselman 2010; Rampling et al. 2004; Popel and Johnson 2005). Since it is difficult to produce micro-deformable particles and to do experiments using real blood (for instance, because of visibility isuues in optical measurement technique), many studies about

suspension of deformable particles were performed numerically (Dupin et al. 2007; Bagchi 2007; Zhang, Johnson, and Popel 2008; Juan, Bing, and Hui-Li 2009). However, it is difficult to simulate blood flow with a large quantity of RBCs.

2.2 Flow geometries

2.2.1 Introduction

For the study of the suspension fluid dynamic, a well-defined flow geometry can facilitate the interpretation of data and allow for a mapping of the observed flow dynamics to the rheological properties of the system (Isa et al. 2010). General used flow geometries can be divided into two groups: drag flow geometries like sliding parallel shear plates, in which shear is produced by the relative movements of the two plates, and pressure driven flow geometries, in which shear is generated by the pressure difference over a closed conduit.

2.2.2 Drag flow geometries

2.2.2.1 Parallel shear plates

Parallel shear plates are implemented simply by placing the fluid between two parallel plates which are much larger than their separation H_{gap}. The motions of the fluid are induced by the movements of the plates (Fig 2.11). However, due to their construction, they can only achieve finite strains after which the direction of motion must be reversed. Thus, they are particularly suited for oscillatory strain studies (Isa et al. 2010).

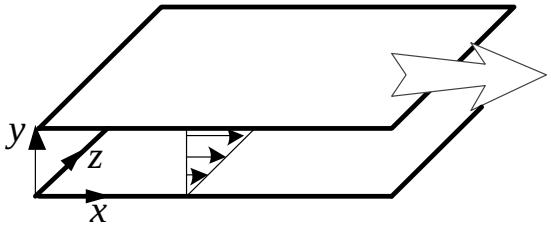

Fig 2.11 Schematic illustration of parallel shear plates

$$v_x = \frac{(v_T - v_B)}{H_{gap}} y \tag{2.11}$$

For a Newtonian fluid without slip and sufficiently far from the edges, the induced flow velocity can be expressed as equation (2.11), where H_{gap} is the distance between the two plates, v_T and v_B are the velocity of the top and the bottom plates respectively.

2.2.2.2 Rotational geometries

Continuous shear can be achieved in rotational geometries such as concentric cylindrical (Couette cell), rotational parallel disks and cone-plate. These geometries are often used for viscosity measurements, as they can provide a great range of shear rates.

In the Couette cell (Fig 2.12), the fluid motions can be induced by the rotation of the inner or the outer cylinders. This geometry provides a unidirectional shear flow under low rotation speed. The tangential velocity is explained as the equation below.

$$v_\theta = \frac{\omega_2 \mathrm{R}_2^2 - \omega_1 \mathrm{R}_1^2}{\mathrm{R}_2^2 - \mathrm{R}_1^2}\mathrm{r} + \frac{1}{\mathrm{r}}(\omega_1 - \omega_2)\frac{\mathrm{R}_2^2 \mathrm{R}_1^2}{\mathrm{R}_2^2 - \mathrm{R}_1^2} \tag{2.12}$$

Where R_1 and R_2 are respectively the inner and outer cylinder radiuses, ω_1 and ω_2 are respectively the inner and outer cylinder rotation speeds, r is the radius of the measured point.

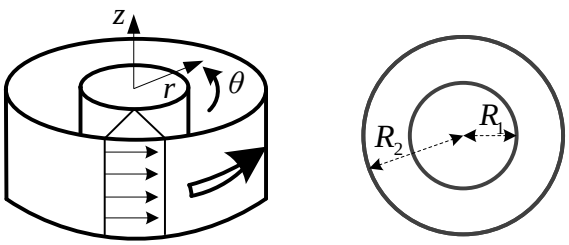

Fig 2.12 Schematic illustration of Couette cell device

For rotational parallel disks (Fig 2.13), the motion is generally induced by the top disk. This geometry offers a flow which shear in two directions: radial and vertical. Without slip and secondary flow, the tangential velocity in the fluid is given by equation (2.13).

$$v_\theta = \frac{\omega \mathrm{r}}{\mathrm{H_{gap}}}\mathrm{z} \tag{2.13}$$

where ω is the relative rotation speed of the disk, r is the distance to the rotation axis, $\mathrm{H_{gap}}$ is the height of gap between the two plates.

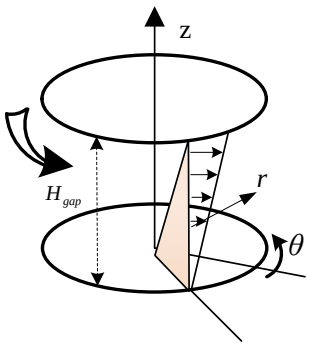

Fig 2.13 Schematic illustration of rotational parallel disks

The cone-plate (Fig 2.14) can offer a constant shear rate in the whole field. For a Newtonian fluid without slip and secondary flow, the tangential velocity (v or v_θ) is expressed as:

$$v_\theta = \frac{\omega R_c}{\mathrm{H_{gap}}} z \tag{2.14}$$

where ω is the rotation speed of the cone, R_c is the cone radius, $\mathrm{H_{gap}}$ is the maximum distance between the cone and the plate.

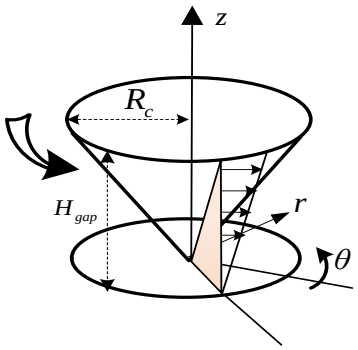

Fig 2.14 Schematic illustration of cone-plate

2.2.3 Pressure driven flow geometries

Capillaries and micro channels (Fig 2.15) are pressure driven flow geometries. They have the advantage to observe the flow behaviors of the suspension under complex conditions, which offer an insight on issues such as confinement, flow instabilities and particle migration effect (Averbakh et al. 1997; Shauly et al. 1997; Koh, Hookham, and Leal 1994).

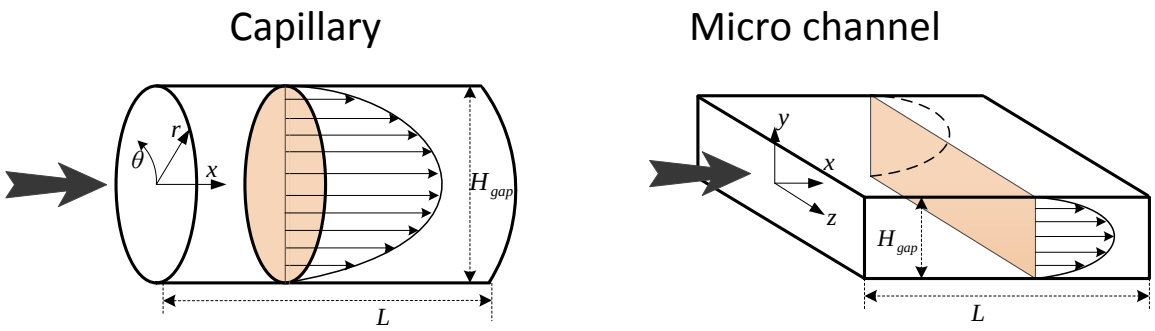

Fig 2.15 Schematic illustration of capillary and micro channel

The velocity profile in micro channel (or capillary) is a parabolic curve (Fig 2.15). For example, in a micro channel flow, the velocity in the flow direction is expressed as:

$$v_x = \frac{\Delta P}{2L\eta}\left(\left(\frac{H_{gap}}{2}\right)^2 - y^2\right) \quad (2.15)$$

Where H_{gap} is the channel height, L is the channel length, ΔP is the pressure drop between the inlet and the outlet of the channel, η is the dynamic viscosity of the fluid. The velocity in a capillary flow is similar to equation (2.15), except for a change of coordinate system. Optical investigation techniques are often used in channel flow experiments, for example, Laser Doppler Velocimetry. To avoid image distortions, rectangular micro channels are generally preferred rather than capillaries (Isa et al. 2010).

2.3 Dense suspension flow dynamics

2.3.1 Introduction

Generally, in the study of dense suspension flows, two properties are observed: the velocity profile and the particle concentration distribution. Concerning the velocity profile, apparent slip is usually encountered which results in the deviation of the velocity profile. For the particle concentration, shear induced particle migration is the main issue to be considered. In addition, the flow conditions should be guaranteed in advance, that there is no unwanted flow movement. Thus the secondary flow effect should be considered.

2.3.2 Secondary flow

In fluid dynamics, a secondary flow is a relatively minor flow superimposed on the primary flow, where the primary flow usually matches very closely the flow pattern predicted using simple analytical techniques and assuming the fluid is inviscid (An inviscid fluid is a theoretical fluid having a zero viscosity).

Here, we only study the secondary flow in cone-plate devices. At low velocities, the movement of fluid is rotational in a cone-plate device (primary flow). The centrifugation force (inertial force) increases proportional to rotational velocity augmentation. When the rotational velocity reaches a certain value, the centrifugal force is larger than the viscous force, at this moment, radial flow movement appears, and the secondary flow is generated.

According to the theoretical deduction based on an asymptotic expansion of Navier-Stokes equations for cone-plate flow (Sdougos et al. 1983), the first order term of the

radial velocity profile (u or v_r) under the cone-plate model can be expressed by the equation below (Detail deduction procedure is shown in appendix A):

$$u = \omega R\widetilde{\mathrm{Re}}(1.8\tilde{z}^2 - \tilde{z}^4 - 0.8\tilde{z}) \tag{2.16}$$

Where $\tilde{z} = \mathrm{H}/\mathrm{H}_{\max}$ is the normalized height, H is the height, $\mathrm{H}_{\max}$ is the maximum height with a radius of measurement, R is the distance of the measured point to the cone axis, $\widetilde{\mathrm{Re}}$ is the pseudo Reynolds number defined in their deduction (Tab 2.1). The ratio of the secondary flow to the primary flow (Equation (2.14)) can then be expressed as:

$$\frac{u}{v} = \widetilde{\mathrm{Re}}(1.8\tilde{z} - \tilde{z}^3 - 0.8) \tag{2.17}$$

The normalized radial velocity profile is shown in Fig 2.16, the radial velocity is inner directed near the plate, and it is outward directed near the cone.

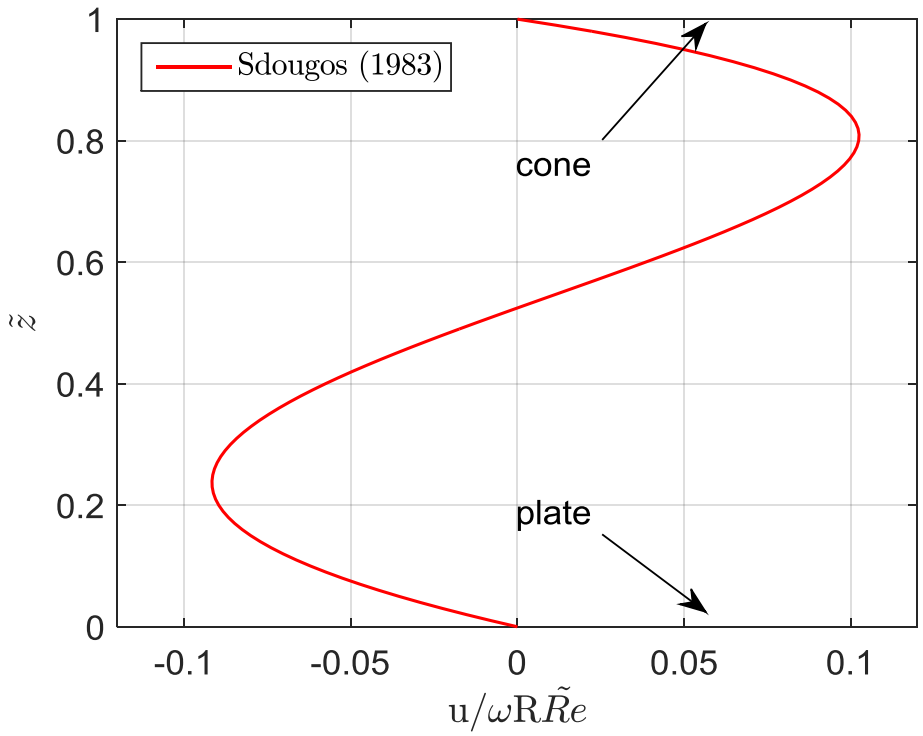

Fig 2.16 Normalized radial velocity profile of the theoretical deduction of Sdougos et al.(1983). Here u positive represents outward radial movement.

References	Description	
(Cheng 1968)	$\widetilde{Re} = 4\frac{R^2\omega\rho\alpha}{\eta}$	When $K \times \left(\frac{\widetilde{Re}}{\alpha}\right)^2 \leq 0.1$, the effect of secondary flow is negligible ($K = 2.505 * 10^{-10}$, at α=2°)
(Sdougos et al. 1983)	$\widetilde{Re} = \frac{R^2\omega\rho\alpha^2}{12\eta}$	$\widetilde{Re}$<0.5, there is no secondary flow
(Ellenberger and Fortuin 1985)	$\widetilde{Re} = \frac{R^2\omega\rho\alpha^2}{\eta}$	When $\widetilde{Re} \leq 10$, the measured torque is almost the same with the torque estimated from the theoretical deduction

Tab 2.1 Models for the estimation of secondary flow in a cone plate device

To calculate the threshold rotational velocity of the cone under which there is no (or negligible) secondary flow, some researchers proposed parameters to estimate this value (Cheng 1968; Sdougos et al. 1983; Ellenberger and Fortuin 1985). As indicated in Tab 2.1, all their criteria depend on a number similar to Reynolds number. This non-dimensional number can be expressed as the ratio of centrifugal force with viscous force, as shown in equation (2.18).

$$\widetilde{Re} = \frac{R^2\omega\rho\alpha^2}{\eta} = \frac{\rho R\omega^2}{\eta\frac{\omega}{R\alpha^2}} = \frac{\rho R\omega^2}{\eta\frac{V_{max}}{H_{max}^2}} = \frac{centrifugal\ force}{viscous\ force} \tag{2.18}$$

Where α is the angle of cone, η is the dynamic viscosity of the fluid, ω is the rotation velocity, ρ is the fluid density, $H_{max} = R\alpha$ is the distance between the cone and the plate at the corresponding position, $V_{max} = R\omega$ is the linear velocity of the cone at radius of R.

In terms of these criteria, it can be found that the secondary flow will be more apparent when the fluid viscosity decreases or the rotational speed increase.

2.3.3 Apparent slip

Wall slip effects are generally observed in dense suspension flows, in rheometers, in pipes, or in any channels with smooth walls. Wall slip is recognized as the difference of velocity between the wall and the near wall fluid (Sochi 2011). But the difference between true slip and apparent slip should be elucidated. True slip means that there is a discontinuity of velocity between the wall and the fluid in contact. While the apparent slip is another case, usually it is because that there is no obvious difference between the wall and the fluid, but there is a large velocity gradient across a thin layer between the wall and the bulk fluid. Fig 2.17 illustrates the differences of no slip, true slip and

apparent slip. Generally, apparent slip is the more common case for the observed suspension wall slip.

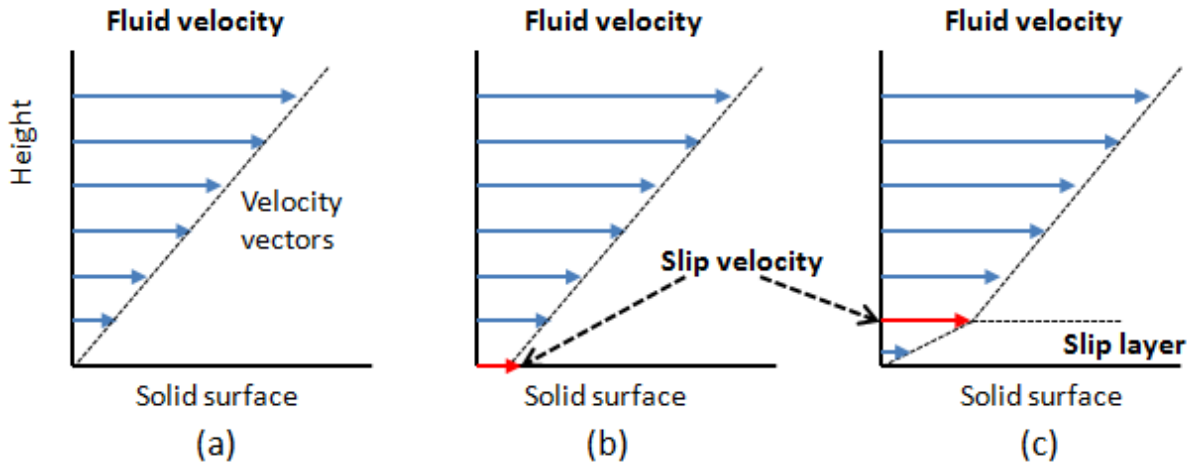

Fig 2.17 Schematic presentation of different boundary conditions: a) no-slip, b) true slip and c) apparent wall slip (Korhonen et al. 2015).

Apparent slip effect on emulsion and suspension in viscometer was reviewed by Barnes (1995). Recently, Sochi (2011) reviewed slip between solid and fluid interface. Apparent slip effect was found in many cases, in Couette Cell flow (Ahuja and Singh 2009; Jana, Kapoor, and Acrivos 1995), in rotational parallel disks flow (Yilmazer and Kalyon 1989; Kok et al. 2004; Gulmus and Yilmazer 2005), in pressure-driven channels (Medhi, Ashok, and Singh 2011) and in capillaries (Yilmazer and Kalyon 1989; Lam et al. 2007)

There are many mechanisms to explain the apparent slip phenomena. However, there is no general accepted theory. Many factors can affect the apparent slip effect. These factors can be divided into two origins. For the wall, there are factors such as wall shape, surface roughness, wettability etc. For the fluid, there are factors such as suspending fluid viscosity, elastic modulus, density, polarity, acidity and electric charge; for suspension, particle size, particle concentration, particle shape should be considered additionally (Sochi 2011; Soltani and Yilmazer 1998; Yilmazer and Kalyon 1989; Kalyon 2005).

For non-Brownian suspensions, there is a widely accepted mechanism which is related to the depletion of the boundary layer. When suspended particles migrate away from the wall, it will form a thin layer near the wall which is rich of fluid. This thin layer acts as a lubricant, which facilitates the flow. There are several reasons behinds the particle movements. It can be explained based on the diffusion movement of the particles. Since they cannot penetrate into the wall, then the particle volume fraction at a distance in the order of a particle radius to the wall is lower than that in the bulk suspension (Jana, Kapoor, and Acrivos 1995). It can also be due to the sedimentation of particle or the

repulsion force between the wall and the particles (Korhonen et al. 2015). Another explanation is associated to the layering of particles near the wall (Fig 2.), which decreases the local viscosity (Blanc, Peters, and Lemaire 2011; Blanc et al. 2013).

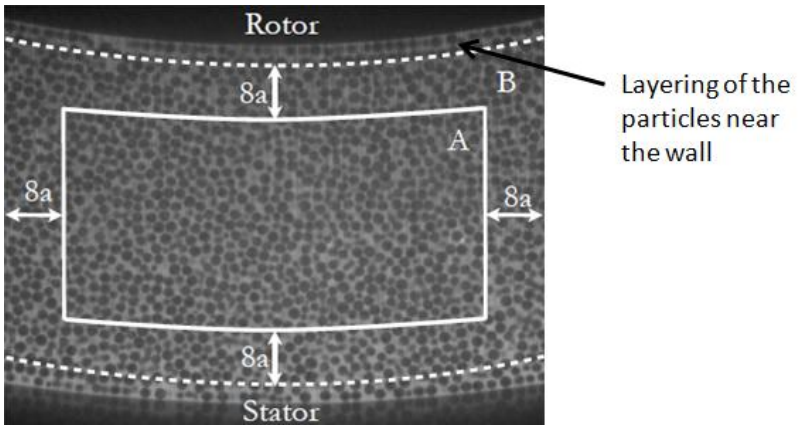

Fig 2.19 Layering of particle near the wall in concentric cylindrical Couette cell (Blanc et al. 2013)

Apparent slip can be characterized by 2 quantities: slip velocity (v_s) and slip layer thickness (δ). To measure the slip velocity, one approach is proposed by Mooney (1931), he thought the slip velocity was a function of the wall shear stress. So in capillary flow, when the wall shear stress is kept constant, by changing the diameter of the tube, and correspondingly recording the shear rate ($\dot{\gamma}$) then the slip velocity can be obtained by linearly relating the two above parameters, as shown in equation (2.19), where R is the radius of the tube. However, this method is only applicable in capillaries.

$$v_s = \frac{\partial \dot{\gamma}}{\partial (1/R)} \tag{2.19}$$

As mentioned above, particle size and particle concentration affect the slip effect. It is found that the slip velocity increase with increasing of the particle concentration and particle size (Gulmus and Yilmazer 2005; Medhi, Ashok, and Singh 2011). Medhi et al. (2011) even found that the slip velocity had a linear relation with respect to the shear rate in their channel flow experiment, and when the viscosity of suspending fluid decreased, the slip velocity increased too.

Lam et al. (2007) observed the apparent slip of non-colloidal glass sphere (d_p≈58μm) suspensions (ϕ=35%, 40%, 45%) in capillaries. In their analysis, the slip velocity is described as a function of the wall shear stress τ_w and the particle concentration. As shown in the equation below, where $k1$ and $k2$ are constants which are related to material properties, such as particle size and particle concentration.

$$v_s = k1 \cdot (\tau_w \cdot \sqrt{\phi})^{k2} \tag{2.20}$$

Concerning the slip layer thickness, Maciel et al. (2002) thought it was also influenced by the shear stress. Chakrabandhu and Singh (2005) indicated that the slip layer thickness should be in the order of the particle size. In the simulation of Kalyon (2005), he has assumed that the slip layer thickness is not affected by the flow shear rate for a Newtonian suspension. Observation in experiments (Kok et al. 2002) and simulations (Korhonen et al. 2015) have shown that the slip layer thickness decreased with the increasing of particle concentration or shear rate. Kok et al. (2004) used the Peclet number to classify the apparent slip effect of colloidal suspension in pressure driven flow. They concluded that the wall slip effect is significant when the Peclet number is bigger than unity, and they found that the slip layer thickness decreased with the increase of the Peclet number.

To reduce wall slip effect, roughed or serrated wall surface can be used. As written by Soltani et Yilmazer (1998):" If the slip layer thickness is comparable to the height of surface irregularities, then wall slip won't develop". This was confirmed by Medhi et al. (2011) who compared the suspension flow velocity profile in channel with smooth and serrated wall surface. No slip was found in the channel with serrated wall surface.

2.3.4 Shear induced particle migration

The problem of particle migration was first brought out by Leighton and Acrivos (1987). In a cylindrical Couette cell device, they found that the particles migrated from regions of high shear rates to regions of low shear rates, even with non-Brownian and non-inertial suspension. This migration resulted in non-homogeneous particle concentration distribution, which has been confirmed by other researchers (Phillips et al. 1992, Ovarlez, Bertrand, and Rodts 2006). One example is shown in Fig 2.. Ovarlez et al. (2006) used magnetic resonance imaging to measure the particle concentration in a rotating concentric cylinder Couette viscometer, where the flow movement was induced by the rotation of the inner cylinder. They found that the particle concentration was lower in the region close to the inner cylinder, where the shear rate is higher (Fig 2.18).

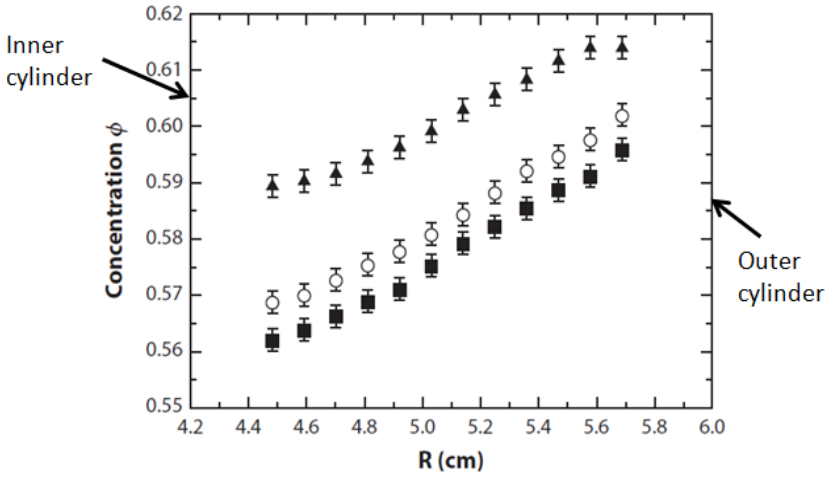

Fig 2.20 Concentration profiles measured across the gap between rotating concentric cylinders using magnetic resonance imaging for suspensions with mean values of ϕ=0.58 (squares), 0.59 (circles), and 0.60 (triangles). (Ovarlez, Bertrand, and Rodts 2006)

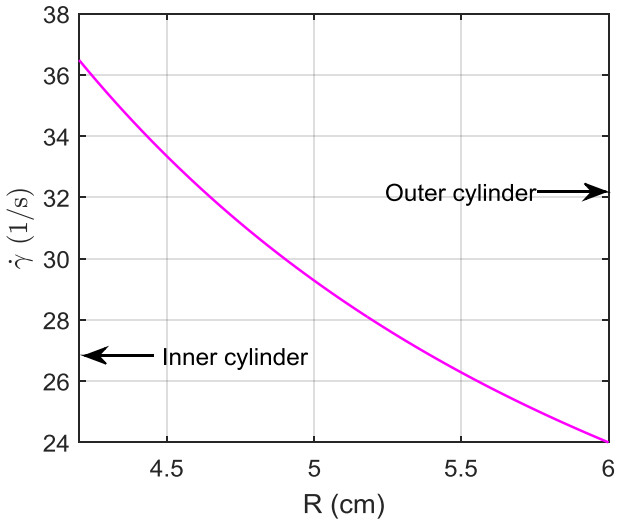

Fig 2.18 Variation of the shear rate across the gap between rotating concentric cylinders, data source from (Ovarlez, Bertrand, and Rodts 2006)

In other flow geometries, the particle migration phenomenon was also studied either by directly measuring the particle concentration or indirectly by measuring the velocity profile of the suspension.

In rotational parallel disks, although there is a radial gradient in the shear rate, the experimental results of some researchers are contradictory. Chow et al. (1994) performed experiments with semi-dilute and concentrated suspension. They did not find particle migration phenomenon. Merhi et al. (2005) found slight outward migration with concentrated suspension. As well, Kim et al. (2008) reported a weak particle migration with dilute suspension.

For the cone-plate model, there are contradictory results also, as reported in the review of Denn and Morris (2014): “The situation in cone-and-plate devices, where the shear rate is (presumably) uniform, is less clear: Chow et al. (1995) reported that particles migrate radially outward, whereas Fall et al. (2013) found that there is no migration in a truncated cone-and-plate device”.

Within pressure driven rectangular channel, Lyon and Leal (1998a; 1998b) performed experiments with mono-dispersed and bi-dispersed suspensions (d_p=50μm and 100μm) at a concentration of 50%. Blunted suspension velocity profiles were observed, and particle migration phenomenon was found as the particle concentration distribution showed a maximum near the channel center line and a minimum at the channel walls. Similar experiments were done by Averbakh et al. (1997) and Shauly et al. (1997) but with different particle sizes (d_p=85μm). They also found blunted velocity profiles and higher concentration of particle near the center line, when the particle concentration was bigger than 0.2.

2.4 Measurement techniques for suspension flow

2.4.1 Introduction

Fluid dynamic investigation methods are various, such as Nuclear Magnetic Resonance (NMR), Particles Image Velocimetry (PIV), Particle Tracking Velocimetry (PTV) and Laser Dopper Velocimetry (LDV). A review about experimental techniques in micro fluidic devices with suspension flows was written by Dinther et al. (2012). They compared the advantages and disadvantages of different techniques focusing on quantitative measurements of the particle concentration distribution and the suspension fluid velocity.

According to their analysis, optical methods are usually employed to measure the velocity profiles, such as LDV, PTV and PIV, because these methods are non-invasive and they can offer a direct insight in the flow behavior. However, LDV can only apply to measure an individual object, to measure a velocity field, PTV and PIV are more appropriate. Williams et al. (2010) reviewed micro fluidic velocimetry techniques, they compared PTV and PIV techniques. PTV techniques are more common for low tracer particle densities. PIV is more appropriate for high tracer particle density fluid.

For particle concentration measurement, it can be done directly by NMR technique, while it can also be measured with other techniques indirectly. For example, when the images of suspended particles are captured by a camera, then the particle positions

related to the focal plane can be determined by image processing methods. Based on the detected particle positions, the particle concentration can then be deduced.

2.4.2 Micro-PIV

2.4.2.1 Measurement principle

Micro-PIV is the application of PIV techniques to micro-scale. There are several published works about micro-PIV arrangement (Raffel et al. 2007b; Wereley and Meinhart 2005; Wereley and Meinhart 2010; Lindken et al. 2009; Koutsiaris 2012). A typical micro-PIV set-up is shown in Fig 2.19. The principle of micro-PIV can be described as follows. Tracer particles are homogeneously dispersed in the fluid by some seeding process. Generally the size of tracer particles is small enough to follow the flow without delay. Then they are illuminated by laser light. A digital camera consecutively records two images of the same field of view within a time interval Δt. The time interval is precisely controlled by the laser pulse, the first image is illuminated by the first pulse.

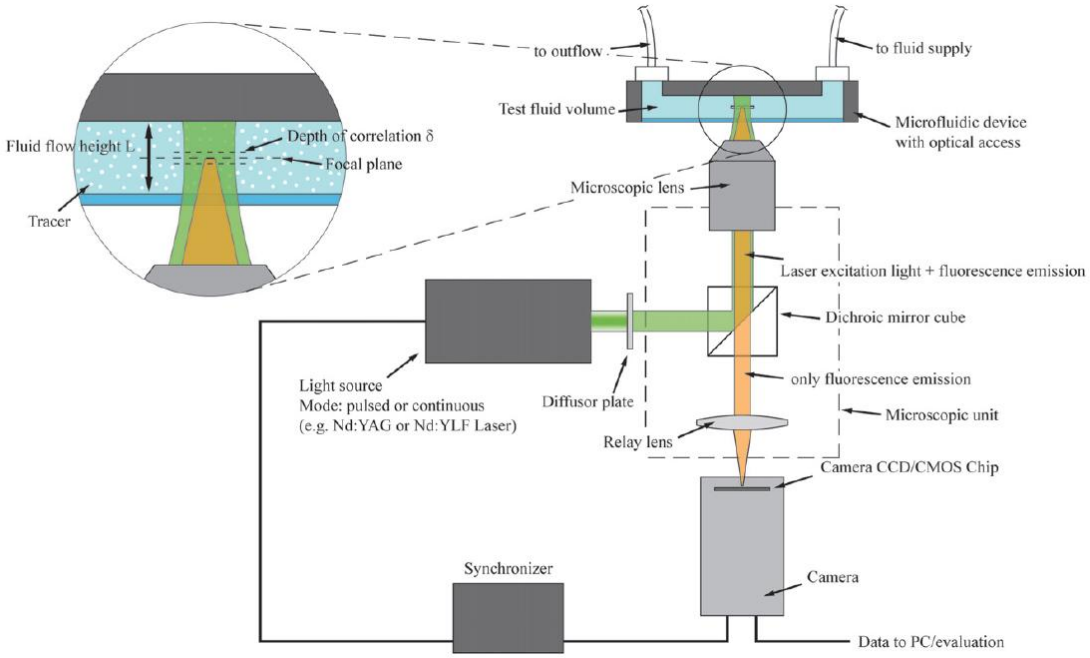

Fig 2.19 Schematic illustration of a micro-PIV set-up (Lindken et al. 2009)

For the analysis, the images are divided into uniform small interrogation windows (IWs). The size of the IWs should be small enough, so that the displacements of tracer particles are uniform in the IW, and it should also be sufficiently large to contain enough information (tracer particles) for the evaluation. Then, the particle image patterns in the IWs are compared between the two images. A cross-correlation algorithm is performed for the two evaluated IWs with different relative shift Δs (x, y) (unit pixel) in the first (I) and the second images (I'), as shown in the equation below:

$$C(x,y) = \sum_{i=-p}^{p} \sum_{j=-q}^{q} I(i,j)I'(i+x, j+y) \tag{2.21}$$

The variables I and I' are the intensity values extracted from the two consecutive images, where I' is larger than the template I, p and q are the maximum shift values, respectively, in the x and y directions. An example of the implementation of the shift for cross-correlation is shown in Fig 2.20.

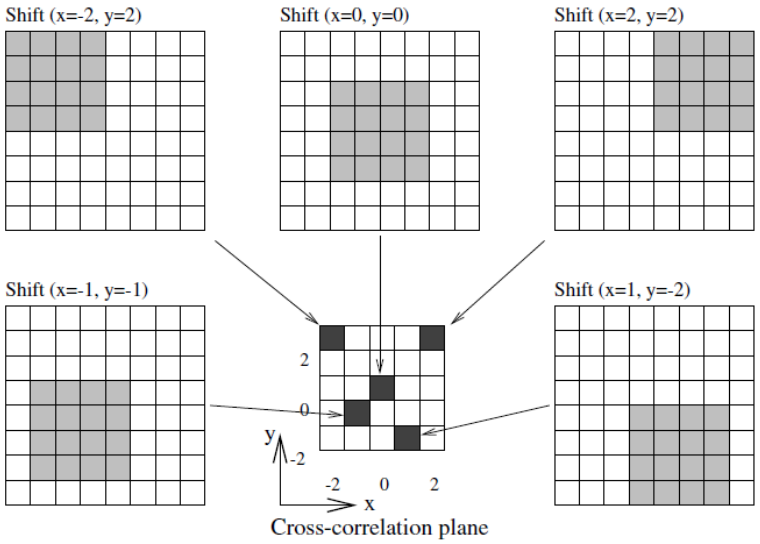

Fig 2.20 An example of the formation of the correlation plane by direct cross-correlation: here a 4×4 pixel template is correlated with a larger 8×8 pixel sample to produce a 5×5 pixel correlation plane (Raffel et al. 2007a)

After the cross-correlation computation, a correlation map is generated. An example is shown Fig 2.21, the correlation peak corresponds to the best match of particle image patterns. Therefore, the displacement of the local fluid between Δt is determined, which is the shift distance corresponding to the correlation peak. The pixel size of the imaging system is determined by calibrating an object of known length, noted as D_{pixel}. Then, the velocity over one interrogation window can be calculated as follows:

$$v = D_{pixel} \frac{\Delta s}{\Delta t} \tag{2.22}$$

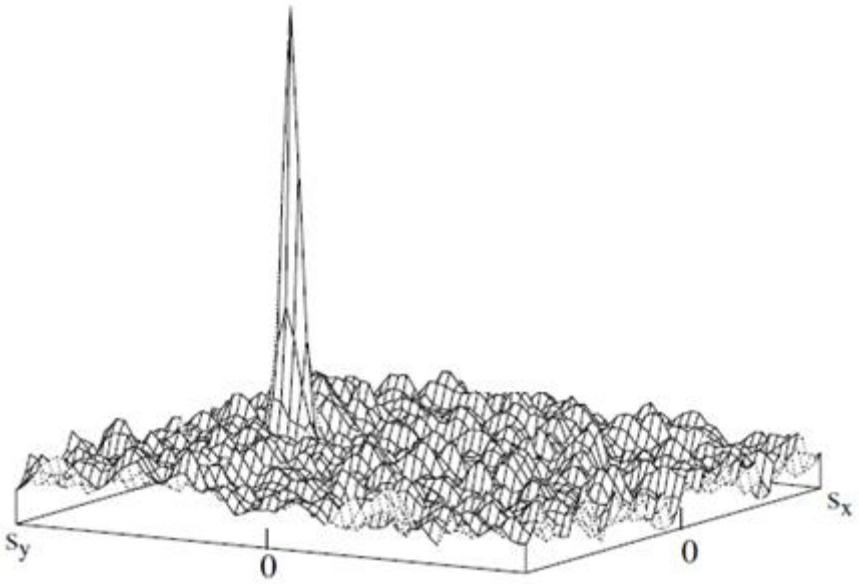

Fig 2.21 Peaks in a cross-correlation map with different shift distances, S_x and S_y represent the shift in the x and y directions respectively (Raffel et al. 2007a)

In addition, a transparent fluid is necessary for micro-PIV experiments. Thus for experiments with suspensions, refractive index matching technique should be employed to make the suspension transparent for an optical access, and to guarantee the quality of the captured images.

2.4.2.2 Volume illumination

In a general PIV system, the laser sheet illumination is the commonly used method to illuminate the tracer particles in the fluid. It will form a thin luminous plane. So only the tracer particles in this thin laser sheet are captured by the camera. In a micro-PIV system, as the observed flow depth is in the order of (or less than) the laser sheet thickness (about 1mm), this illumination method is no more applicable. The volume illumination method is then adopted, in which the measured plane thickness depends on the objective lens.

For volume illumination, in order to increase the signal-to-noise ratio of particle images, tracer particles were stained by fluorescent dye. They are excited by monochrome laser light and emit light with a longer wavelength. A Dichroic mirror is placed in the light path before the camera. On one side of the mirror, it reflect the originated laser light, but on the other side, only the emitted light with a longer wavelength can get through (Fig 2.19). So all other light reflected by the wall or scattered light at the original wavelength can be eliminated. With this optical filter, the signal to noise ratio of images is significantly improved.

Depth of correlation

In a microscope, the objective lens has a focal plane which has a limited depth, only the objects located in this region can be seen clearly. However, when the volume illumination method is employed, all particles in the fluid are illuminated, thus out-focus-effect appears. Particles which are not situated in the focal plane leave a projection on the image. This will influence the measurement as noise or disturbance.

Depth of focus (DoF) or depth of field is the thickness of a thin layer in which objects can be considered in the focal plane (Fig 2.22). It can be calculated by equation (2.23), where λ is the laser wavelength, n_0 is the refractive index (RI) of the objective lens immersion fluid, M and NA are respectively the magnification number and the numerical aperture of the objective lens (Koutsiaris 2012).

$$DoF = \frac{\lambda n_0}{NA^2} + \frac{n_0 \cdot D_{pixel}}{M \cdot NA} \tag{2.23}$$

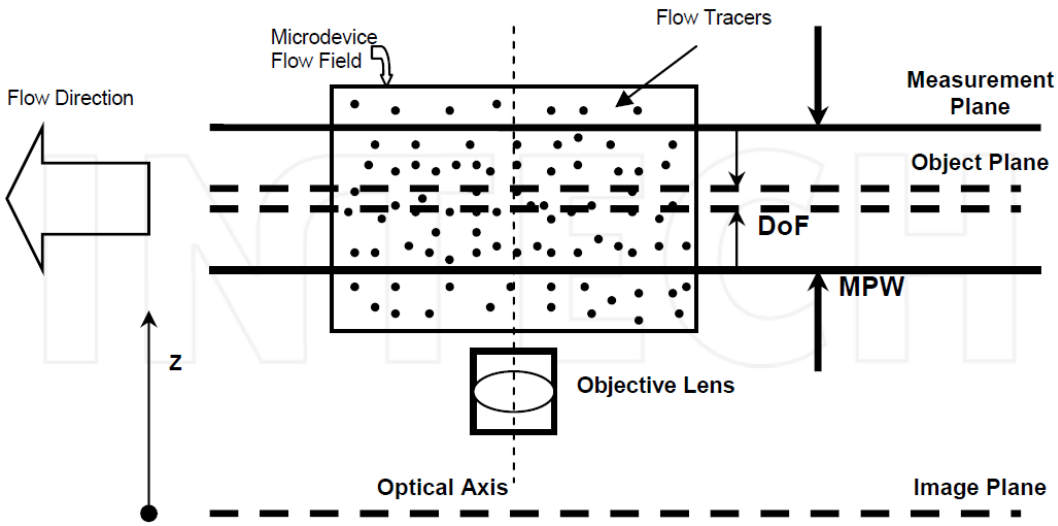

Fig 2.22 Schematic illustration of depth of focus and measurement plane width (Koutsiaris 2012)

Depth of correlation (DOC) is defined as twice the distance beyond which the tracer particle's intensity is sufficiently low that it will not influence the velocity measurement (Raffel et al. 2007b). It is also called Measurement Plan Width (MPW).

The commonly used simplified expression to calculate DOC for micro-PIV was derived by Olsen and Adrian (2000):

$$DOC = 2\left[\frac{(1-\sqrt{\varepsilon})}{\sqrt{\varepsilon}}\left(\frac{n_0^2 d_p^2}{4NA^2} + \frac{5.95(M+1)^2\lambda^2 n_0^4}{16M^2NA^2}\right)\right]^{1/2} \tag{2.24}$$

Where ε is the relative threshold below which the defocused particle images no longer contribute significantly to the displacement correlation peak, normally set to be equal to

0.01. According to this expression, the NA and d_p most affect the DOC value, the magnification has less influence (Bourdon, Olsen, and Gorby 2005).

For tracer particle seeding in micro-PIV experiments, the particles size and concentration should be considered finely.

Seeding particle size

To determine the seeding particle sizes, two constraints should be considered: optic constraint and hydrodynamic constraint. For the optic constraint, according to Lindken et al. (2009), the recommended tracer particle size is 0.5-1.5μm, with particle image diameter equal to 2-3 pixels. For the hydrodynamic constraint, in order to make sure that tracer particles can well follow the flow, the response time of a tracer particle should be much smaller than the smallest time-scale in the flow. The response time τ_p can be calculated based on a simple first order inertial response to a constant flow acceleration (assuming stokes flow for the particle drag), as shown below (Raffel et al. 2007b):

$$\tau_p = \frac{d_p^2 \rho_p}{18\eta} \tag{2.25}$$

Where d_p and ρ_p are the diameter and density of the tracer particle respectively, and η is the dynamic viscosity of the fluid.

Seeding particle concentration

The seeding particle concentration should not be too small in order to make sure that there are enough tracer particles in each IW for the cross-correlation. As well, it should not be too high, as high tracer particle concentration brings undesired problem such as higher background noise or particle agglomeration (Lindken et al. 2009). In general PIV images, there are at least 6 tracer particles in each IW. However, if the same tracer particles concentration is applied to micro-PIV experiments, the tracer particle concentration will be too dense which would change the fluid dynamics. The low tracer particle concentration in IWs can be compensated by ensemble PIV, which will be presented in section (2.4.2.3).

The calculation of tracer particle concentration can be based on a parameter named particle visibility (V_z), which is defined as the ratio of the intensity of a focused particle image to the average intensity of the background light produced by the unfocused particles (Olsen and Adrian 2000). The expression to calculate tracer particle concentration (C_{tr}) at a known visibility is shown below:

$$C_{tr} = \frac{2d_p^3 M^2 \beta^2 (s_o - a)(s_o - a + L_f)}{3V_z L s_o^2 \left\{ M^2 d_p^2 + 1.49(M+1)^2 \lambda^2 \left[\left(\frac{n_0}{NA} \right)^2 - 1 \right] \right\}} \quad (2.26)$$

Where β is a constant that often taken the value as $\beta^2 = 3.67$, for the reason that at this value, the Gaussian distribution of the particle image intensity is best approximated to an airy distribution. s_o is the focal plane distance of the objective, it can be estimated by the sum of working distance of the lens and cover slip thickness (Raffel et al. 2007b). L_f is the thickness of the measured flow, a is the depth of the measurement, λ is the laser wavelength, n_0 is the refractive index of the lens immersion liquid. According to equation (2.26), the visibility can be increased by reducing the tracer particle concentration. According to Raffel et al. (2007b), to obtain high quality velocity measurement, the value of V_z should in general be largrer than 1.5. They recommended that the deduced $C_{tr}(V_z$=1.5) can be used as a reference to determine the tracer particle concentration.

2.4.2.3 Image acquisition and image processing

Image acquisition

For image acquisition, as a starting rule, the maximum particle displacement(Δs), should be no more than 25% of the size of the interrogation window (Lindken et al. 2009), and the closer to this value, the better, as this displacement result in limited in-plane loss of correlation and out of plane loss of correlation. For example, with an interrogation window of 64 × 64 pixels, the best displacement distance is 16 pixels. Therefore, at different velocity, the corresponding time interval should be adjusted to respect this rules.

Image processing

The image processing is divided into 3 steps: pre-processing, processing and post processing.

Pre-processing is used for image restoration or image enhancement, such as image grayscale inversion, image filtering and background removing.

Processing is implemented by cross-correlation of the IW of the two consecutive images. The cross-correlation can be either calculated directly in the spatial domain or through the frequency domain using Fast Fourier Transform (FFT). Direct correlation is computationally expensive $O[N^4]$, (N is the size of the IWs). While in the frequency domain, the cost is reduced to $O[N^2 log_2 N]$ operations, which is less time consuming. Therefore FFT correlation is more preferred, except that care must be taken with aliasing effect, bias error (Raffel et al. 2007a).

The post-processing consists of the validation of the raw data, removal and replacement of spurious velocity vectors. For example, local validation uses the vectors in the neighborhood of each vector to calculate a reference vector for validation. When the difference between the current vector and the reference vector is smaller than the user-defined tolerance, the current vector is valid. The local median validation is the most widely used local validation method, where the median value of all the vectors in the neighborhood is used to be the reference vector. Invalid vector can be replaced by the mean or the median vector of the neighbor vectors.

In addition, for micro-PIV experiment, ensemble averaging PIV is generally used for image processing; it is also called correlation averaging. Because the tracer particle density in a micro-PIV image is much smaller than that of general PIV images, there are not enough tracer particles in each IW. Thus, the percentage of valid vectors is small with only one pair of images. But in a stationary flow, if a series of images is taken, and the correlation peak is obtained by computing the average of all the peaks of the IWs in these images, then a higher percentage of valid vectors and a better correlation result can be acquired (Equation (2.28)).

$$C_k(x,y) = \sum_{i=-p}^{p} \sum_{j=-q}^{q} I_k(i,j) I_k'(i+x, j+y) \tag{2.27}$$

Where C_k is the correlation value of the kth image pair (I_k and I_k'), N is the number of image pairs, then the averaged correlation function is given as:

$$C_{avr}(x,y) = \frac{1}{N} \sum_{k=1}^{N} C_k(x,y) \tag{2.28}$$

Under typical experimental conditions 50 image pairs are sufficient to obtain 100% valid vectors (Vennemann et al. 2006; Lindken et al. 2009).

Another method is image overlapping. It generates an overlapped image which is the maximum image intensity within a series of images (Equation (2.29)). Then the cross-correlation is performed based on the overlapped image pair. However this method is not appropriate for image with high tracer particle density or too many images, due to interference between particle images when the number of particle images is very large.

$$I(i,j) = \max\{I_k(i,j), k = 1,2,3,\cdots,N\} \tag{2.29}$$

2.4.2.4 Measurement uncertainty

According to equation (2.22), there are three components contributing to the total velocity measurement error, the calibrated pixel size D_{pixel}, the displacement Δs, the time interval between two images Δt. The errors of D_{pixel} and Δt are considered negligible, thus the main error is from Δs. The error of Δs is composed of two parts: the random error and the systematic bias error.

If the displacements of the tracer particles in the interrogation window are uniform, and the particle image shape is exact Gaussian, the random error amplitude ε_{rd} can be estimated as (Westerweel 2000):

$$\varepsilon_{rd} \approx c d_{\tau} \tag{2.30}$$

Where c is a constant related to the experimental parameters, d_τ is the effective particle image diameter when a particle is in the focal plane (Equation (2.43)). The value of c is typically around 0.05–0.1. But, when the flow is non-uniform, for example, if shear gradients are present, the random error will further increase due to a broadening of the correlation peak diameter (Westerweel 2007).

For the systematic bias error, it has the following components:

1) Flow error, it depends on whether the tracer particles can well follow the flow, and the Brownian motion of tracer particles.
2) Particle image generation error, which is due to non-uniform illumination, out of focus effect, optical aberrations, electronic and digitization noise.
3) Image processing error, which is due to the inadequacy of the statistical method of cross-correlation in the evaluation of particle displacement (Raffel et al. 2007a).

The Brownian motion error depends on the size of the tracer particles, the time interval Δt and the velocity of fluid u (Wereley and Meinhart 2005), it can be estimated by the equation below:

$$\varepsilon_x = \frac{1}{u}\sqrt{\frac{2D}{\Delta t}} \tag{2.31}$$

Where D is the diffusion coefficient, which is defined as the following:

$$D = \frac{k_B T_a}{3\pi\eta d_p} \tag{2.32}$$

k_B is Boltzmann's constant, T_a is the absolute temperature of the fluid, and η is the dynamic viscosity of the fluid. According to this equation, when the particles size

decreases or the time interval increases, the error increases. However, the Brownian motion error will be reduced by correlation averaging as it takes the average correlation result in a series of images. The other errors depend on system which can be decreased by improving the experimental conditions or using better image processing method.

In general, Wereley and Meinhart (2010) thought the acceptable uncertainty of micro-PIV measurement is 2%.

2.4.3 Particle locating method

To measure the local particle concentration, one method is by determining the particle positions in a suspension. The particle positions can be inferred according to their images, because the particle images are different when their distances to the focal plane are varied. Particle locating methods are thus developed based on their image properties (image diameter and image intensity).

2.4.3.1 Particle image characterization

For particle image diameter which is also called effective image diameter (d_τ), 3 components contribute to it: the geometrical size of the particle (d_p), diffraction effect (d_s), and out of focus effect (d_f). Under the assumption that the particle image intensity can be modeled as a Gaussian function, the particle image diameter can be derived by the following equation (Olsen and Adrian 2000):

$$d_\tau = \sqrt{(Md_p)^2 + {d_s}^2 + {d_f}^2} \tag{2.33}$$

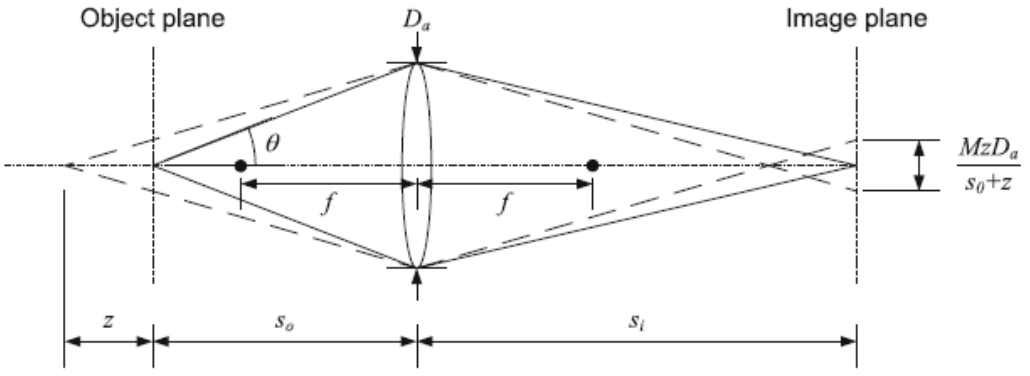

Fig 2.26 Optical geometry used in deriving the particle image diameter (Rossi et al. 2011)

The diffraction component is deduced by Adrian and Yao (1985), which is a property related to objective magnification and light wavelength, as shown below:

$$d_s = 2.44(M+1)f_{\#}\lambda \tag{2.34}$$

Where $f_{\#}$ is called f number, it is defined as $f_{\#}=f/D_a$. As shown in Fig 2.6, D_a, f, s_0, s_i are resectively the diameter, the focal distance, the working distance, and the image plane distance of the objective lens. $M=s_i/s_0$, and the Gaussian lens formula is:

$$\frac{1}{s_0}+\frac{1}{s_i}=\frac{1}{f} \tag{2.35}$$

With these relations, d_s can be rewritten as:

$$d_s = 2.44M\lambda\frac{s_0}{D_a} \tag{2.36}$$

According to trigonometry, the below relationship is obtained:

$$\frac{s_0}{D_a}=\frac{1}{2}\left(\frac{1}{sin^2\theta}-1\right)^{1/2}=\frac{1}{2}\left(\frac{{n_0}^2}{NA^2}-1\right)^{1/2} \tag{2.37}$$

Substituting equation (2.37) to equation (2.36), the final expression of d_s can be expressed as a function of NA, M, λ :

$$d_s = 1.22M\lambda\left(\frac{{n_0}^2}{NA^2}-1\right)^{1/2} \tag{2.38}$$

z is the defocused distance, the defocused term is derived under the case of single thin-lens configuration :

$$d_f=\frac{MzD_a}{s_0+z} \tag{2.39}$$

Assuming $s_0 \gg z$, then d_f can be expressed as:

$$d_f = 2Mz\left(\frac{{n_0}^2}{NA^2}-1\right)^{-1/2} \tag{2.40}$$

Finally, the effective particle image diameter can be given by the following expression (Rossi et al. 2011):

$$d_\tau = M\left[{d_p}^2+1.49\lambda^2\left(\frac{{n_0}^2}{NA^2}-1\right)+4z^2\left(\frac{{n_0}^2}{NA^2}-1\right)^{-1}\right]^{1/2} \tag{2.41}$$

Olsen and Adrian (2000) adopted another expression as shown below, because they used a simplification of the f-number, $f_{\#}=n_0/2NA$.

$$d_\tau = \left[M^2 {d_p}^2 + 1.49\lambda^2 \frac{{n_0}^2}{NA^2}(M+1)^2 + \frac{M^2 z^2 {D_a}^2}{(s_0+z)^2}\right]^{1/2} \tag{2.42}$$

According to the above expression, the effective particle image diameter should be bigger than the magnified geometrical diameter.

In a simple case, a spherical particle located in the focal plane, without the out of focus term d_f, the total effective particle image diameter can be approximated by:

$$\mathrm{d_\tau} = \sqrt{(\mathrm{M d_p})^2 + {\mathrm{d_s}}^2} \tag{2.43}$$

Normally, defocused particles should have larger particle image diameters than that of in-focus particles. However, as they are not in the focal plane, their image intensity is smaller than that of in-focus particles. The distribution of a particle image intensity is assumed to be Gaussian (Adrian and Yao 1985), which can be modeled as the following equation:

$$I(r,z) = \frac{J_p D_a^2 \beta^2}{4\pi d_\tau^2 (s_0+z)^2} exp\left(\frac{-4\beta^2 r^2}{d_\tau^2}\right) \tag{2.44}$$

Where r is the distance from the particle center, J_p is the flux of light emitted from the particle surface, and $\beta^2 = 3.67$, as mentioned in equation (2.26). According to equation (2.42)and (2.44), Kloosterman et al.(2010) drew a schema to illustrate the variation of particle image intensity and particle image diameter as a function of z and r. As shown in Fig 2.237, the particle image radius increases and the intensity decreases following the increase of defocused distance.

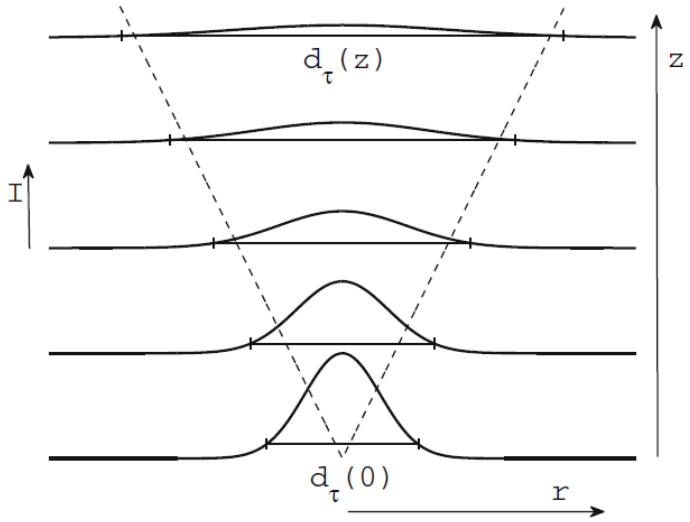

Fig 2.237 Schematic representation of the cross section of particle image intensity for different z-position based on equation (2.42) and (2.44), the particle image diameter d_τ

increases for increasing z, while the peak intensity $I(r,z)$ decreases. The dashed line represents the geometrical spreading of an image of out of focus particle (Kloosterman, Poelma, and Westerweel 2010).

2.4.3.2 Image processing method for particle detection

Image processing methods are used to determine the location of particle centers from the images, as presented in a review about imaging technique for concentrated suspension flow (Besseling et al. 2009). From the determined particle positions, further analysis can be made, for example, particle tracking (Chenouard et al. 2014; Smal et al. 2010).

As described in the section above, the particle image changes following the variation of the distance to the focal plane. Thus, in a general case, the determination the particle position can be separated into two parts: determining the x-y plane (2D) coordinates, and determining the z-positions (Crocker and Grier 1996), as shown in the figure below.

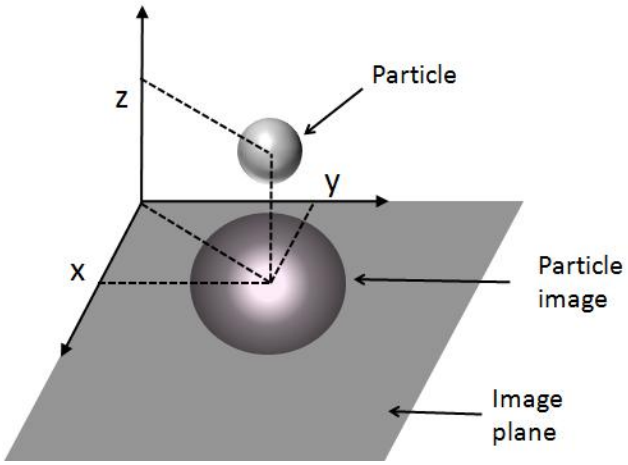

Fig 2.28 Illustration the position of a particle in the Cartesian coordinate based on the image plane

Position in x-y plane

For 2D particle position locating, the conventional method was introduced by Crocker and Grier (1996), which was primarily used to identify circular (2D) or spherical (3D) objects that appear bright on a dark background.

The method is implemented as follows. Firstly, the images are treated with a spatial bandpass filter, which eliminates long-wavelength contrast gradients and pixel-to-pixel noise. Next, the x-y plane coordinates of the particle centers are obtained by locating the local intensity maxima in the filtered images. These coordinates are then refined to a higher accuracy by applying a centroiding algorithm, which locates the brightness-weighted center of mass (centroid) of the particles. With this refinement the coordinates of the particle center can be obtained with sub-pixel precision. The local maxima method

has an advantage to detect particle with a bright image center, and it can be applied to detect particles with different shape. However, this method has some limitations in concentrated systems, as individual particle images start to overlap.

Another method consists in detecting the particle image contour, and then determining the particle position. One example to do so is to use the Hough Transform method, which has been applied successfully for circle detection (Warr, Jacques, and Huntley 1994; Warr and Hansen 1996). The advantage of this method is to detect particle without maximum brightness in the particle image center, and it can work well although there is image overlapping. But this method is restricted to spherical or cylindrical particles. Moreover, it possesses a poor precision for small particle images (diameter <10pixel). Another example is based on image segmentation. As the particle image has a different light intensity compared to the background, the region where the particle is located can be recognized by thresholding based on image intensity (Barnkob, Kähler, and Rossi 2015). But the particle center coordinates remain to be determined finely together with the z-position, as will be introduced later.

Z-position

To determine the Z-position of a particle, the conventional method is to prepare a stack of calibrated particle images at different z-positions. Then, the target particle image (I_t) will be compared to this stack of images (I_c) by cross-correlation. The z-position of a particle is defined when a best match is found (Crocker and Grier 1996; Gao and Kilfoil 2009), and by some subsequent refinement (Ex. Gaussian peak fit and parabolic fit), a better precision can be acquired. One example is the General Defocusing Particle Tracking (GDPT) tool of Barnkob et al. (2015). The principle of their program is as follows. At first, the particle is recognized by image segmentation $I_t(X,Y)$ and a calibrated stack of images $I_c(X,Y)_k$ at different z-position were prepared. Secondly, the image $I_t(X,Y)$ is compared to the calibration image stack $I_c(X,Y)_k$, in order to find the best match with one of the k calibrations. To quantitatively describe the similarity between the $I_t(X,Y)$ and $I_c(X,Y)$, they used a normalized cross-correlation function C(u,v), as shown below:

$$C(u,v) = \frac{\sum_{X,Y}[I_c(X,Y) - \overline{I_c}][I_t(X-u,Y-v) - \overline{I_t}]}{\sqrt{\{\sum_{X,Y}[I_c(X,Y) - \overline{I_c}]^2 \sum_{X,Y}[I_t(X-u,Y-v) - \overline{I_t}]^2\}}} \tag{2.45}$$

Where (u,v) is the in-plane coordinates of the correlation space, $\overline{I_c}$ and $\overline{I_t}$ are respectively the mean intensities of I_c and I_t. Amplitude of the peak is noted as C_m, having value between 0 and 1, with $C_m = 1$ indicates a perfect match, as shown in Fig

2.24. After, the z-position is refined by a three-point parabolic-fit estimator; the in-plane position was refined by a three-point Gaussian-fit estimator.

This method can work well even with a presence of intensity fluctuation of images, which is due to inhomogeneous light distribution. However, this method has some difficulties when particle images start to overlap as well.

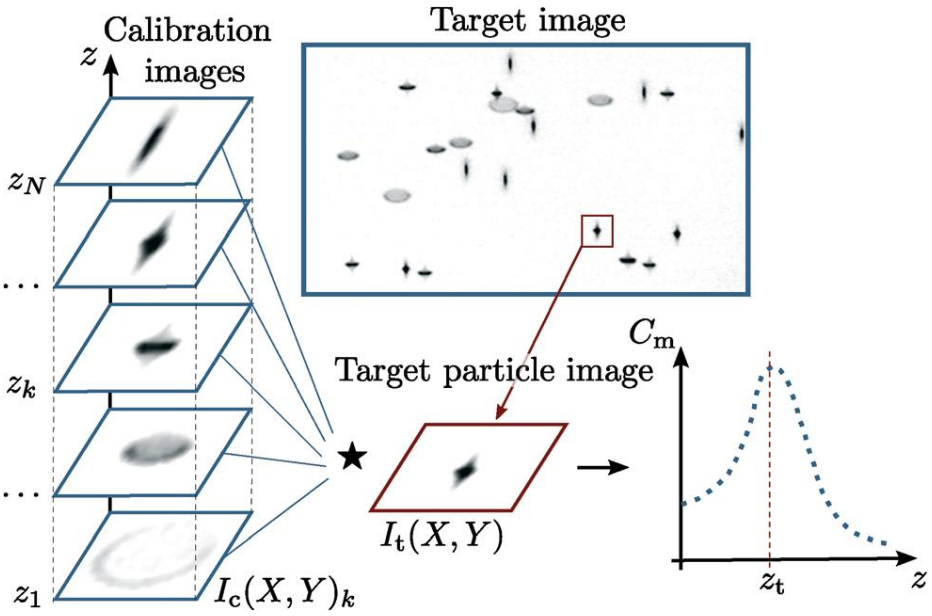

Fig 2.24 GDPT working principle: a target particle image I_t is compared to a set of calibration images I_c by using the normalized cross correlation. The out-of-plane coordinate z_t for the target particle is found where the maximum correlation C_m is the highest as a function of the out-of-plane coordinate Z (Barnkob, Kähler, and Rossi 2015).

Another method is implemented by optimizing the overlap of the measured intensity profile of each particle and the so called 'sphere spread function', which is the image intensity profile of a sphere light source through an optical system (Jenkins and Egelhaaf 2008). This method is similar to the previous method, except that the calibrated stack of images is from a simulation.

The particle image diameter will change following the z-position as described in equation (2.41). Therefore, by evaluating the particle image diameter, the z-position of a particle can be determined (Rossi and Kähler 2014). However, these methods are affected by the fluctuation of image intensity, as the identification of image diameter depends on the image intensity. Therefore, this method is not often used.

In general, based on the methods mentioned above, and incorporated with some image preprocessing approaches, such as Gaussian filters (for image smoothing), median filters (for noise reducing), background removing and image adjustment (for signal to noise ratio improvement), the particle position can be determined. Many open source codes

have been developed, such as Trackpy, u-track, Mtrack2 and GDPTlab, most of them are available on the internet, which facilitate the work of other researchers.

2.5 Positioning of the study

As presented above, there are currently many studies on blood and suspension flows. Although less presented in this literature review, there are many in vitro studies in the field of high hematocrit blood flow. However, to the best of our knowledge, the detailed flow dynamics measurements were limited to flows with characteristic size of the geometry being smaller than 100μm. Moreover the concentrations measurements were limited to bulk hematocrit determinations and the literature lacks the measure of the local particle concentration. In the field of suspensions, there are also studies using suspension with a concentration of about 45%, but then the particle size is often bigger than 50μm, and only a few of them have measured the particle concentration.

In the current study, dense suspensions of mono-dispersed spherical particles were chosen for the experimental conditions were easier to be controlled. The flow velocity profiles were measured by micro-PIV and the local concentrations were measured by image processing method.

The originality of our work resides in the facts that :

- there are two sizes of particle being considered, one is of diameter of 4.62μm, which has a volume equivalent to that of a red blood cell, and the other is 41μm which can be used to mimic the red blood cell aggregations in future research. The maximum particle concentration is 45%.
- the suspensions were sheared under a cone-plate device with a height of about 1mm, which generated flows with constant shear rate.

3 Density and refractive index matched suspension model

In this chapter, the preparation process of the suspensions will be described. The rheology property of the suspensions will be characterized.

3.1 Suspension preparation process

In order to investigate dense particle suspension flow using micro-PIV techniques, a transparent suspension is required for optical access. The refractive index matching technique is thus employed for suspension preparation. Moreover, in order to avoid sedimentation and buoyancy of particles, density matching should be performed simultaneously.

In the current experiment, PMMA spheres (microparticles GmbH) were selected, as it is a material which can be used to make transparent particle (300nm-1000μm) as well as shape desired devices. A new recipe for density and RI matching with particles was developed, which is composed of three products: glycerol (Phocéenne de chimie), Phosphate Buffered Saline (PBS) solution and 2.2'-Thiodiethanol (TDE, Sigma-Aldrich). The principle is as follows: TDE has a bigger RI than that of PMMA particles, Glycerol has a higher density than that of PMMA particles, and PBS is added to adapt the RI and density to that of PMMA particles. The densities and RI of the four components at 25°C is shown in the table below.

Properties	TDE	PBS	glycerol	PMMA
Density (g/ml)	1.18	1.003	1.258	1.18
RI	1.517	1.33	1.474	1.49

Tab 3.1 Densities and refractive indexes of the four components at T=25°C

The detail method to prepare such a suspension was already written in an article (Zhu, Knapp, and Deplano 2016) published in the journal Experiment in Fluids, as shown in the following pages. In the final prepared suspension, the precision for RI matching is about ±0.0003, and the precision for density matching is about ±0.001g/cm^3.

Exp Fluids (2016) 57:68
DOI 10.1007/s00348-016-2150-8

RESEARCH ARTICLE

Low hazard refractive index and density-matched fluid for quantitative imaging of concentrated suspensions of particles

W. Zhu[1] · Y. Knapp[2] · V. Deplano[1]

Received: 15 September 2015 / Revised: 11 March 2016 / Accepted: 13 March 2016
© Springer-Verlag Berlin Heidelberg 2016

Abstract A novel refractive index and density-matched liquid–solid suspension system taking into account chemical hazard and health concerns was developed and characterized. The solid phase is made of PMMA spheres, the refractive index of which being adapted with a mixture of 2,2′-thiodiethanol and phosphate-buffered saline (PBS), while the density is adapted with a mixture of PBS and glycerol. The proposed chemicals present low hazard characteristics in comparison with former solutions. Data collected from density and refractive index measurements of the solid phase and of the different fluid constituents are used to define a specific ternary mixture adapted to commercial grade micron-size particles. The defined mixture is validated in a micron-sized granular flow experiment. The described method can be applied to other low-density solids.

1 Introduction

Refractive index matching (RIM) techniques are often used in the qualitative or quantitative study of bounded flows (see reviews by Isa et al. 2010; Wiederseiner et al. 2011; Saksena et al. 2015) in order to avoid scattering of light at solid–liquid or liquid–liquid interfaces. In these common situations in experimental fluid mechanics, the refractive index (RI) of the fluid is adapted to the RI of the experimental setup (walls, internal sections, porous media solid phase. . .) and to the suspending material. These techniques are implemented to reduce image distortion and to eliminate optical "hot spots" resulting from total internal reflection of illuminating light beams. While applying corrective post-processing can be considered in some limited cases, these solutions are not possible in the case of light sheet transmission for planar imaging (PIV, PTV, pLIF), for deformable liquid–liquid interfaces or for flow of suspensions. In the first case, the light path is disturbed for illumination and image acquisition, and in the two latter cases random image distortions happen due to random location of interfaces in the flow. Moreover, in such cases, RI mismatch resulting phenomena become critical when downsizing experiments to the microscale: the radii of curvature of structures and/or particles become very small, and the average number of interfaces increases. A precise RIM has therefore to be implemented. On the other hand, in the case of small-scale suspension flows, density matching (DM) becomes also a key issue. The settling velocity due to density mismatch between the different phases can lead to unwanted particle distribution/gradients. A precise DM technique has therefore to be implemented. Solving this issue reduces the number of candidates for the solid phase of the suspension because of the limited high-density fluid candidates; typically, only low-density polymers can be considered.

Historically, a great variety of recipes have been developed to match the RI of a fluid with the one of various transparent materials; see Wiederseiner et al. (2011) for a review on solid–liquid matching and Saksena et al. (2015) for a review on liquid–liquid matching. We here limit our considerations to the matching of transparent solid materials: low- or high-density polymers, glasses, fused quartz…. According to this

✉ Y. Knapp
yannick.knapp@univ-avignon.fr

[1] Aix-Marseille Universit , CNRS, Ecole Centrale Marseille, IRPHE UMR7342, 13384 Marseille, France

[2] LAPEC EA4278, Avignon Universit , 84000 Avignon, France

Published online: 27 April 2016

literature the precise RIM can be obtained by mixing different liquids (water, natural or mineral oils, organic liquids as, for example, in Lyon and Leal 1998) or by dissolving salts in water or other solvents (typ. iodide or sodium derivatives are classical candidates as in Bai and Katz 2014). In most cases, the matching is obtained by mixing adequate proportions of different components and concentration is therefore considered as the primary tuning parameter. However, these components and their mixtures have a non-negligible RI temperature coefficient (or thermo-optic constant). The mixtures are then also tunable to the sought RI by a temperature control of the experimental setup. Even if a lot of recipes have been implemented, most of the usual liquids undergo restrictions in usage and disposal due to:

- Life span issues: Iodide solutions, for example, are photosensitive and become yellow, and natural evaporation of solvents modifies the fluid properties,
- Toxicity and/or harmful health effects: Most of the salts are skin and/or eye irritants, tetralin or turpentine, Triton X100, and others are classified as toxic to aquatic life with long-lasting effects, and 1.6-dibromohexane, for example, is classified as "Fatal if swallowed",
- Chemical interaction with the experimental setup or during storage: Potassium thiocyanate becomes red in contact with iron and has a high-RI temperature coefficient, bromocyclohexane is a solvent for PMMA, tetralin or decalin forms potentially explosive peroxides on long-time storage in contact with air/light/heat,
- Volatility, flammability: Kerosene or decahydronaphthalene, for example, has low flash point temperature and needs non-sparking tools and equipment, ventilated rooms.

Some of the raw materials even combine several of such restrictions. A principal goal of our research work was therefore to identify a novel recipe able to overcome as much as possible these limitations. From the many raw materials used for RIM, no attention has been put on the use of $2,2'$-thiodiethanol (TDE) which yet is a clear non-toxic liquid substance capable of matching the RI on a large range when mixed with simple solvents (e.g., water). The goals of the present study are (1) to present an original mixture based on TDE able to match both the RI and the density of commercial PMMA microspheres, (2) to present a simple experimental methodology and models that enable the determination of a recipe of the mixture, (3) to implement the resulting recipe in basic microscopic experiments.

2 Materials and methods

2.1 Materials

2.1.1 Solid phase

Since density matching is considered, only low-density materials such as polymers like PMMA, PS, PVA, PDMS for the solid phase should be considered. PMMA is then a good candidate since it is a widely available and low-cost material. In addition, PMMA has interesting properties: as a bulk material it can be easily bonded or machined into various geometries and exists as raw material in various shapes (rods, tubes, plates, beads). Although it is a widely used and studied material, the physico-chemical properties of commercial grade PMMA can vary in large proportions. The RI of PMMA varies in the range [1.264–3.46] median 1.4916 (Courtesy of NIMS Data Base) mainly depending on the temperature and the wavelength under consideration. Its density varies in the range [1.11–1.58] median 1.193 (Courtesy of NIMS Data Base) depending on the commercial grade of the material. Typical values found in the literature are 1.49 as RI and 1.18 as density. In the present work monodisperse PMMA particles (microparticles GmbH), with diameter $d_P = 41\,\mu$m, are chosen as the solid phase of the suspension. Although these particles are of research grade the RI, n_P, and the density, ρ_P, are not precisely specified and are to be considered as being in the aforementioned ranges. Specific methods are therefore described and implemented to assess both values. This determination step can be ignored in case the data are accurately known.

2.1.2 Liquid phase

$2,2'$-thiodiethanol (TDE) is a clear viscous liquid mainly used as a solvent. It can be mixed in any proportion with water so that any RI between 1.33 and 1.51 (for pure water and TDE, respectively) can be obtained: referring to the available literature a 86 % (v/v) TDE–water mixture can result in a 1.49 refractive index (Staudt et al. 2007). However, phosphate-buffered saline (PBS) solution has been proved to be a better solvent, increasing the stability and life span of the mixture. Adding different amounts of water or PBS will result in a modification of the density of the final mixture; the density range is then between 1 and 1.18 (for pure water/PBS and TDE, respectively). Here, a simple procedure to compensate this density reduction consists in adding a third miscible high-density material. A good candidate for such adaptation is pure glycerol which has a typical density of 1.26 and a RI of 1.47. The reduction in density can obviously be compensated by addition of glycerol with limited impact on the RI. Moreover, Material Safety Data Sheets (MSDS) of these components show that

glycerol and PBS are "Not regarded as a health or environmental hazard under current legislation." Concerning TDE, and to the best of our knowledge, the MSDS present only a hazard warning about high irritation in case of eye contact; wearing eye shields is highly recommended. Another interesting feature of the proposed mixture is its RI temperature coefficient. The coefficients reported in the literature for the different constituents of the mixture are around $-2\ 10^{-4}/°$C for glycerol, $-3\ 10^{-4}/°$C for TDE and $-1\ 10^{-4}/°$C for water/PBS. A mixture of these components should therefore result in a RI and density-matched suspension with a refractive index temperature coefficient differing from the reported value of about $-1\ 10^{-4}/°$C for PMMA. This will allow for a proper adjustment of the RI of the liquid to a desired value by changing its temperature.

2.2 Experimental methods

2.2.1 Mixture definition methodology

Once n_P and ρ_P are determined, it is possible to proceed to the definition of the proper recipe based on the aforementioned components. While usually the preparation of a ternary mixture is based on the assembly of two solutions having a common component, the preparation protocol is here simplified as following: at first a mixture of glycerol and PBS is prepared, noted as solution A. Then an amount of solution A is mixed with pure TDE (noted solution B) to obtain the final mixture solution C which is designed to match the density and RI of the particle at a set temperature. This procedure limits the study to a small range of concentrations and temperatures. Thereby, the proportion of glycerol in solution A and of TDE in solution C will be calculated from Eqs. (1) and (2) for a given temperature.

$$\begin{cases} \rho_A = f_1(T,\chi), & n_A = f_2(T,\chi) \\ \rho_B = f_3(T), & n_B = f_4(T) \end{cases} \tag{1}$$

$$\begin{cases} \phi \cdot n_B + (1-\phi)\cdot n_A = n_C \\ \phi \cdot \rho_B + (1-\phi)\cdot \rho_A = \rho_C \end{cases} \tag{2}$$

where ϕ is the volume fraction of TDE, χ is the mass fraction of glycerol in solution A (mixture of glycerol and PBS), ρ_A, n_A are density and RI of solution A, ρ_B, n_B are density and RI of TDE, ρ_C, n_C are density and RI of solution C. The equation set (1) and the underlying functions f_1, f_2, f_3, f_4 are obtained by linear regressions of measured data. Equation set (2) is based on the hypothesis that both the RI and the density of the mixture follow an Arago–Biot-type equation. The evolution of RI and density of solution A as a function of glycerol proportion and temperature, and the evolution of RI and density of TDE as a function of temperature are necessary input data for the resolution of the system.

2.2.2 Properties of the solid phase

2.2.2.1 Refractive index A method based on absorbance/transmission was implemented to measure the RI of the small PMMA particles (Wiederseiner et al. 2011). For this, a modified commercial spectrophotometer (Uviline 9400, Secomam) was used. The modifications consisted in the implementation of a specific thermal control of the sample cells and the addition of a pinhole on the light path at the output of the wavelength-controlled light source. Temperature-controlled absorbance measurements at a typical 589 nm were taken on PBS/TDE solutions with various concentrations containing about 8 % particles (w/w). For each solution a measurement of the RI (temperature-controlled Abbe refractometer) was taken at the same wavelength so that the minimum absorbance concentration could directly be converted in a RI of the particles. This minimum was inferred from the derivation of a parabolic curve matching the measured data points. Note that this method results in the determination of the RI of the particles at a given temperature. This temperature should be used as input data for the resolution of Eqs. (1) and (2). If necessary this method can be repeated for various PBS/TDE mixtures so that the RI can be determined at different temperatures. This time-consuming work can be avoided by considering the temperature dependence of refractive index of PMMA which is $-1.09\ 10^{-4}/°$C in the range of implemented temperature and wavelength following Kasarova et al. (2010).

The accuracy of the method relies on the thinness of the dilution steps. However, in the present work the dilution steps and their precision were very small and the principal source of error comes from the refractive index measurement apparatus and procedure. The resulting accuracy thereof was ± 0.0003.

2.2.2.2 Density Because the settling velocity of particles can be very low when the matching gets close, the density of the particles is determined indirectly by a centrifugation procedure. Mixtures of water and glycerol with different concentrations obtained by consecutive dilutions of an initial solution serve as a suspending material for the particles. The density of the water–glycerol solutions is determined from the dilution process by weighing, initial densities being determined with a pycnometer. The water–glycerol particle mixtures are sampled with small 70 μm internal diameter and 50 mm long glass capillaries. The capillaries are centrifuged 12 min at 16,000× g before analysis under a microscope. The difference of density between liquid and solid phase results in a clear separation toward the inner or outer direction of the centrifuge. The accuracy of the method relies on the thinness of the dilution steps; in the present case this accuracy was ± 0.0012 g/cm^3 as the half of the density difference between two consecutive dilutions, each inducing an opposite separation of particles after centrifugation.

2.2.3 Properties of the liquid phase

2.2.3.1 Refractive index A traditional Abbe refractometer is used to measure the RI of different liquid samples. The refractometer works based on the optical refraction critical angle detection technique and has a measuring range of 1.3–1.7, a resolution of $0.0005n$ and an accuracy of $\pm 0.0003n$ (± 0.15 %). In order to control the temperature of the samples, the refractometer was connected to a thermal regulation system (Fisher Scientific Isotemp circulator with water running through it as the working fluid) with a temperature stability of ± 0.1 °C.

2.2.3.2 Density For the measurement of the density of liquids, a density meter (Anton Paar) was used. The device can simultaneously measure the temperature and the density of the test medium. The accuracy of the measurement is 0.001 g/cm^3 at temperature accuracy 0.2 °C. In order to limit experiments, 4 mixtures of glycerol and water with densities potentially close to an average 1.18 g/cm^3 are presented. These mixtures have, respectively, 68, 70, 72 and 75 % glycerol mass fractions. The density and refractive index of these solutions and of pure TDE were measured at different temperatures from 18 to 30 °C.

3 Results and discussion

3.1 Results of PMMA particles measurement

3.1.1 Refractive index

The RI of PBS (Fisher Scientific) and TDE (Sigma-Aldrich) mixtures at different temperatures was already determined (data not shown), and a direct transformation gives the relation between relative absorbance and RI measurements (Fig. 1).

According to these data, a parabolic curve fit is applied to each dataset with a coefficient of determination $R^2 = 0.9908$, valid for $T = 16{-}32$ °C. A derivation of the curves gives access to the minimum of the curve for which the RI of fluid and particles is matched. From this method the average RI of the particle is $n_P = 1.4892 \pm 0.0003$ at wavelength 589 nm at 22.25 °C. The accuracy of the method is imposed by the accuracy of the RI measurements. The obtained RI value is consistent with the measurement of Wiederseiner et al. (2011) 1.48847 (0.04 % difference) and with the value 1.4934 (0.28 % difference) inferred from the work by Kasarova et al. (2010). Such slight discrepancies are reasonable considering possible differences in composition and/or manufacturing process.

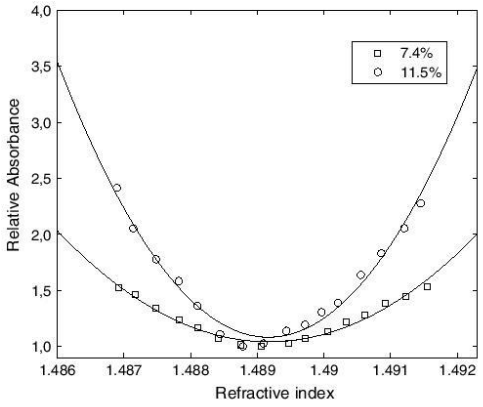

Fig. 1 Relative absorbance as a function of RI for 2 PMMA suspensions in mixtures of PBS and TDE. Measurement is done by variation of temperature

3.1.1.1 Density The application of the procedure described in Sect. 2.2.2.2 and the observation of the capillaries tips under a microscope resulted in clear density separations. For the present case, particles have moved toward the centrifuge outer direction in the solution with a density of 1.1866 g/cm^3 (glycerol mass fraction of 73.96 %), and particles have moved toward the centrifuge inner direction in the solution with a density of 1.1890 g/cm^3 (glycerol mass fraction of 73.1 %). The density of the particle is therefore between these two density values. The resulting density value for the particles is inferred from the average of these two values, and the accuracy can be inferred from the extreme values of the densities in each tube. Therefore, $\rho_P = 1.1878 \pm 0.0012$ g/cm^3 at 22 °C. Note that when compared to the natural sedimentation method (1 week), the present method is far less time-consuming (12 min) with a similar accuracy.

3.2 Results of fluid component properties

3.2.1 Refractive index

Figure 2 shows n_A as a function of temperature for different glycerol mass fractions.

A multiple linear regression on these data gives the following dependency:

$$n_A = 0.1425\chi - 0.00023T + 1.3321 \quad (3)$$

with $R^2 = 1$, valid for $T = 16{-}30$ °C and at glycerol mass fractions $\chi = 68, 70, 72, 75$ %.

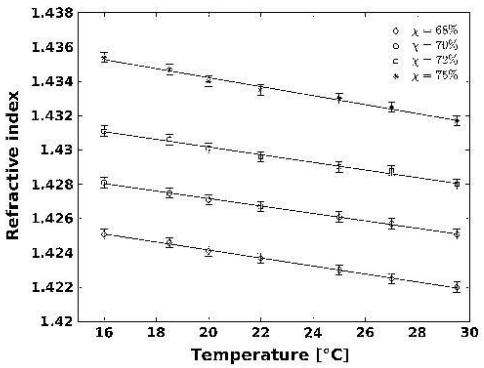

Fig. 2 RI of glycerol–PBS mixtures $n_A \pm$ SD as a function of temperature for glycerol mass fractions $\chi = 68, 70, 72, 75\,\%$

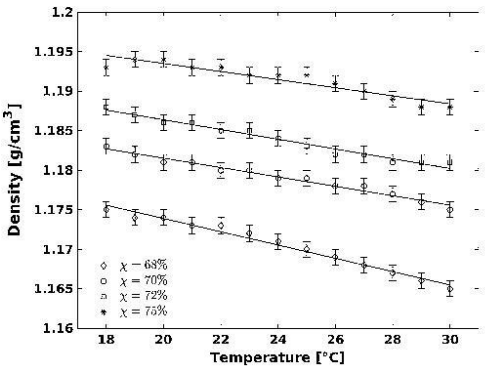

Fig. 4 Density of glycerol–PBS mixtures $\rho_A \pm$ SD as a function of temperature for glycerol mass fractions $\chi = 68, 70, 72, 75\,\%$

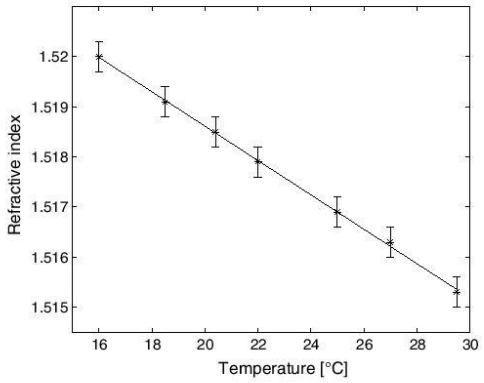

Fig. 3 RI $n_B \pm$ SD of pure TDE as a function of temperature

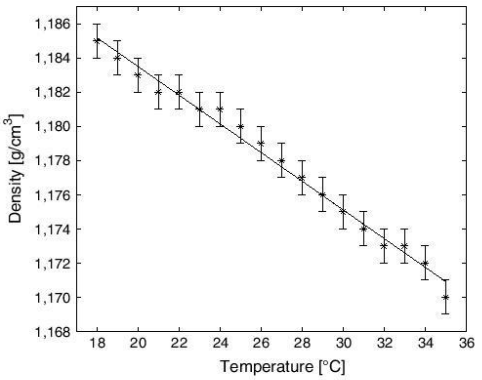

Fig. 5 Density $\rho_B \pm$ SD of pure TDE as a function of temperature

The RI of TDE was measured from 15 to 30 °C. Results are shown in Fig. 3, and a simple linear regression analysis of the data results in Eq. (4), with $R^2 = 0.9977$:

$$n_B = -0.00034T + 1.52548 \tag{4}$$

3.2.1.1 *Density* Figure 4 shows the density of solution A as a function of temperature for different glycerol mass fractions.

A multiple linear regression of these data gives Eq. (5) with $R^2 = 0.9765$ which is valid for $T = 18{-}30\,°C$ and glycerol mass fractions $\chi = 68, 70, 72, 75\,\%$.

$$\rho_A = 0.2917\chi - 0.00065T + 0.989 \tag{5}$$

Measurements of the density of pure TDE were performed, and the resulting data are presented in Fig. 5 as a function of temperature.

A simple linear regression analysis of the measured data gives Eq. (6) with $R^2 = 0.9887$ which is valid for $T = 18{-}30\,°C$.

$$\rho_B = -0.00084T + 1.20029 \tag{6}$$

3.2.2 Determination of the recipe

From the above measurements, the equation set (1) can be rewritten as follows.

$$\begin{cases} \rho_A = 0.2917\chi - 0.00065T + 0.989 \\ n_A = 0.1425\chi - 0.00023T + 1.3321 \\ \rho_B = -0.00084T + 1.20029 \\ n_B = -0.00034T + 1.52548 \end{cases} \tag{7}$$

As the RI and density of the particles were already measured, the recipe can be estimated according to Eq. (8), rewritten from Eq. (2) with the preceding dependencies.

$$\begin{cases} \phi \cdot n_B + (1-\phi) \cdot n_A = n_C = n_P = 1.4892 \\ \phi \cdot \rho_B + (1-\phi) \cdot \rho_A = \rho_C = \rho_P = 1.1878 \end{cases} \quad (8)$$

A recipe can be inferred from both sets of equations by fixing at least one parameter. As an example one can consider straightforwardly that the choice of temperature is dictated by the temperature at which the RI and density were determined, which is 22 °C. Considering this temperature in Eq. (7) and substituting in Eq. (8) results in $\phi = 64\,\%$, $\chi = 77\,\%$. A closer insight into Eq. (8) shows that although the matching relies on both fractions of glycerol in PBS and of TDE in the final mixture, a fine-tuning can be obtained by adjusting the temperature. In particular, a sensitivity analysis of the equation for the refractive index shows that a 2 % error in both fractions can be compensated by a variation of about 6 °C which is quite reasonable and technically realizable in most cases. Note that such a variation affects poorly the RI of the PMMA solid phase with only 0.0087 % variations.

3.3 Trial experiments of the recipe

3.3.1 Static experiments

A mixture, following an identified recipe, was prepared, and particles were added (40 % v/v) before static observation under a microscope (Olympus IX71, Japan). The observations were made through a 1 mm fluid thickness and tried to image a grid from a standard stage micrometer (Edmunds Optics). A $\times 20 - \mathrm{NA} = 0.5$ objective lens allowed to have a depth of field $\mathrm{DOF} = 2.2\,\mu\mathrm{m}$). The system was placed in a temperature-controlled climatic chamber. Images of the grid were taken for stabilized temperatures in the range $T = 14{-}32\,^{\circ}\mathrm{C}$. A clear and sharp image of the grid can be obtained in the case of particle-free mixture (Fig. 6a). The great number of potential optical interfaces (approx. 50 in the present case) results in an impossibility to image the grid in case of unmatched RI (Fig. 6b). A better image quality is obtained when the RI is matched (Fig. 6c, d). In order to determine the temperature for which the best focus of the grid is observed, a diagonal Laplacian focus measure was computed on the images (Pertuz et al. 2013). The relative maximum of this measure allowed to identify the temperature for which the best focus is obtained (Fig. 6d). The identified temperature was in good agreement with the temperature used for the initial condition of equation set (7).

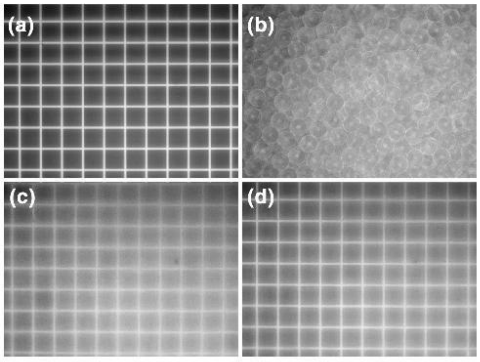

Fig. 6 Image of a grid from a standard stage micrometer with various 1 mm thick interfaces: **a** fluid mixture without particles, **b** 41 μm particles in water, **c** 41 μm particles in fluid mixture at 24 °C, **d** 41 μm particles in fluid mixture at 20 °C

3.3.2 Dynamic experiments

The in-focus image obtained with particles (Fig. 6d) is not as clear as the one without particles (Fig. 6a). Therefore, it is important to quantitatively assess the quality of the suspension in a dynamic experiments. To do so, the prepared mixture was tested in a simple shearing flow generated in the gap of a rotating cone-plate geometry placed above the microscope (same optical system already described). The rotating cone has a 80 mm diameter and 2° angle. The optical window through which optical measurements were taken is placed on a radius of 30 mm from the rotation center. The resulting gap between the cone and the fixed lower plate at this radius is equal to 1047 μm. The data presented hereafter correspond to a shear rate value of $50\,\mathrm{s}^{-1}$, a Reynolds number of 1.22 according to a mixture viscosity of 51 mPa s at 22 °C. Two particle concentrations, 0 and 45 % v/v, were considered, and the most unfavorable plane located at 900 μm from the fixed bottom plate was chosen for the demonstration of the optical quality of the developed suspension. Microparticle image velocimetry, μPIV (Wereley and Meinhardt 2010), measurements were realized in different planes along the gap height. The suspension was seeded with 1 μm fluorescent particles (FluoSpheres F8819, Invitrogen, France) and illuminated in volume by a double-pulsed 532 nm laser light (NdYag Gemini PIV, New Wave Research, USA) through the fixed lower plane. The concentration of seeding particles was set to 0.031 % v/v (Wereley and Meinhardt 2010). The 575 nm emitted light from the seeding particles is filtered by a proper separating cube placed in the microscope. Image pairs of the flow were taken with a 12-bit cooled 1.4 Mpixel digital CCD

camera system (Sensicam qe, PCO, Germany). The depth of correlation was equal to 11.6 μm, and the field of view was 894 × 665 μm^2. As an example, Fig. 7a, b compares representative images of 192 × 192 pix^2 windows extracted from the complete image and their corresponding cross-correlation functions obtained from highlighted 64 × 64 pix^2 interrogation windows. When considering a simple FFT-based cross-correlation computation (1302 vectors resulting from 50 % overlapping, 64 × 64 pix^2, interrogation windows with a Gaussian weighing) on a single image pair, a 48 % signal-to-noise ratio (SNR) rejection of the cross-correlation is observed for the 45 % suspension versus 10 % in the case of 0 % concentration. This rejection comes from a poor peak to noise peak ratio (PNPR) in the peak detection algorithm. This ratio computes the peak pixel intensity divided by the highest noise peak pixel intensity. Its threshold value was strictly set to 1.5. When the cross-correlation is not rejected (distinct peaks observed in Fig. 7a, b), the average PNPR over the 52 % valid peaks is 1.98 (respectively, 2.38 for the 95 % valid peaks for 0 %). PNPR is an indicator of the image quality since it is a metric of the combination of (1) the effects of the number of seeding particles present in the interrogation window and of their mean image diameter and (2) the effects that contribute to loss of correlation (in-plane and out-of-plane loss of correlation) (Raffel et al. 2007). Since the fluid is highly viscous and the flow is laminar, the out-of-plane loss of correlation is strongly limited. Furthermore, the pulse separation time was carefully adjusted to fulfill the gold standard rule of an average displacement of about one quarter of the interrogation window size (typ. about 16 pixels here for a pulse separation of 200 μs). This setting results in a limited in-plane loss of correlation. 0 % experiment shows a very good performance with similar seeding conditions than the 45 % suspension, and the high rejection outcome is therefore mainly related to a loss of image density and/or to small particle image diameter in the interrogation windows when considering high-concentrated suspension. Consequently, rejection can be linked to the small radius of curvature of PMMA particles, the large number of interfaces present in the concentrated suspension and to potential residual RI mismatch. Different solutions can be considered to overcome these issues; for example, a less restrictive rejection ratio, image pre-processing and ensemble-averaged cross-correlation algorithm. This latter solution was implemented. The magnitude of the displacement field at a given height in the flow was determined from computing ensemble-averaged cross-correlations from 30 image pairs (Wereley and Meinhardt 2010). This procedure improves drastically the performance of the cross-correlation peak detection measurements. Only 5 % of the cross-correlation do not pass the SNR filter (same PNPR threshold as above) for the 45 % suspension (respectively, 0.3 % for the 0 % suspension). Moreover, the average PNPR is then 2.67 (respectively, 4.33) improving therefore the displacement determination from the cross-correlation computation.

The obtained displacement magnitude fields for the 0 and 45 % suspension are shown in Fig. 7c, d. Fields differ mainly by their standard deviation (STD): 0.097 pixels in the case of the 45 % suspension and 0.013 pixels in the case of the 0 % suspension. STD values are however small when compared to the mean value of the displacement field (13.94 pixels and 14.08 pixels for 0 and 45 %, respectively). The standard deviation represents 0.7 % of the average displacement in the case of the 45 % suspension (respectively, 0.09 for 0 %). In both cases, the implemented procedures give excellent results.

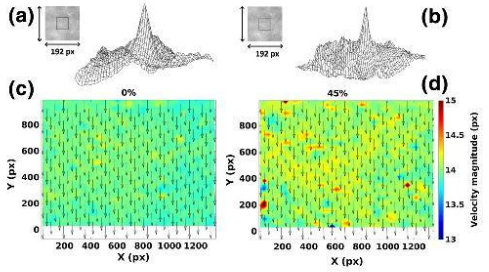

Fig. 7 μPIV experiments. *Top* images of 192 × 192 pix^2 windows taken in the image and the corresponding cross-correlation functions obtained from highlighted 64 × 64 pix^2 interrogation windows for two PMMA particle concentrations. **a** 0 % v/v and **b** 45 % v/v. *Bottom* magnitude of displacement fields [pixels] obtained from ensemble-averaged cross-correlation from 30 image pairs for two PMMA particle concentrations. **c** 0 % v/v and **d** 45 % v/v

4 Conclusion

TDE a novel, low hazard pure fluid has been used as a principal constituent to define a mixture able to match the density and refractive index of transparent low-density PMMA particles. A simple method, based on the resolution of a set of linear equations, has been shown to be able to identify a recipe for the definition of volume fractions of a ternary mixture of TDE, glycerol and PBS. The proposed method shows that a low accuracy in the preparation of the mixture can be corrected by adjusting the temperature of the mixture. The performance in matching the refractive index of the mixture has been demonstrated in a static and in a dynamic flow experiments.

A large range of RI and densities can be achieved by varying the concentration of the three chosen components. Moreover, other secondary components can be considered

to fulfill specific needs; TDE is soluble in a lot of solvents. This range will however be limited to transparent solid low-density materials, mainly because of the difficulty to find high-density transparent liquids with low toxicity. The main drawback of the proposed mixture lies probably in its high Newtonian viscosity. This point will probably limit the implementation of this mixture to low Reynolds number flows. The proposed mixture can finally be considered as another versatile solution for the precise determination of RI of transparent solids, in replacement of other common recipes (Bai and Katz 2014).

Acknowledgments The authors thank the Labex MEC ANR-11-LABX-0092 for financial support.

References

Bai K, Katz J (2014) On the refractive index of sodium iodide solutions for index matching in PIV. Exp Fluids 55(4):1704

Isa L, Besseling R, Schofield AB, Poon WCK (2010) Quantitative imaging of concentrated suspensions under flow. In: Advances in polymer science: high solid dispersions, vol 236, pp 163–202

Kasarova SN, Sultanova NG, Nikolov ID (2010) Temperature dependence of refractive characteristics of optical plastics. J Phys Conf Ser 253:012028

Lyon M, Leal L (1998) An experimental study of the motion of concentrated suspensions in two-dimensional channel flow. Part 1. Monodisperse systems. J Fluid Mech 363:25–56

Pertuz S, Puig D, Garcia MA (2013) Analysis of focus measure operators for shape-from-focus. Pattern Recogn 46:1415–1432

Raffel M, Willert CE, Wereley ST, Kompenhans J (2007) Particle image velocimetry: a practical guide, 2nd edn. Springer, Heidelberg

Saksena R, Christensen KT, Pearlstein AJ (2015) Surrogate immiscible liquid pairs with refractive indexes matchable over a wide range of density and viscosity ratios. Phys Fluids 27:087103-1-21

Staudt T, Lang MC, Medda R, Engelhardt J, Hell SW (2007) 2,2′-Thiodiethanol: a new water soluble mounting medium for high resolution optical microscopy. Microsc Res Tech 70(1):1–9

Wereley ST, Meinhardt CD (2010) Recent advances in micro-particle image velocimetry. Annu Rev Fluid Mech 42:557–576

Wiederseiner S, Andreini N, Epely-Chauvin G, Ancey C (2011) Refractive-index and density matching in concentrated particle suspensions: a review. Exp Fluids 50(5):1183–1206

As described in the article, a new ternary mixture recipe consisted of PBS, glycerol and TDE was developed, which is able to match the density and refractive index of PMMA particles simultaneously. In addition, either by fine tuning of the proportion of the ternary mixture or by adjusting the temperature of the mixture, the suspension can achieve a better matched precision. Furthermore, all these components are low hazard for human health and they are compatible with plastics (e.g. Acrylic, polycarbonate, PVC) and glass. Thus, by varying the proportion of the component, the recipe is accessible and applicable for wide use.

Based on this recipe, two sizes of particle suspensions were prepared. Details about suspended particle sizes and suspension particle concentrations are described as follows.

1) Suspended particle sizes
The diameters of the two spherical PMMA particles are 4.62±0.11μm and 41±0.65μm respectively. For the reason that the volume of 4.62 μm particle is close to that of a red blood cell, and the latter can be used to assimilate the particle aggregations in future research.

2) Suspension concentrations
As the concentration of red blood cell in blood is about 45% in volume fraction (v/v), and in some region the concentration is smaller; suspensions with the following concentrations were prepared: 0%, 2%, 5%, 10%, 20%, 35% and 45%, in order to progressively observe the influence of particle concentration.

At a working temperature of 25°C, for 41μm PMMA particle suspension, the mass fraction of glycerin is 78% in glycerol- PBS mixture, and the volume fraction of TDE is 64% in the final ternary mixture. Due to the some variation in the production procedure, the refractive index of 4.62μm particle (n=1.4901) is a little higher than that of 41μm particles (n=1.4892). Thus the recipe of 4.62μm particle suspension is slightly different, where the mass fraction of glycerin is 78.5% in glycerin PBS mixture, and the volume fraction of TDE is 65.2% in the final ternary mixture.

3.2 Suspension rheology

As non-Newtonian fluid has special flow behaviors, it is better to know the rheology property of the suspension before measuring the velocity fields within the cone-plate gap. In addition, the viscosity is an essential parameter to calculate the threshold velocity of secondary flow (Section 2.3.2). Therefore, the viscosities of suspensions were measured, as described in the following.

3.2.1 Measurement conditions

Since the blood flow is generally submitted to a range of shear rate from $0.1s^{-1}$ to $100s^{-1}$ (Fig 2.10), the suspensions viscosity measurement is performed in a similar range (from $0.5s^{-1}$ to $100s^{-1}$). The measurements were performed by using a rheometer (HAAKE MARS III) at 25°C. A cone and plate model was used (cone angle=2°, cone radius=3cm , 2ml suspension needed).

The suspension testing protocols consisted in 11 levels of shear rate applied step by step in a logarithmic way increasing from 0.5 to $100s^{-1}$ followed by a similar decrease. Each shear rate step is of 150s duration, the viscosity value is obtained using the mean viscosity value of the last 45s. The reported viscosity values are the mean values obtained during both the increasing and the decreasing ramps; the relative error was evaluated to 2%. The data of the measured suspension viscosities are shown in appendix B.

3.2.2 Results

General case

Fig 3.1 and Fig 3.2 respectively show the variations of the viscosity of 41µm and 4.62µm particle suspensions with respect to the shear rate. In general, the suspension viscosity increases following the increase of particle concentration. At a concentration below 10% (included), the suspension behaves like a Newtonian fluid, when the concentration exceeds 20% there is a large increase of viscosity.

41µm particle suspensions

For 41µm particle suspensions, the shear thinning effect is found in suspensions at ϕ= 45%, 35% and 20%, and it is more apparent when the particle concentration increases.

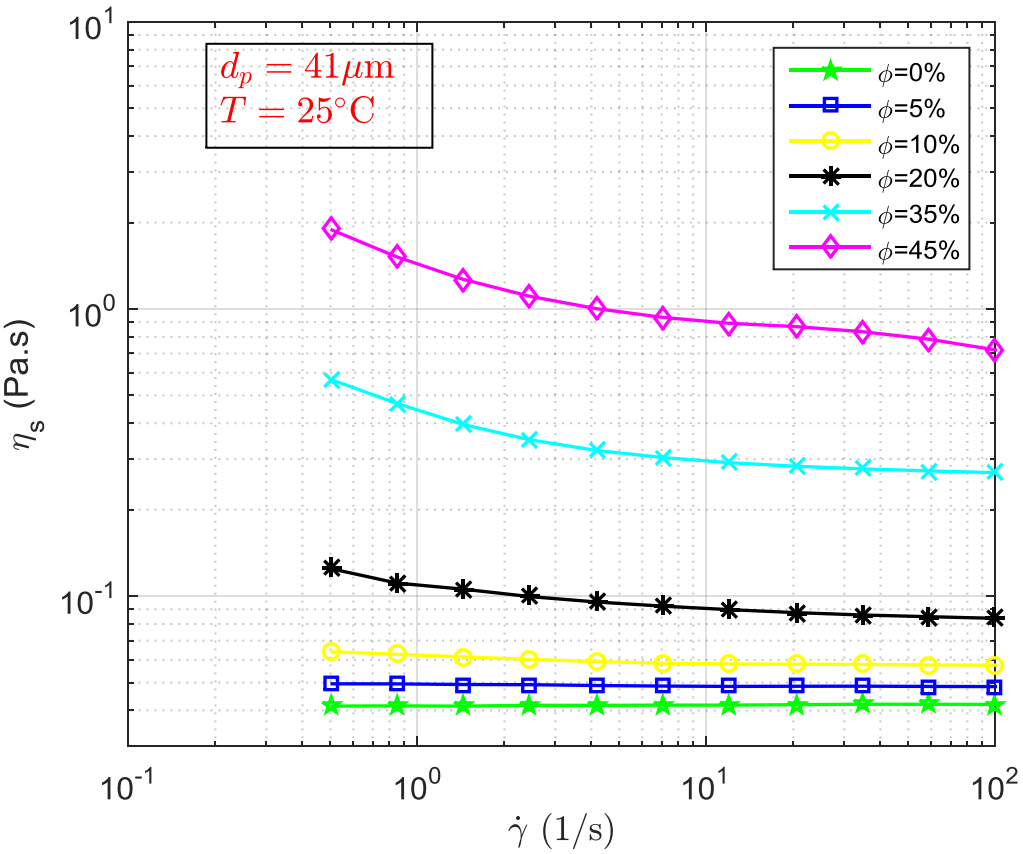

Fig 3.1 Viscosity variations of 41µm particle suspensions at different concentrations with respect to shear rate. (The viscosity of the 2% 41µm particle suspension is not shown since it is too close to that of 0%. All the error bars are removed as they are too small compared to the minimum scale.)

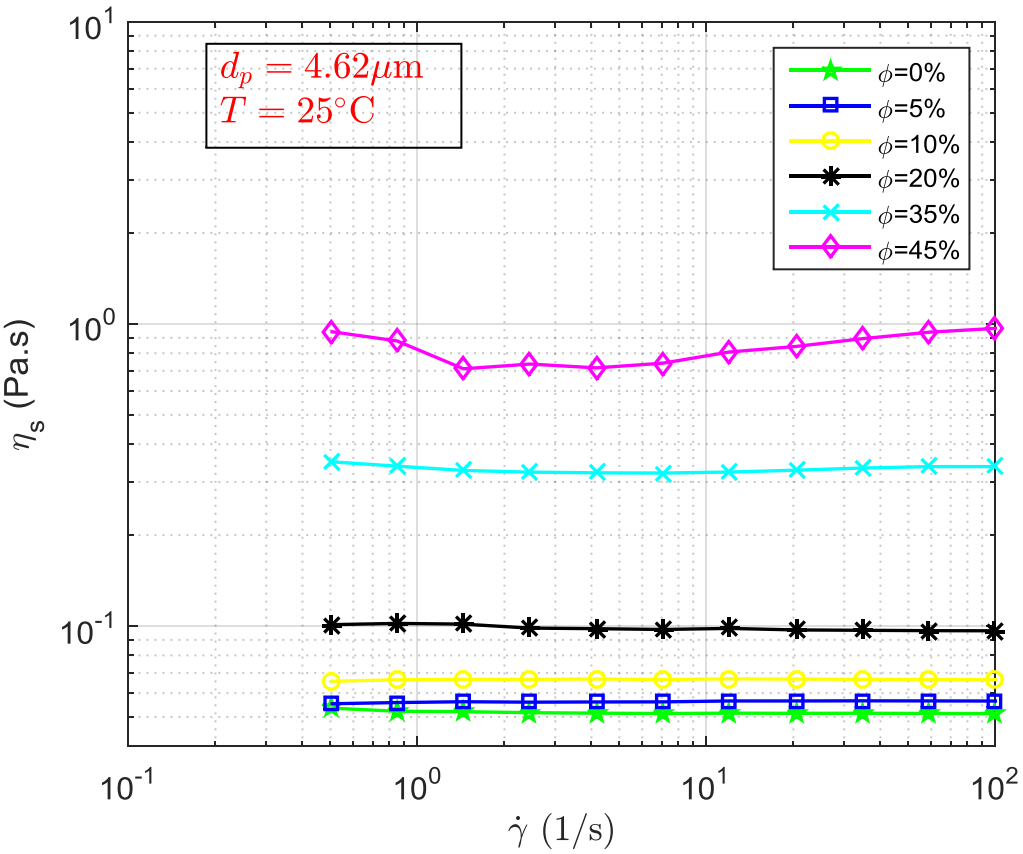

Fig 3.2 Viscosity variations of 4.62μm particle suspensions at different concentrations with respect to shear rate. (The viscosity of the 2% 4.62μm particle suspension is not shown since it is too close to that of 0%. All the error bars are removed as they are too small compared to the minimum scale.)

4.62μm particle suspensions

For 4.62μm particle suspensions, the behaviors are different. When ϕ=20%, the suspension still behaves like a Newtonian fluid. At ϕ=35%, it is slightly shear-thinning at the beginning, and then after the shear rate exceeds 7.07s^{-1}, the viscosity increases about 5% with the shear rate increases to 100s^{-1} (Fig 3.3). This means that the suspension is shear-thinning at the beginning, and then it is shear-thickening.

The same phenomenon is found in 45% 4.62μm particle suspension. As shown in Fig 3.4, compared with the viscosity at 4.16s^{-1}, it increases about 33% at 100s^{-1}. According to the definition of continuous shear-thickening proposed by Brown and Jaeger (2014), if the re-augmentation of viscosity is mild (perhaps up to several tens of percent over the few decades of shear rates), it can be recognized as a continuous shear-thickening phenomenon. This is the case for the 35% and 45% 4.62μm particle suspensions.

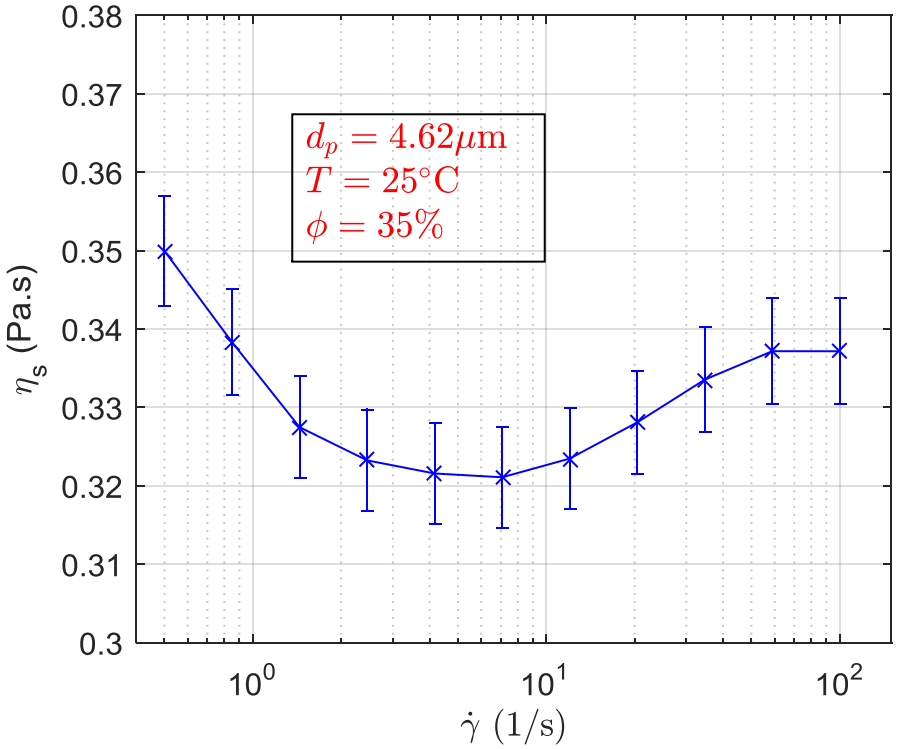

Fig 3.3 Viscosity variation of 4.62µm particle suspension at ϕ=35% with respect to shear rate

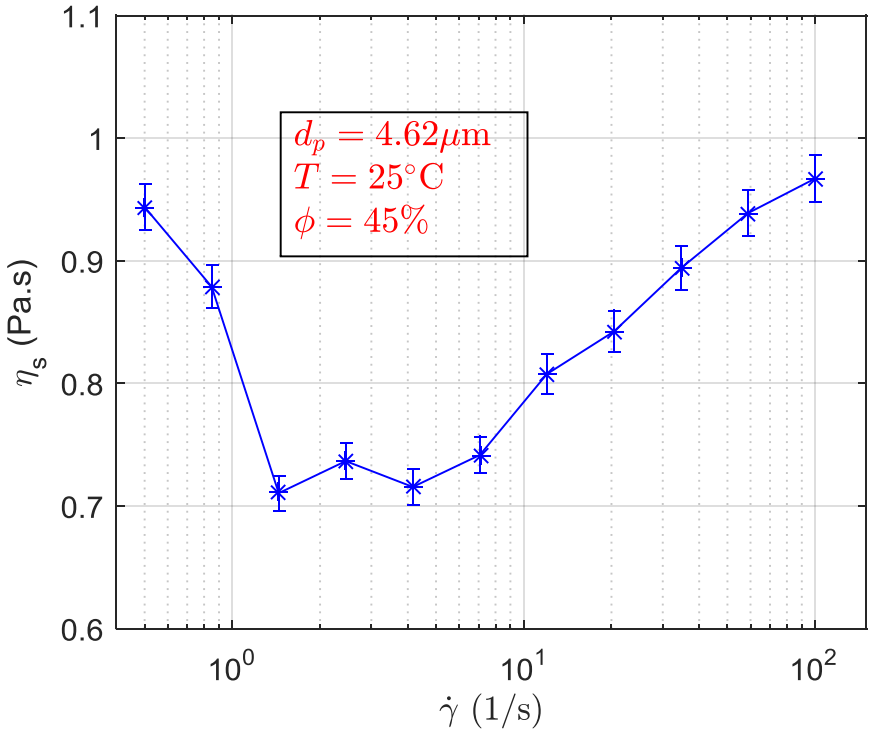

Fig 3.4 Viscosity variation of 4.62µm particle suspension at ϕ=45% with respect to shear rate

Relative viscosities

Next, the relative viscosities of the two sizes of particle suspension are calculated. Fig 3.5 and Fig 3.6 respectively show the variations of relative viscosity (η_r) of 41 μm and 4.62μm particle suspensions as a function of particle concentration. In both sizes of particle suspensions, the relative viscosity is close to the prediction by Einstein's equation when ϕ≤10%.

For 41 μm particle suspensions, at ϕ=20%, 35% and 45%, the value of η_r is varied and the fluctuation is much larger at higher concentration (Fig 3.5). For example, at ϕ=45%, the relative viscosity is varied from 17.2 to 45.6. This is due to the shear-thinning effect of the suspension, which is more apparent at higher concentration.

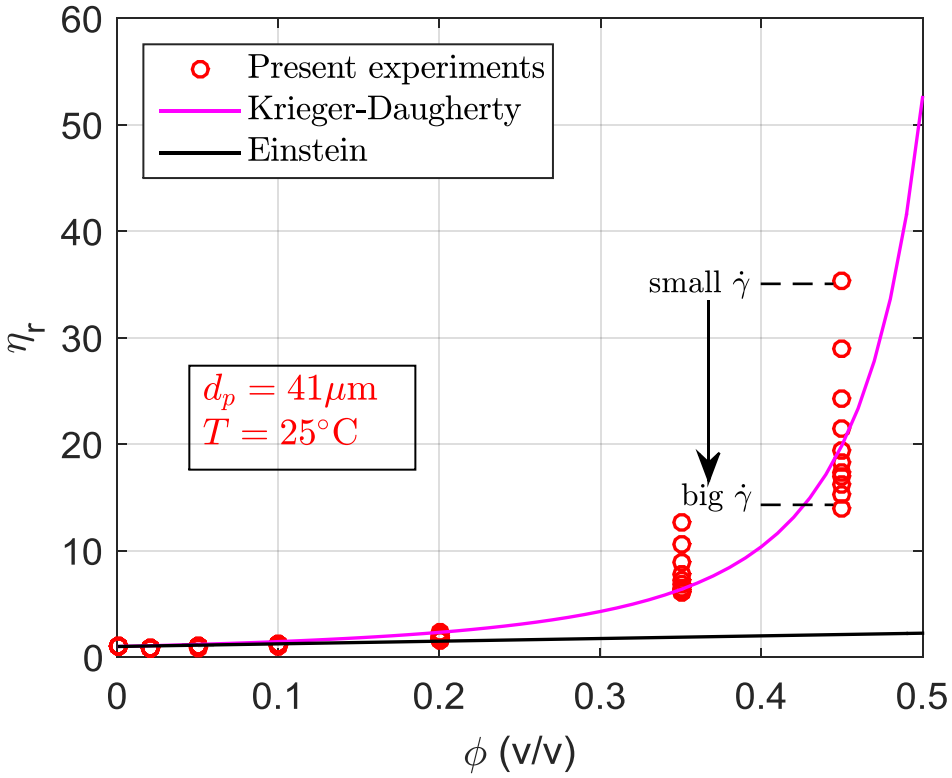

Fig 3.5 Relative viscosities of 41μm particle suspensions at different shear rates as a function of particle concentration, where ϕ_m=0.582 is taken for the Krieger-Daugherty model.

For 4.62μm particle suspensions, the fluctuation of the relative viscosity is only noticeable at ϕ=45%, and it is much smaller compared to that of 41 μm particle suspensions, it is varied from 13.6 to 17.6. This can be related to the continuous shear-thickening effect of the suspension, where the viscosity decreases at the beginning, then increases, thus the range of viscosity variation is smaller.

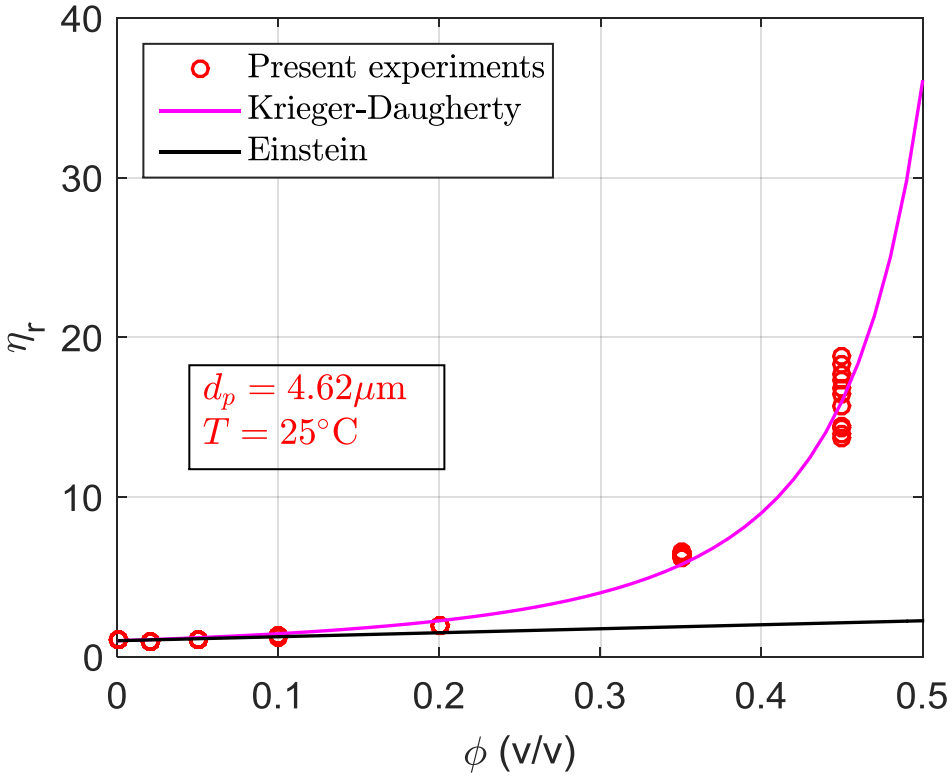

Fig 3.6 Relative viscosities of 4.62μm particle suspensions at different shear rate as a function of particle concentration, where ϕ_m=0.596 is taken for the Krieger-Daugherty model.

In addition, the variation of relative viscosity with respect to particle concentration is least squares fitted to the Krieger-Daugherty's model (Equation (2.9)). For 41 μm particle suspensions, the fitted maximum packing fraction is ϕ_m=0.582. While, for 4.62μm particle suspensions, ϕ_m=0.596. Both of the fitted ϕ_m values are between the observed ranges of ϕ_m which is from 0.55 to 0.68 (Greenwood, Luckham, and Gregory 1997).

3.2.3 Suspension rheology discussion

According to the measured results, shear-thinning effect was observed in 41 μm particle suspension when particle concentration exceeds 20%, and continuous shear-thickening was observed in 45% and 35% 4.62μm particle suspensions. Through this comparison, it is found that the particle size plays an important role in the shear-thickening effect of suspension. Since shear-thinning effect is a common situation for dense suspensions (Section 2.1.3.2), it will not be discussed here.

Concerning continuous shear-thickening, as have mentioned in the section (2.1.3.2), multiple mechanisms are proposed to explain this effect. Such as hydro-clustering formation of particles(N. J. Wagner and Brady 2009), excluded volume augmentation of

suspended particles (Picano et al. 2013), order-disorder transition of the particle (Hoffman 1974; Stickel and Powell 2005). To elucidate the real mechanism of continuous shear-thickening is not the main objective of the current study, so, here, we only adopt the order-disorder transition mechanism to do simple explanation of this phenomenon. At the stationary state, the particles are disordered and randomly distributed. When the flow velocity increases, the particles are well organized, in a state following the flow direction, thus the viscosity decreases. If the flow velocity continues to increase, the organized state will be disrupted. As when the fluid velocity increases, the state of particles becomes unstable. After the fluid velocity exceeds a threshold value, the higher the fluid velocity is, the more disorganized the particles are, causing the viscosity to increase again.

The same principle can also be used to explain the different rheological behaviors of the two sizes of particle suspensions. Since the bigger particles have bigger mass, it is more difficult to change their state in a suspension flow. At the stationary state, they need more force to change their state from disordered to well-organized, so a higher relative viscosity at low shear rate. When the big particles have reached a stable state following the increase of shear rate, it is also more difficult to disrupt this state, thus they have a lower relative viscosity at higher shear rate. Nevertheless, for smaller particles, it is much easier for them to reach a stable state; and also it is easier to disrupt this stable state, thus it exhibits shear-thinning followed by continuous shear-thickening effect.

Through this comparison, it can be found that shear-thickening effect is only appeared in small size particle suspension. Why it is so easy for small size particle suspension to exhibit shear-thickening effect, and is there some criteria to quantify this phenomenon?

Based on the Peclet number (Equation (2.3)), the Reynolds number (Equation (2.2)) and the Schimidt numbers (Equation (2.4)), Stickel and Powell (2005) proposed a dimensional criteria to predict the rheological behaviors of suspensions, as shown in Fig 3.7.

	$d_p = 41\mu m$			$d_p = 4.62\mu m$		
$\dot{\gamma}$(1/s)	Pe	Re	Sc	Pe	Re	Sc
100	1.87E+08	1.05E-03	1.78E+11	2.93E+05	1.22E-05	2.4E+10
12.01	2.25E+07	1.26E-04	1.78E+11	3.66E+04	1.46E-06	2.4E+10
4.16	7.79E+06	4.37E-05	1.78E+11	1.22E+04	5.07E-07	2.4E+10
1.44	2.68E+06	1.50E-05	1.78E+11	4.19E+03	1.74E-07	2.4E+10
0.5	9.36E+05	5.26E-06	1.78E+11	1.52E+03	6.34E-08	2.4E+10

Tab 3.2 Corresponding Pe, Re and Sc values for the two sizes of particles at different shear rates

The Pe, Re and Sc values of the 4.62μm and the 41μm particles at different shear rates are shown in Tab 3.2. According to the criterion, all the values of the suspensions at different shear rates are situated in the Newtonian region and Sc≫1, but the real rheology behaviors of the suspensions are not the same as the prediction. Only the rheological behavior of 4,62μm particle suspension approximately follows the black arrow, which indicates that when the shear rate increases, the suspension will consecutively pass 3 regions: shear thinning, Newtonian, and then shear thickening.

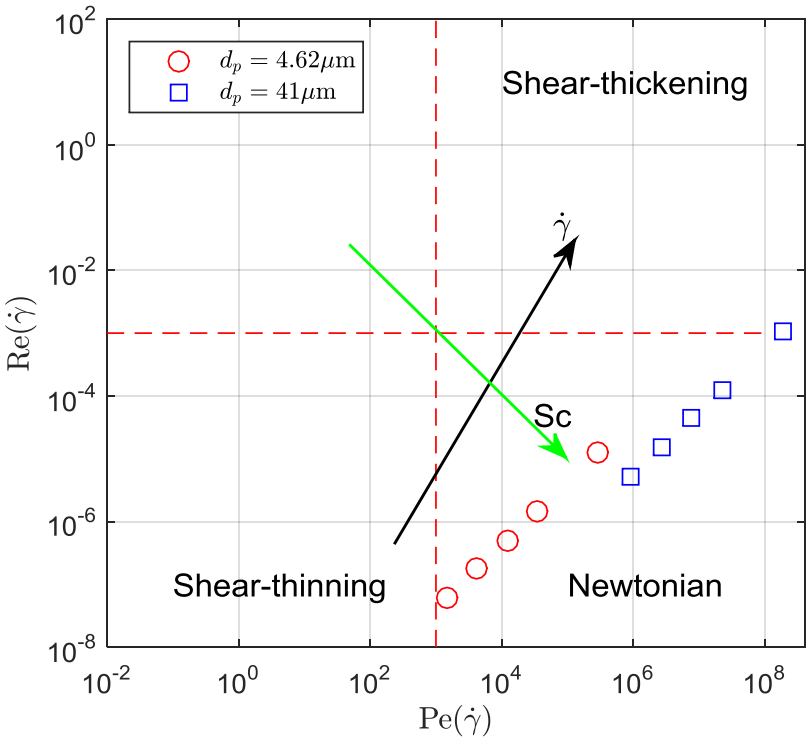

Fig 3.7 “Phase diagram” for suspension rheology, based solely on a dimensional analysis. Image source from (Stickel and Powell 2005).

Comparing the rheology of the current suspensions at concentration of 45% with real blood, there is a big difference on viscosity value. For example, at $1s^{-1}$, the viscosity of blood is about 0.024pa.s, but the viscosities of 41μm and 4.62μm particle suspensions are about 1.4pa.s and 0.84pa.s respectively. Since the suspending fluid and the measured temperature are different, it is better to compare their relative viscosities. As shown in Fig 3.8, the red line is the measurement result of Chien (1970) using real blood at 37°C, the dashed line is the upper and lower bound of the reported measurement result with real blood summarized by Whitmore (1968). It can be found that the relative viscosity of the 4.62μm particle suspension is under the limits at shear rate varying from 0.5 to $2s^{-1}$. For greater values of shear rate, the relative viscosity goes beyond the limits. This is due to the shear-thickening effect of the suspensions. For 41μm particle suspension, its

relative viscosity is bigger than that of real blood, but it has shown the effect of shear-thinning.

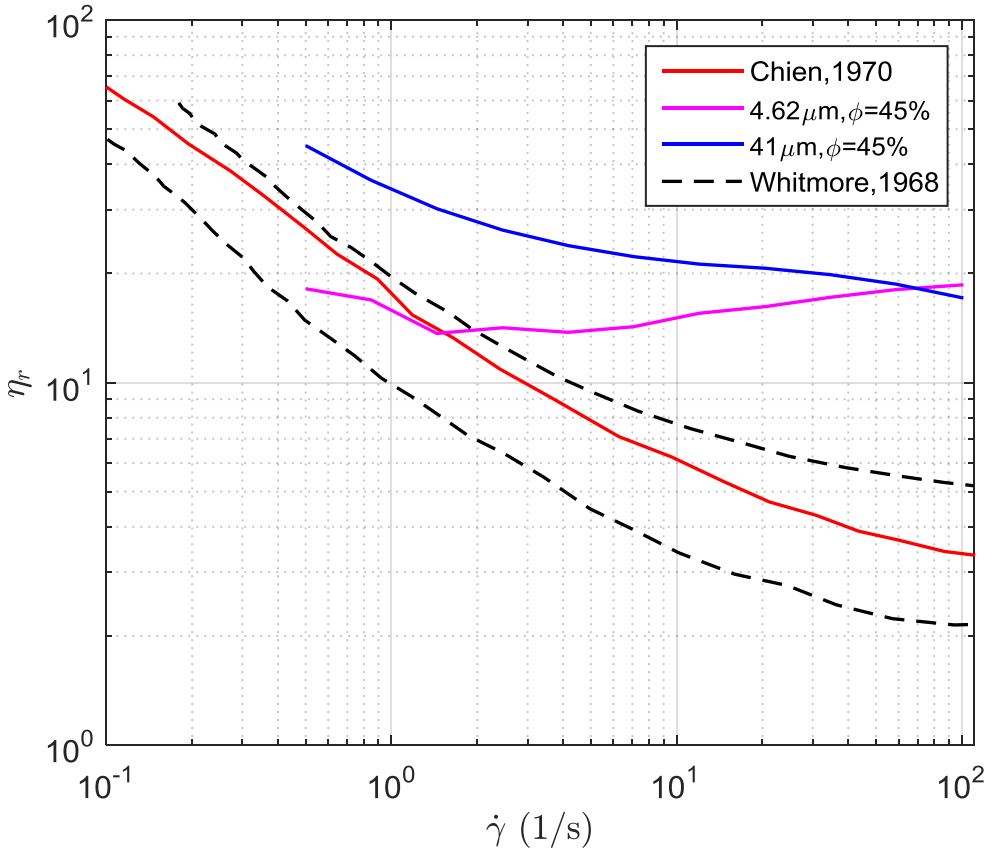

Fig 3.8 Relative viscosities of 4.62µm and 41µm particle suspensions at concentration of 45% compared to the relative viscosities of blood measured by Chien (1970) and Whitmore (1968) as a function of shear rate.

4 Experimental set-up and measurement techniques

In this chapter, firstly the experimental set-up will be presented. Secondly, the fluid investigation techniques for the velocity profile measurement will be described. Then, the measurement result of 0% particle suspension will be shown, which makes sure that no secondary flow occurred in the suspension flow with the considered rotational speeds. Finally the approach for local particle concentration measurement will be introduced.

4.1 Experimental set-up

The experimental set-up is composed of three parts:

1. Flow generation system: a cone-plate device, a stepper motor and a reducer (Fig 4.1);
2. Flow measurement system (micro-PIV): a microscope, a camera, a laser source, a synchronizer and a computer for micro-PIV experiment controlling and image processing (Fig 4.1 and Fig 4.2);
3. Environment control system: a cover equipped with a temperature control module and an aluminum plane (Fig 4.2).

The objective of the experiment set-up is to offer a stable and well controlled platform for the investigation of dense suspension flow under a large range of shear rates. Some strict conditions are thus required:

a) A stable low velocity flow in order to observe the flow behavior of a dense suspension under low shear rate;
b) A well-controlled environmental temperature to guarantee that the suspension is well refractive index and density matched;
c) A low vibration experimental environment to make sure that there is no vibration which will alter the velocity fields (obtained through micro-PIV measurements) at low flow velocity, where a long time interval is applied.

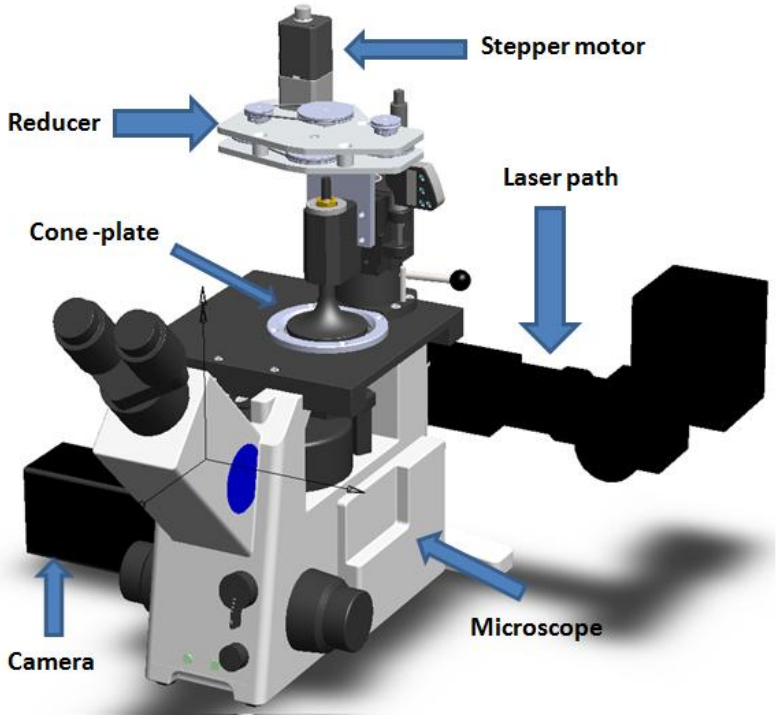

Fig 4.1 Illustration of the components under the cover

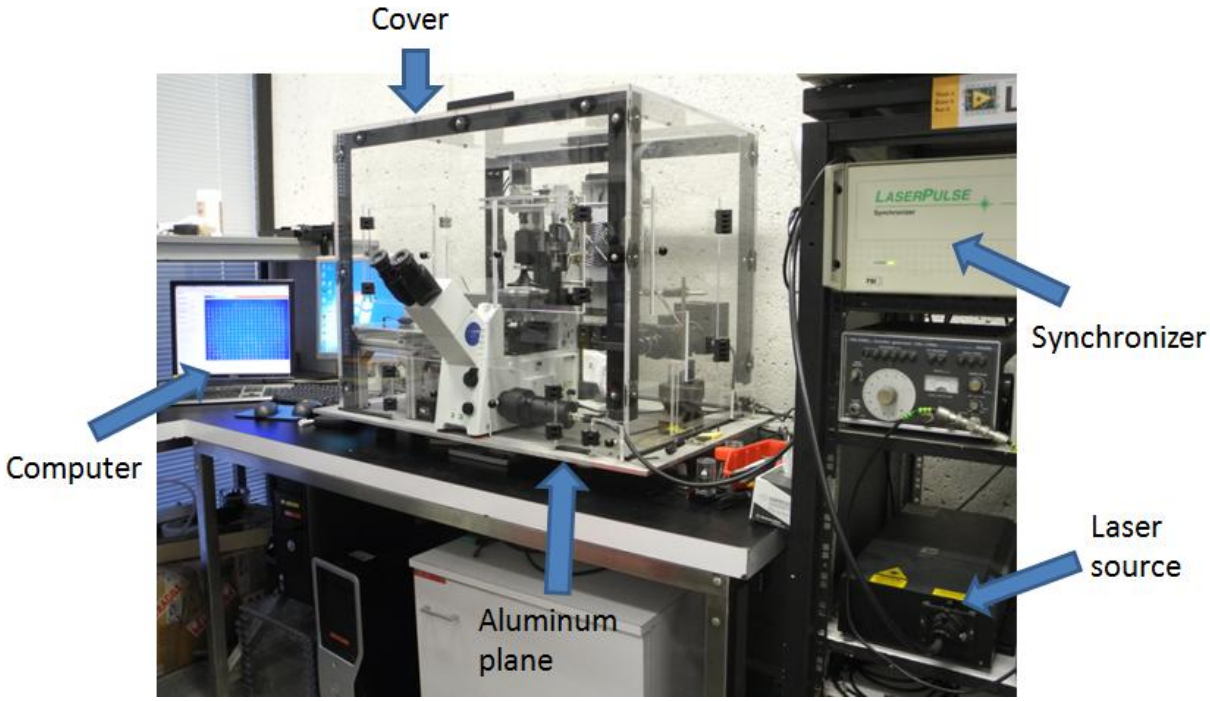

Fig 4.2 Illustration of the experimental set-up

4.1.1 Flow generation system

Cone-plate

The cone-plate model was chosen because under this flow geometry a constant shear rate (primary flow) can be acquired in the whole fluid. A schematic illustration of the

device is shown in Fig 4.3, where ω is the rotational speed of the cone, R is the distance from the center of the measured region to the cone axis (R=30mm), H_{max} is the height of the gap at the center of the measured region (H_{max}=1.047mm), α is the cone angle ($\alpha = 2°$). In order to protect the plate, the tip of the cone is truncated with a height of 200μm. x, y and z respectively designate the radial, tangential and vertical directions. The objective is fixed in a position of the x-y plane, where the measured rectangular region is parallel to the y direction (Fig 4.4). In addition, the objective can be moved up and down following the z direction. The plate is made of transparent plexiglass which gives an optical access for measurement. The cone is made of aluminum with black painted surface, which reduces the reflection of laser light.

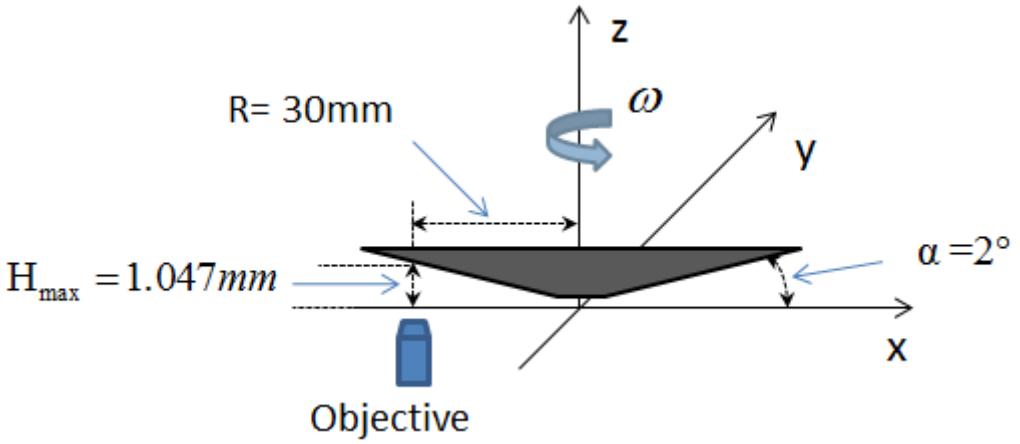

Fig 4.3 Schematic illustration of the cone-plate device

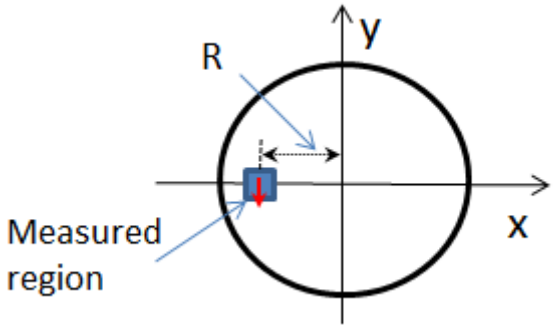

Fig 4.4 Schematic illustration of the measured region in the x-y plane

Theoretically, for homogeneous fluids with no slip and no secondary flow, the velocity profile in the cone-plate model is a linear function (Fig 4.5-a) and the normalized velocity is a line with a slope of unity (Fig 4.5-b). Here, v, u respectively designates the velocity component in the y direction and in the x direction. The generated shear rate $\dot{\gamma}$ is expressed as the following:

$$\dot{\gamma} = \frac{\omega \times R}{\mathrm{H}_{max}} = \frac{\mathrm{V}_{max}}{\mathrm{H}_{max}} \tag{4.1}$$

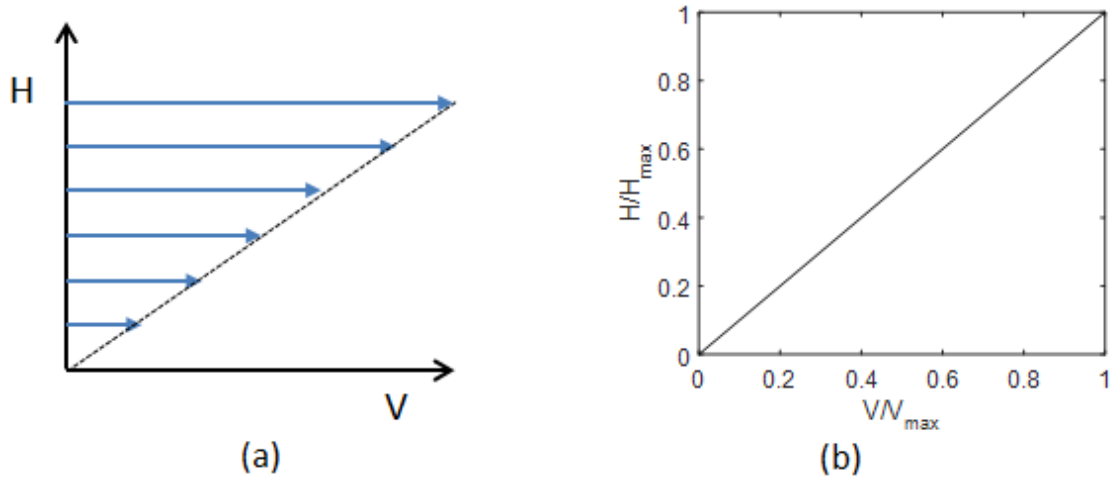

Fig 4.5 Velocity profile (a) and the normalized velocity profile (b) of the flow under the cone-plate device with no slip and no secondary flow

Stepper motor and reducer

The movement of the cone was driven by a computer controlled stepper motor. As the suspension would be tested under a large range of shear rates, a large range of rotational speeds were thus required (Tab 4.1). Here the lowest shear rate $0.5s^{-1}$ corresponds to a rotational speed of 0.167 RPM (Rotation Per Minute), which is an extremely low rotational speed. Generally used motors are not able to work at this speed. To satisfy the required velocity range, a two phase stepper motor with micro-stepping function (Zaber T-NM 17A04) is therefore employed.

Shear rate (s^{-1})	ω (RPM)
100	33.344
50	16.672
10	3.334
5	1.667
1	0.333
0.5	0.167

Tab 4.1 Shear rates and corresponding rotational speeds

A stepper motor is a brushless direct current electric motor that divides a full rotation into a number of equal steps. The motor's position can be commanded to move and hold at one of these steps without any feedback sensor (an open-loop controller). In addition, by controlling the input current, each step can be further divided into micro-steps, which is called micro-stepping. When the micro-steps become smaller, the operation of the motor becomes smoother, thereby, reducing the vibration of the motor, as well as

the resonance in any parts the motor may be connected to. The full step value of the current stepper motor is 1.8° (200 steps for a rotation) and the maximum micro-step resolution is 128 (this means each full step can be divided into 128 micro-steps).

A reducer is connected to the stepper motor. Because it is difficult for the stepper motor to maintain a stable output torque at small velocity, when the stepper motor merely moved several micro steps within the interval time. For example, at a rotational speed of 0.167RPM, with the maximum micro-step resolution of 128 and the measurement time interval equal to 0.02s, the stepper motor will only move about 1.42 micro-steps.

Nevertheless, there is a good stability at higher rotational speed. Thus, if we keep the stepper motor working at high rotational speed, then a good stability can be achieved at all the rotational speeds. In order to accommodate the large variation of the rotation speed, the reducer has adopted two reduction ratios which are 1/4.62 and 1/25.68. At $100s^{-1}$, $50s^{-1}$ and $10s^{-1}$, the reduction ratio of 1/4.62 is used, at the other three shear rates, the reduction ratio of 1/25.68 is employed.

4.1.2 Flow measurement system

To measure the velocity profile of a suspension flow at micro scale, a micro-PIV system was employed. The system consist of five components: an inverted microscope (OLYMPUS IX 71), a frequency doubled Nd:YAG 532nm laser, a high-sensitivity camera (PCO Sensicam, Germany), a synchronizer and a computer. A commercial micro-PIV analysis software (TSI, USA) is used for experiment controlling and image processing. The transparent plate of the truncated cone-plate device is placed over the optical window of the inverted microscope. More information about the micro-PIV system will be presented in section (4.2.3).

4.1.3 Environment control system

To maintain a stable experimental environment, a cover made of plexiglass enveloped the microscope, the camera, the cone-plate device, the stepper motor and the reducer, as shown in Fig 4.2. This would prevent the intrusion of dust and also provide insulation. Because the refractive index and density matched suspension needed a well-controlled temperature, a temperature control module was installed on the cover (Fig 4.6). The entire cover was put on an aluminum plane supported by 5 damping feet in order to isolate incoming vibrations from the environment.

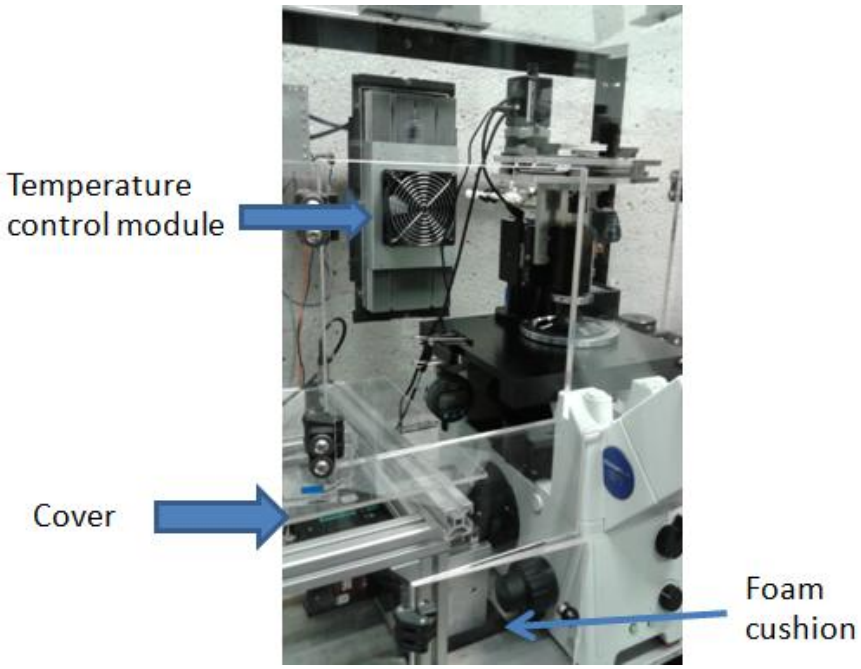

Fig 4.6 Cover, temperature control module and foam cushion

Moreover, to reduce and isolate the vibrations most of the components under the cover were put on foam cushion (Fig 4.6), such as the camera, the stepper motor and the microscope. In addition, the cover and the aluminum plane were separated by short width foam cushion.

4.2 Velocity profile measurement

4.2.1 Determination of the velocity profile

The velocity profile was determined from the measured velocity fields. The velocity fields at different heights within the cone-plate gap were measured using the micro-PIV system. The mean value of each velocity field at different heights was computed. Then the velocity profile was obtained. An example is depicted in Fig 4.7. Here the velocity $V=\sqrt{u^2+v^2}$.

For each shear rate value, 7 planes between the cone and the plate were investigated for the measurement. The distance between adjacent planes was similar (≈130μm). The height of the measured plane was defined by the following procedure: firstly, the bottom position (H=0mm) was calibrated by watching clearly certain cracks on the plate. Based on this plane, the height of the measured plane was calculated by multiplying the displacement of the objective with the ratio $-dH_{plane}/dH_{objective}$ (Section 4.2.2). The displacement of the objective was measured by a micrometer (Mitutoyo Absolute) with

micron precision. The shear rate was deduced by linear regression of the velocities and the heights (7 points), as shown in the equation below.

$$\dot{\gamma} = \frac{V}{H} \tag{4.2}$$

The blood is generally submitted to a range of shear rate from $0.1s^{-1}$ to $100s^{-1}$, the suspensions were thus tested in a similar range. 6 shear rates 0.5 s^{-1}, 1 s^{-1}, 5 s^{-1}, 10 s^{-1}, 50 s^{-1} and 100 s^{-1} were chosen. The two sizes of particle suspensions at concentrations of 0%, 5%, 10%, 20%, 35% and 45% were tested.

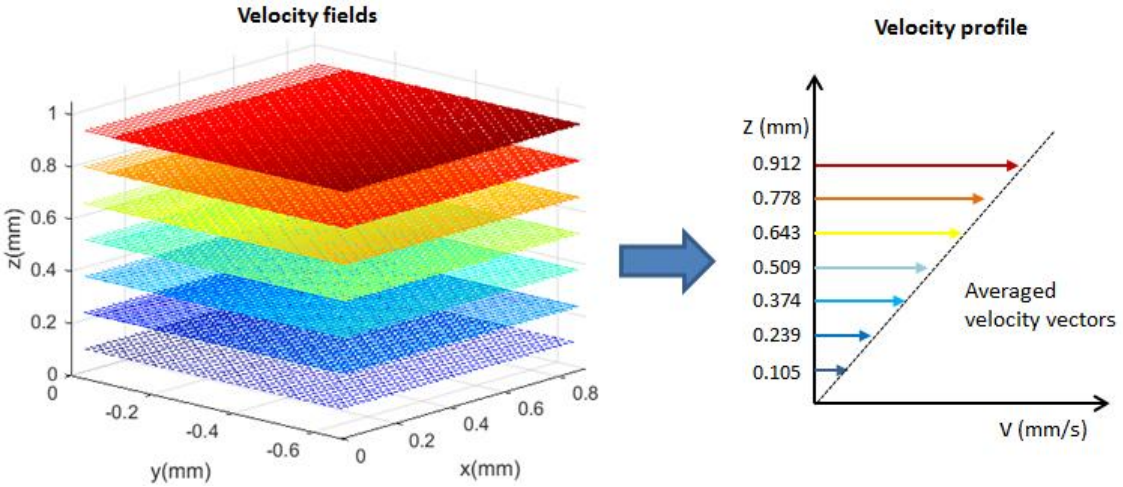

Fig 4.7 An example of multi-plane of velocity fields and the generation of the corresponding velocity profile

4.2.2 $dH_{plane}/dH_{objective}$ ratio

To determine the exact height of the measured plane, the relationship between the displacement of the measured plane in the suspension (dH_{plane}) and the displacement of objective ($dH_{objective}$) needs to be determined (Fig 4.8). Normally, dH_{plane} can be estimated by multiplying $dH_{objective}$ with the ratio of the refractive indexes of the lens immersion fluids (n_0) and the experimental fluids (n_L), as expressed in the equation below:

$$dH_{plane} = -\frac{n_L}{n_0} \times dH_{objective} \tag{4.3}$$

Knowing that n_L=1.49, n_0=1, the ratio $dH_{plane}/dH_{objective}$ is 1.49. To verify this, a test was made as follows. A needle was immersed in the fluid to be measured. It was lifted vertically by a precise positioning system. The objective was moved up to watch clearly the needlepoint. The corresponding heights of the needle and the objective were recorded. By performing linear fitting of these two sets of data, the ratio $-dH_{plane}/$

$dH_{objective}$ was acquired as the slope of the fitted line. Different tests within water, air, and suspending fluid were performed to verify the feasibility of this method (Fig 4.9). The measured ratios were 0.9998 in air and 1.3349 in water, and both correlation coefficients are approximated to 1, thus proving the reliability of the approach.

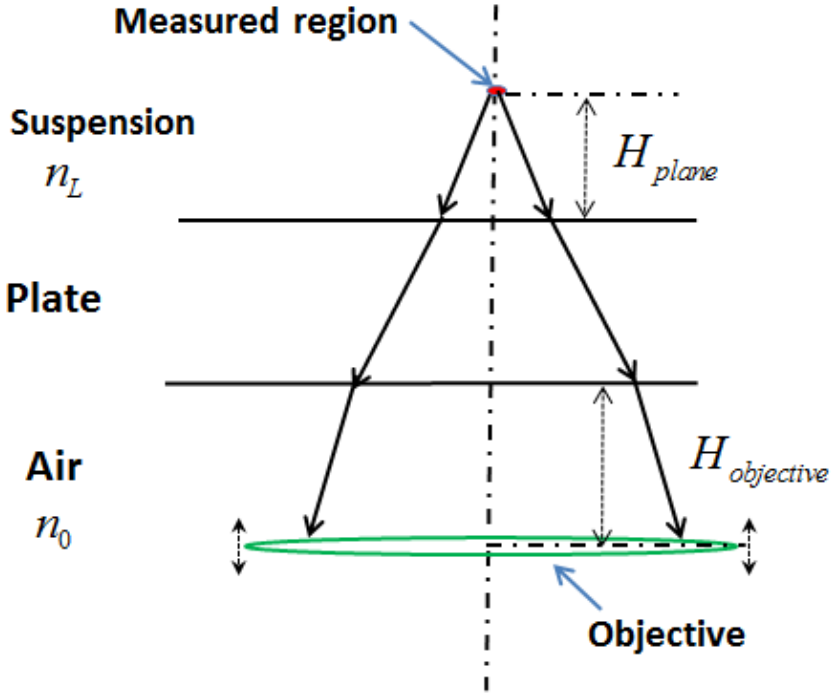

Fig 4.8 Schematic illustration of the light path in the experimental set-up

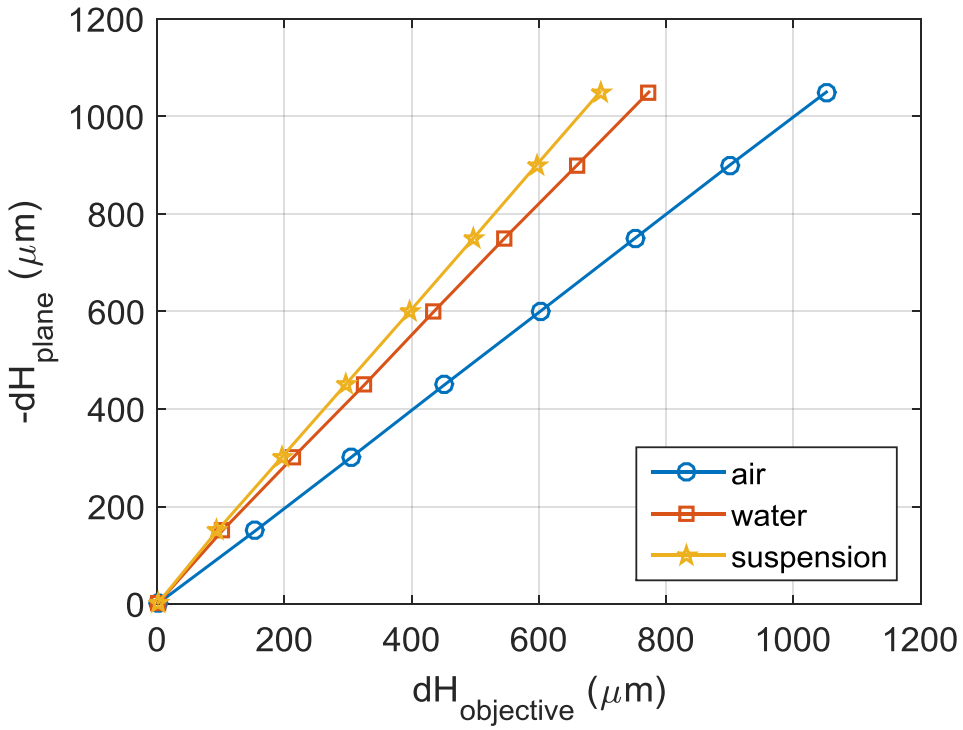

Fig 4.9 Illustrations of the measured $-dH_{plane}$ and $dH_{objective}$

Several tests were undertaken with the suspending fluid at different temperature values. The induced ratios are shown in Tab 4.2. It was found that the temperature variation of several degrees had only little influence on the ratio. Thereby the final ratio was obtained by averaging these values, which is 1.502.

Test	T(°C)	$-\mathrm{dH}_{\mathrm{plane}}/\mathrm{dH}_{\mathrm{objective}}$
1	25.0	1.502
2	21.6	1.502
3	21.4	1.505
4	19.3	1.502
5	17.6	1.500
Average	21.0	1.502

Tab 4.2 Measured $-\mathrm{dH}_{\mathrm{plane}}/\mathrm{dH}_{\mathrm{objective}}$ ratios at different temperatures

4.2.3 Micro-PIV system parameters

In section (2.4.2), the principle of micro-PIV was already presented. Several special characters of micro-PIV were introduced, including volume illumination (depth of correlation, seeding particle size and seeding particle concentration), image acquisition, image processing and measurement error. In the following, all the values of the related parameters are shown.

General parameters

General parameters of a micro-PIV experiment are presented in Tab 4.3, including parameters about objective lens, laser, Dichroic filter, camera, tracer particle and suspension fluid. An Olympus ×20 objective was used. The objective working distance is bigger than the maximum observation depth of the fluid. A 562nm fluorescence Dichroic filter was used (Edmund optics) to eliminate disturbing laser light (532nm). The pixel size of the images is 0.65μm/pixel which was calibrated by a grid with known size.

Objective parameters (OLYMPUS UPlan FL N)		
Objective magnification	20	M
Numerical aperture	0.5	NA
Working distance (mm)	2.1	
Cover slip thickness (mm)	0.17	
Refractive index of lens immersion fluid	1	n_0
Laser parameter		
Laser wavelength (μm)	0.532	λ
Dichroic filter (Edmund optics)		
Minimum transmitted wavelength (μm)	0.562	
Camera parameters		
Image size (pixels)	1376×1024	
Pixel size of images (μm/pixel)	0.65	D_{pixel}
Tracer particle properties (microparticles GmbH, F8819)		
Excitation wavelength (μm)	0.532	
Emission wavelength (μm)	0.575	
Tracer particle diameter (μm)	1	
Tracer particle density (g/cm^3)	1.12	
Minimum visibility for tracer particles	1.5	
Suspension fluid properties		
Refractive index of observed fluid	1.4891	n_L
Minimum viscosity of the observed fluid (Pa.s)	0.042	
Depth of observed fluid (mm)	1	a
Maximum depth of observation (mm)	1.047	L_f

Tab 4.3 General parameters of the micro-PIV experiments

Based on the above values, other characterization parameters related to the micro-PIV experiment were calculated, as shown in Tab 4.4. The response time of tracer particles is $\tau_p = 1.53 \times 10^{-9} s$, which is much smaller than the smallest time interval 100μs (Tab 4.5). Thus the tracer particles can follow the flow. The effective image diameter of tracer particle is 2.69 pixels, which is in the range of recommendation (2-3 pixels). The applied tracer particle volume fraction was 0.031%, which was in the order of the estimated maximum volume fraction of tracer particles of 0.021%, thus, a good visibility of tracer particles was guaranteed. The depth of correlation of the tracer particles is 11.23μm, which is smaller than the distance between adjacent measured planes (≈130μm).

Tracer particle response time (s)	1.53E-9	τ_p
Tracer particle effective image diameter (pixels)	2.69	d_τ
Maximum volume fraction of tracer particle	0.021%	C_{tr}
Depth of focus (μm)	2.19	DoF
Depth of correlation (μm)	11.23	DOC

Tab 4.4 Micro-PIV experiment characterization parameters

Image acquisition

For image acquisition, the time interval (Δt) has to be adjusted according to the fluid velocity and the size of the interrogation window (IW). The chosen interrogation window size was 64×64 pixels. According to the starting rule of PIV measurement, the displacement should be smaller than one fourth of the interrogation window size, and the more close to this value, the better. Thus, the displacement should be smaller than 16 pixels and be close to 16pixels. Taking into account the fluctuation of the measured velocity vectors, 14pixels are set to be the desired displacement. The estimated Δt values at different heights (H) and at different shear rates are shown in Tab 4.5.

H (μm)	Δt_100s^{-1}	Δt_50s^{-1}	Δt_10s^{-1}	Δt_5s^{-1}	Δt_1s^{-1}	$\Delta t\_0.5s^{-1}$
105	869	1738	8691	17383	86915	173830
239	380	761	3803	7605	38025	76051
374	243	487	2434	4867	24336	48672
509	179	358	1789	3579	17894	35789
643	141	283	1415	2830	14149	28298
778	117	234	1170	2340	11700	23400
912	100	199	997	1995	9974	19948

Tab 4.5 An example of the estimated Δt at different heights and at different shear rates for a displacement of 14 pixels, the time unit is μs.

Since, the maximum time interval allowed by the system is 65000μs, there were some cases where the time interval is not sufficient for a displacement of 14 pixels. This can be improved by using a smaller size (32×32 pixels) IWs. In addition, even though the displacement is not perfectly close to one fourth of the IW size, the measurement result can still be used.

Image processing

In the current experiments, the suspended particles were refractive index matched with the fluid, the quality of images was guaranteed. Thus, no pre-processing was performed. Averaging correlation was used for image processing. Following the recommendation of Lindken et al. (2009), 50 pairs of images were taken for each measurement. FFT correlation was used for image processing. For post-processing, the vectors were validated by a local median validation program, not valid vectors were replaced by the median of the neighbor vectors.

Measurement error estimation

The measurement errors come from the Brownian motion, the random error and other environmental factors. According to equation (2.30), the maximum Brownian motion error will occur when the interval time is the maximum and the fluid velocity is the minimum.

As indicated in Tab 4.6, the maximum error induced by the Brownian effect is about 1.07%. According to equation (2.31), when c is equal to 0.1, the random error is 0.27pixels. Thus, for a displacement about 14 pixels, the total error is about 0.42 pixels, which is equal to 3%. However, this error will be reduced by correlation averaging with a sufficiently large number of image pairs. A test described in the following shows the influence of the number of image pairs.

Brownian motion error estimation		
Boltzmann's constant	1.38E-23	K_B
Absolute temperature of the fluid (K)	295.5	T_a
Minimum viscosity of observation fluid (Pa.s)	0.042	n_L
Diffusion coefficient	7.56E-15	D
Maximum Time interval (s)	0.065	Δt
Minimum measured velocity (mm/s)	0.05	v
Maximum induced Brownian motion error	1.07%	ε_x
Random error estimation		
Tracer particle effective image diameter (pixels)	2.69	d_τ
Random error (pixels)	0.27	ε_{rd}

Tab 4.6 Measurement error estimation

A large series of images were taken in a measurement. The correlation averaging was performed with different numbers of image pairs. The corresponding mean vector length was recorded. Then, the variation of the obtained vector length with respect to the number of image pairs was observed. As shown in Fig 4.10, when the number of image pairs is more than 40, the relative fluctuation of vector length is under 1.5%. This is smaller than 3%. In addition, this value is under the acceptable measurement uncertainty of 2% for micro-PIV (Wereley and Meinhart 2010). Therefore 50 pairs of images are sufficient for the measurement in the current experiments. For suspension with higher particle concentration, since the suspension viscosity is higher than the pure suspending fluid, the influence of Brownian motion is much smaller. As shown in Fig 4.10, in a 20% 41μm particle suspension, the fluctuation of velocity vector length is much smaller compared with that of 0% particle suspension. Hence, 50 pairs of images are also sufficient.

In general, correlation averaging can reduce the Brownian motion error, the measurement errors are controlled within the acceptable range of uncertainty (<2%).

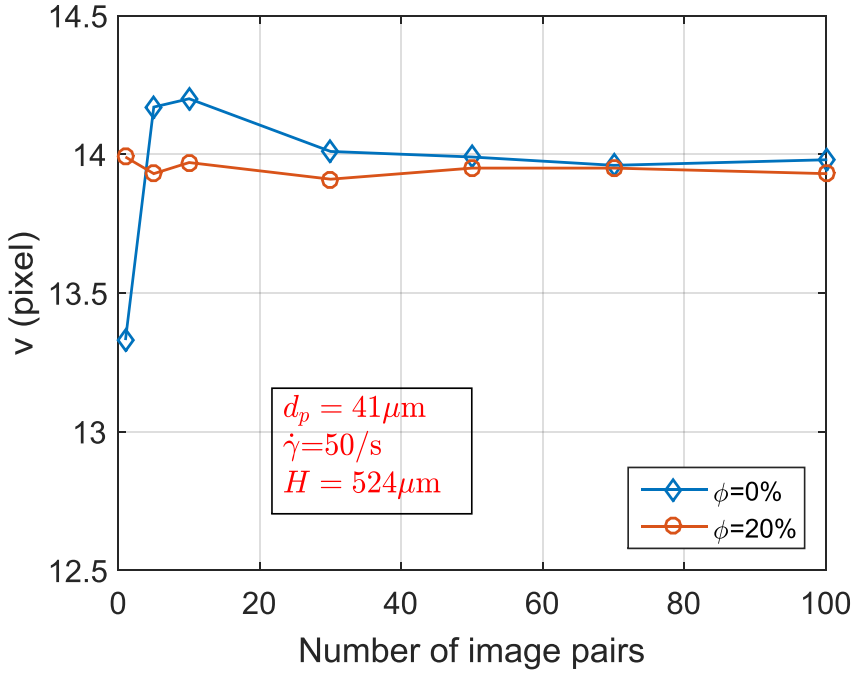

Fig 4.10 Variations of the vector length (v) as a function of image pair of 0% and 20% 41μm particle suspension at 50 s^{-1} and at H=524μm.

4.3 Validation of experimental set-up

To make sure that a rotational constant shear flow can be acquired in the cone-plate device, the threshold rotational speed of the cone under which there was negligible secondary flow was calculated. In addition, a measurement with 0% particle suspension was performed, in order to verify that the secondary flow was negligible in the experiment under the previous established range of rotational speeds (Tab 4.1).

4.3.1 Threshold velocity of secondary flow

As shown in Fig 4.11, if secondary flows occur, the measured radial velocity component (u) near the cone surface will be a little directed outward, and those near the plate surface will be directed inward (Fig 4.11-b), thus there will appear a circular flow (Fig 4.11-a). In the current experiments, we want to observe the flow behavior of suspension under a stable primary flow. The secondary flow is not desired. Therefore, it is necessary to know the threshold rotary speed of the cone under which there is no secondary flow.

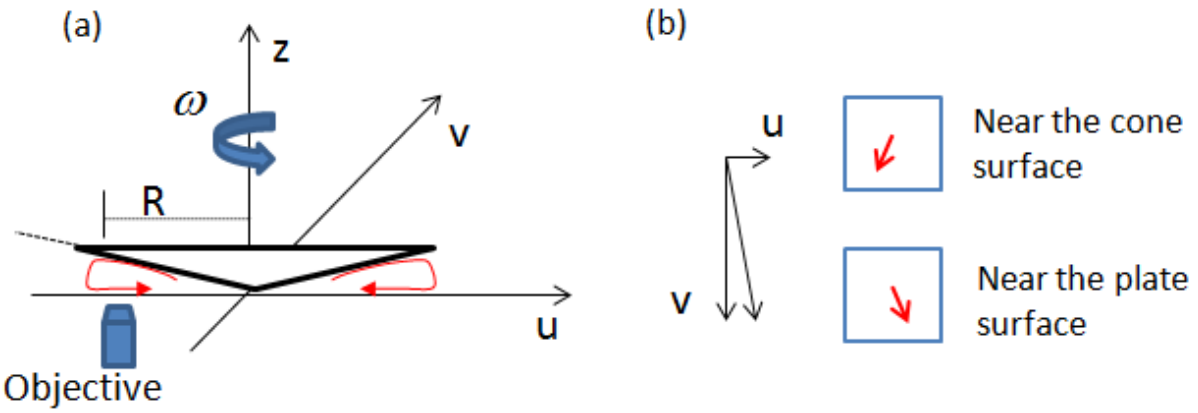

Fig 4.11 Illustrations of secondary flow in a cone-plate device, a) the flow direction of secondary flow, b) illustration of the velocity vector near the cone surface and near the plate surface

According to the results of viscosity measurements in chapter 3, the 0% particle suspension has the minimum viscosity. Thus, at this suspension, it is the most possible case for secondary flow to appear. Then the threshold rotary speeds are calculated based on the 3 different criteria shown in Tab 4.7. The distance from the center of the measured region to the cone axis R=0.03m, the angle of cone α=2°, the dynamic viscosity η=0.042Pa.s, the density ρ=1.18kg/cm^3.

References	Description		Result
(D. C.-H. Cheng 1968)	$\widetilde{\mathrm{Re}} = 4\frac{\mathrm{R}^2\omega\rho\alpha}{\eta}$	When $\mathrm{B} * \left(\frac{\tilde{\mathrm{R}}_e}{\alpha}\right)^2 \leq 0.1$, the effect of secondary flow is negligible ($\mathrm{B} = 2.505 * 10^{-10}$, at α=2°)	$\omega = 1886$ RPM
(Sdougos, Bussolari, and Dewey 1983)	$\widetilde{\mathrm{Re}} = \frac{\mathrm{R}^2\omega\rho\alpha^2}{12\eta}$	$\tilde{\mathrm{R}}$<0.5, there is no secondary flow	$\omega = 1860$ RPM
(Ellenberger and Fortuin 1985)	$\widetilde{\mathrm{Re}} = \frac{\mathrm{R}^2\omega\rho\alpha^2}{\eta}$	When $\tilde{\mathrm{R}}_e \leq 10$, the measured torque is almost the same with the theoretical estimated torque	$\omega = 3101$RPM

Tab 4.7 Threshold rotary speeds of secondary flow

The minimum value among the three is 1860RPM. This value is much higher than the maximum rotational speed encountered in the current experiments (33.3RPM). So according to their deduction, the secondary flow in the experiments under the previous established range of rotational speeds is negligible.

4.3.2 Velocity profiles of 0% particle suspension

To verify the conclusion deduced in the section above, a measurement with 0% particle suspension was performed. To better show the velocity profiles, the velocity and the height are made to be non-dimensional. Concretely, the height (H) was divided by H_{max} and the measured velocity (V) was divided by V_{max}. H_{max} was the distance between the

cone and the plate surface at a radius of measurement. V_{max} was the maximum velocity, which was defined as the rotational speed multiplied by the distance of the measured plan center to cone axis $\omega \times R$.

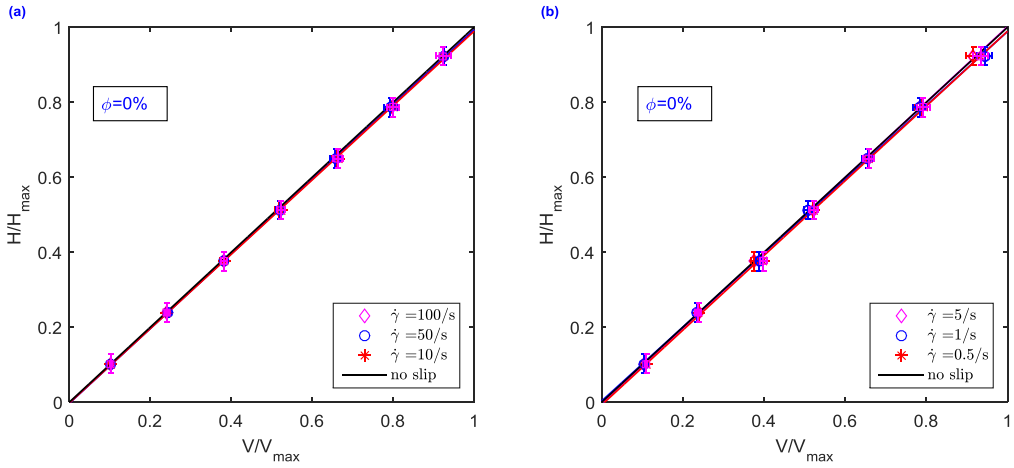

Fig 4.12 Normalized velocity profiles of 0% particle suspension at: a)100s^{-1}, 50s^{-1} and 10s^{-1}, b) 5s^{-1}, 1$s^{-1}$and 0.5s^{-1}.

In Fig 4.12, it can be seen that at different shear rates the normalized velocity profiles of 0% particle suspension fit the no slip case (Fig 4.5). The relative differences ($\Delta\dot{\gamma}/\dot{\gamma}$, where $\Delta\dot{\gamma} = \dot{\gamma} - \dot{\gamma}_m$) of the measured shear rates ($\dot{\gamma}_m$) with that of the no slip case ($\dot{\gamma}$) are smaller than 1.7%. The relative error of the measured shear rate is about 2.83%. (The calculation of uncertainty is shown in appendix E)

In addition, the measured radial velocity profile at 100s^{-1} (the maximum shear rate) is compared to the theoretical deduction (Equation (2.16)) of Sdougos et al.(1983). Fig 4.13 shows the two normalized radial velocity profiles with respect to the normalized height. It can be found that there is no similarity between the two profiles. Moreover, the small values of radial velocity are possible due to the measurement uncertainty, or due to the non-alignment between the optic window with the flow direction (the measured region is not parallel to the y direction). Therefore, the ratio of the radial and the tangential vector components u/v is observed (Fig 4.14). Compared to the u/v ratio based on the deduction of (Equation(2.17)) of Sdougos et al.(1983), at 100s^{-1}, the u/v ratio of the current experiment is smaller, and there is no negative u/v ratio.

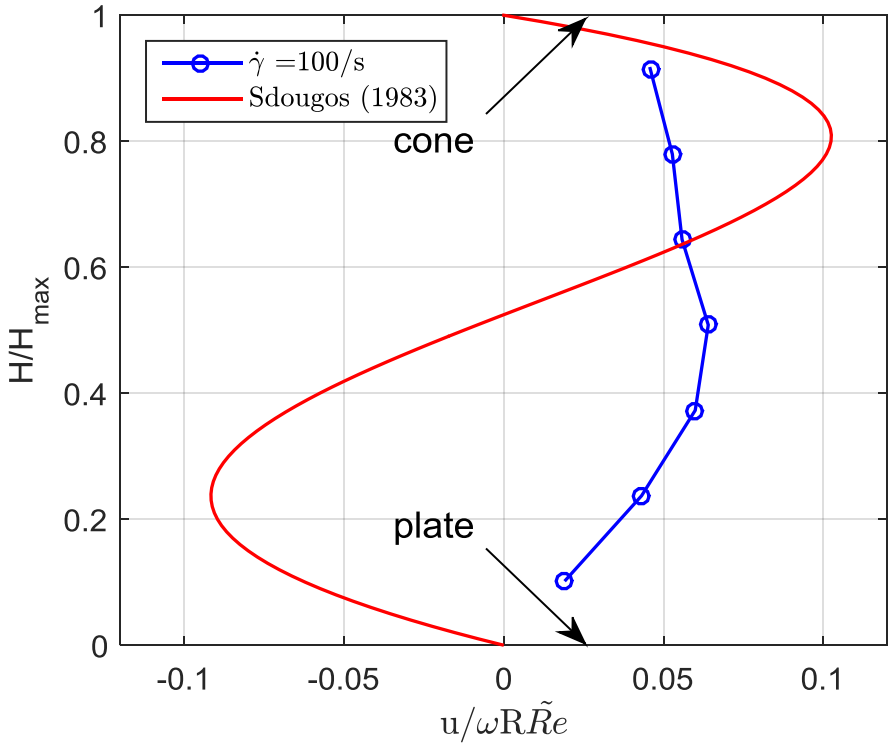

Fig 4.13 Normalized radial velocity profile of the theoretical deduction of Sdougos et al.(1983), and normalized radial velocity profile of the 0% particle suspension at 100s^{-1}, here u positive means outward radial movement.

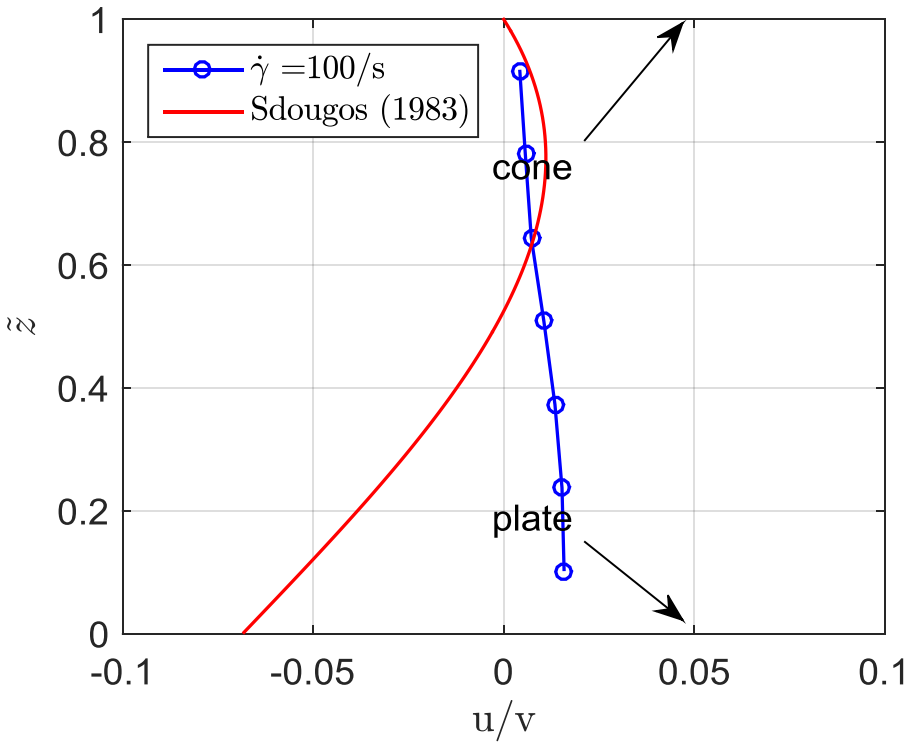

Fig 4.14 u/v ratio based on the theoretical deduction of Sdougos et al.(1983), and of the 0% particle suspension at 100s^{-1}, here u positive means outward radial movement.

For the other 5 different shear rates, the u/v ratios are show in Tab 4.8, it is found that all the u/v ratios are below 1.67%, which is smaller than the acceptable uncertainty for micro-PIV of 2%. Thus, it can be concluded that secondary flow was negligible in the flow of the 0% particle suspension. Furthermore, it was also negligible in other suspension flows within the current rotary speed range. Therefore the experiment set-up can be validated.

H (μm)	u/v ($100s^{-1}$)	u/v ($50s^{-1}$)	u/v ($10s^{-1}$)	u/v ($5s^{-1}$)	u/v ($1s^{-1}$)	u/v ($0.5s^{-1}$)
105	1.59%	1.66%	1.28%	0.67%	0.63%	0.73%
239	1.53%	1.39%	1.29%	1.05%	0.83%	1.43%
374	1.35%	1.23%	0.78%	1.06%	1.10%	0.14%
509	1.05%	0.91%	0.77%	0.70%	1.13%	1.22%
643	0.72%	0.84%	0.65%	0.56%	0.56%	0.15%
778	0.57%	0.57%	0.42%	0.72%	0.50%	0.36%
912	0.42%	0.42%	0.42%	0.36%	0.36%	0.34%

Tab 4.8 u/v ratios of the 0% particle suspension at different heights and at different shear rates

4.4 Particle concentration measurement

4.4.1 Measurement principle

The flow induced by the cone-plate is stationary, thus the local particle concentration should be the same in the region with the same height and with the same distance to the cone axis. Therefore, a statistic approach can be adopted to evaluate the local particle concentration. The principle is to use dyed particles as representative particles. Firstly, some particles were stained with fluorescent dye (ACAL BFI France, Part NO. colds698, LDS 698), of which the excitation wavelength is 532nm and the emission wavelength is 690nm. Then they were mixed with other PMMA particles in the suspension by agitation and ultrasonic bath, to make sure that the dyed particles were homogeneously dispersed in suspension. Next, a series of images were taken at a fixed place in the suspension flow. As all other particles were refractive index matched with the fluid, only dyed particles can be captured by the camera. Then by an image processing method (it will be introduced in the following section), the 2D positions and the distances to the focal plane of detected particles in all this series of images are determined.

A cubic region based on the measured plane with a limited width was selected, for example, the entire image window with the depth equal to the diameter of a particle (Fig 4.15). Next, as the pixel size (0.65μm/pixel) is the same at different depth, the real area of the captured region can be determined, where 1376×1024 pixels are equivalent to $894.4\times665.6\mu m^2$. The volume of dyed particles which belonged to this cubic region was

counted. By multiplying N_{rp} which is the average number of particles represented by each dyed particle (Fig 4.15), the locale particle concentration can then be evaluated.

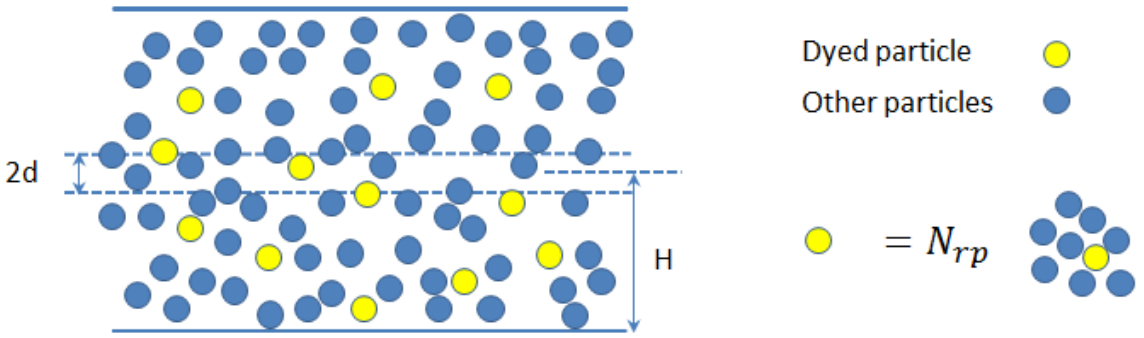

Fig 4.15 Schematic illustration of the local particle concentration measurement principle, where H is the measured height, the measurement plane width is 2d which will be described in section (4.4.3).

For a preliminary test, only PMMA particles with diameter 41±0.65μm were employed. Two concentrations of particle suspension were used: 45% and 20%, the latter was prepared by diluting the 45% particle suspension with the suspending fluid. Only a few particles were dyed. Much effort had been undertaken to well control the dyed particle volume fraction. If too many particles were dyed, it would be impossible to take pictures at a deeper depth in the suspension. In addition, if the volume fraction of dyed particle was a little higher, the probability of particle image overlapping would increase which would influence the measurement of local particle concentration. Moreover, due to the large image of the dyed particles (Out of focus effect), the velocity field measurements could not be performed at the same time.

In the current experiment, the fraction of dyed particle was about 0.27%. However, it was not accurate, because the noted weight of dyed particle was too small (≈0.0115g), and many environmental factors could affect this value in the preparation procedure. Thus, the N_{rp} value was calibrated in an experiment by the approach described in the following.

To determine the value of N_{rp}, a Malassez Hemo-cytometer (Optik Labor) was used which had a calibrated depth of 200μm. A drop of 45% particle suspension was put between the Malassez slide and a glass slide. At a fixed place, the number of particles in the volume of the image window with a depth of 200μm was counted. Multi tests were performed at different region between the gaps. Then by dividing the total number of dyed particles by the number of tests, the average number of dyed particles in a volume with an area of the image window and a depth of 200μm is determined. Based on this,

N_{rp} value can be deduced as dividing the number of all the particles by the averaged number of dyed particles in this volume.

The experimental set-up was the same as for velocity profile measurement, except that the Dichroic mirror was changed, a 675nm hard coated bandpass (50nm) interference Filter (Edmund optics) was used. For 45% particle suspension, a series of 50 images were taken, and it is 100 images for 20% particle suspension as the particle concentration is smaller. The suspensions were sheared at two different shear rates $50s^{-1}$ and $1s^{-1}$. At each shear rate, the measurements were performed at 3 different heights: 181μm (near the surface of the plate), 496μm (in the middle of the fluid) and 812 μm (near the surface of the cone). The capture frequency of the camera was adjusted to make sure that the sampling was taken randomly in a large region of the suspension, not concentrated on a certain region. For $50s^{-1}$, it was 4.83Hz, and for $1s^{-1}$ (small velocity), it was 0.61Hz at low position, 1.21 Hz at middle position and 2.43 Hz at high position.

4.4.2 Particle locating program

The particle positions were determined by the GDPTlab (General Defocusing Particle Tracking lab) tool which was developed by Barnkob et al (2015). Because PMMA particles were spherical, and image overlapping can be reduced significantly by controlling the dyed particle concentration, it was suitable to use the GDPTlab tool in the current experiments. The program is divided into 4 steps: image preprocessing, image segmentation, image calibration, particle position calculation (Fig 4.16).

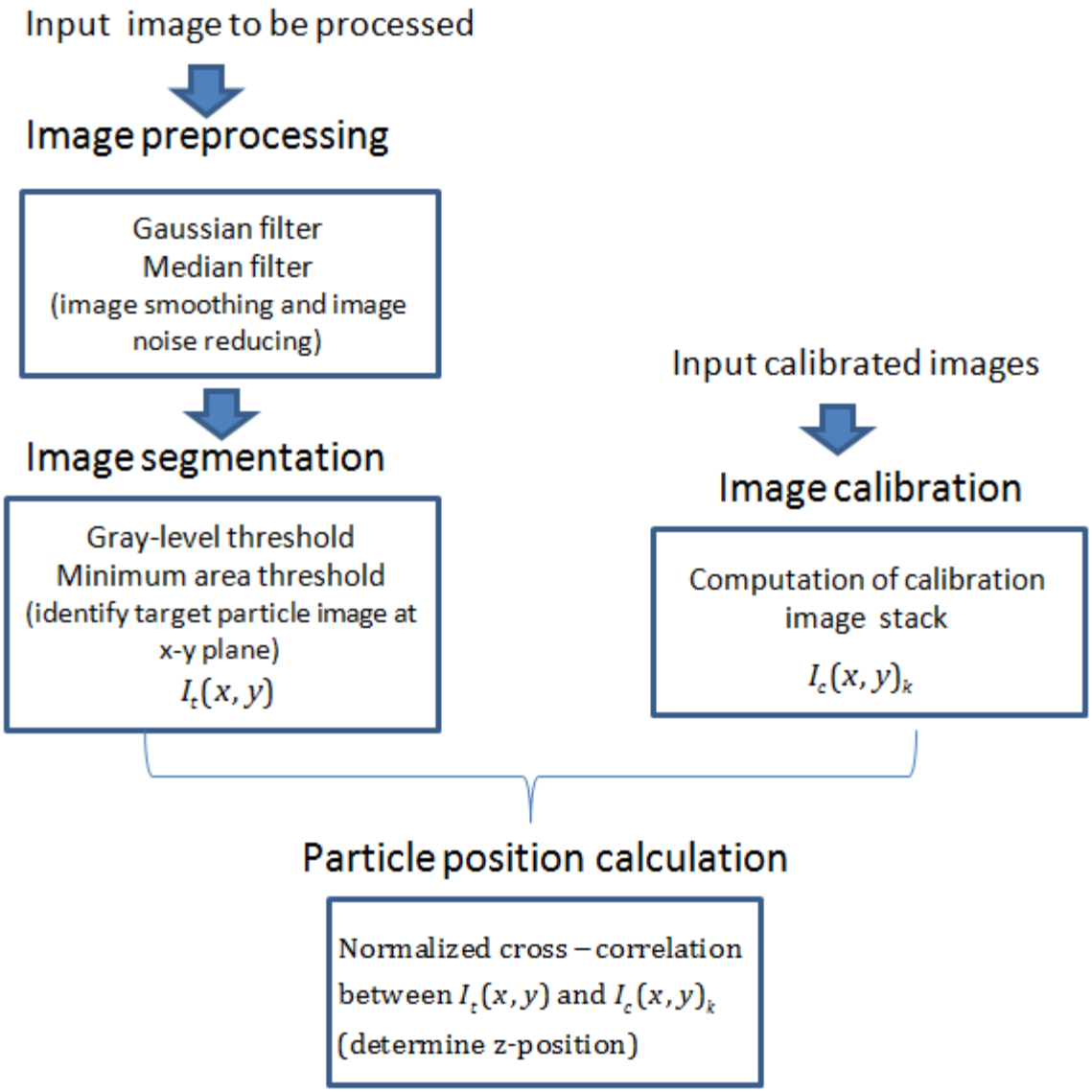

Fig 4.16 Illustrations of the particle position locating procedures

Image preprocessing

Before the normalized cross-correlation program, Gaussian filter and median filter are used to smooth images and to remove image noise.

Image segmentation

Particle image was segmented by a gray-level threshold and a minimum area threshold. The gray-level threshold was set to be higher than the background intensity and smaller than the minimum target particle image intensity. The minimum area threshold was set to be the minimum area of a target particle image. Together, these two thresholds helped to identify the region where the particle is located. The pixel size is 0.65 μm/pixel. For 41μm particle, the magnification term is $\mathrm{Md_p} = 41/0.65 = 63$pixel, then the effective image diameter of dyed particle $d_\tau > 63$pixel. Based on this diameter, an

estimation of the minimum area is $\pi \times 63^2/4=3115.6$, the area threshold was set to be 3000 (a little smaller than the estimated value).

Image calibration

The calibrated stack of images was acquired by capturing the particle image at a fixed frequency, and at the same time by moving the objective with a constant speed from down to up of the particle position. Because the suspension was density matched, the dyed particle can be considered as not moving during the time of image capturing. The calibrated depth was determined by the wanted maximum measurement plane width. In a stack of calibrated images, the first image was assigned as z=0, the k^{th} image was assigned as $z_k=(k-1)\times d_{step}$ (Fig 4.17), where d_{step} is the incremental distance between the two adjacent images. The exact focal plane position was determined by identifying the minimum effective particle image diameter. To guarantee the measurement precision, a high quality calibrated stack of images was required. Several series of images with different step distance (d_{step}=1.52μm, 2.04μm and 3.04μm) were taken. The stack of images who offered the best quality was chosen.

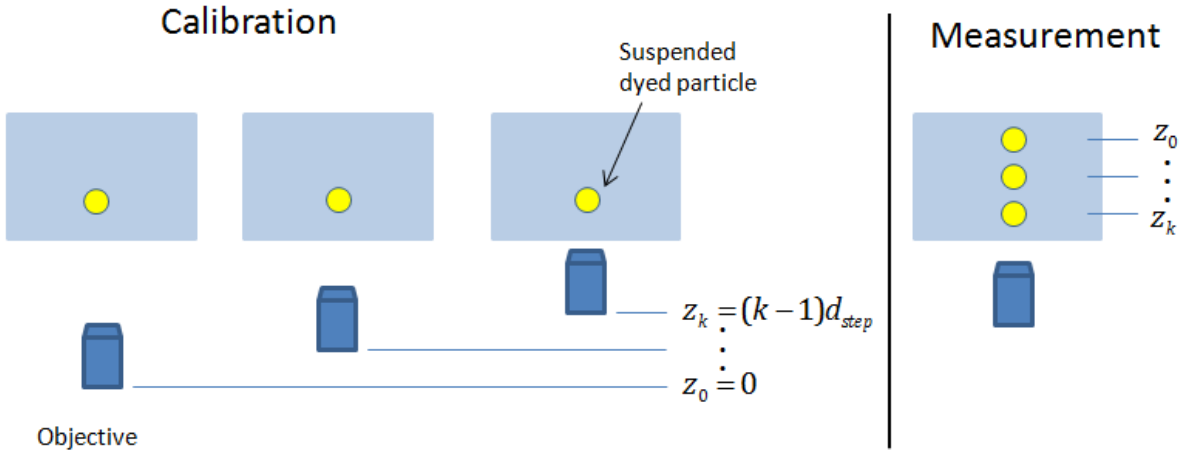

Fig 4.17 Illustration of the image calibration and z-position determination in measurement

Particle position calculation

The processing result gives the 3d coordinates (x, y, z) of each detected particle and the corresponding maximum correlation coefficient C_m. Here, z coordinate was based on the calibrated particle image position, and the z axis orientation between the calibration and the measurement will be inverse, as shown in Fig 4.17 for example. All the particles out of the calibrated distance can be excluded according to their low correlation coefficient values.

4.4.3 Local particle concentration calculation

To determine the local particle concentration around the focal plane, two limited planes are set respectively below and above the focal plane with an equal distance (d), as shown in Fig 4.18 in a side view. Then, the volume of dyed particles between these two planes is counted in a number of images (N_{im}) taken at the same position, noted as V_{dye}. Only the part of the particle body between these two planes is included. For example, in Fig 4.18, particle 1 is counted as a complete particle. Particle 2 and 3 is noted as incomplete particles, of which the counted volume depends on the part of their body between the two planes.

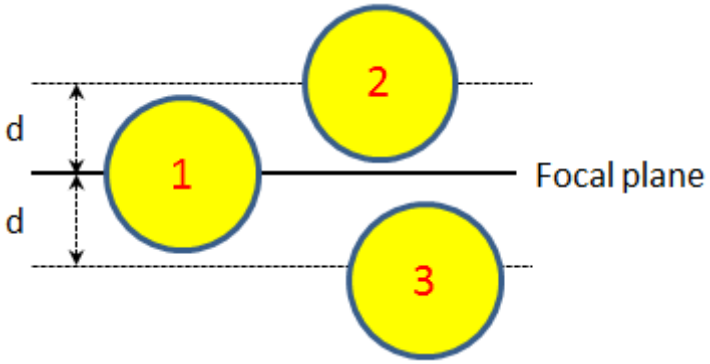

Fig 4.18 Illustrations of the particle positions for local particle concentration calculation

Then, the total volume of particles between these two planes can be estimated as $N_{rp} \times V_{dye}$. The local volume fraction ϕ_{local} is expressed as equation (4.4), where A is the area of the image window, N_{im} is the number of images.

$$\phi_{\mathrm{local}} = \frac{\mathrm{N_{rp}} \times \mathrm{V_{dye}}}{\mathrm{N_{im}} \times 2\mathrm{d} \times \mathrm{A}} \tag{4.4}$$

5 Experimental results

After the experimental set-up is validated and the techniques for experiment are defined, in this chapter, the experimental result measured under the predefined experimental conditions will be presented. Firstly the velocity profiles of suspension flows under the cone-plate device will be characterized. The phenomenon of velocity profile deviation of dense suspensions flow will be studied. Then, the result of local particle concentration measurements will be shown. The correlation between the suspension flow behavior and the particle concentration distribution will be discussed.

5.1 Suspension velocity profiles

5.1.1 Evolution of velocity profiles

To show the measurement result, two comparisons are made, respectively, based on the particle concentrations and on the flow shear rates. The velocity profiles of particle suspension at ϕ =10% and 5% are not considered in the two comparisons, because they are similar to the velocity profiles of the no slip case (Appendix C).

5.1.1.1 Comparisons based on particle concentration

At first, the influence of particle concentration on the velocity profiles is investigated for both 41μm and 4.62μm particle suspensions. Before the comparison, it is necessary to mention that due to the under or over estimation of the plate and the cone positions, the gap heights were not same at different measurements, thus the real applied shear rates ($\dot{\gamma}$) had a little variation with respect to the set values.

Fig 5.1 shows the normalized velocity profiles of 41μm particle suspensions at $10s^{-1}$. All the velocity profiles are approximately linear. However, they stray away from that of the no slip case, and the deviation is more important at ϕ=45%. Besides, the deviations are closely symmetric in the bottom and the top surfaces.

At the same shear rate, the velocity profiles of 4.62μm particle suspension are shown in Fig 5.2. Here, only the velocity profile of 45% particle suspension deviates from that of the no slip case. As well, all the velocity profiles are approximately linear, and the deviation of 45% particle suspension velocity profile is closely symmetric in both the two surfaces.

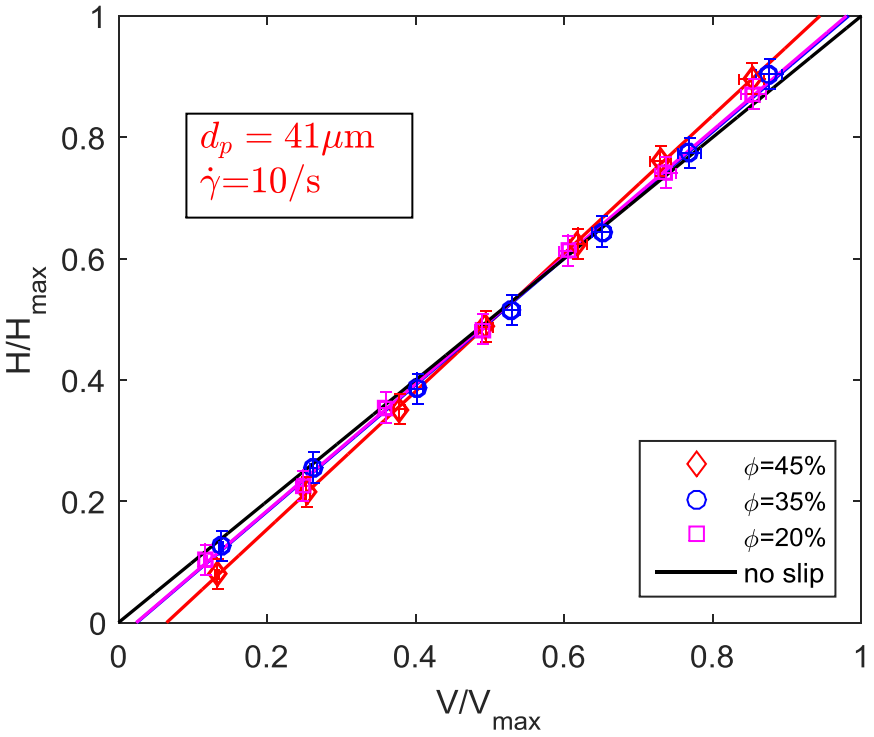

Fig 5.1 Normalized velocity profiles of 41μm particle suspensions at ϕ=45%, 35%, 20% and at 10s^{-1}.

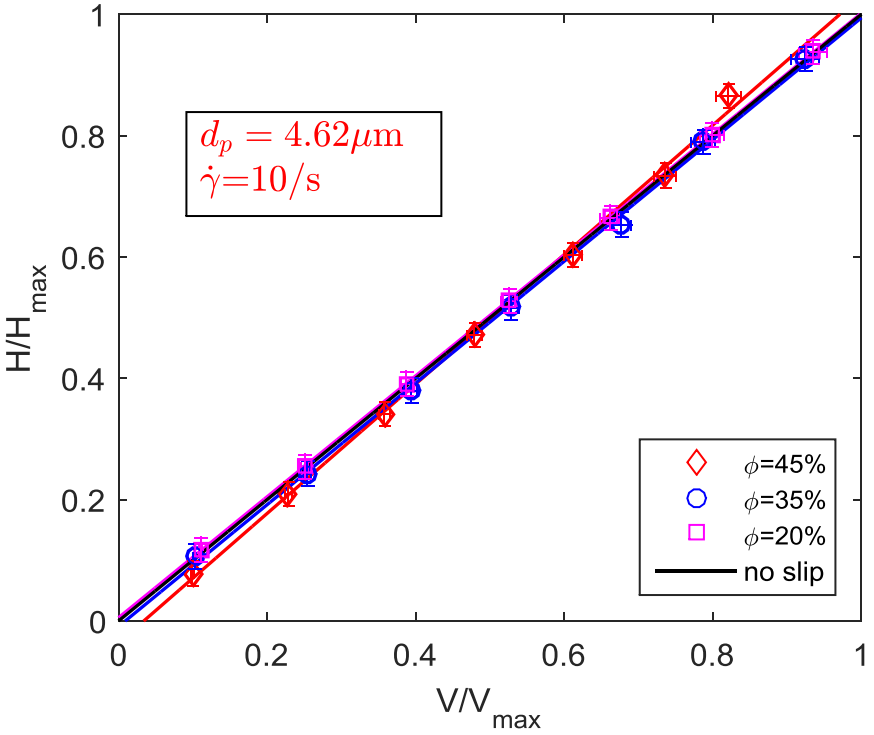

Fig 5.2 Normalized velocity profiles of 4.62μm particle suspensions at ϕ=45%, 35%, 20% and at 10s^{-1}.

Those general situations are similar at other shear rates, as it can be observed in Fig 5.3 and Fig 5.4 respectively, for 41μm and 4.62μm particle suspensions at $1s^{-1}$ for examples.

The deviation can be quantified by the relative difference of the measured shear rates ($\dot{\gamma}_m$) with that of the no slip case ($\dot{\gamma}$), which is noted as $\Delta\dot{\gamma}/\dot{\gamma}$, where $\Delta\dot{\gamma} = \dot{\gamma} - \dot{\gamma}_m$. For examples, at $10s^{-1}$, the values of $\Delta\dot{\gamma}/\dot{\gamma}$ are 12.2%, 4.3% and 5.9% for 41μm particle suspensions at ϕ=45%, 35% and 20% repectively. For 4.62μm particle suspensions, at the same concentrations, the values of $\Delta\dot{\gamma}/\dot{\gamma}$ are 6.5%, 1.4% and 0.5% respectively.

In some instances, the deviation of the velocity profile is not exactly symmetric at the bottom (H/H_{max}=0) and the top (H/H_{max}=1) surface. This was principally due to the under or over estimating about certain microns of the bottom plane position, thus the normalized velocity profile was translated.

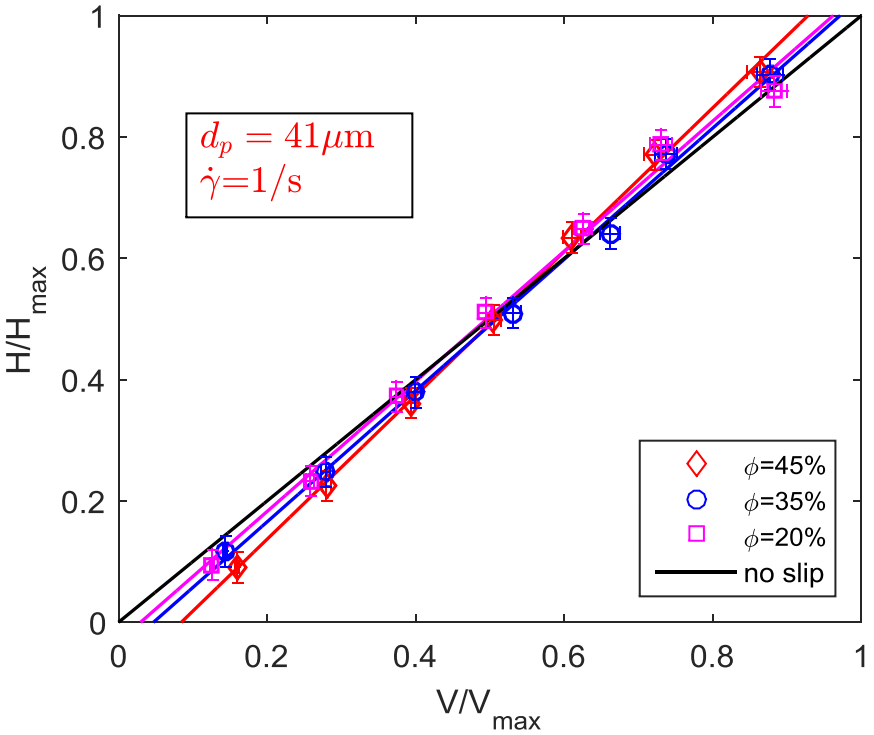

Fig 5.3 Normalized velocity profiles of 41μm particle suspensions at ϕ=45%, 35%, 20% and at $1s^{-1}$.

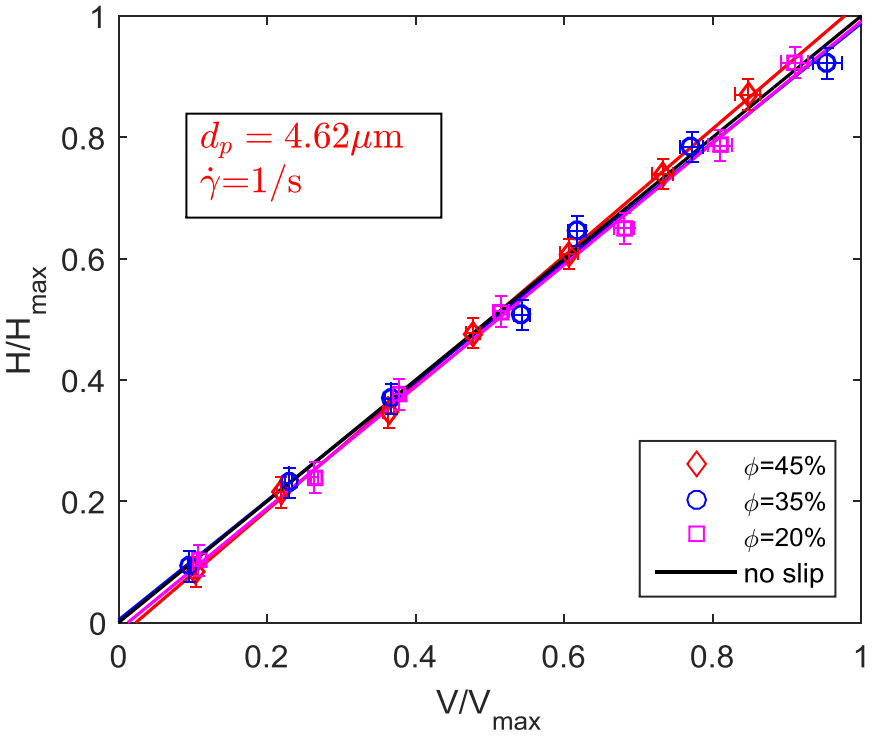

Fig 5.4 Normalized velocity profiles of 4.62μm particle suspensions at ϕ=45%, 35%, 20% and at 1s^{-1}.

For those suspensions with deviated velocity profiles, a further comparison is made to observe the evolution of velocity profiles at different shear rates, which are 41μm particle suspensions at ϕ=45%, 35% and 20%, and 4.62μm particle suspension at ϕ=45%.

5.1.1.2 Comparisons based on shear rate

41μm particle suspensions

The normalized velocity profiles of 45% 41μm particle suspension at 1s^{-1}, 10s^{-1}, and 100s^{-1} are shown in Fig 5.5. It seems that the deviation of the velocity profile is less important following the increase of shear rate. At 1s^{-1}, 10s^{-1}, and 100s^{-1}, the values of $\Delta\dot{\gamma}/\dot{\gamma}$ are 15.8%, 12.2%, 10.7% respectively. This trend is also shown in the other two suspensions at ϕ=35% (Fig 5.6) and 20% (Fig 5.7). In the following section, this variation with respect to the shear rate will be discussed.

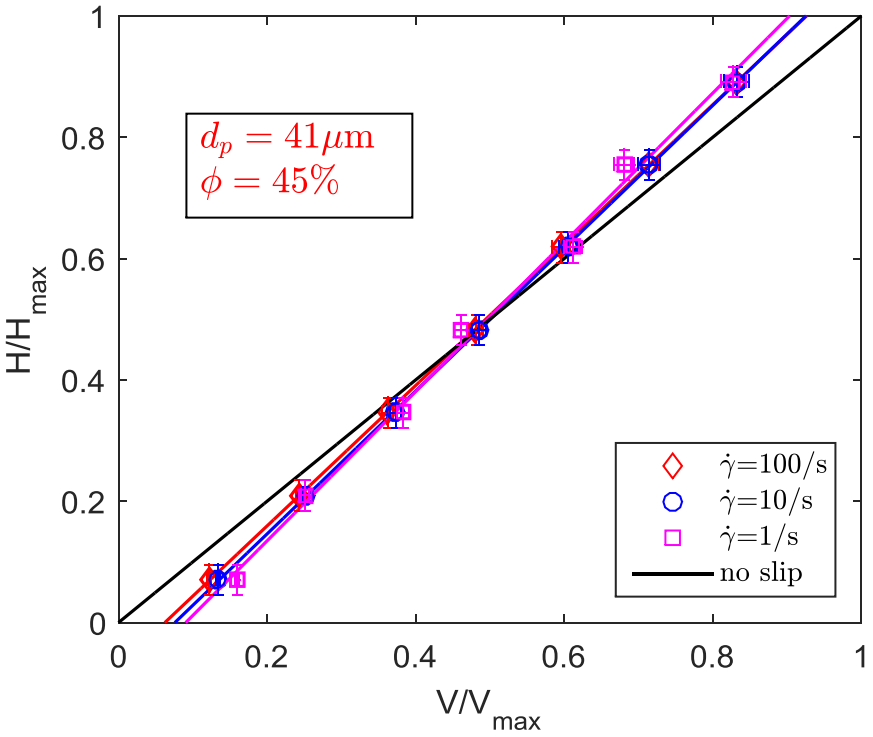

Fig 5.5 Normalized velocity profiles of 45% 41µm particle suspension at $1s^{-1}$, $10s^{-1}$, and $100s^{-1}$.

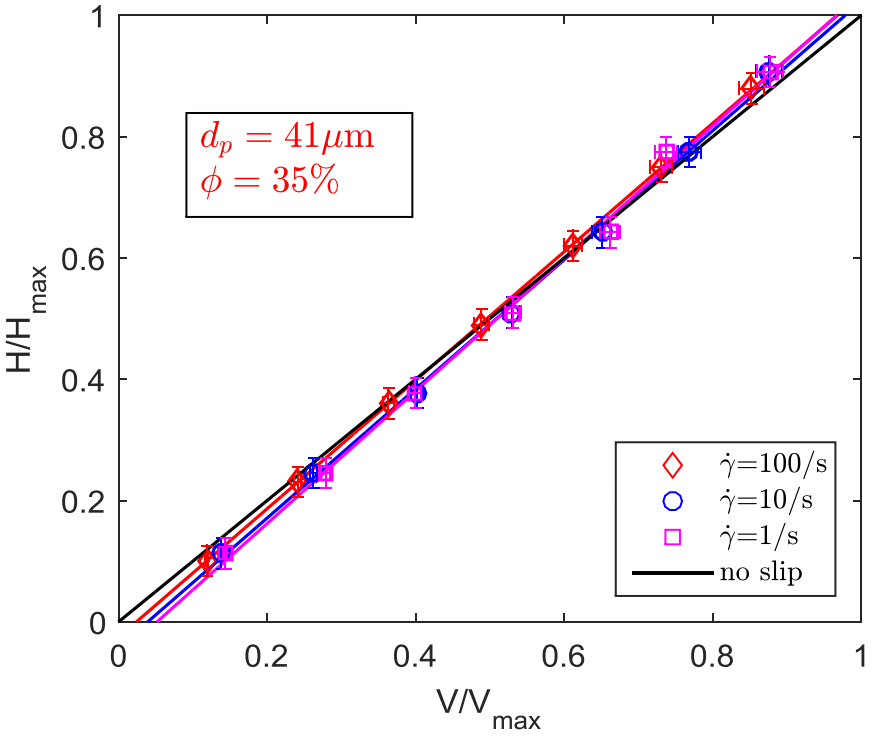

Fig 5.6 Normalized velocity profiles of 35% 41µm particle suspension at $1s^{-1}$, $10s^{-1}$, and $100s^{-1}$.

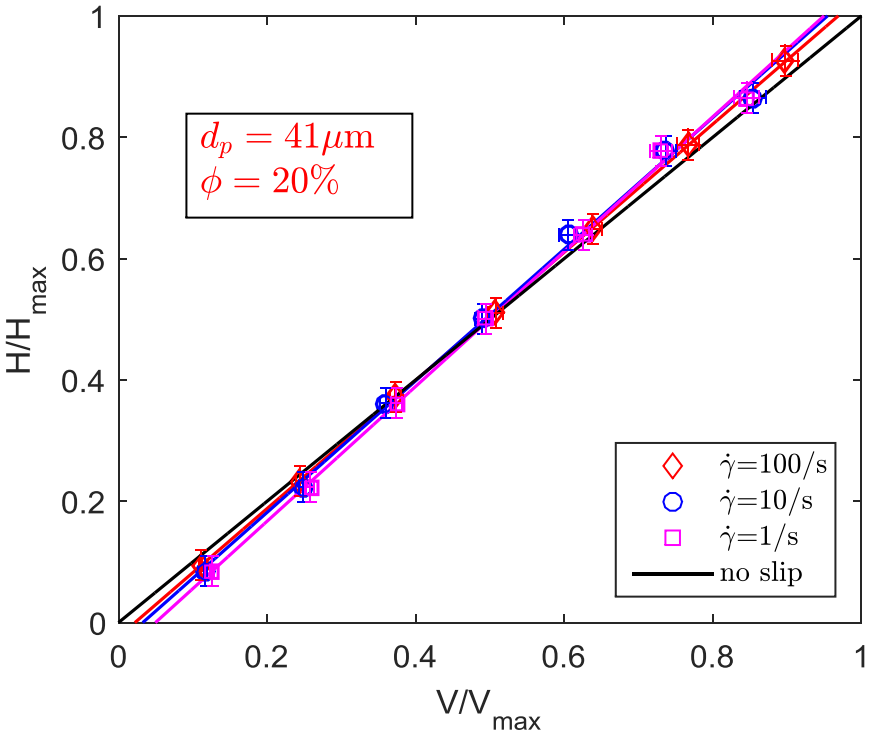

Fig 5.7 Normalized velocity profiles of 20% 41μm particle suspension at $1s^{-1}$, $10s^{-1}$, and $100s^{-1}$.

4.62μm particle suspension

For 4.62μm particle suspensions at ϕ =45%, the normalized velocity profiles are shown in Fig 5.8 and Fig 5.9. There is no clear trend of the deviation with respect to shear rate. With the shear rate varying from $1s^{-1}$, $10s^{-1}$ to $100s^{-1}$, the deviation becomes more important, the values of $\Delta\dot{\gamma}/\dot{\gamma}$ are 4.6%, 6.5%, 7.4% respectively. However, the same trend is not shown at $0.5s^{-1}$, $5s^{-1}$and $50s^{-1}$, the values of $\Delta\dot{\gamma}/\dot{\gamma}$ are 4.8%, 3.8%, 7.2% respectively.

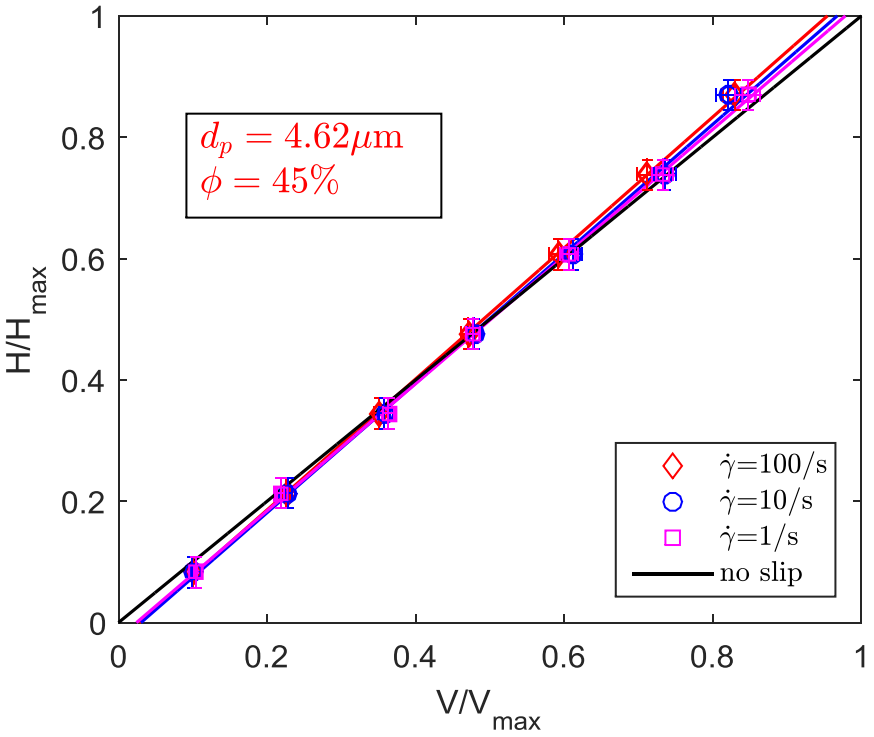

Fig 5.8 Normalized velocity profiles of 45% 4.62µm particle suspension at 1s^{-1}, 10s^{-1}, and 100s^{-1}.

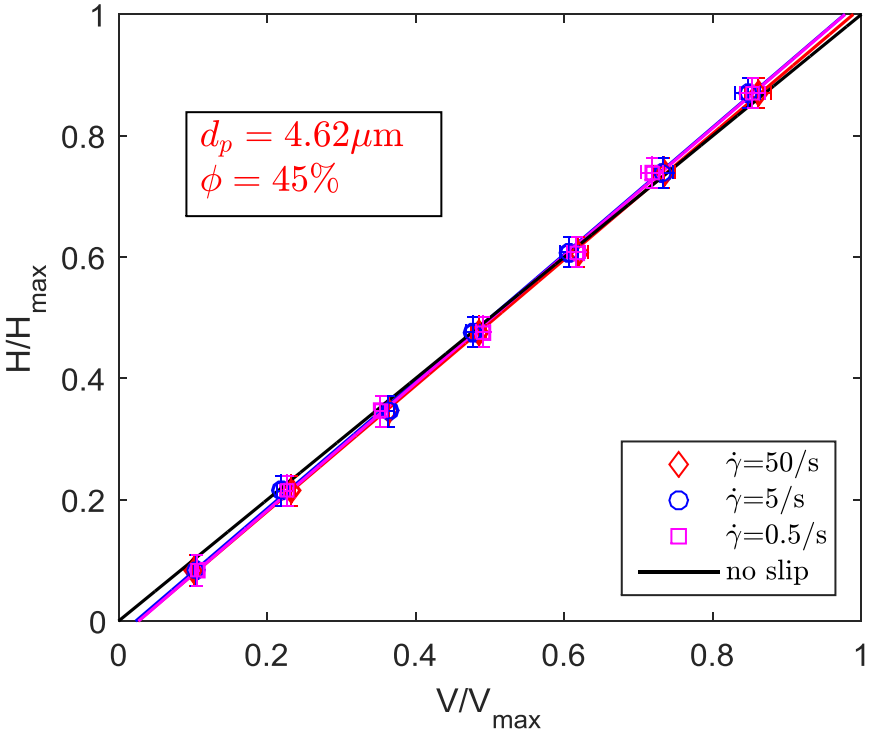

Fig 5.9 Normalized velocity profiles of 45% 4.62µm particle suspension at 0.5s^{-1}, 5s^{-1}, and 50s^{-1}.

5.1.2 Relative difference of shear rates

To better observe the evolution of the relative differences of shear rates, the values of $\Delta\dot{\gamma}/\dot{\gamma}$ for the two sizes of particle suspensions are plotted in two figures respectively (Data are in appendix D).

Fig 5.10 shows the values of $\Delta\dot{\gamma}/\dot{\gamma}$ with respect to $\dot{\gamma}$ for 41μm particle suspensions. It can be seen that the absolute value of $\Delta\dot{\gamma}/\dot{\gamma}$ is under 2% when the concentration is below 20%. Here, the measurement uncertainty of shear rate is 2.83% (The detail deduction is shown in appendix E). Above this concentration, it tends to increase following the increase of ϕ. At ϕ=20%, 35%, 45%, the average $\Delta\dot{\gamma}/\dot{\gamma}$ values are 4.95%, 6.24% and 11.74% respectively. Moreover, it seems that $\Delta\dot{\gamma}/\dot{\gamma}$ decrease following the increase of $\dot{\gamma}$, but this is possible due to the measurement uncertainty, as they have relatively large error bars.

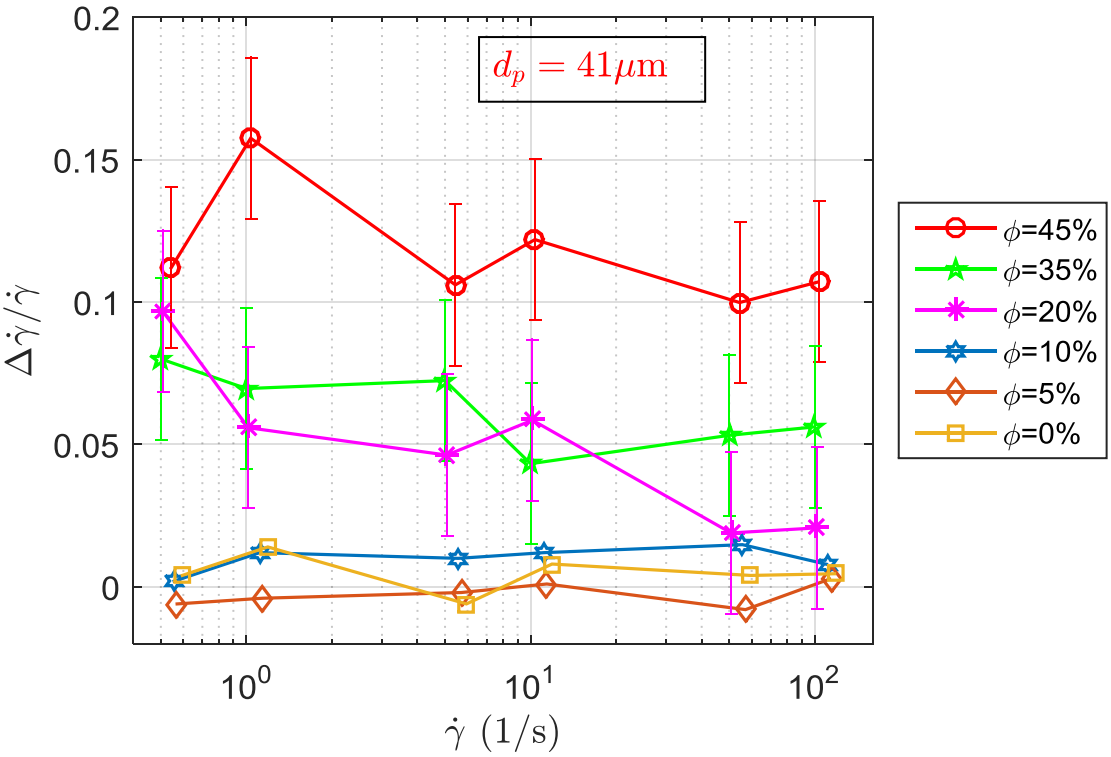

Fig 5.10 Relative differences of shear rates as a function of $\dot{\gamma}$ of 41μm particle suspension, the error bars of suspension at ϕ=10%, 5% and 0% are not shown.

The $\Delta\dot{\gamma}/\dot{\gamma}$ of 4.62μm particle suspension is shown in Fig 5.11. Here, most of the absolute values of $\Delta\dot{\gamma}/\dot{\gamma}$ are under 2%, except for the 45% particle suspension, of which the relative difference decreases then increases following the increase of $\dot{\gamma}$. As well, this is also possible due to the measurement uncertainty.

In addition, at ϕ=45%, the $\Delta\dot{\gamma}/\dot{\gamma}$ of 4.62μm particle suspensions (average $\Delta\dot{\gamma}/\dot{\gamma}$=5.72%) is smaller than that of 41μm particle suspensions.

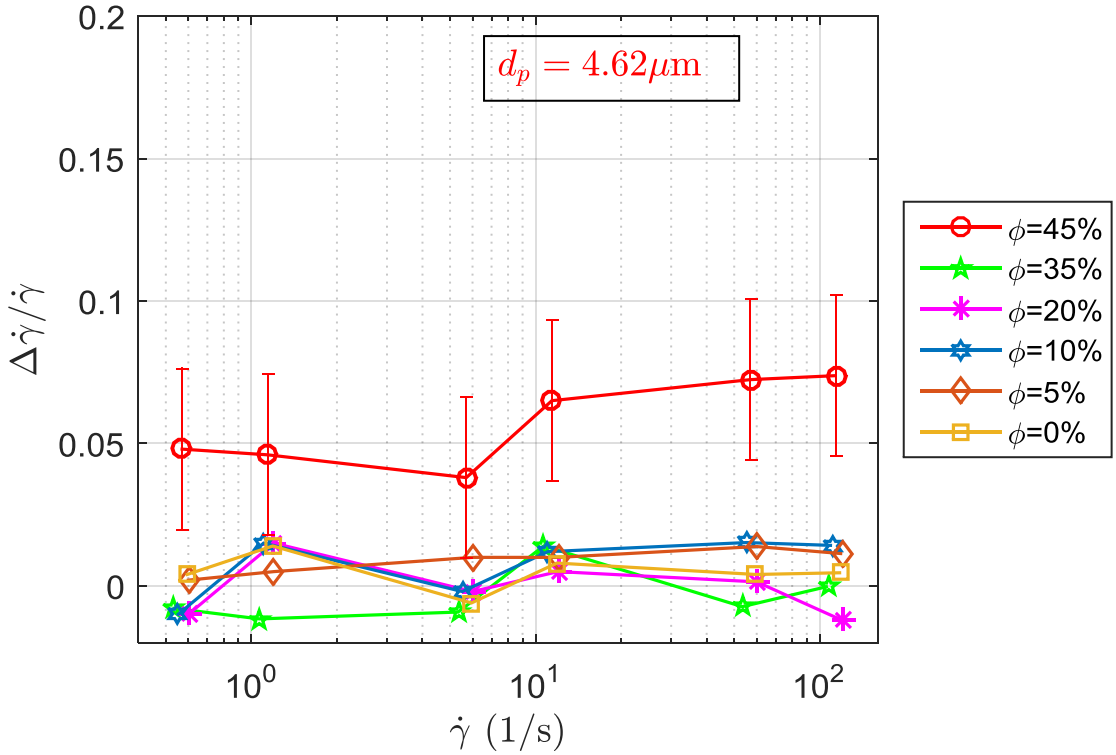

Fig 5.11 Relative differences of shear rates as a function of $\dot{\gamma}$ of 4.62μm particle suspension, the error bars of suspension at ϕ=35%, 20%, 10%, 5% and 0% are not shown.

On the whole, compared to the no slip case, these deviations are abnormal. Considering the cone and the plate surface are smooth, one plausible explanation is wall slip. Although true slip is possible reason, as the fluids in the current experiments are suspensions, the more possible case is apparent slip (Barnes 1995). In the following section, this phenomenon will be analyzed based on the assumption of apparent slip and some simplified conditions.

5.2 Apparent slip

5.2.1 Apparent slip characterization

For dense suspension, the generally accepted mechanism to explain the apparent slip is the depletion of the boundary layer. When the suspended particles migrate away from the wall, then, it will form a thin layer near the wall which is rich of fluid (Sochi 2011). Based on this mechanism, a simplified parallel shear plates model (Fig 5.12 and Fig 5.13) can be used to analyze the apparent wall slip effect in the current experiments. Because the fluid motion induced by this geometry is similar to that of the cone-plate device.

Both they are drag flow geometries, and both the velocity profiles are linear under low fluid velocity. Except that the flow in parallel plates is rectilinear, while the flow in cone-plate is rotational.

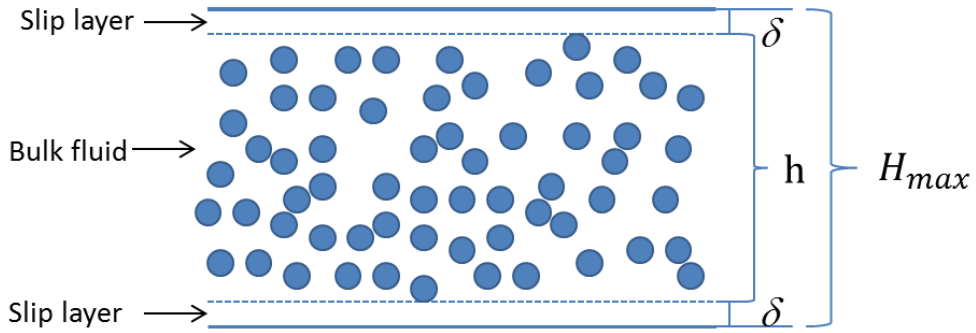

Fig 5.12 Schematic illustration of the slip layer in the parallel shear plates device

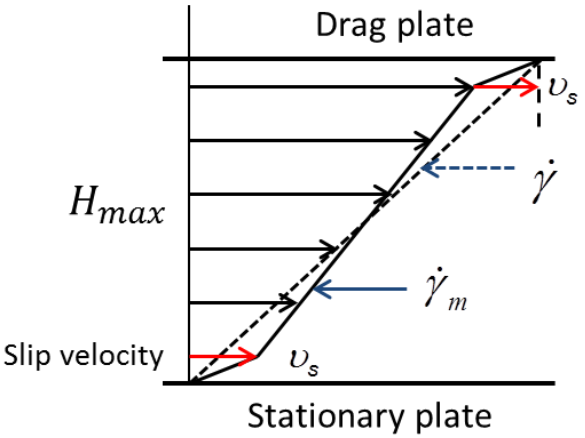

Fig 5.13 Schematic illustration of the velocity profile in the parallel shear plates device with the presence of apparent slip

Here, to simulate the cone-plate device, the bottom plate is supposed to be stationary, and the flow is induced by the movement of the top plate. Assuming that there is an apparent slip in the parallel shear plates device with suspension flow, since most of the deviation from the no slip case is closely symmetric near the top and the bottom surfaces, and considering that all the velocity profiles are linear in the current experiments, two suppositions are made to simplify the parallel shear plates flow model:

a) The top and the bottom plate surfaces are perfectly smooth;
b) The bulk fluid is a density matched homogeneous hard sphere non Brownian suspension, it is incompressible.

Thus, the slip layer thicknesses will be the same near the top surface and the bottom surface. As shown in Fig 5.12, where H_{max} is the gap height, h is the height of the bulk fluid, δ is the slip layer thickness. In addition, the shear rate $\dot{\gamma}_m$ of the bulk fluid is

constant, as shown in Fig 5.13, where $\dot{\gamma}$ is the apparent shear rate (dashed line), which is equal to the shear rate of the no slip case, and v_s is the slip velocity.

In addition, to idealize the slip layer and the bulk fluid, three supplementary suppositions are made:

c) There is no particle in the thin slip layer (Fig 5.12), and the suspending fluid adhere to the wall;
d) The slip layer thickness is constant under steady flow conditions.
e) The viscosity of the bulk fluid does not change following the variation of the time of shearing.

Based on the above 5 conditions, the slip velocity and the slip layer thickness can be deduced by the following group of equations:

$$\begin{cases} h + 2\delta = H_{max} \\ \dot{\gamma}_m \times h + 2v_s = \dot{\gamma} \times H_{max} \\ \dfrac{v_s}{\delta} \times \eta_L = \dot{\gamma}_m \times \eta_s \end{cases} \tag{5.1}$$

Where η_L is the viscosity of the suspending fluid and η_s is the viscosity of the bulk suspension. The third equation is derived from the condition that the shear stress at the interface between the slip layer and the bulk fluid is equal (Yoshimura and Prud'homme 1988). With $\eta_r = \eta_s/\eta_L$ and $\Delta\dot{\gamma} = \dot{\gamma} - \dot{\gamma}_m$, by solving the equations, we obtain:

$$\delta = \frac{\Delta\dot{\gamma} \cdot H_{max} \cdot \eta_L}{2(\eta_s - \eta_L)\dot{\gamma}} = \frac{\Delta\dot{\gamma} \cdot H_{max}}{2(\eta_r - 1)\dot{\gamma}} \tag{5.2}$$

$$v_s = \frac{\Delta\dot{\gamma} \cdot H_{max} \cdot (2\eta_s - \eta_L)}{2(\eta_s - \eta_L)} = \frac{\Delta\dot{\gamma} \cdot H_{max} \cdot (2\eta_r - 1)}{2(\eta_r - 1)} \tag{5.3}$$

According to these two expressions, the difference of shear rates $\Delta\dot{\gamma}$ and the suspension relative viscosity η_r play important roles in determining the slip layer thickness and the slip velocity.

The values of H_{max}, η_r, $\dot{\gamma}_m$ and $\dot{\gamma}$ are already known, the slip layer thicknesses and slip velocities of suspensions are thus calculated according to equation (5.2) and (5.3). Tab 5.1 to Tab 5.3 show the results of 41μm particle suspensions. Tab 5.4 shows the result of 4.62μm particle suspension at ϕ =45%. Since the measurement uncertainty of $\Delta\dot{\gamma}/\dot{\gamma}$ is 2.83%, all the suspensions without $\Delta\dot{\gamma}/\dot{\gamma}$ >2.83% are not calculated here.

$\dot{\gamma}$	$\dot{\gamma}_m$	$\Delta\dot{\gamma}/\dot{\gamma}$	η_r	δ (μm)	v_s (μm/s)	v_s/V_{max}
0.544	0.483	11.16%	44.58	**1.39**	59.1	**11.29%**
1.036	0.873	15.75%	34.72	**2.67**	159.4	**15.22%**
5.438	4.861	10.60%	23.34	**2.56**	567.5	**10.84%**
10.357	9.095	12.19%	21.71	**3.23**	1245.0	**11.89%**
54.375	48.948	9.98%	18.89	**2.98**	5371.9	**10.26%**
103.57	92.476	10.71%	15.90	**3.88**	11042.0	**10.55%**

Tab 5.1 Slip layer thicknesses and slip velocities of 45% 41μm particle suspension with H_{max}=963μm

$\dot{\gamma}$	$\dot{\gamma}_m$	$\Delta\dot{\gamma}/\dot{\gamma}$	η_r	δ (μm)	v_s (μm/s)	v_s/V_{max}
0.501	0.460	8.00%	12.69	**3.89**	43.7	**8.34%**
1.02	0.930	6.96%	10.10	**4.30**	76.9	**7.34%**
5.01	4.638	7.24%	7.11	**6.69**	410.0	**7.83%**
10.2	9.568	4.32%	6.67	**4.17**	492.6	**4.70%**
50.1	47.341	5.32%	6.15	**5.71**	3054.3	**5.83%**
100.2	94.386	5.61%	5.94	**6.30**	6472.7	**6.18%**

Tab 5.2 Slip layer thicknesses and slip velocities of 35% 41μm particle suspension with H_{max}=1046μm

$\dot{\gamma}$	$\dot{\gamma}_m$	$\Delta\dot{\gamma}/\dot{\gamma}$	η_r	δ (μm)	v_s (μm/s)	v_s/V_{max}
0.508	0.458	9.67%	3.00	**27.57**	63.3	**12.09%**
1.015	0.958	5.59%	2.64	**18.59**	76.3	**7.29%**
5.075	4.840	4.62%	2.27	**19.77**	337.9	**6.45%**
10.15	9.556	5.85%	2.17	**27.34**	874.2	**8.35%**
50.75	49.790	1.89%	2.03	**9.68**	1472.7	**2.81%**
101.5	99.400	2.07%	1.99	**11.01**	3446.0	**3.12%**

Tab 5.3 Slip layer thicknesses and slip velocities of 20% 41 μm particle suspension with H_{max}=1032μm

$\dot{\gamma}$	$\dot{\gamma}_m$	$\Delta\dot{\gamma}/\dot{\gamma}$	η_r	δ (μm)	v_s (μm/s)	v_s/V_{max}
0.571	0.543	4.80%	17.47	**1.41**	25.9	**4.95%**
1.141	1.089	4.60%	15.26	**1.55**	49.9	**4.76%**
5.705	5.488	3.80%	14.19	**1.37**	206.6	**3.95%**
11.41	10.668	6.50%	15.53	**2.20**	704.3	**6.73%**
57.05	52.920	7.24%	18.21	**2.08**	3901.9	**7.45%**
114.1	105.679	7.38%	18.84	**2.05**	7946.7	**7.59%**

Tab 5.4 Slip layer thicknesses and slip velocities of 45% 4.62 μm particle suspension with H_{max}=918μm

To compare the v_s values at different velocities (shear rates), they are normalized as v_s/V_{max}, named slip ratio, where $V_{max} = H_{max} \times \dot{\gamma}$. It can be found that the value of v_s/V_{max} is close to that of $\Delta\dot{\gamma}/\dot{\gamma}$ in all these suspensions. This can be explained as follows. Generally, for dense suspension, the relative viscosity $\eta_r \gg 1$, so $2\eta_r - 1 \approx 2(\eta_r - 1)$. As a result, equation (5.3) can be simplified as:

$$v_s = \frac{\Delta\dot{\gamma} \cdot H_{max} \cdot (2\eta_r - 1)}{2(\eta_r - 1)} \approx \Delta\dot{\gamma}\frac{V_{max}}{\dot{\gamma}} \tag{5.4}$$

Furthermore, the slip ratio can be expressed as:

$$\frac{v_s}{V_{max}} \approx \frac{\Delta\dot{\gamma}}{\dot{\gamma}} \tag{5.5}$$

Based on equation (5.5), the variation of slip ratio can be inferred by the variation of $\Delta\dot{\gamma}/\dot{\gamma}$. Thus, when v_s/V_{max} are plotted against $\Delta\dot{\gamma}/\dot{\gamma}$, the points are close to the line with a slope equal to 1(Fig 5.14).

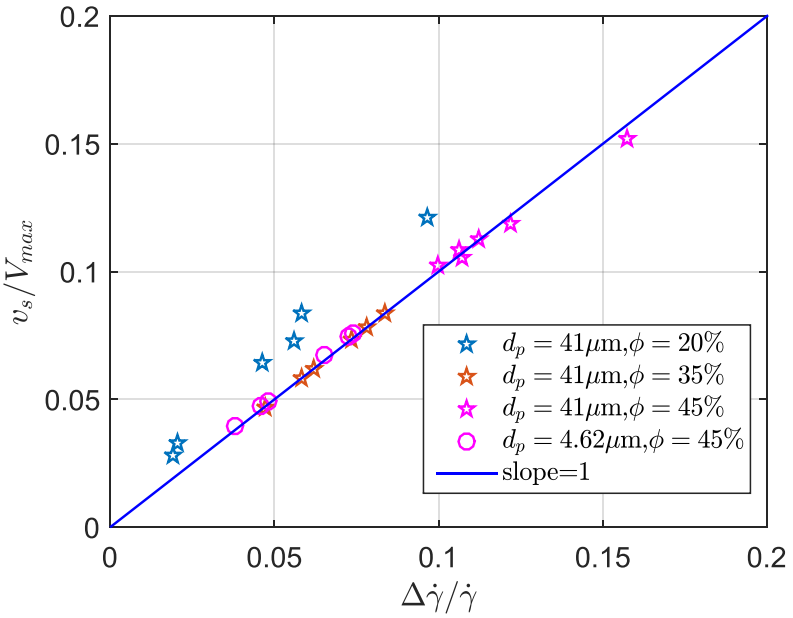

Fig 5.14 v_s/V_{max} with respect to $\Delta\dot{\gamma}/\dot{\gamma}$

Fig 5.15 shows the variation of slip ratio with respect to the shear rate. The slip ratio is bigger at ϕ =45%. For 41μm particle suspensions, at ϕ =20%, 35% and 45%, the average slip ratios are 6.69%, 6.71% and 11.68% respectively.

At ϕ =45%, the slip ratio of 41μm particle suspension is bigger than that of 4.62μm particle suspension (average v_s/V_{max}=5.9%). The variations of v_s/V_{max} with respect to $\dot{\gamma}$ show the same trend as that of $\Delta\dot{\gamma}/\dot{\gamma}$, but this is also possible due to the measurement uncertainty (Appendix E).

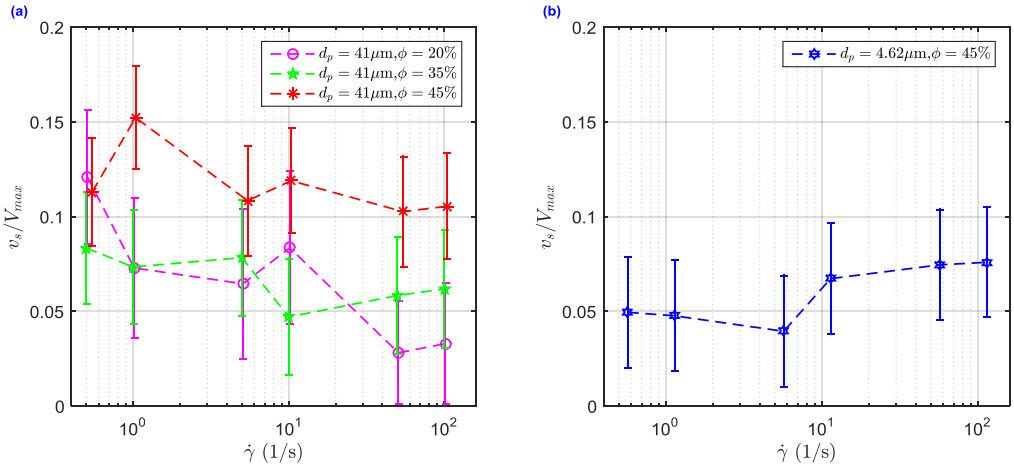

Fig 5.15 Variations of the slip ratios: a) for 41μm particle suspensions at ϕ=45%, 35%, 20%, b) for 4.62μm particle suspensions at ϕ=45%.

Concerning the slip layer thickness, for 41μm particle suspensions, all the δ values are smaller than the diameter of suspended particles (Fig 5.16). At ϕ= 45% and 35%, δ are in the order of microns, and it seems to increase with $\dot{\gamma}$ increasing, for example, at ϕ=45%, with $\dot{\gamma}$ varying from 0.544s^{-1} to 103.57s^{-1}, δ increases from 1.39μm to 3.88μm.

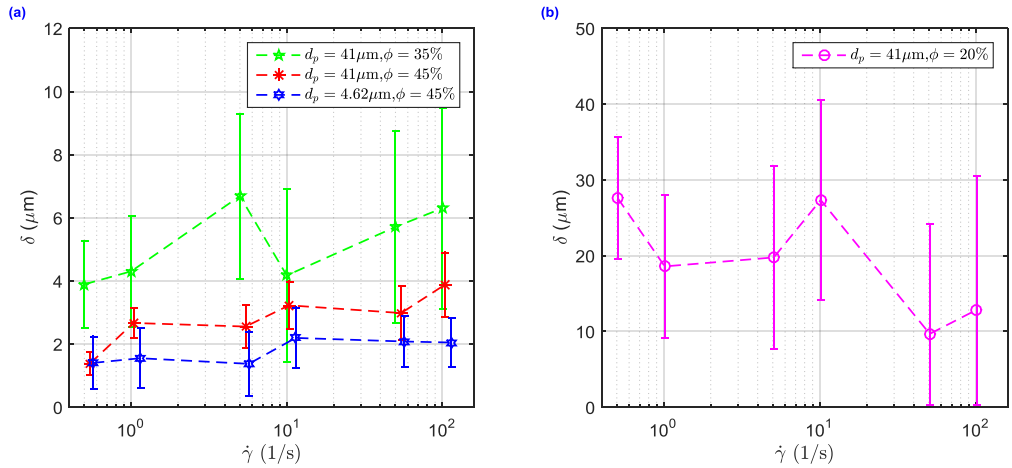

Fig 5.16 Variations of slip layer thickness: a) for 41μm particle suspensions at ϕ=45%, 35% and 4.62μm particle suspensions at ϕ=45%, b) for 41μm particle suspensions at ϕ=20%.

In addition, δ increases with ϕ decreasing, when ϕ =45%, 35% and 20%, the average δ values are 2.78μm, 5.18μm and 18.99μm respectively. However, at ϕ=20%, δ seems to decrease following the increase of shear rate (Fig 5.16-b), it decreases from 27.57μm to 11.01μm, with $\dot{\gamma}$ varying from 0.5s^{-1} to 100s^{-1}.

For 4.62μm particle suspensions at ϕ =45%, the values of δ are also smaller than the diameter of suspended particle. It seems to increase following the increase of $\dot{\gamma}$ (Fig 5.16-a). The average of δ is 1.78μm.

One supplementary point should be mentioned is that the variation of δ values with respect to $\dot{\gamma}$ is possible due to the measurement uncertainty, as they have relatively large error bars (The calculation of uncertainty is shown in appendix E).

5.2.2 Apparent slip discussion

In the following, the above deduced slip velocities and slip layer thicknesses based on the apparent slip assumption are compared to that in other articles.

Slip velocity

According to the calculated results, the normalized slip velocity (slip ratio) increases following the increase of particle concentration, and the slip ratio of big particle (d_p =41μm) suspension is larger than that of small particle (d_p =4.62μm) suspension at the ϕ=45%. This trend is similar to what is described in the article of Gulmus and Yilmazer (2005) with PMMA particles (d_p =83.6μm and 188.2μm) suspensions at ϕ=52.3%, 54.9% and 58.1%, under parallel disks flow; and in the article of Medhi et al. (2011) with PMMA particles (d_p =200μm) suspensions and polystyrene particles (d_p =500μm) suspensions at ϕ = 40%, 45%, 48% and 50%, under channel flow.

Medhi et al. (2011) even found that the slip velocity had a linear relation with respect to the shear rate in their channel flow experiments, which means that the slip ratios are constant at different shear rates. However, the slip ratios in the current measurements are varied. Although this can be due to the measurement uncertainty, it can also be explained by the difference of the measured range of shear rate. Their measurements were performed within very small variation of shear rate (Ex. $\dot{\gamma}$=8s^{-1}, 9s^{-1} and 10s^{-1}), there is little difference on the rheological behavior of the suspension, thus the variation of slip ratio was not evident. Nevertheless, the current experiments had a relatively much larger range of shear rates ($\dot{\gamma}$=0.5s^{-1} to 100s^{-1}), the viscosities varied much at different shear rates, thus the variation of slip ratio can be observed.

Slip layer thickness

The slip layer thicknesses have been estimated using a simplified parallel shear plates model. They are in the order of (or less than) the suspended particle size (r_p). As shown in table (Tab 5.5), for 41μm PMMA particle suspension at ϕ=45%, δ is close to the values of Soltani and Yilmazer (1998) with 45μm PMMA particle suspension at ϕ=63%. For 4.62μm PMMA particle suspension at ϕ=45%, the values of δ are less than half of the particle diameter. Compared with the simulation result of Korhonen et al. (2015) using hard spheres, the deducted values of δ are reasonable.

References	Particle	d_p	ϕ	$\dot{\gamma}$	δ
Soltani and Yilmazer (1998)	PMMA	45μm	63%	0.005s^{-1} to 0.5s^{-1}	1.58 to 1.63μm
Current experiment	PMMA	41μm	45%	0.5s^{-1} to 100s^{-1}	1.39to 3.88μm
Current experiment	PMMA	41μm	35%	0.5s^{-1} to 100s^{-1}	3.89 to 6.69μm
Current experiment	PMMA	41μm	20%	0.5s^{-1} to 100s^{-1}	27.57 to 9.68μm
Korhonen et al. (2015)	Hard sphere	1μm	10%, 20%, 40%, 55%	0.7s^{-1} to 100s^{-1}	<1μm
Current experiment	PMMA	4.62μm	45%	0.5s^{-1} to 100s^{-1}	1.37 to 2.20μm

Tab 5.5 Comparisons of the slip layer thicknesses at different experiments

In addition, for 41μm particle suspensions, the slip layer thickness increases when the particle concentration is reduced. At ϕ=20%, the slip layer thickness shows a tendency to decrease following the increase of $\dot{\gamma}$. All these are similar to the results of Korhonen et al. (2015) by simulation.

However, at other concentrations, δ seems to increase following the increase of $\dot{\gamma}$, although their values are close. This can be explained by the difference in suspension rheological behavior. The suspension of their simulation (Korhonen et al. 2015) is shear-thickening at small to intermediate shear rates.

Nevertheless, in the current experiments, the 41μm particle suspensions are shear-thinning. Since $\dot{\gamma} \approx \dot{\gamma}_m$, equation (5.2) can be rewritten to equation (5.6). According to this, the variation of δ is mainly affected by η_r and $\Delta\dot{\gamma}/\dot{\gamma}$.

$$\delta = \frac{\Delta\dot{\gamma} \cdot H_{max}}{2(\eta_r - 1)\dot{\gamma}_m} \approx \frac{H_{max}}{2(\eta_r - 1)} \times \frac{\Delta\dot{\gamma}}{\dot{\gamma}} \tag{5.6}$$

At ϕ=20%, for 41μm particle suspension, the η_r has little variation at different shear rates, thus the variation of δ follows the variation of $\Delta\dot{\gamma}/\dot{\gamma}$, δ decreases with increasing $\dot{\gamma}$. At ϕ=35%, 45%, η_r decreases following the increase of shear rate due to the shear-thinning effect. With increasing $\dot{\gamma}$, when the decrease percentage of η_r is bigger than that of $\Delta\dot{\gamma}/\dot{\gamma}$, δ will increase. Thus the situation is different.

Based on the same principle, the variation of δ in 45% 4.62μm particle suspension can also be explained, the suspension is shear-thinning followed by shear-thickening (η_r has a large variation) and $\Delta\dot{\gamma}/\dot{\gamma}$ has little variation, thus δ decreases then increases.

Compared with the assumption made by Kalyon (2005) that the slip layer thickness of a given concentration only depends on particle size, the δ in the current experiment varied at different shear rates. Despite the measurement uncertainty, this can also be

due to the difference of suspension rheological behavior. The current suspensions are non-Newtonian, but the suspension in the model of Kalyon is assumed to be Newtonian.

According to the conclusion made by Kok et al.(2004) with colloidal suspensions (d_p=60, 108, 210 and 394nm, ϕ =29%, Pe=0.01 to 100), that apparent slip is significant when the Peclet number is more than unity, and the depletion layer thickness (δ) decreases with increasing Pe. In the current experiments, all the Pe values are larger than unity as shown in Tab 5.6, thus the observed apparent slip agrees with their conclusion. However, the variation of δ is different, in some cases (ex. d_p =41μm, ϕ=45%), δ increases with increasing Pe. In addition, due to the measurement uncertainty, it is not clear whether there is an apparent slip at low particle concentrations. Moreover, the Peclet number does not reflect the influence of particle concentration, thus it is not available to use Pe to differentiate the apparent slip at different particle concentrations.

	$d_p = 41\mu m$	$d_p = 4.62\mu m$
$\dot{\gamma}$(1/s)	Pe	Pe
100	1.65E+08	2.93E+05
50	8.27E+07	1.47E+05
10	1.65E+07	2.93E+04
5	8.27E+06	1.47E+04
1	1.65E+06	2.93E+03
0.5	8.27E+05	1.47E+03

Tab 5.6 Corresponding Pe values of the two sizes of particle at different shear rates

Conclusion

On the whole, based on the assumption of apparent slip and some simplified conditions, the characterization the deviation of dense suspension under the cone-plate device is reasonable to some extent. The deduced slip ratio is more important at high particle concentrations, this agree with the conclusion proposed by other researchers (Gulmus and Yilmazer 2005; Medhi, Ashok, and Singh 2011). The variations with respect to the shear rates are different with that of Medhi et al. (2011), this is possible due to the measurement uncertainty, but this can also be explained by the difference on rheological behavior of the suspensions.

The calculated slip layer thicknesses are in the recognized range (in the order of the suspended particle radius), and the slip layer thickness decrease following the increase of the particle concentration. But the variation following the shear rates remains to be clarified. Some researchers declaimed that the δ decreases with increasing $\dot{\gamma}$ (Kok et al. 2004; Korhonen et al. 2015). The current analysis based on some simplified conditions shows that it may increases or decreases with increasing $\dot{\gamma}$, depending on the values of η_r and $\Delta\dot{\gamma}/\dot{\gamma}$.

Although this can be partly explained by the difference of suspension rheological behavior, to completely determine δ, the value of $\Delta\dot{\gamma}/\dot{\gamma}$ needs to be determined with a better precision. In the current experiments, $\Delta\dot{\gamma}/\dot{\gamma}$ has an uncertainty about ±0.0283, this is a big variation compared to their values (Ex. $\Delta\dot{\gamma}/\dot{\gamma}$=0.08), more data are thus required to clarify their relationship. In addition, the η_r values used for calculation are measured under a cone-plate device. As there is an apparent slip in this geometry, η_r should be bigger than the measured value. Therefore, the calculated δ values have to be corrected.

Moreover, some simplified conditions for the deduction may not be true in reality. For example, the particle concentration in the slip layer is not 0% or the bulk fluid is inhomogeneous. This will influence the calculated results.

The result of the current study gives us an insight on the wall slip effect of dense suspension flow under the cone-plate device. This will help us to identify the region in the fluid where a constant shear rate can be obtained.

For further research, to verify whether it is apparent slip (As it is possible to be a true slip), it is necessary to perform a measurement of the velocity profile or of the local particle concentration in this assumed thin slip layer. However, according to the calculation above, the thicknesses of slip layers are in the order of microns, most of them are thus smaller than the depth of correlation of the actual micro-PIV system (11.2μm). A possible solution is to use a higher magnification objective with an enough long working distance.

5.3 Local particle concentration

The local particle concentration is determined by the calibrated N_{rp} value and the measured particle positions. In the following, the calibrated N_{rp} value is presented. Then, the reliability of the measured particle positions via image processing is studied. Finally, the results of local particle concentration are introduced, and the influence of related parameters is analyzed.

5.3.1 N_{rp} value

To determine the N_{rp} value, fifteen measurements were done with the Hemo-cytometer. The average number of dyed particles found in the cube is about 7.67 with a standard error equal to 2.17.

The particle concentration is ϕ =45%, the cube volume is 894.4×665.6×200μm^3, and d_p=41μm. The total volume of particles in this cube is divided by the volume of one

particle. The number of particles within this cube is obtained, which is 1487. Then, this number is divided by the average number of found dyed particles, 1487/7.67=194, which means that one dyed particle represents 194 particles ($N_{rp} = 194$). The 20% particle suspension was prepared by diluting the 45% particle suspension with the suspending fluid, so N_{rp} held the same.

5.3.2 Particle position determination

The particle position locating program is implemented by four steps: image preprocessing, image segmentation, image calibration and particle position calculation. In the following, the influences of these steps are analyzed and verified step by step.

Image preprocessing

For image preprocessing, Gaussian filter and median filter are used for image smoothing and noise reducing. The filter size should be restricted to a value which is neither too large nor too small which depends on the image. If it is too large, it will modify the original information of the image. If it is too small, it will not arrive to smooth images or to reduce noise. In the current experiments, a Gaussian filter 5×5 and a median filter 3×3 were used, which is the default filter size recommended by the manual of GDPTlab.

Image segmentation

The next process was image segmentation which was implemented by two thresholds: gray-level threshold and minimum area threshold. The influence of these two thresholds can be evaluated through a comparison. A typical image (Fig 5.17) was processed under the same conditions (a Gaussian filter 5×5, a median filter 3×3, and a well calibrated stack of images), but with different threshold values. As shown in Tab 5.7 and Tab 5.8, with the gray-level threshold ranging from 400 to 700, and the minimum area threshold ranging from 2000 to 5000, it is found that the two thresholds act as a discriminator. For example, the test 4 compared to the test 2, when a much higher gray-level threshold is applied, there are two particles unrecognized due to their lower particle image intensities. When a particle can be detected, the variations of the two threshold values have little influence on the detected 3D particle coordinates (<0.1μm).

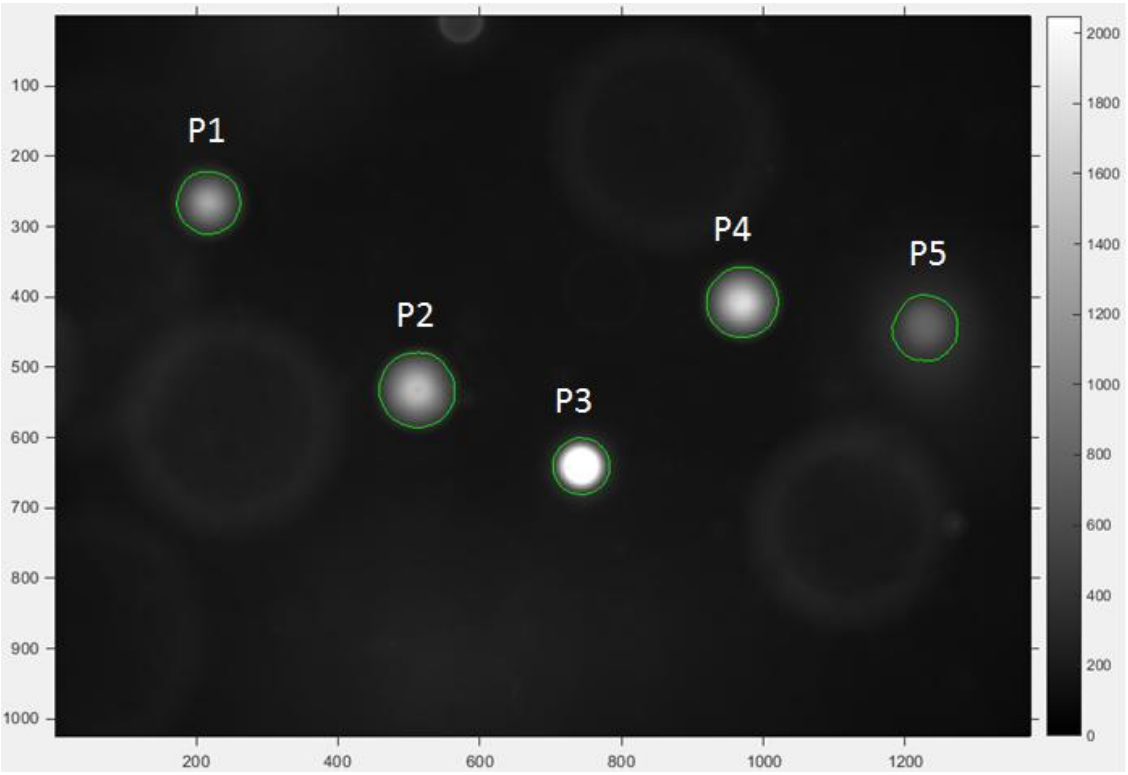

Fig 5.17 An example of identified particle images, where the gray level threshold is 500, and the mini area threshold is 3000. The unit is pixels.

Test	Gray-level Threshold	Minimum area (pixel)	Result
1	400	3000	P1, P2, P3, P4, P5
2	500	3000	P1, P2, P3, P4, P5
3	600	3000	P1, P2, P3, P4, P5
4	700	3000	P2, P3, P4
5	500	2000	P1, P2, P3, P4, P5
6	500	4000	P1, P2, P3, P4, P5
7	500	5000	P2, P4

Tab 5.7 Comparison of detected particles with different gray level thresholds and minimum area thresholds

Particle	X (pixel)	Y (pixel)	Z (μm)	C_m
P1	217.3	265.4	41.6	0.996
P2	511.3	531.6	26.4	0.998
P3	742.7	639.5	92.4	0.998
P4	969.8	407.9	34.6	0.998
P5	1228.8	443.1	21.8	0.959

Tab 5.8 Coordinates and correlation coefficients of detected particles in Fig 5.17, with gray level threshold equal to 500, and the mini area threshold equal to 3000.

Image calibration

The quality of the calibrated stack of images is important, as they are used to construct the calibration matrix for cross correlation. According to the GDPTlab manual, the quality of the calibration can be verified by a correlation curve, an example is shown in

Fig 5.18. If everything is done correctly, the measured Z will equal to the actual Z (black line), and all the C_m values will be close to 1 (small deviation from the black line is acceptable within $0.98 < C_m < 1$). This means that when the calibrated images are cross correlated with the generated calibration matrix, the determined Z positions are approximated to their real Z positions.

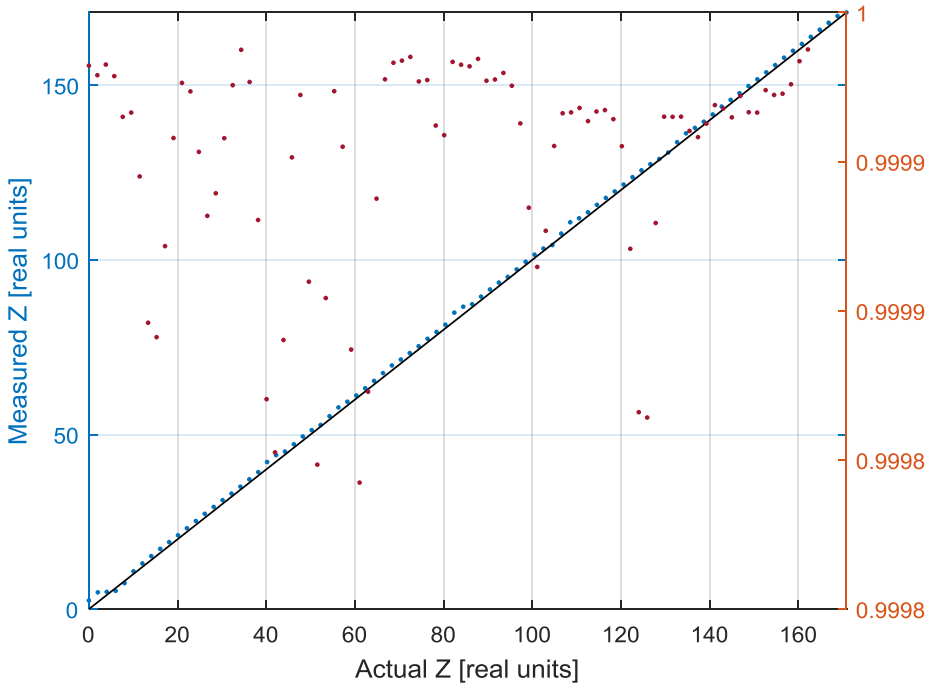

Fig 5.18 The measured Z position (blue, left Y-axis) with the corresponding correlation coefficient (orange, right Y-axis) as a function of the actual *Z* position, here the real unit is μm.

In the current experiments, the adopted calibration was a stack of 87 images, which were taken within 18s. The distance between adjacent images is 2.04μm. As shown in Fig 5.18, all the C_m of the calibrated images are bigger than 0.9998, and the measured Z positions approximate to the actual Z positions (black line), thus it is a calibration with good quality. As this stack of images could already satisfy the request for a considerably large measurement plane width, no more images were taken.

The focal plane position was determined by observing the variation of effective particle image diameter (d_τ). Fig 5.19 shows some calibrated particle images at different Z positions, the image at Z=0 was taken when the distance between the particle and the objective is the furthest.

As the particle image is symmetric, a line with a width of 1 pixel passes the image center can represent the whole information of the particle image. Based on this, Fig 5.20 shows the variation of the image intensity following the increase of image numbers, where

number 1 image corresponds to Z=0. The variation reflects that the particle images at different positions are not the same.

Fig 5.19 Variations of particle image at different Z positions, where the objective is approaching, then leaving the particle, Z=0 corresponds to the image taken at the furthest distance to the objective.

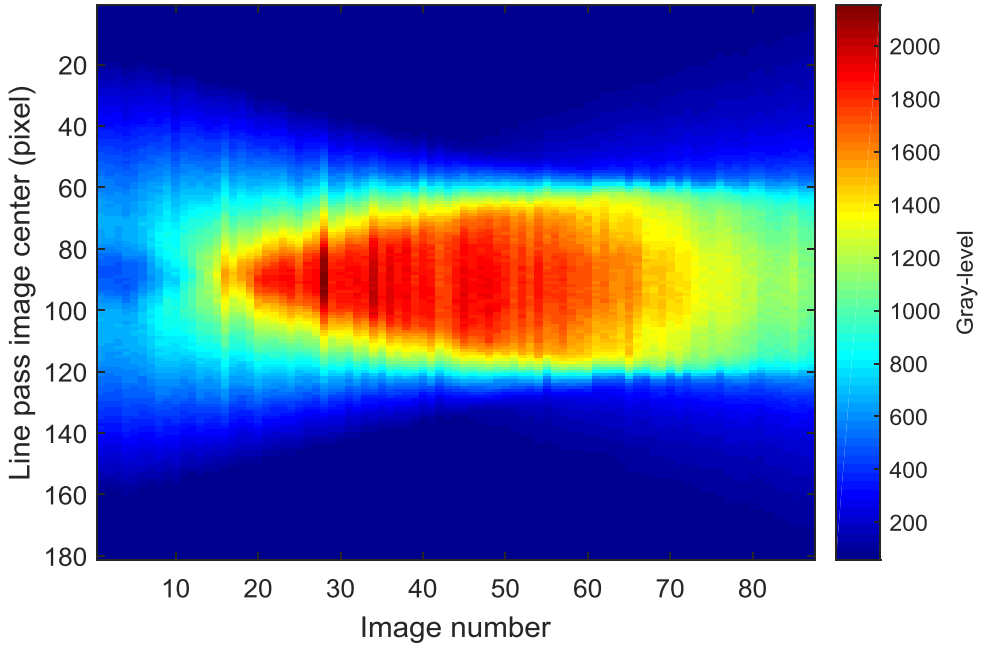

Fig 5.20 Variations of the intensity of the line pass image center following the increase of image number

To determine the focal plane position, the variation of d_τ following the Z position is investigated, as shown in Fig 5.21. It decreases then increases with the objective focal plane approaching and then leaving the particle. Except that at the beginning (Z=0 to 10μm), d_τ has little variation which is due to low image intensity. Thus some of image information is ignored, and d_τ do not increase. Here, the effective particle image diameter at Z=85.7μm is the minimum, where is the focal plane position.

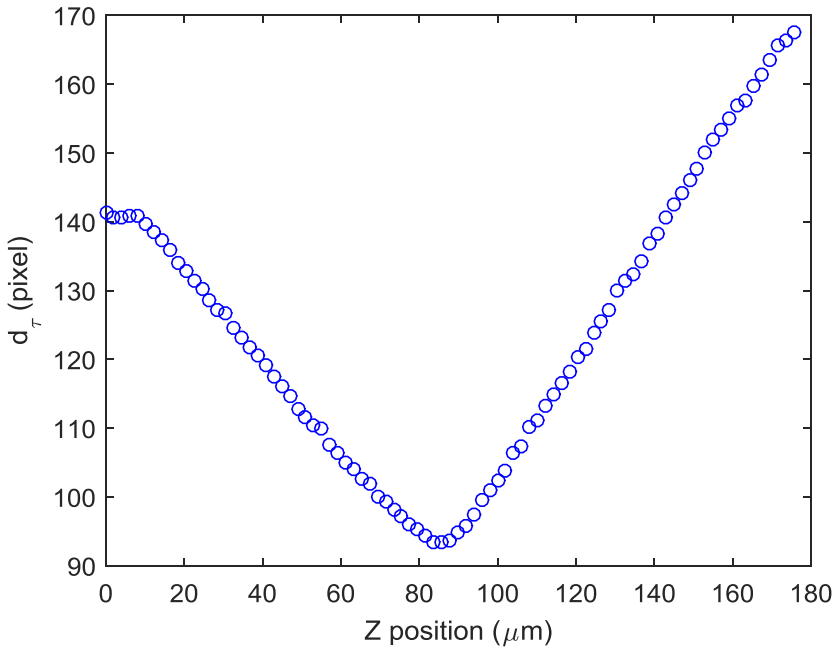

Fig 5.21 Variation of the effective particle diameter (d_τ) with respect to Z position

Particle position calculation

The particle locating program returns the 3D coordinates of detected particles, the reliability of the detected positions can be quantified by the maximum correlation coefficients C_m. Tab 5.9 shows the percentages of detected particles with C_m>0.9 at different conditions (ϕ, $\dot{\gamma}$, H). Most of (>95%) the correlation values are larger than 0.9. Thus the determined particle positions are reliable to some extent.

ϕ =45%			ϕ =20%		
$\dot{\gamma}$ (s^{-1})	H (μm)	Percentage	$\dot{\gamma}$ (s^{-1})	H (μm)	Percentage
50	181	**96,01%**	50	181	**97,65%**
50	496	**95,25%**	50	496	**98,73%**
50	812	**97,79%**	50	812	**98,92%**
1	181	**96,37%**	1	181	**99,16%**
1	496	**93,88%**	1	496	**96,65%**
1	812	**97,36%**	1	812	**98,29%**

Tab 5.9 Percentage of detected particles with C_m value > 0.9

Moreover, the distribution of C_m with respect to Z position was investigated. Fig 5.22 and Fig 5.23 show the distribution of C_m with respect to Z position at 50s^{-1} and at H=181μm, 812μm for the two concentrations of particle suspension respectively. It can be found that in the region around the focal plane (±20μm), almost all the detected particles have a correlation coefficient > 0.9, and most of them have a $C_m > 0.98$. When the distance from the focal plane is larger than about 40μm, lots of the C_m values are smaller than 0.98, which means the reliability is reduced.

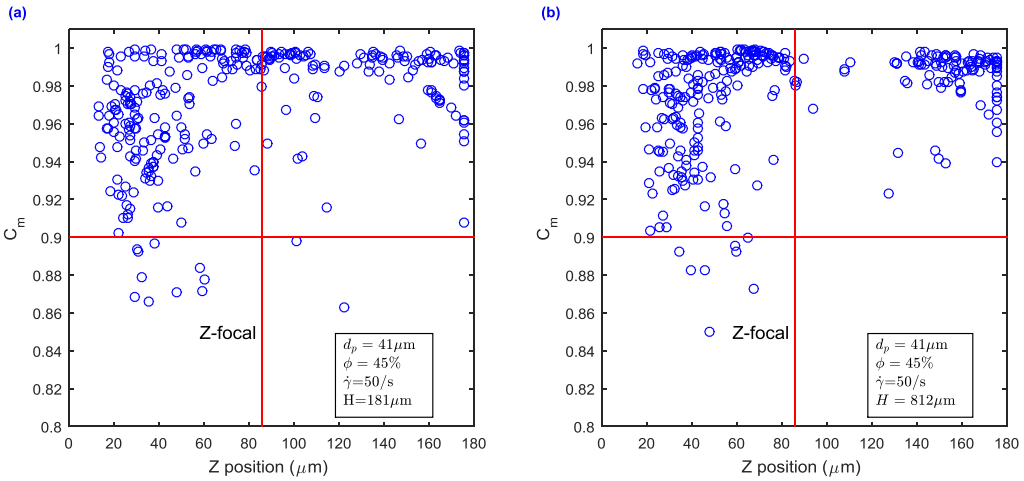

Fig 5.22 C_m values with respect to Z positions in 45% 41μm particle suspension at $50s^{-1}$: a) H=181μm, b) H=812μm

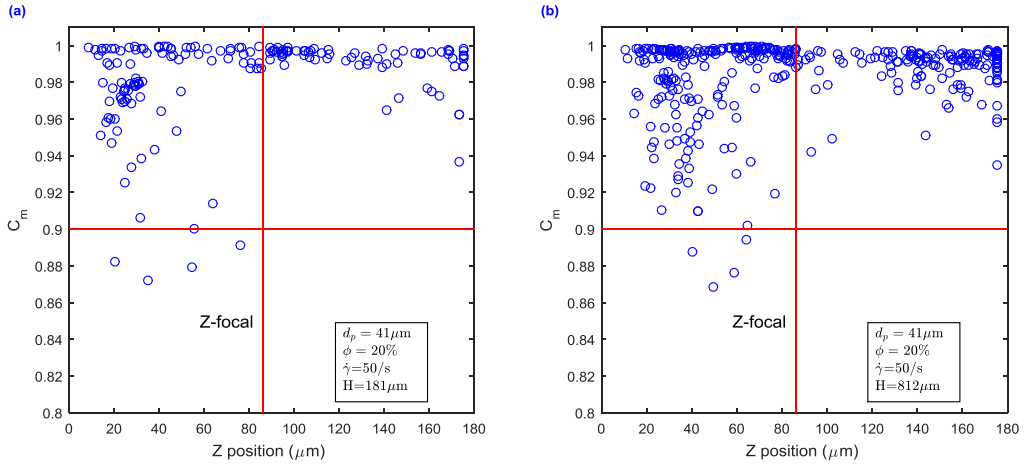

Fig 5.23 C_m values with respect to Z position in 20% 41μm particle suspension at $50s^{-1}$: a) H=181μm, b) H=812μm

Image overlapping

Besides, it is necessary to mention a special case that for overlapped particle images, the normalized cross-correlation method has a poor reliability on the calculated particle Z positions (Barnkob, Kähler, and Rossi 2015). As the particle image patterns are changed due to overlapping, especially when the images are partly overlapped. In the current case, the image window was 1376×1024 pixels, and averagely about 7.67 particles (Section 5.3.1) were located in this region with a depth about 200μm. So, on average each particle occupied an area about 183706 pixels. The maximum d_τ of the calibrated stack of images is about 170 pixels (Fig 5.21), its image area is 22687 pixels. Dividing these two areas, 183706/22687 =8.1, this means that on average, each dyed particle occupies an area about 8 times larger than its particle image. In the 20% particle suspension, the ratio is 17.46. Considering these ratios, even though there still were

some overlapped particle images, their proportion should be small, thus they were not considered in the current analysis.

5.3.3 Local particle concentration calculation

5.3.3.1 Preliminary calculation of local particle concentrations

After the N_{rp} value, the particle positions and the focal plane position were determined, the local particle concentrations (ϕ_{local}) were calculated according to equation (5.7). The region around the focal plane was selected. For a preliminary calculation, the whole image window was set to be the measured area (A). To count at least an entire particle, the measurement plane width was set to be the diameter of a particle (2d=41μm).

$$\phi_{local} = \frac{N_{rp} \times V_{dye}}{N_{im} \times 2\mathrm{d} \times \mathrm{A}} \tag{5.7}$$

The calculated ϕ_{local} values of 45% particle suspension are shown in Tab 5.10. All the ϕ_{local} values are smaller than the initial average particle concentration (ϕ). At 50s^{-1}, the ϕ_{local} at high position (H=812μm) is smaller than that of the low position (H=181μm). However, at 1s^{-1}, it is the contrary. Especially, ϕ_{local} increases from 31.0% to 41.1% at high position, and it decreases from 39.8% to 34.4% at low position.

ϕ(v/v)	$\dot{\gamma}$ (s^{-1})	H (μm)	ϕ_{local} (v/v)
45%	50	181	**39.80%**
45%	50	496	**41.40%**
45%	50	812	**31.00%**
45%	50	**Avrg**	**37.40%**
45%	1	181	**34.40%**
45%	1	496	**40.70%**
45%	1	812	**41.10%**
45%	1	**Avrg**	**38.73%**

Tab 5.10 Estimated local particle concentrations of 45% 41 μm particle suspension

Tab 5.11 shows the calculated ϕ_{local} values of 20% 41 μm particle suspension. Here, both the ϕ_{local} values at high position are bigger than the global concentration ϕ. However, ϕ_{local} values of the rest are smaller than ϕ. Especially, at 1s^{-1}, both the ϕ_{local} at low position and middle (H=496μm) position are only about half of the global concentration ϕ.

ϕ(v/v)	$\dot{\gamma}$ (s^{-1})	H (µm)	ϕ_{local} (v/v)
20%	50	181	**12.20%**
20%	50	496	**19.40%**
20%	50	812	**22.60%**
20%	50	**Avrg**	**18.07%**
20%	1	181	**9.80%**
20%	1	496	**11.20%**
20%	1	812	**27.10%**
20%	1	**Avrg**	**16.03%**

Tab 5.11 Estimated local particle concentrations of 20% 41 µm particle suspension

In general, all the averages of the calculated C_{local} values at the 3 heights are smaller than the initial particle concentration. Thus, the calculation of the local particle concentration should be verified.

Based on equation (5.7), the influence of related parameters can be analyzed. N_{rp} depends on the calibration result, it has a large standard deviation, which will affect much the calculated local particle concentration. V_{dye} depends on the measurement plane area (A), the measurement plane width (2d) and the determined particle positions. A is equal to 1376×1024pixels, for a local particle concentration measurement, it is already sufficiently large compared to the area of a particle image. The reliability of the particle position has been verified in the section above. So putting aside the value of N_{rp}, the parameters which need to be verified are the number of particle images N_{im} and measurement plane width 2d. In the following, the influences of these two parameters are investigated.

5.3.3.2 The influence of N_{im}

Assuming that all the particles are randomly distributed in the region around the measured height, then the influence of the N_{im} value can be verified by observing the variation of ϕ_{local} with respect to N_{im}. An acceptable N_{im} is defined at which ϕ_{local} starts to converge.

Fig 5.24 shows the variations of ϕ_{local} with respect to N_{im} for 45% particle suspension. It is found that following the augmentation of the number of images, the fluctuations of C_{local} become smaller, the variations are controlled to be less than 0.01 after N_{im} >35. Thus, the values of ϕ_{local} converge. The same trend is found in the 20% particle suspension, as shown in Fig 5.25, when N_{im} >70, the variations of ϕ_{local} are in the range ±0.01. This indicates that the current maximum number of images can already offer a

relatively stable measured result, although better precision is expected by taking more images,.

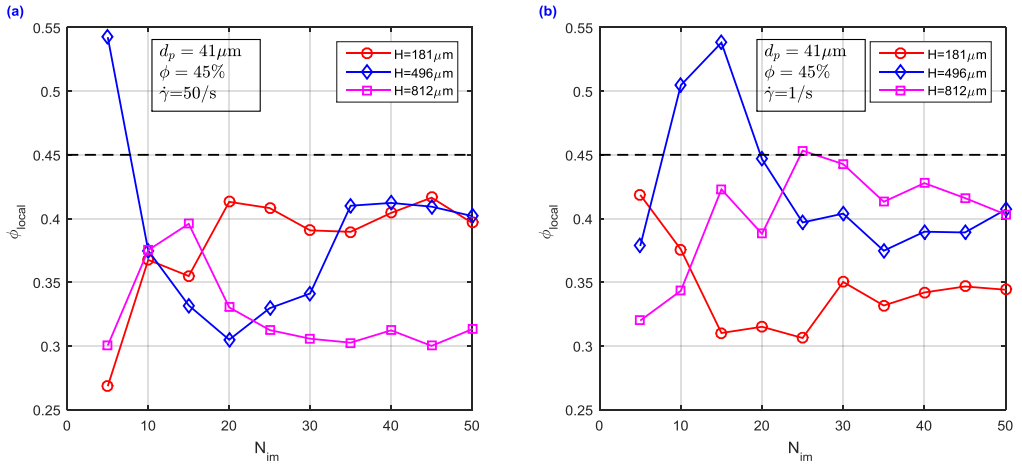

Fig 5.24 Variations of ϕ_{local} following the increase of N_{im} for 45% 41μm particle suspension at different heights and at: a) $\dot{\gamma}$=50s^{-1}, b) $\dot{\gamma}$=1s^{-1}, the black line indicates the global particle concentration.

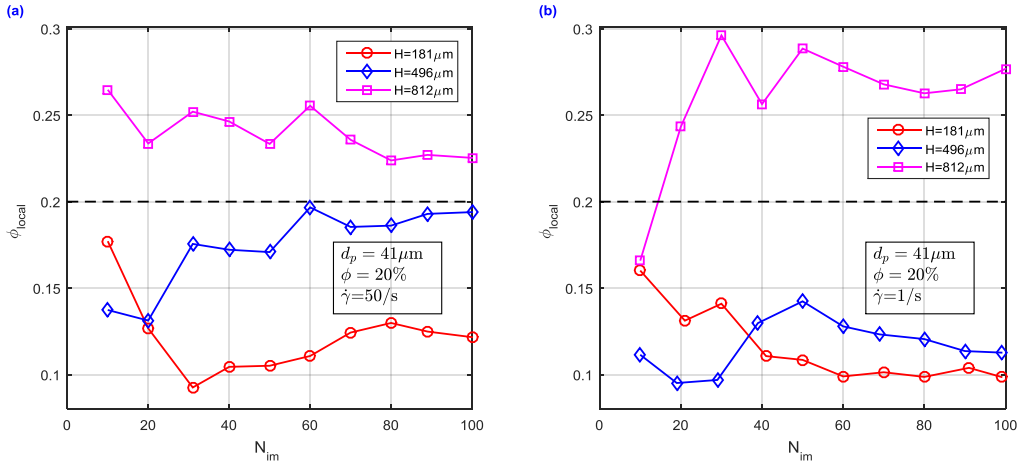

Fig 5.25 Variations of ϕ_{local} following the increase of N_{im} for 20% 41μm particle suspension at different heights and at: a) $\dot{\gamma}$=50s^{-1}, b) $\dot{\gamma}$=1s^{-1}, the black line indicates the global particle concentration.

5.3.3.3 The Influence of the measurement plane width

If all the particles are homogeneously distributed in the local regions, the ϕ_{local} will be stable with the measurement plane width varying a certain value. As have been proved in the section above, a stability of result can be obtained with more images. Thus the analysis here is based on the maximum number of images. The minimum width is the diameter of a particle. To guarantee the reliability of the measurement, the maximum measurement plane width is limited to 85μm, because the correlation coefficients of

particles beyond this distance are relatively lower (<0.98), an example is shown in Fig 5.22.

Fig 5.26 and Fig 5.27 show the variation of ϕ_{local} following the increase of measurement plane width for the two suspensions respectively. In both suspensions, with the measurement plane width varying from 41μm to 85μm, it is found that the variation of ϕ_{local} in the low and the middle positions was small (<0.01). This means that the local distribution of particles is relatively homogeneous in these two positions.

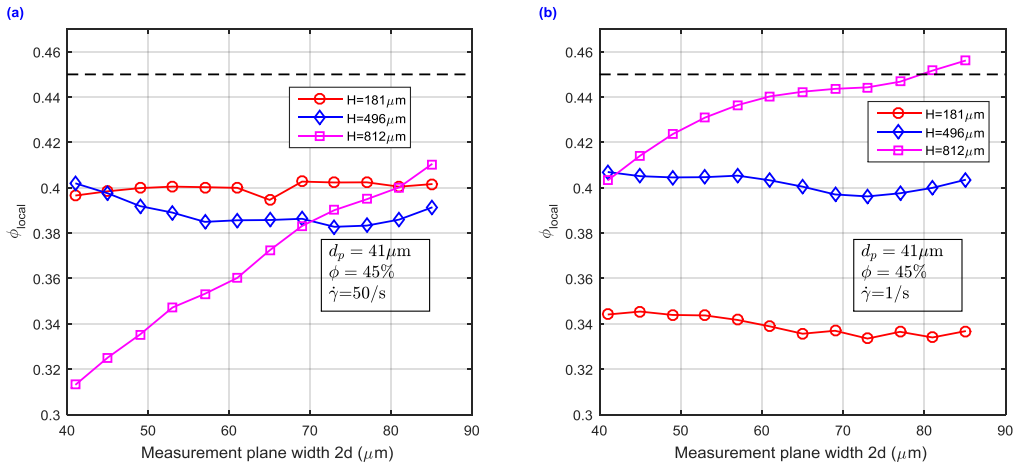

Fig 5.26 Variations of ϕ_{local} following the increase of measurement plane width for 45% 41μm particle suspension at different heights and at: a)$\dot{\gamma}$=50s^{-1}, b) $\dot{\gamma}$=1s^{-1}, the black line indicates the global particle concentration.

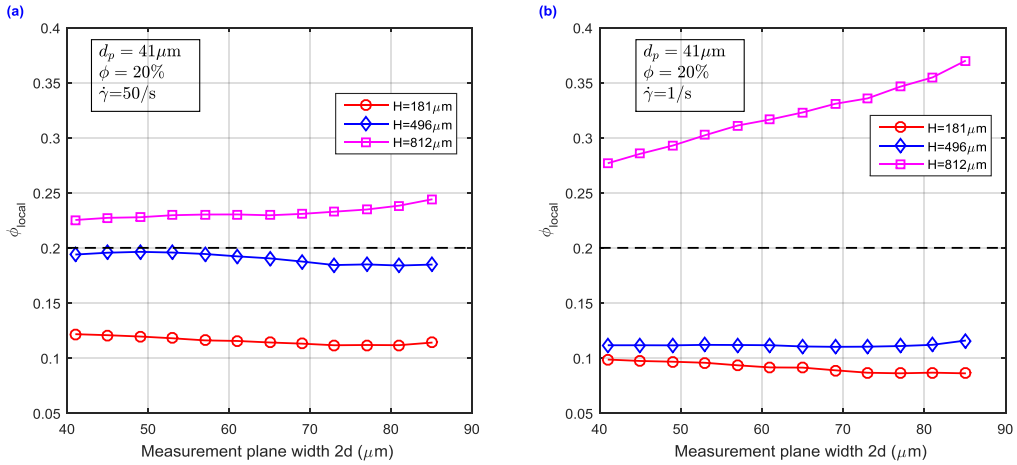

Fig 5.27 Variations of ϕ_{local} following the increase of measurement plane width for 20% 41μm particle suspension at different heights and at: a) $\dot{\gamma}$=50s^{-1}, b) $\dot{\gamma}$=1s^{-1}, the black line indicates the global particle concentration.

However, at high positions, there are noticeable increases of the local particle concentration following the increase of measurement plane width. In 45% particle suspension, at 1s^{-1}, ϕ_{local} increases from 40.2% to 45.7%. At 50s^{-1}, ϕ_{local} increases even

more, it changes from 31.3% to 41.1%. This means that the local particle distribution is inhomogeneous. To verify it, the local distribution of particle Z positions is observed and compared with that of the low position. Fig 5.28 shows the distribution of particle Z positions of 45% particle suspension at the two positions at $50s^{-1}$. It is found that at the low position, the distribution of particle Z positions is more homogeneous around the focal plane than that of the high position. In addition, more particles are detected above the focal plane at the high position.

In 20% particle suspension, the ϕ_{local} of high position at $50s^{-1}$ is relatively stable (from 22.5% to 24.5%). However, it has a larger variation at $1s^{-1}$, which increases from 27.8% to 36.9%. In this case, the distribution of particle Z positions is investigated and compared as well. As shown in Fig 5.29, the distribution around the focal plane at H=812μm is non homogeneous, and more particles are found above the focal plane. A possible reason to explain this inhomogeneous local distribution of particles is the migration of dyed particles. This will be discussed in the section (5.4.1).

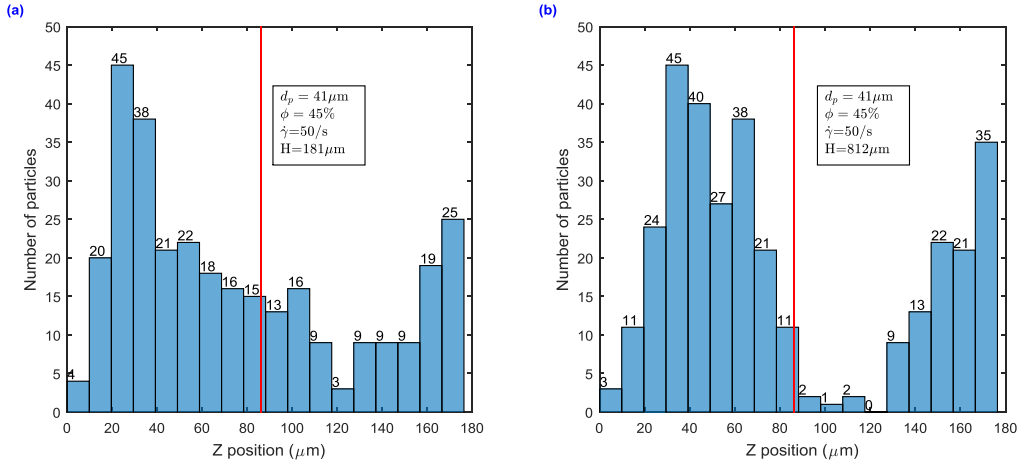

Fig 5.28 Comparison of the particle Z position distributions of 45% 41μm particle suspension at $50s^{-1}$ and at: a) H=181μm, b) H=812μm, the red line indicates the focal plane position.

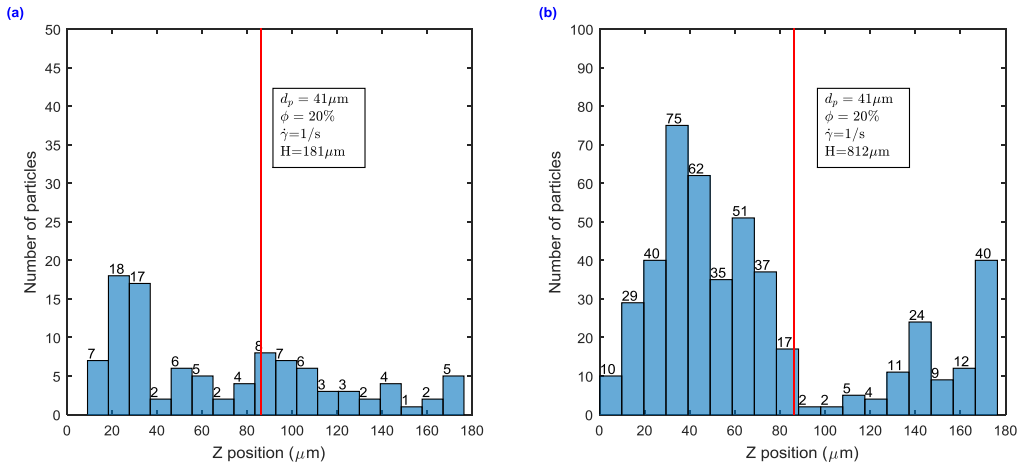

Fig 5.29 Comparison of the particle Z position distributions of 20% 41um particle suspension at $1s^{-1}$ and at: a) H=181μm, b) H=812μm, the red line indicates the focal plane position.

Comparison of ϕ_{local} at different heights

For the 45% particle suspension, at $50s^{-1}$, the values of ϕ_{local} at different heights are close, except that at high position, the ϕ_{local} shows a big variation following the increase of the measurement plane width. At $1s^{-1}$, the values of ϕ_{local} differentiate, the ϕ_{local} of high position is even higher. The ϕ_{local} of the middle position has little change. The ϕ_{local} of the low position is noticeably reduced compared to the that at $50s^{-1}$ (from 40% to 34%).

For the 20% particle suspension, at $50s^{-1}$, the values of ϕ_{local} at different heights already show a big difference, the values of ϕ_{local} are much higher at high and middle positions; and following the increase of the measurement plane width, the ϕ_{local} of high position increases, however that of other two positions decrease. At $1s^{-1}$, the difference between the ϕ_{local} of high position with that of the other two position is even higher; and the ϕ_{local} of high position continues to increase following the increase of the measurement plane width, that of other two position have little variation, they seem to be stabilized.

5.4 Discussion

5.4.1 Particle migration

According to the measurement result, in most of the case, the local particle concentrations in low position are smaller, and that of high positions are higher. In addition, the local particle concentrations at high position increase following the increase of the measurement plane width. One possible reason for these behaviors is the buoyancy effect of particles. Therefore the float velocity of particle should be calculated. The maximum float (or sedimentation) velocity (assuming only one particle exists in the suspension) can be estimated by the Stokes' law, as shown in the equation below

$$V_{\infty} = \frac{1}{18}\frac{(\rho_p - \rho_L)gd_p^2}{\eta_L} \tag{5.8}$$

Where V_{∞} is the sedimentation velocity, ρ_p is the particle density, ρ_L is the liquid density, d_p is particle diameter, η_L is the liquid dynamic viscosity, g is the gravitational acceleration.

For suspension with mono-dispersed spheres, since interactions between particles happen, the particle volume fraction has an influence in the float (or sedimentation) velocity. According to the deduction and experimental work of Richardson and Zaki

(1954), the float (or sedimentation) velocity of particle in a suspension can be expressed as:

$$V_{fs} = V_{\infty}(1-\phi)^{4.65} \tag{5.9}$$

In the current experiments, ρ_p=1.1878±0.0012g/ml, ρ_L=1.187±0.001g/ml, d_p=41μm. Assuming that the difference of density is 0.001g/ml, the corresponding float (or sedimentation) velocities are calculated, as shown in Tab 5.12. At concentration of 45%, the float velocity is about 4.9μm/h, it is very slow. However, if considering the float velocity within the pure suspending fluid, it is a little bigger (78.4μm/h). When the difference of density increase to the maximum Δρ=0.0016g/ml, the corresponding float velocity is 125.4μm/h.

d_p (μm)	ϕ(v/v)	Δρ (g/ml)	η_L (Pa.s)	V_{fs} (μm/h)
41	0%	0.001	0.042	78.4
41	20%	0.001	0.042	27.8
41	35%	0.001	0.042	10.6
41	45%	0.001	0.042	4.9

Tab 5.12 Float (or sedimentation) velocity of particle 41 μm within different suspensions

Generally, at each shear rate, the measurement at 3 heights lasts on average 8 minutes. Between this time interval, particles will float up about 17μm with the above calculated maximum float velocity. Thus, the local particle distribution is changed. This can explain why few dyed particles were found below the focal plane at high positions. Because initial dyed particles at high positions floated up, and those from low positions were prevented by non-dyed particles, they were not able to reach this height. One example is the 45% particle suspension, at 50s^{-1} and 812 μm, few particles were found below the focal plane (Fig 5.28-b).

According to the particle floating explanation, as the measurement at 1s^{-1} is undertaken after that of 50s^{-1} with the same suspension, the differences of ϕ_{local} between high position with that of the other two positions are thus much higher at 1s^{-1}. Due to the accumulation of the floated particles at high positions, there is thus an increase of the local particle concentration with the increasing measurement plane width at higher position. In the case of 45% particle suspension, at 50s^{-1} and 812 μm, at small measurement plane width, the ϕ_{local} is much smaller than that of the other two positions (Fig 5.26-a). Except for the float of particles in the local region, this is possibly due to the inhomogeneous distribution of the dyed particles at the initial moment.

However, with this float velocity, it was not possible for particles to migrate about hundreds of microns within the experiment time. So a further explanation is needed to

explain the much higher ϕ_{local} at high position for 20% particle suspension. Especially, at 50s^{-1}, the ϕ_{local} at high position is already about twice as that of low position (Fig 5.27), and at 1s^{-1}, with a measurement width equal to 85μm, ϕ_{local} at high position is more than three times as that of low position (Fig 5.27).

In addition, one thing should be mentioned as follows. At the beginning, the density of the suspending fluid was 1.187g/ml (ρ_p =1.1878 g/ml), which was lower than the particle density. However, in the current experiments, particles were lighter than the suspending fluid. Possible reasons are water evaporation or the aging effect of suspending fluid, which change the density of the suspending fluid. But this did not happen in the experiments. If there was water evaporation or aging effect, then the suspending fluid refractive index should be changed and images taken at high positions would become blurring. However, the images taken at high positions are still clear.

To make sure whether there was a large float velocity, a measurement was performed directly within the suspension. A drop of 10% particle suspension was put on the plate. The movement of the dyed particles under gravitational force was observed. Multi measurements were performed, but the results were different. For example, in a measurement, after 31minutes, the dyed particles floated up about 43.6μm, so the corresponding sedimentation velocity was 84.4μm/h, this was normal compared with the estimated value. However, in another measurement, after 32 minutes, the dyed particles floated up about 563.9μm (or even more), so the corresponding velocity was 1057μm/h. It was much bigger, if this was due to the difference of density, Δρ would be 0.0135 g/ml, which was ten times as that of the estimated (0.0012g/ml). But this was not true for other dyed particles. After a long time (more than 1 h), there were still some dyed particles staying stable in the suspension with little displacement (<20μm). This means that the suspension density was in the range of particle density (1.1866-1.189g/ml).

So maybe there are other reasons for the buoyancy of particles. A possible reason is the electric force, the material of the cone is aluminum which is electric conductible. The fluid is also electric conductible (PBS is conductible), but the plate is on plexiglass which is insulating. If the cone and PMMA particles are charged, it will be possible for particles to move close to the cone surface when the sedimentation force is smaller. Another possible cause is that the fluorescent dye has already changed the physical property of dyed particles (Isa et al. 2010). For example, the density of dyed particles is changed, they are lighter than other particles, and thus they float up to the top. At concentration 45%, the particle concentration is high, they are not easy to move, thus there is not a big difference between the local particle concentrations at different heights. However, at

concentration 20%, the dyed particles are easier to move, so the local particle concentration at 812μm can increase to about 3 times that of 181 μm. Also, due to this reason, the ϕ_{local} in the middle position of the 45% particle suspension did not change much between the two different shear rate, while that of the 20% particle suspension is noticeable reduced (Fig 5.27).

To estimate the distance between particles in the suspensions, each particle is supposed to occupy a cubic volume and the distance between the adjacent two particles is equal. Thus the distance between the centers of two particles can be estimated as the length of the side of the cube, which is $d_p \times \sqrt[3]{\pi/6 \times \phi}$. For 20% particle suspension, the estimated distance is about 56.4μm, and for 45% particle suspension, the estimated distance is about 43μm, which is much closer.

Concerning the shear induced particle migration effect; contradictory conclusions were reported within cone-plate device. As described in the review of Denn and Morris (2014): "The situation in cone-and-plate devices, where the shear rate is (presumably) uniform, is less clear: Chow et al. (1995) reported that particles migrate radially outward, whereas Fall et al. (2013) found that there is no migration in a cone-plate device". In the current experiments, the measurement of particle concentration was undertaken following the vertical direction. For particle migration in the vertical direction, the main cause is more probably due to density mismatch or electrical force. However, the above reported shear-induced particle migration is in the radial direction, thus no further comparison is made.

5.4.2 The influence on velocity profile measurement

Since the deviation of velocity profile was found in experiments (Section 5.2), it is natural to relate this phenomenon with the particle concentration distribution. Buoyancy or sedimentation forces can be considered as a reason for the deviation of velocity profile. One example is shown in the article of Korhonen et al. (2015), they simulated the apparent slip of non-Brownian suspension in a Couette cell under sedimentation forces.

In addition, if there was a particle concentration gradient in the height, the assumption for the analysis of the deviation of velocity profile should be changed, the bulk fluid would be inhomogeneous, and since particle floated, the slip layer thickness near the bottom and the top surface should be different.

In order to verify the possible influence of particle floating, a test with 41 μm particle suspension at concentration of 20% was performed. Since it is easier for particles to

float at this concentration, the effect will be more obvious if there is. In addition, because there was re-suspension effect of particles at high shear rates (Tripathi and Acrivos 1999), the measurement was performed at a lower shear rate. Here, the suspension was sheared at $5s^{-1}$ for a long time without stopping. The velocity profiles at different time (10h22, 14h10 and 17h43) were obtained, as shown in Fig 5.30. It is found that there is little difference on the velocity profiles measured at different time. The relative difference of shear rates are 5.4%, 4.9% and 7.2% respectively, the differences between the measured shear rates are under the range of the measurement uncertainty (2.83%). In addition, the slip occurred in both surfaces in all the cases.

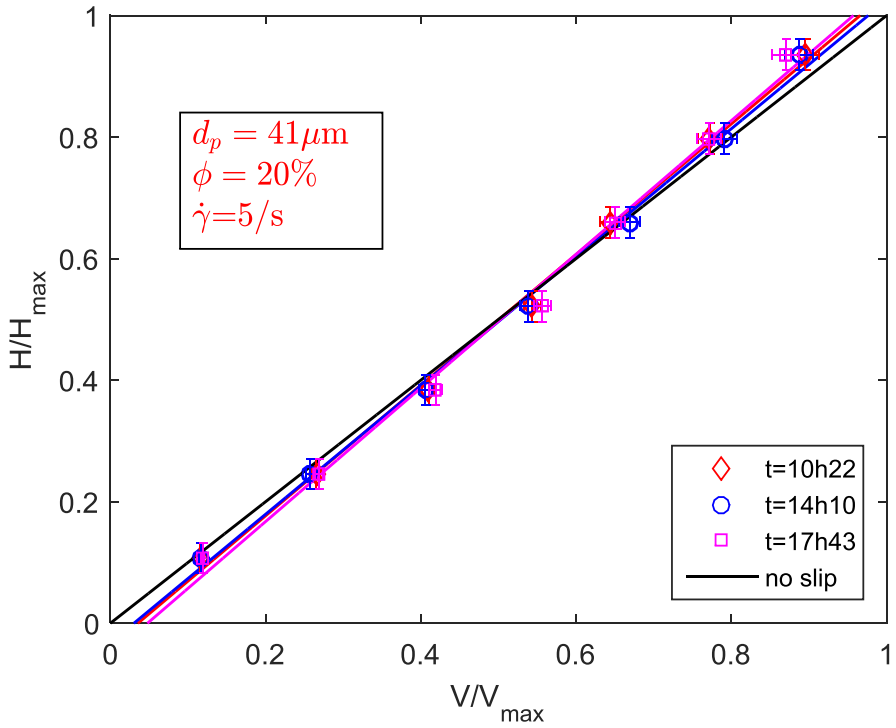

Fig 5.30 Normalized velocity profiles of 20% 41µm particle suspension at 5s-1, measured at different time

Thereby, this comparison demonstrates that the influence of the buoyancy of the particles on the deviation of velocity profile is under the measurement uncertainty, even with a long experiment time. Probably, only the dyed particle floated up, thus the suspension was still homogeneous. This can explain why the measured velocity profile is still linear and the deviation is closely symmetric in both surfaces, although there is a big difference of the measured local particle concentration at different height. Because the density of the dyed particle is different with that of other particles, they cannot represent other particles. Another possible explanation is that although there is a gradient of particle concentration, it is not large enough to have a noticeable impact on the measured velocity profile.

Moreover, for 41μm particle suspensions, if we want the float (or sedimentation) velocity to be smaller than 8μm/h (one tenth of the above estimated sedimentation velocity), the difference of density should be smaller than 0.0001kg/cm^3. However, it is too difficult to prepare such kind of suspensions. For example, in the experiment of Wiederseiner et al. (2010), they prepared a suspension with density difference about 0.0005 g/ml, which is the closest density matched suspension. In their experiment, particle size is 180-200 μm, the fluid dynamic viscosity is 0.124±0.0025Pa.s, and the mixture density is about 1.184±0.0005g/ml. If taking d_p =190μm, η =0.124Pa.s, Δρ=0.0005g/ml, the corresponding sedimentation velocity will be 285.3 μm/h. This is already bigger than the estimated maximum sedimentation velocity in the current experiment. In addition, to prepare such a suspension, firstly one has to make sure that the density difference between particles is smaller than 0.0001kg/cm^3.

For 4.62μm particle suspensions, according to equation (5.8), the maximum float (or sedimentation) velocity was 0.8μm/h with a density difference about 0.001g/ml. This means that particles will float about 0.8 μm within an hour. Compared to the deduced slip layer thickness, it is much smaller. Considering the shorter experiment time for velocity profile measurement (about 20 minutes at each shear rate) and the re-suspension effect of particle at higher velocity, the influence of sedimentation on the apparent slip is thus negligible for 4.62μm particle suspensions.

6 Conclusion and perspective

In conclusion, in the current study, 4 tasks have been achieved:

1) Density and refractive index matched suspension

A new recipe for density and refractive index matched suspension with PMMA particles was developed, which consist of PBS, glycerol and TDE. All these products are low hazard for human body, and they are compatible with plastics (e.g. Acrylic, polycarbonate, PVC) and glass. In addition, either by fine tuning of the proportion of the ternary mixture or by adjusting the temperature, the suspension can achieve a better matched precision. With these characteristics, the recipe is accessible and applicable for wide use.

The rheological properties of PMMA particle suspensions were characterized. Shear-thinning effect was found in 41μm particle suspensions at at ϕ= 45%, 35% and 20%, and shear-thinning followed by continuous shear-thickening effect was found in 4.62μm particle suspensions at ϕ= 45% and 35%. Below these concentrations, the suspensions are Newtonian.

2) Experimental set-up

A cone-plate device was installed in order to obtain a constant shear flow. A stepper motor equipped with a reducer was used in order to generate a stable movement of the cone within a large range of rotational speeds. A micro-PIV system was installed for the measurement of velocity fields. In addition, by using a cover, an aluminum plane and temperature control module the environmental temperature can be well controlled, and by using foam cushion, and the vibration the system is isolated and reduced.

A measurement with the pure suspending fluid was undertaken, to make sure that no secondary flow occurred in the cone-plate device within the established rotational speed. Therefore, the experimental set-up was validated.

3) Measurement of the velocity profiles

The velocity profiles of the two sizes of particle suspensions at ϕ= 0%, 5%, 10%, 20%, 35% and 45% under the cone-plate device were measured. Deviation of the velocity profile from that of the no-slip case was found in dense suspensions, which are 41μm particle suspensions at ϕ=45%, 35% and 20%, and 4.62μm particle suspension at ϕ=45%. The deviation of velocity profiles was assumed to be apparent slip.

Later, based on the general accepted mechanism for apparent slip (depletion of boundary layer) and some simplified conditions, the assumed apparent slip of dense suspension flow between the cone-plate gaps was characterized. The slip ratio increased following the increase of particle concentration and the increase of particle size. The slip layer thickness increased following the decrease of the particle concentration and the increase of particle size. These variations agree with what is described in other articles. However, the variations with respect to the shear rate is different with these articles, the slip ratios are varied at different shear rates, the slip layer thickness is increased or decreased following the increase of the shear rate. These variations can partly be due to the measurement uncertainty, but this can also be explained by the differences in the rheological behaviors of the suspensions.

Although it remains to be verified whether it is apparent slip, the current measurement can already help us to identify the region in the flow where a constant shear rate can be obtained.

4) Measurement of the locale particle concentrations

By using some dyed particles as representatives and by determining the dyed particle position related to the focal plan in a series of images, the local particle concentration can therefore be evaluated. The particle positions were obtained through image processing with the GDPTlab tool, which is based on a normalized cross-correlation between the image to be processed and a stack of calibrated particle images. By observing the influence of related parameters for the calculation of local particle concentration, the method is proved to be feasible, except the consideration of image overlapping. Therefore, to measure the local particle concentration, the fraction of dyed particle should be well controlled for the purpose of reducing image overlapping. If not, the program should be improved to have the ability for the detection of particle with image overlapping.

According to the measured result, dyed particles exhibited a trend to float up. The migration of dyed particles was possible due to the change of the particle density or due to the electrical force in the suspension. This remains to be verified in future research.

Perspective

For future research, the refractive and density matched suspension can be applied to observe the dense suspension flow under more complex flow geometries, such as capillaries and bifurcations.

To confirm whether it is apparent slip, a measurement of the velocity or the particle concentration in the assumed slip layer is required. If it is, the correlation between apparent wall slip and suspension rheological property can further be explored, in order to clarify the relationship of the slip ratio and the slip layer thickness with respect to the shear rate.

The local particle concentration measurement method is applicable in steady flow conditions. However, this method is not viable in non-steady flow, as it is based on statistically counting the local dyed particles. If the flow situation is changed within a short duration of time, the images taken at different time will not represent the same situation, thus the statistical method is not applicable any more.

To observe the local particle concentration at different distance to the cone axis in the cone-plate device, the whole device can be installed on a plane which is movable in one direction of the x-y plane.

To overcome the problem of image overlapping, the circle Hough transforms can be used to detect the 2D position of overlapped particle image. But to determine their Z positions, this is still a difficulty. Some researchers have tried to use multi-pass tracking to resolve this problem (Jaqaman et al. 2008; Gao and Kilfoil 2009). The method is implemented as follows: once a particle is successfully located, its images at different Z positions will be removed from the raw data, thus the overlapping is reduced; then another pass is performed, through several iterations, most of the particles can be detected. In the current cases, all the images are taken in a plane at the same height. If there is image overlapping, it is not possible to find an image at a different height where one of the overlapped particle images is separated with the others, so this method is not applicable, better methods are required.

Although some suspensions have a concentration of 45%, and the particle has a volume equivalent to a red blood cell, the rheology of the suspension is different from that of real blood. As mentioned before, using real blood for in vitro experiments present many drawbacks. Therefore, for future research, two ways of fabricating particles which are similar to red blood cells are considered :

- extracting hemoglobin within the red blood cells in order to obtain so called red blood cell ghosts
- using micro fluidic devices in order to synthetize or fabricate deformable micro particles. This second approach has already started in collaboration with laboratory Centre inter-disciplinary of Nano-sciences of Marseille (CINaM).

In the end, it should be noted that although there remains an analogy problem with the rheology of blood, the current suspensions should not be a problem for the work concerning the validation of the ultrasonic model and method.

Appendix A Equations of motion for cone-plate flow

The following deduction of the solution of Navier-Stokes equations for cone-plate flow with a Newtonian incompressible fluid is according to the work of Sdougos et al.(1983).

In a cylindrical coordinates, u, v, w respectively designates the velocity in the radial, tangential and the vertical direction. As the cone angle is smaller than $0.035(\alpha = 2°)$, ratio of velocity in the vertical direction (w) to the radial velocity (u) will be of the order of the cone angle (α):

$$\frac{w}{u} \approx \alpha \ll 1 \tag{A.1}$$

Similarly the velocity gradient in the vertical-direction is larger than that of the radial direction. The flow is rotationally symmetric about the cone axis, so all the θ-direction gradient are zero. Thus,

$$\frac{\partial}{\partial r} \ll \frac{\partial}{\partial z}, w \ll u \; and \; v, \frac{\partial}{\partial \theta} = 0 \tag{A.2}$$

With these simplifications, the Navier-Stokes equations can be written as follows:

$$\mathrm{r-momentum:} -\frac{\mathrm{v}^2}{\mathrm{r}} = -\frac{1}{\rho}\frac{\partial \mathrm{p}}{\partial \mathrm{r}} + \frac{\eta}{\rho}\frac{\partial^2 \mathrm{u}}{\partial \mathrm{z}^2} \tag{A.3}$$

$$\theta-\mathrm{momentum:}\, \mathrm{u}\frac{\partial \mathrm{u}}{\partial \mathrm{r}} + \frac{\mathrm{uv}}{\mathrm{r}} + \mathrm{w}\frac{\partial \mathrm{v}}{\partial \mathrm{z}} = \frac{\eta}{\rho}\frac{\partial^2 \mathrm{v}}{\partial \mathrm{z}^2} \tag{A.4}$$

$$\mathrm{z-momentum:}\, 0 = -\frac{1}{\rho}\frac{\partial \mathrm{p}}{\partial \mathrm{z}} + \frac{\eta}{\rho}\frac{\partial^2 \mathrm{w}}{\partial \mathrm{z}^2} \tag{A.5}$$

$$\mathrm{continuity:}\, \frac{\partial \mathrm{u}}{\partial \mathrm{r}} + \frac{\mathrm{u}}{\mathrm{r}} + \frac{\partial \mathrm{w}}{\partial \mathrm{z}} = 0 \tag{A.6}$$

The boundary conditions that no slip happens at the cone and the plate surfaces can be expressed as follows (for $\alpha \ll 1$):

$$\left.\begin{array}{ll} u = v = w = 0, & (z = 0) \\ u = w = 0, v = r\omega, & (z = r\alpha) \end{array}\right\} \tag{A.7}$$

To solve the equation of motion, the following transformation of variables is performed:

$$\tilde{v} = \frac{v}{\omega r}, \tilde{u} = \frac{u}{\omega r}, \tilde{w} = \frac{w}{\alpha\omega r}, \tilde{z} = \frac{z}{r\alpha}, \tilde{r} = r \tag{A.8}$$

The three velocity components $\tilde{u}, \tilde{v}, \tilde{w}$ are assumed to be the following forms:

$$\tilde{u} = (\tilde{u}_0 + \widetilde{\mathrm{Re}}\tilde{u}_1 + \cdots) \tag{A.9}$$

$$\tilde{v} = (\tilde{v}_0 + \widetilde{\mathrm{Re}}\tilde{v}_1 + \cdots) \tag{A.10}$$

$$\tilde{w} = (\tilde{w}_0 + \widetilde{\mathrm{Re}}\tilde{w}_1 + \cdots) \tag{A.11}$$

Where the expansion parameter $\widetilde{\mathrm{Re}}$ is defined as:

$$\widetilde{Re} = \frac{R^2\omega\rho\alpha^2}{12\eta} \tag{A.12}$$

And $\tilde{u}_0, \tilde{u}_1, \cdots, \tilde{v}_0, \cdots, \tilde{w}_0, \cdots,$ are normalized components of velocity. Using these transformed variables, the Navier-stokes equations can be rewritten as:

$$r - momentum: \frac{\partial^2\tilde{u}}{\partial\tilde{z}^2} + 12\widetilde{Re}\tilde{v}^2 - \frac{\tilde{r}\alpha^2}{\eta\omega}\frac{\partial p}{\partial\tilde{r}} = 0 \tag{A.13}$$

$$\theta - momentum: \frac{\partial^2\tilde{v}}{\partial\tilde{z}^2} - 12\widetilde{Re}\left[2\tilde{u}\tilde{v} + \tilde{r}\tilde{u}\frac{\partial\tilde{v}}{\partial\tilde{r}} + (\tilde{w} - \tilde{z}\tilde{v})\frac{\partial\tilde{v}}{\partial\tilde{z}}\right] = 0 \tag{A.14}$$

$$z - momentum: \frac{\partial^2\tilde{w}}{\partial\tilde{z}^2} - \frac{1}{\eta\omega}\frac{\partial p}{\partial\tilde{z}} = 0 \tag{A.15}$$

$$continuity: \tilde{r}\frac{\partial\tilde{u}}{\partial\tilde{r}} - \tilde{z}\frac{\partial\tilde{u}}{\partial\tilde{z}} + \tilde{u} + \frac{\partial\tilde{w}}{\partial\tilde{z}} = 0 \tag{A.16}$$

The corresponding boundary conditions at the cone and the plate surface are transformed as:

$$\left.\begin{array}{c}\tilde{u}_0 = \tilde{u}_1 = \cdots = 0, \\ \tilde{v}_0 = \tilde{v}_1 = \cdots = 0 \\ \tilde{w}_0 = \tilde{w}_1 = \cdots = 0\end{array}\right\} (\tilde{z} = 0) \tag{A.17-a}$$

$$\left.\begin{array}{c}\tilde{u}_0 = \tilde{u}_1 = \cdots = 0, \\ \tilde{w}_0 = \tilde{w}_1 = \cdots = 0 \\ \tilde{v}_0 = 1 \\ \tilde{v}_1 = \cdots = 0\end{array}\right\} (\tilde{z} = 1) \tag{A.17-b}$$

The transformed Navier-Stokes equations are solved by the method of asymptotic expansion. The normalized velocity components (A.9)-(A.11) are substituted into (A.13)-(A.16). The terms in each of the transformed equations are grouped according to their order of magnitude of $\widetilde{Re}$, as shown below.

$$r - momentum: \left[\frac{\partial^2\tilde{u}_0}{\partial\tilde{z}^2}\right] + \widetilde{Re}\left[\frac{\partial^2\tilde{u}_1}{\partial\tilde{z}^2} + 12\tilde{v}_0^2 - \frac{12}{\rho\omega^2\tilde{r}}\frac{\partial p}{\partial\tilde{r}}\right] + \widetilde{Re}^2[\cdots] + \cdots = 0 \tag{A.18}$$

$$\theta - momentum: \left[\frac{\partial^2 \tilde{u}_0}{\partial \tilde{z}^2}\right] + \widetilde{Re}\left[\frac{\partial^2 \tilde{v}_1}{\partial \tilde{z}^2} - 24\,\tilde{u}_0\,\tilde{v}_0 - 12\tilde{r}\,\tilde{u}_0\frac{\partial \tilde{v}_0}{\partial \tilde{z}} - 12\,\tilde{w}_0\frac{\partial \tilde{v}_0}{\partial \tilde{z}} + 12\tilde{z}\,\tilde{u}_0\frac{\partial \tilde{v}_0}{\partial \tilde{z}}\right] + \widetilde{Re}^2[\cdots] + \cdots = 0 \quad (A.19)$$

$$z - momentum: \left[\frac{\partial^2 \tilde{w}_0}{\partial \tilde{z}^2} - \frac{1}{\mu\omega}\frac{\partial p}{\partial \tilde{z}}\right] + \widetilde{Re}\left[\frac{\partial^2 \tilde{w}_1}{\partial \tilde{z}^2}\right] + \widetilde{Re}^2[\cdots] + \cdots = 0 \quad (A.20)$$

$$continuity: \left[\tilde{r}\frac{\partial\,\tilde{u}_0}{\partial \tilde{r}} - \tilde{z}\frac{\partial\,\tilde{u}_0}{\partial \tilde{z}} + 2\,\tilde{u}_0 + \frac{\partial\,\tilde{w}_0}{\partial \tilde{z}}\right] + \widetilde{Re}\left[\tilde{r}\frac{\partial\,\tilde{u}_1}{\partial \tilde{r}} - \tilde{z}\frac{\partial\,\tilde{u}_1}{\partial \tilde{z}} + 4\,\tilde{u}_1 + \frac{\partial\,\tilde{w}_1}{\partial \tilde{z}}\right] + \widetilde{Re}^2[\cdots] + \cdots = 0 \quad (A.21)$$

According to the method, each grouping on the left-hand side of equations (A.18) to (A.21) is set to be equal to zero, thus solutions for each of the velocity components can be obtained, as shown in the following.

Zeroth-order solution: O($\widetilde{Re}$)

From (A.18)-(A.21) the zeroth-order equations are obtained as follows:

$$\frac{\partial^2 \tilde{u}_0}{\partial \tilde{z}^2} = 0 \quad (A.22)$$

$$\frac{\partial^2 \tilde{v}_0}{\partial \tilde{z}^2} = 0 \quad (A.23)$$

$$\frac{\partial^2 \tilde{w}_0}{\partial \tilde{z}^2} - \frac{1}{\mu\omega}\frac{\partial p}{\partial \tilde{z}} = 0 \quad (A.24)$$

$$\tilde{r}\frac{\partial\,\tilde{u}_0}{\partial \tilde{r}} - \tilde{z}\frac{\partial\,\tilde{u}_0}{\partial \tilde{z}} + 2\,\tilde{u}_0 + \frac{\partial\,\tilde{w}_0}{\partial \tilde{z}} = 0 \quad (A.25)$$

With the boundary conditions (A.17), the solutions of (A.22)-(A.25) are:

$$\tilde{u}_0 = 0, \tilde{v}_0 = \tilde{z}, \tilde{w}_0 = 0 \quad (A.26)$$

As $\tilde{w}_0 = 0$, substituting it to equation (A.25), which results in:

$$\frac{\partial p}{\partial \tilde{z}} = 0$$

Thus

$$p = p(r) \quad (A.27)$$

Equation (A.26) and (A.27) are conditions which describe the ***primary flow***.

First-order solution: $O(\widetilde{Re}^1)$

For the first-order equations, after substituting the equations (A.26) and (A.27), they are:

$$\frac{\partial^2 \tilde{u}_1}{\partial \tilde{z}^2} + 12\tilde{z}^2 - \frac{12}{\rho\omega^2\tilde{r}}\frac{dp}{d\tilde{r}} = 0 \tag{A.28}$$

$$\frac{\partial^2 \tilde{v}_1}{\partial \tilde{z}^2} = 0 \tag{A.29}$$

$$\frac{\partial^2 \widetilde{w}_1}{\partial \tilde{z}^2} = 0 \tag{A.30}$$

$$\tilde{r}\frac{\partial \tilde{u}_1}{\partial \tilde{r}} - \tilde{z}\frac{\partial \tilde{u}_1}{\partial \tilde{z}} + 4\,\tilde{u}_1 + \frac{\partial \widetilde{w}_1}{\partial \tilde{z}} = 0 \tag{A.31}$$

Integrating (A.28) twice and substituting the no-slip boundary condition (A.17) gives

$$\tilde{u}_1 = \frac{1}{2}\Psi\tilde{z}^2 - \tilde{z}^4 + C\tilde{z}, \tag{A.32}$$

Where

$$\Psi = \frac{12}{\rho\omega^2\tilde{r}}\frac{dp}{d\tilde{r}}$$

, C is a constant of integration which can be evaluated by the continuity condition that the radial flow integrated across the gap height is zero:

$$\int_{\tilde{z}=0}^{\tilde{z}=1} \tilde{u}_1\, d\tilde{z} = 0 \tag{A.33}$$

Based on the boundary and continuity conditions, the values of Ψ and C are obtained $\Psi = 3.6$ and $C = -0.8$. Thus the first-order radial velocity (A.32) may finally be written as:

$$\tilde{u}_1 = 1.8\tilde{z}^2 - \tilde{z}^4 + 0.8\tilde{z} \tag{A.34}$$

This non-dimensional radial velocity profile is shown in figure 2.16, which is the ***secondary flow***. The ratio of the secondary to primary flows can be expressed as:

$$\frac{\tilde{u}_1}{\tilde{v}_0} = \widetilde{Re}(1.8\tilde{z} - \tilde{z}^3 + 0.8) \tag{A.35}$$

From (A.29) and boundary conditions (A.17), the normalized first-order tangential component of velocity $\tilde{v}_1$ is found to be equal to zero.

By substituting the equation (A.34) for $\tilde{u}_1$ into the first-order continuity equation (A.31), the first-order vertical velocity component $\widetilde{w}_1$ can then be obtained. After simplification, equation (A.31) becomes

$$\frac{\partial \widetilde{w}_1}{\partial \tilde{z}} = -3.6\tilde{z}^2 + 2.4\tilde{z} \tag{A.36}$$

By integrating (A.36) and considering the boundary conditions, the expression for $\widetilde{w}_1$ is obtained:

$$\widetilde{w}_1 = 1.2(\tilde{z}^2 - \tilde{z}^3) \tag{A.37}$$

Appendix B Viscosity data

Shear rate (1/s)	η_0% (Pa.s)	η_2% (Pa.s)	η_5% (Pa.s)	η _10% (Pa.s)	η _20% (Pa.s)	η _35% (Pa.s)	η _45% (Pa.s)
0.50	0.0414	0.0447	0.0495	0.0640	0.1247	0.5690	1.8934
0.85	0.0415	0.0446	0.0495	0.0627	0.1111	0.4689	1.5182
1.44	0.0414	0.0447	0.0492	0.0615	0.1057	0.3959	1.2675
2.45	0.0417	0.0446	0.0492	0.0602	0.0996	0.3504	1.1068
4.16	0.0417	0.0445	0.0488	0.0592	0.0954	0.3217	1.0029
7.07	0.0417	0.0445	0.0486	0.0584	0.0923	0.3039	0.9350
12.01	0.0417	0.0445	0.0485	0.0580	0.0897	0.2916	0.8915
20.41	0.0419	0.0446	0.0486	0.0579	0.0876	0.2834	0.8685
34.66	0.0420	0.0447	0.0486	0.0578	0.0860	0.2776	0.8336
58.87	0.0420	0.0447	0.0485	0.0576	0.0848	0.2730	0.7848
99.99	0.0420	0.0446	0.0484	0.0575	0.0837	0.2692	0.7204

Tab B.1 Measured viscosities of 41μm particle suspensions at different concentration and at different shear rate

Shear rate (1/s)	η_0% (Pa.s)	η_2% (Pa.s)	η_5% (Pa.s)	η _10% (Pa.s)	η _20% (Pa.s)	η _35% (Pa.s)	η _45% (Pa.s)
0.50	0.0535	0.0521	0.0553	0.0657	0.1011	0.3290	0.9438
0.85	0.0522	0.0512	0.0558	0.0664	0.1021	0.3383	0.8789
1.44	0.0521	0.0511	0.0562	0.0667	0.1015	0.3275	0.7106
2.45	0.0517	0.0509	0.0560	0.0666	0.0985	0.3232	0.7367
4.16	0.0515	0.0507	0.0561	0.0668	0.0980	0.3216	0.7156
7.07	0.0514	0.0506	0.0561	0.0665	0.0975	0.3211	0.7417
12.01	0.0515	0.0507	0.0565	0.0669	0.0982	0.3235	0.8077
20.41	0.0514	0.0507	0.0565	0.0668	0.0971	0.3281	0.8424
34.66	0.0515	0.0508	0.0566	0.0667	0.0968	0.3335	0.8941
58.87	0.0514	0.0508	0.0565	0.0666	0.0966	0.3372	0.9389
99.99	0.0513	0.0507	0.0565	0.0665	0.0965	0.3372	0.9671

Tab B.2 Measured viscosities of 4.62μm particle suspensions at different concentration and at different shear rate

Appendix C Velocity profiles

Velocity profiles of 41µm particle suspensions

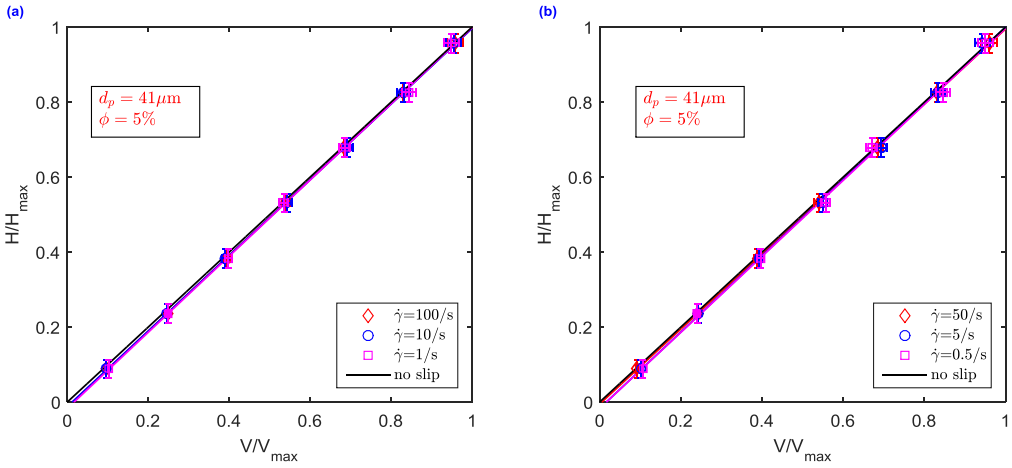

Fig C.1 Normalized velocity profiles of 5% 41µm particle suspension at: a)100s^{-1}, 10s^{-1} and 1s^{-1}, b) 50s^{-1}, 5$s^{-1}$and 0.5s^{-1}.

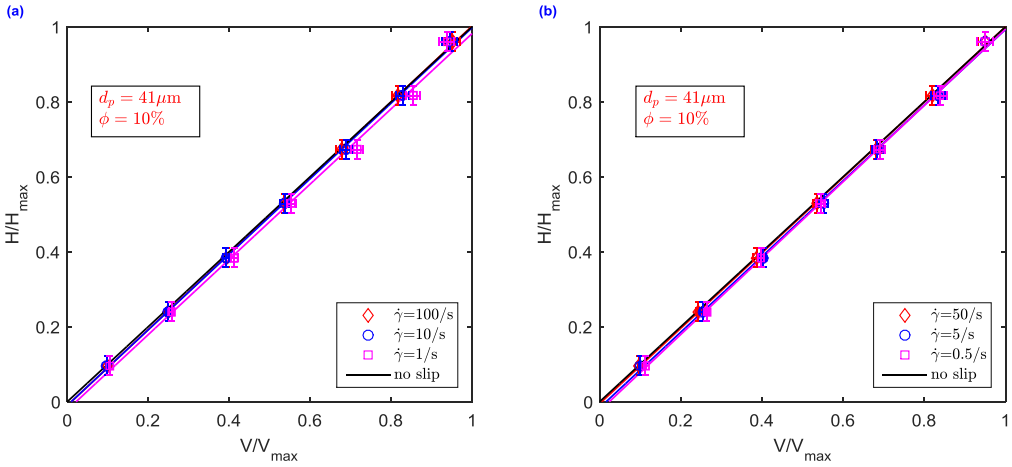

Fig C.2 Normalized velocity profiles of 10% 41µm particle suspension at: a)100s^{-1}, 10s^{-1} and 1s^{-1}, b) 50s^{-1}, 5$s^{-1}$and 0.5s^{-1}.

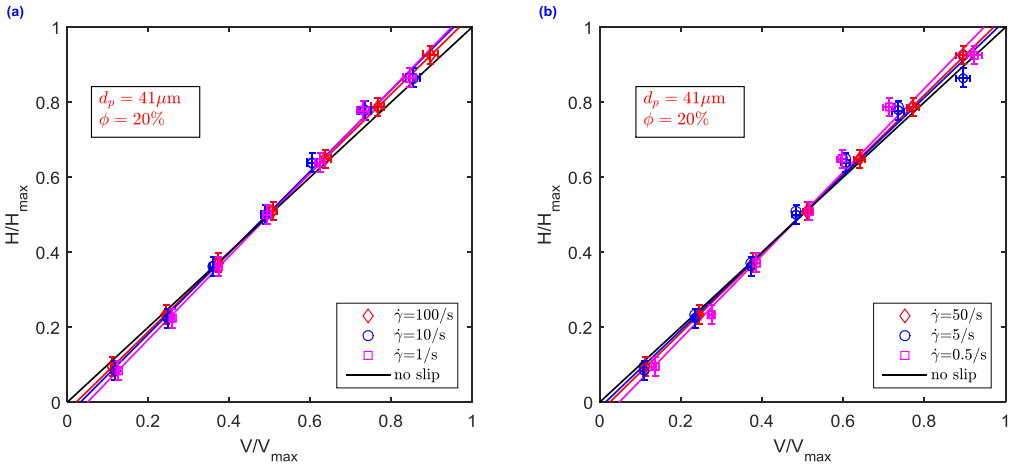

Fig C.3 Normalized velocity profiles of 20% 41µm particle suspension at: a)100s^{-1}, 10s^{-1} and 1s^{-1}, b) 50s^{-1}, 5s^{-1}and 0.5s^{-1}.

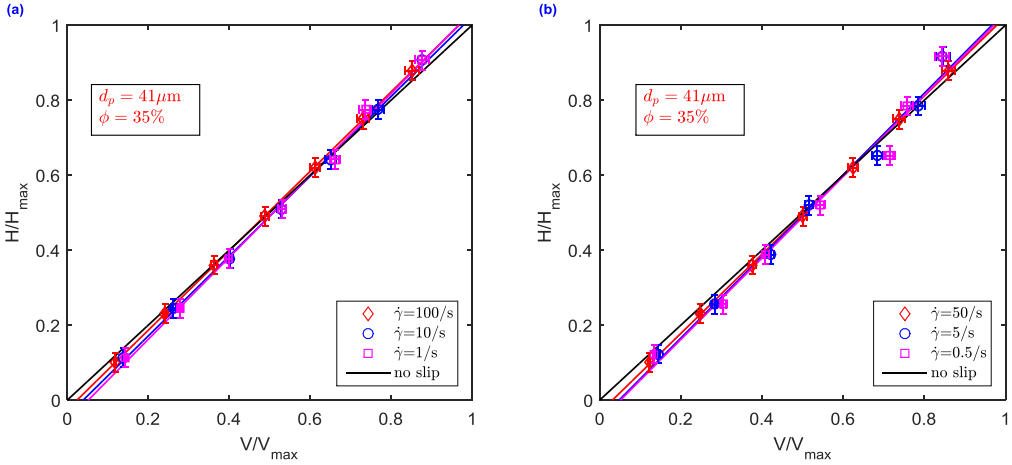

Fig C.4 Normalized velocity profiles of 35% 41µm particle suspension at: a)100s^{-1}, 10s^{-1} and 1s^{-1}, b) 50s^{-1}, 5s^{-1}and 0.5s^{-1}.

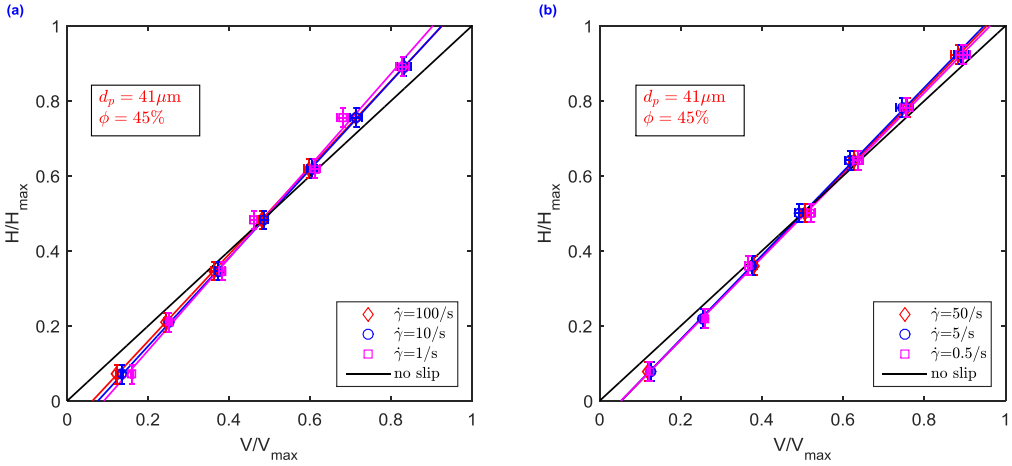

Fig C.5 Normalized velocity profiles of 45% 41µm particle suspension at: a)100s^{-1}, 10s^{-1} and 1s^{-1}, b) 50s^{-1}, 5s^{-1}and 0.5s^{-1}.

Velocity profiles of 4.62µm particle suspensions

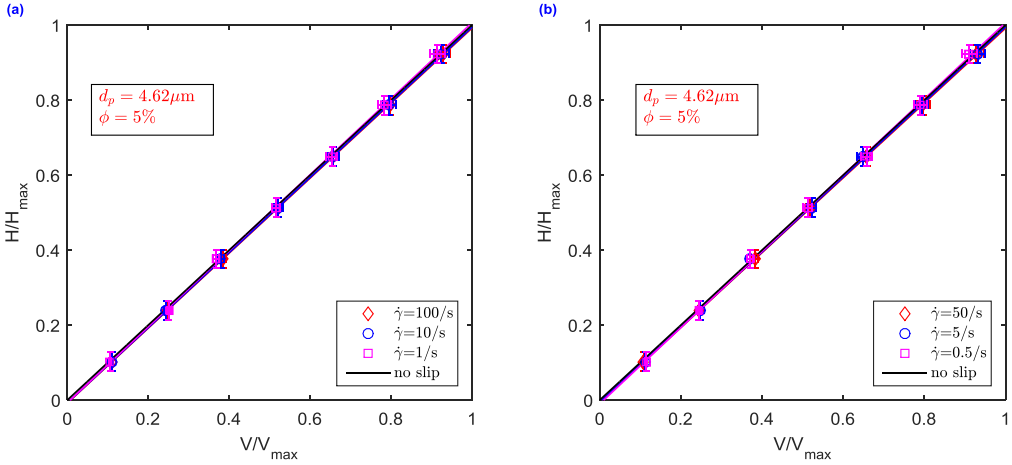

Fig C.6 Normalized velocity profiles of 5% 4.62µm particle suspension at: a)100s^{-1}, 10s^{-1} and 1s^{-1}, b) 50s^{-1}, 5$s^{-1}$and 0.5s^{-1}.

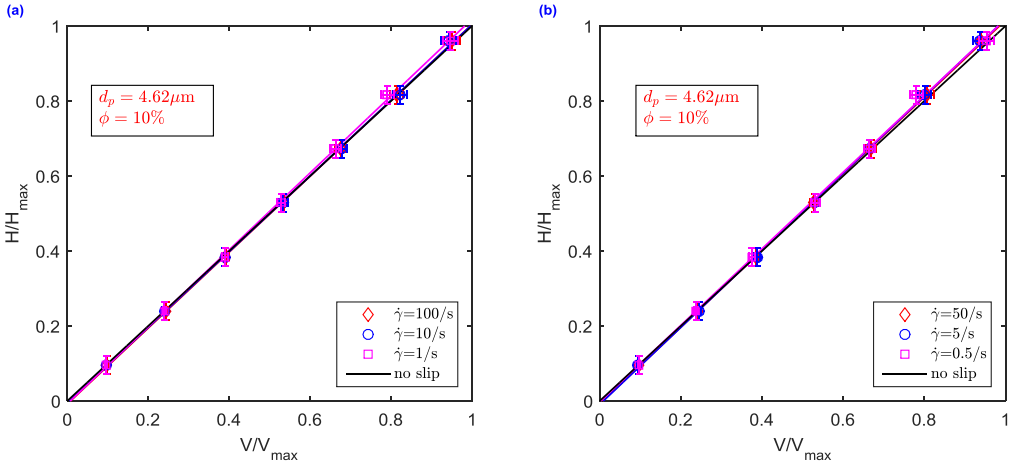

Fig C.7 Normalized velocity profiles of 10% 4.62µm particle suspension at: a)100s^{-1}, 10s^{-1} and 1s^{-1}, b) 50s^{-1}, 5$s^{-1}$and 0.5s^{-1}.

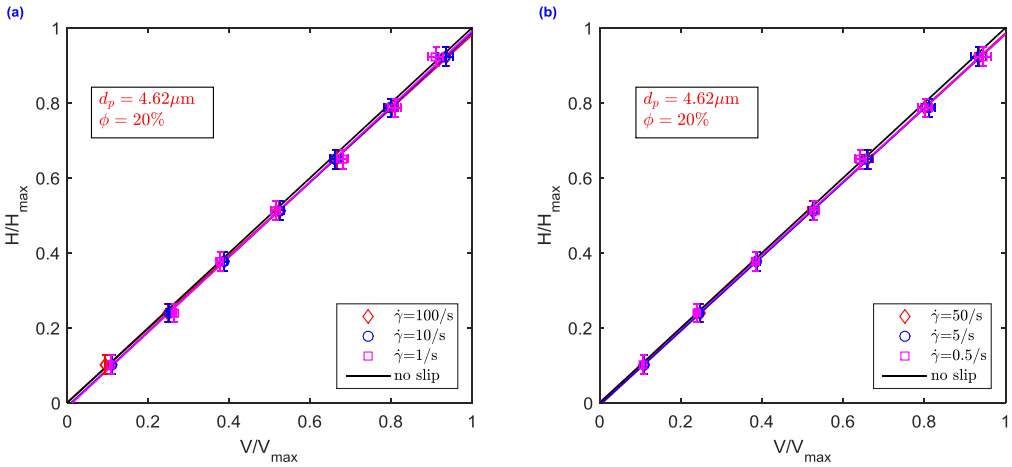

Fig C.8 Normalized velocity profiles of 20% 4.62µm particle suspension at: a)100s^{-1}, 10s^{-1} and 1s^{-1}, b) 50s^{-1}, 5$s^{-1}$and 0.5s^{-1}.

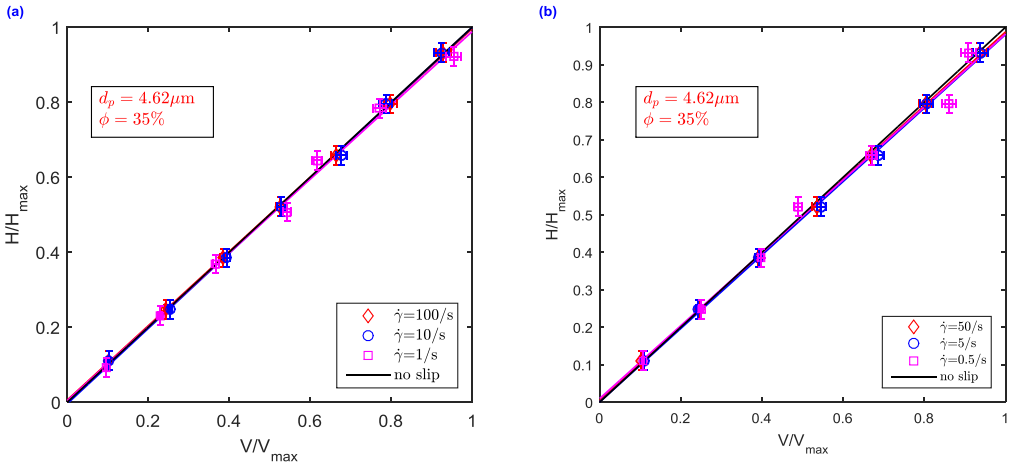

Fig C.9 Normalized velocity profiles of 35% 4.62µm particle suspension at: a)100s^{-1}, 10s^{-1} and 1s^{-1}, b) 50s^{-1}, 5$s^{-1}$and 0.5s^{-1}.

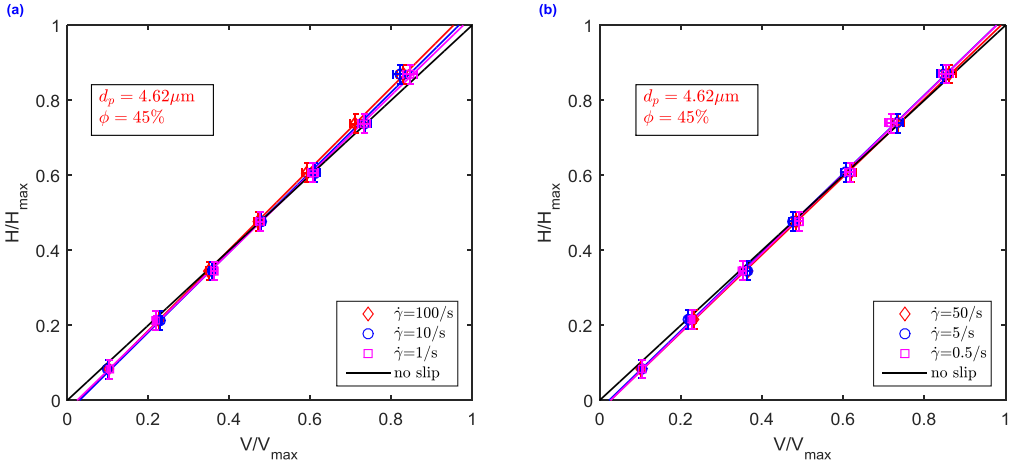

Fig C.10 Normalized velocity profiles of 45% 4.62µm particle suspension at: a)100s^{-1}, 10s^{-1} and 1s^{-1}, b) 50s^{-1}, 5$s^{-1}$and 0.5s^{-1}.

Appendix D Relative differences of shear rates

ϕ =45%	$\dot{\gamma}$	103.570	54.375	10.357	5.438	1.036	0.544
	$\Delta\dot{\gamma}/\dot{\gamma}$	10.71%	9.98%	12.19%	10.60%	15.75%	11.20%
ϕ =35%	$\dot{\gamma}$	101.5	50.75	10.15	5.075	1.015	0.508
	$\Delta\dot{\gamma}/\dot{\gamma}$	5.61%	5.32%	4.32%	7.24%	6.96%	8.00%
ϕ =20%	$\dot{\gamma}$	101.500	50.750	10.150	5.075	1.015	0.508
	$\Delta\dot{\gamma}/\dot{\gamma}$	2.07%	1.89%	5.85%	4.62%	5.59%	9.67%
ϕ =10%	$\dot{\gamma}$	111.360	55.680	11.136	5.568	1.114	0.557
	$\Delta\dot{\gamma}/\dot{\gamma}$	0.78%	1.48%	1.20%	1.00%	1.20%	0.20%
ϕ =5%	$\dot{\gamma}$	114.100	57.050	11.410	5.705	1.141	0.571
	$\Delta\dot{\gamma}/\dot{\gamma}$	0.29%	-0.80%	0.10%	-0.20%	-0.40%	-0.60%
ϕ =0%	$\dot{\gamma}$	118.970	59.485	11.897	5.949	1.190	0.595
	$\Delta\dot{\gamma}/\dot{\gamma}$	0.46%	0.40%	0.80%	-0.60%	1.40%	0.40%

Tab D.1 Relative difference of shear rates of 41μm particle suspension at different shear rates and at different particle concentrations

ϕ =45%	$\dot{\gamma}$	114.1	57.05	11.41	5.705	1.141	0.5705
	$\Delta\dot{\gamma}/\dot{\gamma}$	7.38%	7.24%	6.50%	3.80%	4.60%	4.80%
ϕ =35%	$\dot{\gamma}$	105.8	52.9	10.58	5.29	1.058	0.529
	$\Delta\dot{\gamma}/\dot{\gamma}$	-0.02%	-0.73%	1.40%	-0.92%	-1.16%	-0.79%
ϕ =20%	$\dot{\gamma}$	120	60	12	6	1.2	0.6
	$\Delta\dot{\gamma}/\dot{\gamma}$	-1.21%	0.14%	0.50%	-0.20%	1.50%	-1.00%
ϕ =10%	$\dot{\gamma}$	110.476	55.238	11.048	5.524	1.105	0.552
	$\Delta\dot{\gamma}/\dot{\gamma}$	1.42%	1.52%	1.20%	-0.20%	1.50%	-1.00%
ϕ =5%	$\dot{\gamma}$	120	60	12	6	1.2	0.6
	$\Delta\dot{\gamma}/\dot{\gamma}$	1.13%	1.38%	1.00%	1.00%	0.50%	0.20%
ϕ =0%	$\dot{\gamma}$	118.970	59.485	11.897	5.949	1.190	0.595
	$\Delta\dot{\gamma}/\dot{\gamma}$	0.46%	0.40%	0.80%	-0.60%	1.40%	0.40%

Tab D.2 Relative difference of shear rates of 4.62μm particle suspension at different shear rates and at different particle concentrations

Appendix E Calculation of uncertainties

According to the rule of propagation of uncertainties (Taylor 1996), for equation Z=f(A, B), if the uncertainties of a and b are independent and random, the error of c can be expressed as the below:

$$\Delta Z = \sqrt{\left(\frac{\partial f}{\partial A}\Delta A\right)^2 + \left(\frac{\partial f}{\partial B}\Delta B\right)^2} \tag{E.1}$$

Some basic rules for the measurement uncertainty are shown below:

$$\text{Z=A+B, } \Delta Z = \sqrt{\Delta A^2 + \Delta B^2} \tag{E.2}$$

$$\text{Z=A-B, } \Delta Z = \sqrt{\Delta A^2 + \Delta B^2} \tag{E.3}$$

$$\text{Z=A×B, } \frac{\Delta Z}{Z} = \sqrt{\left(\frac{\Delta A}{A}\right)^2 + \left(\frac{\Delta B}{B}\right)^2} \tag{E.4}$$

$$\text{Z=A/B, } \frac{\Delta Z}{Z} = \sqrt{\left(\frac{\Delta A}{A}\right)^2 + \left(\frac{\Delta B}{B}\right)^2} \tag{E.5}$$

Uncertainty for the measurement of shear rate

In the current experiments, for the measurement of the shear rate $\dot{\gamma} = V/H$,

$$\Delta\dot{\gamma} = \sqrt{\left(\frac{1}{H}\Delta V\right)^2 + \left(\frac{V}{H^2}\Delta H\right)^2} \tag{E.6}$$

$$\frac{\Delta\dot{\gamma}}{\dot{\gamma}} = \sqrt{\left(\frac{\Delta V}{V}\right)^2 + \left(\frac{\Delta H}{H}\right)^2} \tag{E.7}$$

As $\Delta V/V = 2\%$, and $\Delta H/H = 2\%$, then $\Delta\dot{\gamma}/\dot{\gamma}$=2.83%.

Uncertainty for the measurement of slip layer thickness

The equation for the calculation of the slip layer thickness is shown in the below:

$$\delta = \frac{(\dot{\gamma} - \dot{\gamma}_m)\cdot H_{max}}{2(\eta_r - 1)\dot{\gamma}} \tag{E.8}$$

The value of $\dot{\gamma}$ is exact, $\Delta\dot{\gamma}_m/\dot{\gamma}_m = 2.83\%$, and $\Delta H_{max}/H_{max} = 2\%$, $\Delta\eta_r/\eta_r$is the root of square sum of uncertainties $\Delta\eta_s/\eta_s = 2\%$ and $\Delta\eta_L/\eta_L = 2\%$, thus $\Delta\eta_r/\eta_r$=2.83%. As η_r is much bigger than 1, the uncertainty of $(\eta_r - 1)$ approximates to that of η_r. The relative uncertainty of $(\dot{\gamma} - \dot{\gamma}_m)$ is estimated as $\Delta\dot{\gamma}_m/(\dot{\gamma} - \dot{\gamma}_m)$. The uncertainties of the slip layer thickness can be estimated as:

$$\frac{\Delta\delta}{\delta}=\sqrt{\left(\frac{\Delta\dot{\gamma}_m}{\dot{\gamma}-\dot{\gamma}_m}\right)^2+\left(\frac{\Delta H_{max}}{H_{max}}\right)^2+\left(\frac{\Delta\eta_r}{\eta_r}\right)^2} \tag{E.9}$$

Since the value of $\Delta\dot{\gamma}_m$ is close to that of $\dot{\gamma}-\dot{\gamma}_m$, $\Delta\dot{\gamma}_m/(\dot{\gamma}-\dot{\gamma}_m)$>20%, the other two uncertainties are negligle in front of $\Delta\dot{\gamma}_m/(\dot{\gamma}-\dot{\gamma}_m)$, thus the uncertainty of the slip layer thickness can be simplified as:

$$\frac{\Delta\delta}{\delta}=\frac{\Delta\dot{\gamma}_m}{\dot{\gamma}-\dot{\gamma}_m}=\frac{2.83\%\cdot\dot{\gamma}_m}{\dot{\gamma}-\dot{\gamma}_m} \tag{E.10}$$

Uncertainty for the measurement of slip velocity

The equation for the calculation of slip velocity is show in the below:

$$v_s=\frac{(\dot{\gamma}-\dot{\gamma}_m)\cdot H_{max}\cdot(2\eta_r-1)}{2(\eta_r-1)} \tag{E.11}$$

$$v_s=(\dot{\gamma}-\dot{\gamma}_m)\cdot H_{max}\cdot\left[1+\frac{1}{2(\eta_r-1)}\right] \tag{E.12}$$

Based on the same deduction for the calculation of uncertainty of slip layer thickness, If X=$1/2(\eta_r-1)$, then $\Delta X/X$=$\Delta\eta_r/\eta_r$, the relative uncertainty of 1+X can be expressed as:

$$\frac{\Delta(1+X)}{1+X}=\frac{\Delta X}{1+X}=\frac{X}{1+X}\frac{\Delta\eta_r}{\eta_r}<\frac{\Delta\eta_r}{\eta_r} \tag{E.13}$$

The uncertainties of the slip layer thickness can be estimated as:

$$\frac{\Delta v_s}{v_s}=\sqrt{\left(\frac{\Delta\dot{\gamma}_m}{\dot{\gamma}-\dot{\gamma}_m}\right)^2+\left(\frac{\Delta H_{max}}{H_{max}}\right)^2+\left(\frac{X}{1+X}\frac{\Delta\eta_r}{\eta_r}\right)^2} \tag{E.14}$$

Since $\Delta H_{max}/H_{max}$ and $\Delta\eta_r/\eta_r$ are much smaller than $\Delta\dot{\gamma}_m/(\dot{\gamma}-\dot{\gamma}_m)$, the uncertainty is also simplified as:

$$\frac{\Delta v_s}{v_s}=\frac{\Delta\dot{\gamma}_m}{\dot{\gamma}-\dot{\gamma}_m}=\frac{2.83\%\cdot\dot{\gamma}_m}{\dot{\gamma}-\dot{\gamma}_m} \tag{E.15}$$

Glossary

Airy distribution: the diffraction pattern resulting from a uniformly-illuminated circular aperture has a bright region in the center, known as the Airy disk, which together with the series of concentric bright rings around is called the Airy distribution.

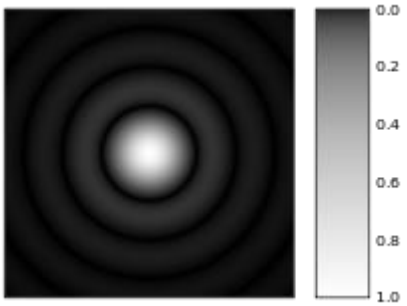

Fig 1 Computer-generated image of an Airy disk, the gray scale intensities have been adjusted to enhance the brightness of the outer rings of the Airy pattern.

Excluded volume: the 'excluded volume' of a molecule is the volume that is inaccessible to other molecules in the system as a result of the presence of the first molecule.

In-plane loss of correlation: within an image pairs, a tracer particle appeared in one interrogation window, which moves out the other interrogation window within the plane parallel to optical axis.

Interrogation window: a small size area in the image to be processed.

Newtonian fluid: the viscosity of which is independent of shear rate.

Out-plane loss of correlation: within an image pairs, a tracer particle appeared in one interrogation window, which moves out the other interrogation window following the direction of the optical axis.

Particle pair relative flux: the probability to find other particles with a distance from the current particle

Point spread function: the response of an imaging system to a point source or point object.

Response time: the time requested for a particle to attain the same velocity as the surrounding fluid

Resuspension: the suspension was renewed after the particles have been precipitated

Shear-thinning: the viscosity decrease with shear rate increasing.

Shear-thickening: the viscosity increase with shear rate increasing.

References

Adrian, R. J., and C. S. Yao. 1985. 'Pulsed Laser Technique Application to Liquid and Gaseous Flows and the Scattering Power of Seed Materials'. *Applied Optics* 24 (1): 44–52.

Ahuja, Amit, and Anugrah Singh. 2009. 'Slip Velocity of Concentrated Suspensions in Couette Flow'. *Journal of Rheology (1978-Present)* 53 (6): 1461–85. doi:10.1122/1.3213090.

Averbakh, A., A. Shauly, A. Nir, and R. Semiat. 1997. 'Slow Viscous Flows of Highly Concentrated suspensions—Part I: Laser-Doppler Velocimetry in Rectangular Ducts'. *International Journal of Multiphase Flow* 23 (3): 409–24. doi:10.1016/S0301-9322(96)00078-X.

Bagchi, Prosenjit. 2007. 'Mesoscale Simulation of Blood Flow in Small Vessels'. *Biophysical Journal* 92 (6): 1858–77. doi:10.1529/biophysj.106.095042.

Barnes, H. A. 1989. 'Shear-Thickening ("Dilatancy") in Suspensions of Nonaggregating Solid Particles Dispersed in Newtonian Liquids'. *Journal of Rheology (1978-Present)* 33 (2): 329–66. doi:10.1122/1.550017.

Barnes, Howard A. 1995. 'A Review of the Slip (Wall Depletion) of Polymer Solutions, Emulsions and Particle Suspensions in Viscometers: Its Cause, Character, and Cure'. *Journal of Non-Newtonian Fluid Mechanics* 56 (3): 221–51. doi:10.1016/0377-0257(94)01282-M.

Barnes, Howard A. 1999. 'The Yield Stress—a Review or "παντα Ρει"—everything Flows?' Journal of Non-Newtonian Fluid Mechanics 81 (1–2): 133–78. doi:10.1016/S0377-0257(98)00094-9.

Barnes, Howard A., John Fletcher Hutton, and Kenneth Walters. 1989. *An Introduction to Rheology*. Elsevier.

Barnkob, Rune, Christian J. Kähler, and Massimiliano Rossi. 2015. 'General Defocusing Particle Tracking'. *Lab on a Chip* 15 (17): 3556–60. doi:10.1039/C5LC00562K.

Baskurt, Oguz K., and Herbert J. Meiselman. 2003. 'Blood Rheology and Hemodynamics'. *Seminars in Thrombosis and Hemostasis* 29 (5): 435–50. doi:10.1055/s-2003-44551.

Baskurt, Oguz K., and Herbert J. Meiselman. 2010. 'Le Phénomène D'agrégation Érythrocytaire : De Nouvelles Découvertes'. Sang Thrombose Vaisseaux 22 (3): 137–43. doi:10.1684/stv.2010.0466.

Batchelor, G. K. 1977. 'The Effect of Brownian Motion on the Bulk Stress in a Suspension of Spherical Particles'. *Journal of Fluid Mechanics* 83 (1): 97–117. doi:10.1017/S0022112077001062.

Batchelor, G. K., and J. T. Green. 1972. 'The Determination of the Bulk Stress in a Suspension of Spherical Particles to Order c2'. *Journal of Fluid Mechanics* 56 (3): 401–427. doi:10.1017/S0022112072002435.

Besseling, Rut, Lucio Isa, Eric R. Weeks, and Wilson C. K. Poon. 2009. 'Quantitative Imaging of Colloidal Flows'. *Advances in Colloid and Interface Science* 146 (1–2): 1–17. doi:10.1016/j.cis.2008.09.008.

Bishop, Jeffrey J., Aleksander S. Popel, Marcos Intaglietta, and Paul C. Johnson. 2001. 'Rheological Effects of Red Blood Cell Aggregation in the Venous Network: A Review of Recent Studies'. *Biorheology* 38 (2,3): 263–74.

Blanc, Frédéric, Elisabeth Lemaire, Alain Meunier, and François Peters. 2013. 'Microstructure in Sheared Non-Brownian Concentrated Suspensions'. *Journal of Rheology -New York-* 57 (1): 273.

Blanc, Frédéric, François Peters, and Elisabeth Lemaire. 2011. 'Local Transient Rheological Behavior of Concentrated Suspensions'. *Journal of Rheology* 55 (4): 835. doi:10.1122/1.3582848.

Bourdon, Christopher J., Michael G. Olsen, and Allen D. Gorby. 2005. 'The Depth of Correlation in Micro-PIV for High Numerical Aperture and Immersion Objectives'. *Journal of Fluids Engineering* 128 (4): 883–86. doi:10.1115/1.2201649.

Brader, J. M. 2010. 'Nonlinear Rheology of Colloidal Dispersions'. *Journal of Physics: Condensed Matter* 22 (36): 363101. doi:10.1088/0953-8984/22/36/363101.

Brown, Eric, and Heinrich M. Jaeger. 2012. 'The Role of Dilation and Confining Stresses in Shear Thickening of Dense Suspensions'. *Journal of Rheology (1978-Present)* 56 (4): 875–923. doi:10.1122/1.4709423.

Brown, Eric, and Heinrich M Jaeger. 2014. 'Shear Thickening in Concentrated Suspensions: Phenomenology, Mechanisms and Relations to Jamming'. *Reports on Progress in Physics* 77 (4): 46602. doi:10.1088/0034-4885/77/4/046602.

Chakrabandhu, Krittalak, and Rakesh K. Singh. 2005. 'Wall Slip Determination for Coarse Food Suspensions in Tube Flow at High Temperatures'. *Journal of Food Engineering* 70 (1): 73–81. doi:10.1016/j.jfoodeng.2004.07.025.

Chang, Chingyi, and Robert L. Powell. 1994. 'The Rheology of Bimodal Hard-sphere Dispersions'. *Physics of Fluids (1994-Present)* 6 (5): 1628–36. doi:10.1063/1.868226.

Cheng, D. C. -H. 1968. 'The Effect of Secondary Flow on the Viscosity Measurement Using the Cone-and-Plate Viscometer'. *Chemical Engineering Science* 23 (8): 895–99. doi:10.1016/0009-2509(68)80023-5.

Cheng, Xiang, Jonathan H. McCoy, Jacob N. Israelachvili, and Itai Cohen. 2011. 'Imaging the Microscopic Structure of Shear Thinning and Thickening Colloidal Suspensions'. *Science* 333 (6047): 1276–79. doi:10.1126/science.1207032.

Chenouard, Nicolas, Ihor Smal, Fabrice de Chaumont, Martin Maška, Ivo F. Sbalzarini, Yuanhao Gong, Janick Cardinale, et al. 2014. 'Objective Comparison of Particle Tracking Methods'. *Nature Methods* 11 (3): 281–89. doi:10.1038/nmeth.2808.

Chien, S. 1970. 'Shear Dependence of Effective Cell Volume as a Determinant of Blood Viscosity'. *Science (New York, N.Y.)* 168 (3934): 977–79.

Chingyi Chang, Robert L. Powell. 1994. 'Effect of Particle Size Distributions on the Rheology of Concentrated Bimodal Suspensions'. *Journal of Rheology - J RHEOL* 38 (1): 85–98. doi:10.1122/1.550497.

Chong, J. S., E. B. Christiansen, and A. D. Baer. 1971. 'Rheology of Concentrated Suspensions'. *Journal of Applied Polymer Science* 15 (8): 2007–21. doi:10.1002/app.1971.070150818.

Chow, Andrea W., Joseph H. Iwamiya, Steven W. Sinton, and David Leighton. 1995. 'Particle Migration of Non-Brownian, Concentrated Suspensions in a Truncated Cone-and-Plate'. In . Sacramento, CA.

Chow, Andrea W., Steven W. Sinton, Joseph H. Iwamiya, and Thomas S. Stephens. 1994. 'Shear-induced Particle Migration in Couette and Parallel-plate Viscometers: NMR Imaging and Stress Measurements'. *Physics of Fluids (1994-Present)* 6 (8): 2561–76. doi:10.1063/1.868147.

Coussot, P., and C. Ancey. 1999. 'Rheophysical Classification of Concentrated Suspensions and Granular Pastes'. *Physical Review E* 59 (4): 4445–57. doi:10.1103/PhysRevE.59.4445.

Cristini, Vittorio, and Ghassan S. Kassab. 2005. ‘Computer Modeling of Red Blood Cell Rheology in the Microcirculation: A Brief Overview’. *Annals of Biomedical Engineering* 33 (12): 1724–27. doi:10.1007/s10439-005-8776-y.

Crocker, John C., and David G. Grier. 1996. ‘Methods of Digital Video Microscopy for Colloidal Studies’. *Journal of Colloid and Interface Science* 179 (1): 298–310. doi:10.1006/jcis.1996.0217.

Dabak, T., and O. Yucel. 1987. ‘Modeling of the Concentration Particle Size Distribution Effects on the Rheology of Highly Concentrated Suspensions’. *Powder Technology* 52 (3): 193–206. doi:10.1016/0032-5910(87)80105-5.

Denn, Morton M., and Jeffrey F. Morris. 2014. ‘Rheology of Non-Brownian Suspensions’. *Annual Review of Chemical and Biomolecular Engineering* 5 (1): 203–28. doi:10.1146/annurev-chembioeng-060713-040221.

D’Haene, P., and Prof J. Mewis. 1994. ‘Rheological Characterization of Bimodal Colloidal Dispersions’. *Rheologica Acta* 33 (3): 165–74. doi:10.1007/BF00437301.

Dinther, A. M. C. van, C. G. P. H. Schroën, F. J. Vergeldt, R. G. M. van der Sman, and R. M. Boom. 2012. ‘Suspension Flow in Microfluidic Devices — A Review of Experimental Techniques Focussing on Concentration and Velocity Gradients’. *Advances in Colloid and Interface Science* 173 (May): 23–34. doi:10.1016/j.cis.2012.02.003.

Dörr, Aaron, Amsini Sadiki, and Amirfarhang Mehdizadeh. 2013. ‘A Discrete Model for the Apparent Viscosity of Polydisperse Suspensions Including Maximum Packing Fraction’. *Journal of Rheology* 57 (3): 743. doi:10.1122/1.4795746.

Dupin, Michael M., Ian Halliday, Chris M. Care, Lyuba Alboul, and Lance L. Munn. 2007. ‘Modeling the Flow of Dense Suspensions of Deformable Particles in Three Dimensions’. *Physical Review E* 75 (6): 66707. doi:10.1103/PhysRevE.75.066707.

Dzuy, Nq, and Dv Boger. 1983. ‘Yield Stress Measurement for Concentrated Suspensions’. *Journal of Rheology* 27 (4): 321–49. doi:10.1122/1.549709.

Einstein, albert. 1956. *Investigation on the Theory of the Brownian Movement*.

Ellenberger, J., and J. M. H. Fortuin. 1985. ‘A Criterion for Purely Tangential Laminar Flow in the Cone-and-Plate Rheometer and the Parallel-Plate Rheometer’. *Chemical Engineering Science* 40 (1): 111–16. doi:10.1016/0009-2509(85)85051-X.

Fall, A., MM Denn, and D Bonn. 2013. ‘Why Is (Wet) Granular Rheology So Complicated?’ In . Univ. Amsterdam (unpublished manuscript).

Farris, R. J. 1968. ‘Prediction of the Viscosity of Multimodal Suspensions from Unimodal Viscosity Data’. *Transactions of The Society of Rheology (1957-1977)* 12 (2): 281–301. doi:10.1122/1.549109.

Fornari, Walter, Luca Brandt, Pinaki Chaudhuri, Cyan Umbert Lopez, Dhrubaditya Mitra, and Francesco Picano. 2016. ‘Rheology of Confined Non-Brownian Suspensions’. *Physical Review Letters* 116 (1): 18301. doi:10.1103/PhysRevLett.116.018301.

Franceschini, Emilie, François T. H. Yu, François Destrempes, and Guy Cloutier. 2010. ‘Ultrasound Characterization of Red Blood Cell Aggregation with Intervening Attenuating Tissue-Mimicking Phantoms’. *The Journal of the Acoustical Society of America* 127 (2): 1104–15. doi:10.1121/1.3277200.

Frith, W. J., and A. Lips. 1995. ‘The Rheology of Concentrated Suspensions of Deformable Particles’. *Advances in Colloid and Interface Science* 61: 161–89. doi:10.1016/0001-8686(95)00264-Q.

Fung, Yuan-Cheng. 1993. *Biomechanics*. New York, NY: Springer New York. http://link.springer.com/10.1007/978-1-4757-2257-4.

Gao, Yongxiang, and Maria L. Kilfoil. 2009. ‘Accurate Detection and Complete Tracking of Large Populations of Features in Three Dimensions’. *Optics Express* 17 (6): 4685–4704.

Genovese, D. B., J. E. Lozano, and M. A. Rao. 2007. 'The Rheology of Colloidal and Noncolloidal Food Dispersions'. *Journal of Food Science* 72 (2): R11–20. doi:10.1111/j.1750-3841.2006.00253.x.

Genovese, Diego B. 2012. 'Shear Rheology of Hard-Sphere, Dispersed, and Aggregated Suspensions, and Filler-Matrix Composites'. *Advances in Colloid and Interface Science* 171–172 (March): 1–16. doi:10.1016/j.cis.2011.12.005.

Greenwood, R., PF Luckham, and T. Gregory. 1997. 'The Effect of Diameter Ratio and Volume Ratio on the Viscosity of Bimodal Suspensions of Polymer Latices'. *Journal of Colloid and Interface Science* 191 (1): 11–21.

Gulmus, Sergul Acikalin, and Ulku Yilmazer. 2005. 'Effect of Volume Fraction and Particle Size on Wall Slip in Flow of Polymeric Suspensions'. *Journal of Applied Polymer Science* 98 (1): 439–48. doi:10.1002/app.21928.

Heymann, Lutz, Sigrid Peukert, and Nuri Aksel. 2002. 'On the Solid-Liquid Transition of Concentrated Suspensions in Transient Shear Flow'. *Rheologica Acta* 41 (4): 307–15. doi:10.1007/s00397-002-0227-1.

Hoffman, R. L. 1972. 'Discontinuous and Dilatant Viscosity Behavior in Concentrated Suspensions. I. Observation of a Flow Instability'. *Transactions of The Society of Rheology (1957-1977)* 16 (1): 155–73. doi:10.1122/1.549250.

Hoffman, Richard L. 1992. 'Factors Affecting the Viscosity of Unimodal and Multimodal Colloidal Dispersions'. *Journal of Rheology (1978-Present)* 36 (5): 947–65. doi:10.1122/1.550324.

Hoffman, Rl. 1974. 'Discontinuous and Dilatant Viscosity Behavior in Concentrated Suspensions .2. Theory and Experimental Tests'. *Journal of Colloid and Interface Science* 46 (3): 491–506. doi:10.1016/0021-9797(74)90059-9.

Isa, Lucio, Rut Besseling, Andrew B. Schofield, and Wilson C. K. Poon. 2010. 'Quantitative Imaging of Concentrated Suspensions Under Flow'. In *High Solid Dispersions*, edited by Michel Cloitre, 163–202. Advances in Polymer Science 236. Springer Berlin Heidelberg. http://link.springer.com/chapter/10.1007/12_2009_38.

Jana, S. C., B. Kapoor, and A. Acrivos. 1995. 'Apparent Wall Slip Velocity Coefficients in Concentrated Suspensions of Noncolloidal Particles'. *Journal of Rheology (1978-Present)* 39 (6): 1123–32. doi:10.1122/1.550631.

Jaqaman, Khuloud, Dinah Loerke, Marcel Mettlen, Hirotaka Kuwata, Sergio Grinstein, Sandra L. Schmid, and Gaudenz Danuser. 2008. 'Robust Single-Particle Tracking in Live-Cell Time-Lapse Sequences'. *Nature Methods* 5 (8): 695–702. doi:10.1038/nmeth.1237.

Jenkins, M. C., and S. U. Egelhaaf. 2008. 'Confocal Microscopy of Colloidal Particles: Towards Reliable, Optimum Coordinates'. *Advances in Colloid and Interface Science* 136 (1–2): 65–92. doi:10.1016/j.cis.2007.07.006.

Jomha, A. I., A. Merrington, L. V. Woodcock, H. A. Barnes, and A. Lips. 1991. 'Recent Developments in Dense Suspension Rheology'. *Powder Technology*, A Special Volume Devoted to the Second Symposium on Advances in Particulate Technology, 65 (1–3): 343–70. doi:10.1016/0032-5910(91)80198-R.

Juan, Shi, Qiu Bing, and Tan Hui-Li. 2009. 'Deformation and Motion of a Red Blood Cell in a Shear Flow Simulated by a Lattice Boltzmann Model'. *Communications in Theoretical Physics* 51 (6): 1117–20. doi:10.1088/0253-6102/51/6/28.

Kalyon, Dilhan M. 2005. 'Apparent Slip and Viscoplasticity of Concentrated Suspensions'. *Journal of Rheology (1978-Present)* 49 (3): 621–40. doi:10.1122/1.1879043.

Kim, Ju Min, Song Geun Lee, and Chongyoup Kim. 2008. 'Numerical Simulations of Particle Migration in Suspension Flows: Frame-Invariant Formulation of Curvature-Induced

Migration'. *Journal of Non-Newtonian Fluid Mechanics* 150 (2–3): 162–76. doi:10.1016/j.jnnfm.2007.10.012.

Kitano, T., T. Kataoka, and T. Shirota. 1981. 'An Empirical Equation of the Relative Viscosity of Polymer Melts Filled with Various Inorganic Fillers'. *Rheologica Acta* 20 (2): 207–9. doi:10.1007/BF01513064.

Kloosterman, A., C. Poelma, and J. Westerweel. 2010. 'Flow Rate Estimation in Large Depth-of-Field Micro-PIV'. *Experiments in Fluids* 50 (6): 1587–99. doi:10.1007/s00348-010-1015-9.

Kok, P. J. A. Hartman, S. G. Kazarian, B. J. Briscoe, and C. J. Lawrence. 2004. 'Effects of Particle Size on near-Wall Depletion in Mono-Dispersed Colloidal Suspensions'. *Journal of Colloid and Interface Science* 280 (2): 511–17. doi:10.1016/j.jcis.2004.08.032.

Kok, P. J. A. Hartman, S. G. Kazarian, C. J. Lawrence, and B. J. Briscoe. 2002. 'Near-Wall Particle Depletion in a Flowing Colloidal Suspension'. *Journal of Rheology (1978-Present)* 46 (2): 481–93. doi:10.1122/1.1446882.

Korhonen, Marko, Mikael Mohtaschemi, Antti Puisto, Xavier Illa, and Mikko J. Alava. 2015. 'Apparent Wall Slip in Non-Brownian Hard-Sphere Suspensions'. *The European Physical Journal E* 38 (5): 1–9. doi:10.1140/epje/i2015-15046-y.

Koutsiaris, Aristotle. 2012. 'Digital Micro PIV (μPIV) and Velocity Profiles In Vitro and In Vivo'. In *The Particle Image Velocimetry - Characteristics, Limits and Possible Applications*, edited by Giovanna Cavazzini. InTech. http://www.intechopen.com/books/the-particle-image-velocimetry-characteristics-limits-and-possible-applications/digital-micro-piv-piv-and-velocity-profiles-in-vitro-and-in-vivo.

Krieger, Irvin M., and Thomas J. Dougherty. 1959. 'A Mechanism for Non-Newtonian Flow in Suspensions of Rigid Spheres'. *Transactions of The Society of Rheology (1957-1977)* 3 (1): 137–52. doi:10.1122/1.548848.

Lam, Y. C., Z. Y. Wang, X. Chen, and S. C. Joshi. 2007. 'Wall Slip of Concentrated Suspension Melts in Capillary Flows'. *Powder Technology* 177 (3): 162–69. doi:10.1016/j.powtec.2007.03.044.

Leighton, David, and Andreas Acrivos. 1987b. 'The Shear-Induced Migration of Particles in Concentrated Suspensions'. Journal of Fluid Mechanics 181 (September): 415–439. doi:10.1017/S0022112087002155.

Lindken, Ralph, Massimiliano Rossi, Sebastian Große, and Jerry Westerweel. 2009. 'Micro-Particle Image Velocimetry (μPIV): Recent Developments, Applications, and Guidelines'. *Lab on a Chip* 9 (17): 2551–67. doi:10.1039/B906558J.

Lyon, M. K., and L. G. Leal. 1998a. 'An Experimental Study of the Motion of Concentrated Suspensions in Two-Dimensional Channel Flow. Part 1. Monodisperse Systems'. *Journal of Fluid Mechanics* 363 (May): 25–56. doi:10.1017/S0022112098008817.

Lyon, M. K., and L. G. Leal. 1998b. 'An Experimental Study of the Motion of Concentrated Suspensions in Two-Dimensional Channel Flow. Part 2. Bidisperse Systems'. Journal of Fluid Mechanics 363 (May): 57–77. doi:10.1017/S0022112098008829.

Maciel, A., V. Salas, J. F. A. Soltero, J. Guzmán, and O. Manero. 2002. 'On the Wall Slip of Polymer Blends'. *Journal of Polymer Science Part B: Polymer Physics* 40 (4): 303–16. doi:10.1002/polb.10093.

Mari, Romain, Ryohei Seto, Jeffrey F. Morris, and Morton M. Denn. 2014. 'Shear Thickening, Frictionless and Frictional Rheologies in Non-Brownian Suspensions'. *Journal of Rheology (1978-Present)* 58 (6): 1693–1724. doi:10.1122/1.4890747.

Maron, Samuel H., and Percy E. Pierce. 1956. ‘Application of Ree-Eyring Generalized Flow Theory to Suspensions of Spherical Particles’. *Journal of Colloid Science* 11 (1): 80–95. doi:10.1016/0095-8522(56)90023-X.

McGEARY, R. K. 1961. ‘Mechanical Packing of Spherical Particles’. *Journal of the American Ceramic Society* 44 (10): 513–22. doi:10.1111/j.1151-2916.1961.tb13716.x.

Medhi, Bhaskar Jyoti, A.Kumar Ashok, and Anugrah Singh. 2011. ‘Apparent Wall Slip Velocity Measurements in Free Surface Flow of Concentrated Suspensions’. *International Journal of Multiphase Flow* 37 (6): 609–19. doi:10.1016/j.ijmultiphaseflow.2011.03.006.

Merhi, Dima, Elisabeth Lemaire, Georges Bossis, and Fadl Moukalled. 2005. ‘Particle Migration in a Concentrated Suspension Flowing between Rotating Parallel Plates: Investigation of Diffusion Flux Coefficients’. *Journal of Rheology (1978-Present)* 49 (6): 1429–48. doi:10.1122/1.2079247.

Metzner, A. B. 1985. ‘Rheology of Suspensions in Polymeric Liquids’. *Journal of Rheology* 29 (6): 739. doi:10.1122/1.549808.

Moller, Peder, Abdoulaye Fall, Vijayakumar Chikkadi, Didi Derks, and Daniel Bonn. 2009. ‘An Attempt to Categorize Yield Stress Fluid Behaviour’. *Philosophical Transactions of the Royal Society of London A: Mathematical, Physical and Engineering Sciences* 367 (1909): 5139–55. doi:10.1098/rsta.2009.0194.

Mooney, Melvin. 1931. ‘Explicit Formulas for Slip and Fluidity’. *Journal of Rheology (1929-1932)* 2 (2): 210–22. doi:10.1122/1.2116364.

Mueller, S., E. W. Llewellin, and H. M. Mader. 2010. ‘The Rheology of Suspensions of Solid Particles’. *Proceedings of the Royal Society of London A: Mathematical, Physical and Engineering Sciences* 466 (2116): 1201–28. doi:10.1098/rspa.2009.0445.

Nguyen, Q D, and D V Boger. 1992. ‘Measuring the Flow Properties of Yield Stress Fluids’. *Annual Review of Fluid Mechanics* 24 (1): 47–88. doi:10.1146/annurev.fl.24.010192.000403.

Olsen, M. G., and R. J. Adrian. 2000. ‘Out-of-Focus Effects on Particle Image Visibility and Correlation in Microscopic Particle Image Velocimetry’. *Experiments in Fluids* 29 (1): S166–74. doi:10.1007/s003480070018.

Ouchiyama, Norio, and Tatsuo Tanaka. 1981. ‘Porosity of a Mass of Solid Particles Having a Range of Sizes’. *Industrial & Engineering Chemistry Fundamentals* 20 (1): 66–71. doi:10.1021/i100001a013.

Ovarlez, Guillaume, François Bertrand, and Stéphane Rodts. 2006. ‘Local Determination of the Constitutive Law of a Dense Suspension of Noncolloidal Particles through Magnetic Resonance Imaging’. *Journal of Rheology (1978-Present)* 50 (3): 259–92. doi:10.1122/1.2188528.

Phillips, Ronald J., Robert C. Armstrong, Robert A. Brown, Alan L. Graham, and James R. Abbott. 1992. ‘A Constitutive Equation for Concentrated Suspensions That Accounts for Shear-induced Particle Migration’. *Physics of Fluids A: Fluid Dynamics (1989-1993)* 4 (1): 30–40. doi:10.1063/1.858498.

Picano, Francesco, Wim-Paul Breugem, Dhrubaditya Mitra, and Luca Brandt. 2013. ‘Shear Thickening in Non-Brownian Suspensions: An Excluded Volume Effect’. *Physical Review Letters* 111 (9): 98302. doi:10.1103/PhysRevLett.111.098302.

Popel, Aleksander S., and Paul C. Johnson. 2005. ‘Microcirculation and Hemorheology’. *Annual Review of Fluid Mechanics* 37 (January): 43–69. doi:10.1146/annurev.fluid.37.042604.133933.

Qi, Fuzhong, and Roger I. Tanner. 2011. ‘Relative Viscosity of Bimodal Suspensions’. *Korea-Australia Rheology Journal* 23 (2): 105–11. doi:10.1007/s13367-011-0013-7.

Qin, Kuide, and Abbas A Zaman. 2003. 'Viscosity of Concentrated Colloidal Suspensions: Comparison of Bidisperse Models'. *Journal of Colloid and Interface Science* 266 (2): 461–67. doi:10.1016/S0021-9797(03)00615-5.

Quemada, D. 2002. 'Energy of Interaction in Colloids and Its Implications in Rheological Modeling'. *Advances in Colloid and Interface Science* 98 (1): 51–85. doi:10.1016/S0001-8686(01)00093-8.

Raffel, Markus, Christian E. Willert, Steve T. Wereley, and Jürgen Kompenhans. 2007a. 'Image Evaluation Methods for PIV'. In *Particle Image Velocimetry*, 123–76. Experimental Fluid Mechanics. Springer Berlin Heidelberg. doi:10.1007/978-3-540-72308-0_5.

Raffel, Markus, Christian E. Willert, Steve T. Wereley, and Jürgen Kompenhans. 2007b. 'Micro-PIV'. In Particle Image Velocimetry, 241–58. Experimental Fluid Mechanics. Springer Berlin Heidelberg. http://link.springer.com/chapter/10.1007/978-3-540-72308-0_8.

Rampling, M. W., H. J. Meiselman, B. Neu, and O. K. Baskurt. 2004. 'Influence of Cell-Specific Factors on Red Blood Cell Aggregation'. *Biorheology* 41 (2): 91–112.

Richardson, J. F., and W. N. Zaki. 1954. 'The Sedimentation of a Suspension of Uniform Spheres under Conditions of Viscous Flow'. *Chemical Engineering Science* 3 (2): 65–73. doi:10.1016/0009-2509(54)85015-9.

Roman, Sophie, Sylvie Lorthois, Paul Duru, and Frédéric Risso. 2013. 'Flow of Concentrated Red Blood Cell Suspensions at Micro-Bifurcations: An in Vitro Experimental Study'. *Computer Methods in Biomechanics and Biomedical Engineering* 16 (sup1): 33–35.

Rossi, Massimiliano, and Christian J. Kähler. 2014. 'Optimization of Astigmatic Particle Tracking Velocimeters'. *Experiments in Fluids* 55 (9). doi:10.1007/s00348-014-1809-2.

Rossi, Massimiliano, Rodrigo Segura, Christian Cierpka, and Christian J. Kähler. 2011. 'On the Effect of Particle Image Intensity and Image Preprocessing on the Depth of Correlation in Micro-PIV'. *Experiments in Fluids* 52 (4): 1063–75. doi:10.1007/s00348-011-1194-z.

Russel, W.B., and P.R. Sperry. 1994. 'Effect of Microstructure on the Viscosity of Hard Sphere Dispersions and Modulus of Composites'. *Progress in Organic Coatings* 23 (4): 305–24. doi:10.1016/0033-0655(94)87001-2.

Sdougos, H. P., S. R. Bussolari, and C. F. Dewey. 1983. 'Secondary Flow and Turbulence in a Cone-and-Plate Device'. *Journal of Fluid Mechanics* 138: 379–404. doi:10.1017/S0022112084000161.

Servais, Colin, Richard Jones, and Ian Roberts. 2002. 'The Influence of Particle Size Distribution on the Processing of Food'. *Journal of Food Engineering* 51 (3): 201–8. doi:10.1016/S0260-8774(01)00056-5.

Shapiro, Andrew P., and Ronald F. Probstein. 1992. 'Random Packings of Spheres and Fluidity Limits of Monodisperse and Bidisperse Suspensions'. *Physical Review Letters* 68 (9): 1422–25. doi:10.1103/PhysRevLett.68.1422.

Shauly, A., A. Averbakh, A. Nir, and R. Semiat. 1997. 'Slow Viscous Flows of Highly Concentrated suspensions—Part II: Particle Migration, Velocity and Concentration Profiles in Rectangular Ducts'. *International Journal of Multiphase Flow* 23 (4): 613–29. doi:10.1016/S0301-9322(96)00077-8.

Smal, Ihor, Marco Loog, Wiro Niessen, and Erik Meijering. 2010. 'Quantitative Comparison of Spot Detection Methods in Fluorescence Microscopy'. *IEEE Transactions on Medical Imaging* 29 (2): 282–301. doi:10.1109/TMI.2009.2025127.

Snabre, P., and P. Mills. 1999. ‘Rheology of Concentrated Suspensions of Viscoelastic Particles’. *Colloids and Surfaces A: Physicochemical and Engineering Aspects* 152 (1–2): 79–88. doi:10.1016/S0927-7757(98)00619-0.

Sochi, Taha. 2011. ‘Slip at Fluid-Solid Interface’. *Polymer Reviews* 51 (4): 309–40. doi:10.1080/15583724.2011.615961.

Soltani, Faezeh, and Ülkü Yilmazer. 1998. ‘Slip Velocity and Slip Layer Thickness in Flow of Concentrated Suspensions’. *Journal of Applied Polymer Science* 70 (3): 515–22. doi:10.1002/(SICI)1097-4628(19981017)70:3<515::AID-APP13>3.0.CO;2-#.

Spangenberg, Jon, George W. Scherer, Adam B. Hopkins, and Salvatore Torquato. 2014. ‘Viscosity of Bimodal Suspensions with Hard Spherical Particles’. *Journal of Applied Physics* 116 (18): 184902. doi:10.1063/1.4901463.

Stickel, Jonathan J., and Robert L. Powell. 2005. ‘Fluid Mechanics and Rheology of Dense Suspensions’. *Annual Review of Fluid Mechanics* 37 (1): 129–49. doi:10.1146/annurev.fluid.36.050802.122132.

Taylor, John R. 1996. *An Introduction to Error Analysis: The Study of Uncertainties in Physical Measurements*. 2nd edition. Sausalito, Calif.: University Science Books.

Tripathi, Anubhav, and Andreas Acrivos. 1999. ‘Viscous Resuspension in a Bidensity Suspension’. *International Journal of Multiphase Flow* 25 (1): 1–14. doi:10.1016/S0301-9322(98)00036-6.

Vennemann, Peter, Kenneth T. Kiger, Ralph Lindken, Bianca C. W. Groenendijk, Sandra Stekelenburg-de Vos, Timo L. M. ten Hagen, Nicolette T. C. Ursem, Rob E. Poelmann, Jerry Westerweel, and Beerend P. Hierck. 2006. ‘In Vivo Micro Particle Image Velocimetry Measurements of Blood-Plasma in the Embryonic Avian Heart’. *Journal of Biomechanics* 39 (7): 1191–1200. doi:10.1016/j.jbiomech.2005.03.015.

Wagner, Christian, Patrick Steffen, and Saša Svetina. 2013. ‘Aggregation of Red Blood Cells: From Rouleaux to Clot Formation’. *Comptes Rendus Physique*, Living fluids / Fluides vivants, 14 (6): 459–69. doi:10.1016/j.crhy.2013.04.004.

Wagner, Norman J., and John F. Brady. 2009. ‘Shear Thickening in Colloidal Dispersions’. *Physics Today* 62 (10): 27–32. doi:10.1063/1.3248476.

Warr, S., and J.-P. Hansen. 1996. ‘Relaxation of Local Density Fluctuations in a Fluidized Granular Medium’. *EPL (Europhysics Letters)* 36 (8): 589. doi:10.1209/epl/i1996-00273-1.

Warr, Stephen, George T. H. Jacques, and Jonathan M. Huntley. 1994. ‘Tracking the Translational and Rotational Motion of Granular Particles: Use of High-Speed Photography and Image Processing’. *Powder Technology* 81 (1): 41–56. doi:10.1016/0032-5910(94)02863-X.

Wereley, S. T., and C. D. Meinhart. 2005. ‘Micron-Resolution Particle Image Velocimetry’. In *Microscale Diagnostic Techniques*, edited by Prof Kenneth S. Breuer, 51–112. Springer Berlin Heidelberg. http://link.springer.com/chapter/10.1007/3-540-26449-3_2.

Wereley, Steven T., and Carl D. Meinhart. 2010. ‘Recent Advances in Micro-Particle Image Velocimetry’. *Annual Review of Fluid Mechanics* 42 (1): 557–76. doi:10.1146/annurev-fluid-121108-145427.

Westerweel, J. 2000. ‘Theoretical Analysis of the Measurement Precision in Particle Image Velocimetry’. *Experiments in Fluids* 29 (1): S003-S012. doi:10.1007/s003480070002.

Westerweel, J. 2007. ‘On Velocity Gradients in PIV Interrogation’. Experiments in Fluids 44 (5): 831–42. doi:10.1007/s00348-007-0439-3.

Whitmore, Raymond Leslie. 1968. *Rheology of the Circulation*. Pergamon Press.

Wiederseiner, Sébastien, Nicolas Andreini, Gaël Epely-Chauvin, and Christophe Ancey. 2010. 'Refractive-Index and Density Matching in Concentrated Particle Suspensions: A Review'. *Experiments in Fluids* 50 (5): 1183–1206. doi:10.1007/s00348-010-0996-8.

Williams, Stuart J., Choongbae Park, and Steven T. Wereley. 2010. 'Advances and Applications on Microfluidic Velocimetry Techniques'. *Microfluidics and Nanofluidics* 8 (6): 709–26. doi:10.1007/s10404-010-0588-1.

Wyart, M., and M. E. Cates. 2014. 'Discontinuous Shear Thickening without Inertia in Dense Non-Brownian Suspensions'. *Physical Review Letters* 112 (9): 98302. doi:10.1103/PhysRevLett.112.098302.

Xu, Yuan-Qing, Fang-Bao Tian, and Yu-Lin Deng. 2012. 'An Efficient Red Blood Cell Model in the Frame of Ib-Lbm and Its Application'. *International Journal of Biomathematics* 6 (1): 1250061. doi:10.1142/S1793524512500611.

Yilmaz, Fuat, and Mehmet Yasar Gundogdu. 2008. 'A Critical Review on Blood Flow in Large Arteries; Relevance to Blood Rheology, Viscosity Models, and Physiologic Conditions'. *Korea-Australia Rheology Journal* 20 (4): 197–211.

Yilmazer, Ulku, and Dilhan M. Kalyon. 1989. 'Slip Effects in Capillary and Parallel Disk Torsional Flows of Highly Filled Suspensions'. *Journal of Rheology (1978-Present)* 33 (8): 1197–1212. doi:10.1122/1.550049.

Yoshimura, Ann, and Robert K. Prud'homme. 1988. 'Wall Slip Corrections for Couette and Parallel Disk Viscometers'. *Journal of Rheology (1978-Present)* 32 (1): 53–67. doi:10.1122/1.549963.

Zhang, Junfeng, Paul C. Johnson, and Aleksander S. Popel. 2007. 'An Immersed Boundary Lattice Boltzmann Approach to Simulate Deformable Liquid Capsules and Its Application to Microscopic Blood Flows'. *Physical Biology* 4 (4): 285–95. doi:10.1088/1478-3975/4/4/005.

Zhang, Junfeng, Paul C. Johnson, and Aleksander S. Popel. 2008. 'Red Blood Cell Aggregation and Dissociation in Shear Flows Simulated by Lattice Boltzmann Method'. Journal of Biomechanics 41 (1): 47–55. doi:10.1016/j.jbiomech.2007.07.020.

Zhou, Zhongwu, Peter J Scales, and David V Boger. 2001. 'Chemical and Physical Control of the Rheology of Concentrated Metal Oxide Suspensions'. *Chemical Engineering Science* 56 (9): 2901–20. doi:10.1016/S0009-2509(00)00473-5.

Zhu, Lixuan, and Daniel De Kee. 2002. 'Slotted-Plate Device To Measure the Yield Stress of Suspensions: Finite Element Analysis'. *Industrial & Engineering Chemistry Research* 41 (25): 6375–82. doi:10.1021/ie010606b.

Zhu, W., Y. Knapp, and V. Deplano. 2016. 'Low Hazard Refractive Index and Density-Matched Fluid for Quantitative Imaging of Concentrated Suspensions of Particles'. *Experiments in Fluids* 57 (5): 1–8. doi:10.1007/s00348-016-2150-8.

Zou, R. P, J. Q Xu, C. L Feng, A. B Yu, S Johnston, and N Standish. 2003. 'Packing of Multi-Sized Mixtures of Wet Coarse Spheres'. *Powder Technology* 130 (1–3): 77–83. doi:10.1016/S0032-5910(02)00229-2.